



MONASH University

**GAS-SOLID FLOW
CHARACTERISTICS AND SCALING
OF SPOUTED BEDS WITH NON-
SPHERICAL PARTICLES**

By
Xuejiao Liu

A THESIS SUBMITTED FOR THE DEGREE

OF

DOCTOR OF PHILOSOPHY

**IN THE LABORATORY FOR SIMULATION AND MODELLING
OF PARTICULATE SYSTEMS, DEPARTMENT OF CHEMICAL
ENGINEERING, MONASH UNIVERSITY, CLAYTON, VIC 3800,**

AUSTRALIA

January 2019

CONTENTS

ABSTRACT	V
COPYRIGHT NOTICE	VII
ACKNOWLEDGMENTS	IX
LIST OF FIGURES	X
LIST OF TABLES	XVI
CHAPETER 1 INTRODUCTION	1
1.1 Background and research gaps.....	2
1.2 Thesis outline	5
CHAPTER 2 LITERATURE REVIEW	8
2.1 Experiments	9
2.1.1 Drying	9
2.1.2 Coating.....	12
2.1.4 Combustion, gasification and pyrolyzation	14
2.1.5 Studies on the dynamic characteristics of spouting non-spherical particles	16
2.2 Modeling of spouted beds with non-spherical particles	18
2.3 Scale-up of spouted beds	22
2.4 Summary	25
Reference	26
CHAPTER 3 EXPERIMENTAL STUDY ON THE SPOUTING AND MIXING BEHAVIORS OF CYLINDROID PARTICLES	34
3.1 Introduction.....	35
3.2 Experiments	36
3.3 Evolution of the spouting process.....	40
3.4 Characteristics of pressure drops	46
3.4.1 Effects of volume fraction of cylindroid particles on the pressure drop	46
3.4.2 Effects of particle size on the pressure drop	48
3.5 Characteristics of stable spouting	51
3.5.1 The maximum volume fraction of bamboo particles, $X_{c,max}$ in mixture	51
3.5.2 Fountain height	53
3.6 Key parameters and their influence on the mixing behaviors.....	54
3.6.1 Effects of particle shapes	54
3.6.2 Effects of the size of bed materials	57
3.6.3 Effects of the volume fraction of cylindroid particles	59
3.6.4 Effects of the static bed height.....	61
3.7 Summaries.....	62
Reference:	64

CHAPTER 4 CFD-DEM SIMULATIONS ON THE SPOUTING BEHAVIORS OF CYLINDROID PARTICLES	67
4.1 Introduction.....	68
4.2 CFD-DEM models for the gas-solid flows with cylindroid particles	70
4.2.1 Turbulence model of gas phase.....	70
4.2.2 Representation of cylindroid particles	72
4.2.3 Motion equations of cylindroid particles	73
4.2.4 Calculations of forces on cylindroid particles	75
4.2.5 Initial conditions and boundary conditions.....	86
4.2.6 Numerical solutions	88
4.2.7 Validation of models	90
4.3 CFD-DEM study on the spouting of cylindroid particles in a spouted bed....	91
4.3.1 Computational conditions	91
4.3.2 Macroscale flow patterns	93
4.3.3 Particle velocity	95
4.3.4 Orientations of cylindroid particles in the spouted bed	98
4.3.5 Coordination number (CN) of cylindroid particles in the spouted bed	104
4.4 Summaries.....	108
Reference	110
CHAPTER 5 GAS-SOLID FLOW CHARACTERISTICS AND SCALE-UP OF SPOUTED BEDS	116
5.1 Introduction.....	117
5.2 TFM approach for spouted beds and model validations.....	119
5.2.1 TFM models for spouted beds	120
5.2.2 Model validations.....	122
5.3 Evaluation on the effect of conical geometry on flow behaviors in spouted beds	125
5.3.1 Gas and solid flow distributions	126
5.3.2 Particle velocity	129
5.3.3 Voidage in the spout.....	131
5.3.4 Diameter of the spout.....	131
5.4 Interactions of spout jets in a multiple-spouted bed.....	133
5.4.1 Properties of objects and numerical parameters	134
5.4.2 Effects of central spouting gas flow rate.....	135
5.4.3 Effects of lateral spouting gas flow rate.....	137
5.4.4 Effects of the effects of baffles	138
5.5 Prediction of minimum spouting velocity by TFM	142
5.5.1 Determination of minimum spouting velocity.....	142
5.5.2 Approach evaluation	145

5.6 Hydrodynamic characteristics of the scaling spouted bed.....	150
5.6.1 Typical flow patterns.....	151
5.6.2 Effects of key parameters on the minimum spouting velocity in scaling	152
5.6.3 Development of a new correlation.....	155
5.7 Summaries.....	159
Reference	160
CHAPTER 6 MIXING BEHAVIORS IN AN INDUSTRIAL SPOUT-FLUID MIXER.....	165
6.1 Introduction.....	166
6.2 Particle properties and mixer structure	168
6.3 Model description and numerical solutions	169
6.4 Model validation	173
6.5 Typical mixing process	174
6.5.1 Flow behaviors of solids in the mixer.....	174
6.5.2 Mixing effectiveness.....	177
6.6 Effects of spouting gas flowrate.....	181
6.7 Effects of fluidizing gas flowrate.....	184
6.8 Summaries.....	187
Reference	188
CHAPTER 7 CONCLUSIONS AND FURTHER STUDIES.....	192
7.1 Conclusions.....	193
7.2 Future work.....	196
List of publications.....	198

ABSTRACT

A spouted bed as one of the typical fluidization reactors has been widely used in agriculture, food, pharmacy, energy, environment, chemical industry and many other fields, showing the commercial success in a variety of physical operations such as drying, blending, granulation, cooling, coating, as well as the attractive prospects in the thermochemical processes including coal gasification, resource utilization of biomass, oil shale pyrolysis, petroleum catalytic cracking, etc. In these processes, more than 70% of particles are non-spherical. The gas-solid flow behaviors of non-spherical particles in spouted beds are significantly different from that of spherical particles. However, up to today, our knowledge on the spouting dynamics of non-spherical particles is very limited, leading to numerous difficulties in the design, operation or optimization of spouted beds. On the other hand, the technological gap in scale-up of spouted beds has also limited their application in large industrial processes. This thesis represents some efforts to reveal the complex spouting characteristics of non-spherical particles and the scaling relationships of spouted beds by experiments and simulations.

The spouted bed experimental system was established and the spouting behaviors of the mixtures of cylindroid particles and spherical bed materials were investigated. Results indicated that in the spouted bed with two kinds of particles, the spouting process and mixing process usually develop synchronously. Once the spouting is well established, the particles in the bed will easily achieve the complete mixing. Detailed relationships between spouting characteristics and operating parameters were also obtained. Based on such relationships, two different non-spherical particle spouting systems, i.e., the spouting system dominated by the non-spherical particles and that dominated by bed materials were distinguished.

The CFD-DEM model of spouting cylindroid particles was improved in the current dissertation. The combined geometric elements method was used to construct the realistic cylindroid particles. The various contact criterions and contact forces between cylindrical surface, flats and edges were comprehensively analyzed and investigated, and the Syamlal-O'Brien model was improved to calculate the interaction forces between cylinders and fluid. Based on the CFD-DEM simulations on "turbulent gas phase + real cylinders + spouting", the particle-scale spouting behaviors of cylinders and the effects of particle shape were revealed.

The numerical scale-up and design method were developed. By directly predicting the gas-solid flow behaviors in small- and large-scale spouted bed with the CFD approach, the effects of particle properties, bed structures and operating conditions on the dynamic behaviors in spouted beds with different scales were systematically studied and a new correlation was proposed to predict the minimum spouting velocity in both small and large spouted beds. Lastly this developed numerical scale-up method was successfully used to design an industrial scale biomass-carrier mixer.

Key words: Spouted bed; Non-spherical particle; Scale-up; CFD-DEM

COPYRIGHT NOTICE

I certify that I have made all reasonable efforts to secure copyright permissions for third-party content included in this thesis and have not knowingly added copyright content to my work without the owner's permission.

DECLARATION

This thesis contains no material which has been accepted for the award of any other degree or diploma at any university or equivalent institution and that, to the best of my knowledge and belief, this thesis contains no material previously published or written by another person, except where due reference is made in the text of the thesis.

Signature:



Print Name: Xuejiao Liu

Date: January 2019

ACKNOWLEDGMENTS

I would like to express my sincere gratitude to my supervisors Prof. Wenqi Zhong and Prof. Aibing Yu, for their thorough and valuable guidance, help, inspiration and financial support for the completion of this project. I also wish to thank them for giving me the opportunity to study in Monash University and greatly improve my work. This work would not be possible without their wise guidance and strong supports.

I would like to acknowledge with appreciation the numerous and valuable supports and suggestions for the project implementation from my partners, colleagues and mentors. Especially, Dr. Xi Chen, Dr. Huibin Xu, Xiaofeng Jiang and Lei Pang provided me strong assistance for the successful construction, maintenance and operation of the spouted bed experimental system in the chapter 1. Prof. Aibing Yu and Prof. Ruiping Zou provided me the advanced computational resources for the simulation works in Chapter 3, and Dr. Ganjie Qing helped establish the numerical simulation platform for the cylindroid particles on the basis of their excellent academic accumulations. Prof. N Epstein and Prof. J R Grace from University of British Columbia suggested the idea to obtain the minimum spouting velocity using numerical methods and provided the detailed review with significant improvement in writing the published papers in Chapter 4. Dr. Dailin Chen provided the valuable help in the simulation experimentations on the multiple-spouted beds. The engineering application in Chapter 5 came from the scientific project of Hongkong and China Goup and they provided a lot of valuable suggestions for the design of the mixer. The draft drawing and the design of the control system were finished by Dr. Guanwen Zhou. Prof. Mingyao Zhang and Prof. Aibing Yu provided the valuable guidance, experience and evaluation for the mixer design and paper writing. Thanks are also given to Bernard Xu for his careful and patient assistance in revising my thesis. Their supports and suggestions greatly helped to improve the quality of my project and thesis.

Finally, I would like to give special thanks and endless love to my family.

LIST OF FIGURES

- Figure 1-1 Typical non-spherical particles in spouted bed applications
- Figure 2-1 Drying and deformation of non-spherical particles in spouted beds:(a) carrot cubes [10], (b) carrageenan gel particles [9]
- Figure 2-2 Picture of Ikerlan IK-4 pyrolysis pilot plant with the conical spouted bed reactor designed by the Olazar's team [33]
- Figure 2-3 Changes of minimum spouting velocity U_{ms} with particle sphericity ϕ [43]
- Figure 2-4 Typical CFD-DEM studies on the non-spherical particles: (a) the fluidizing behaviors of ellipsoidal particles, (b) the mixing behaviors of spherical particles and cuboid particles in the fluidized bed, (c) the spouting of corn-shape particles
- Figure 2-5 Three typical scaling modes of spouted beds: (a) scaling up with the dimensional similitude methodology, (b) extending the small-scale spouted bed in a certain single dimension to construct the slot-rectangular spouted bed, (c) parallel merging the small-sized spout units to assemble spouted beds with multiple-spout geometries
- Figure 2-6 Experiments on the multiple-spout bed with continuous operations [99]
- Figure 3-1 Experiment setup of the spouted bed: (a) diagram scheme; (b) scene photograph
- Figure 3-2 Evolutions of flow patterns and total pressure drops in gas flow ascending and descending processes with Cylinders A and glass beads ($H_0=300$ mm, $X_c=0.4$)
- Figure 3-3 Evolutions of total pressure drop in the gas flow ascending when handling Cylinders A and glass beads with varying X_c ($H_0=300$ mm)
- Figure 3-4 Evolutions of total pressure drop in the gas flow ascending when handling glass beads and different cylindroid particles ($H_0=300$ mm, $X_c=0.4$)
- Figure 3-5 The maximum pressure drop when handling glass beads and different cylindroid particles with varying X_c ($H_0=300$ mm)
- Figure 3-6 Snapshots of external spouting states handling the mixtures of glass beads and different cylindroid particles with varying X_c ($H_0=300$ mm, $u=106$ m/s): (a) Cylinder A with $d_v=9.9$ mm and $l/d=1.25$; (b) Cylinder B with $d_v=6.8$ mm and $l/d=2.5$; (c) Cylinder C with $d_v=7.2$ mm and $l/d=5$.
- Figure 3-7 Fountain heights when spouting the mixtures of glass beads and different cylindroid particles with varying X_c ($H_0=300$ mm, $u=106$ m/s)
- Figure 3-8 u_{ms} of the mixing system including the cylinders with varying shape: (a) $d_s=2.6$ mm; (b) $d_s=1.4$ mm

Figure 3-9 The change of u_{ms} in the spouted bed with the particle sizes of bed material varying from 1.41 mm to 3.4 mm: (a) cylinder E1 6×13.5; (b) cylinder D2 5×19.4; (c) cylinder D3 4×30.4

Figure 3-10 The effects of volume fraction of cylindroid particles on u_{ms} in the spouted bed with binary particles: (a) $d_s=2.6$ mm, (b) $d_s=1.4$ mm

Figure 3-11 The effects of the static bed height on u_{ms} in the spouted bed with binary particles ($d_s=1.4$ mm) : (a) D1 ($d \times L = 6 \text{ mm} \times 13.5 \text{ mm}$), (b) D2 ($d \times L = 5 \text{ mm} \times 19.4 \text{ mm}$)

Figure 4-1 Representation of the realistic cylindroid particles in DEM

Figure 4-2 Comparisons between experimental phenomena and the simulated results with the different contact force models ($U=2.0$ m/s, $H_0=0.08$ m, $L=6.0$ mm, $d=2.6$ mm): (a) the experimental results from Zhong et al. [14]; (b) simulation with the Hertz-Mindlin contact force model (Equation 4-19); (c) simulation with the linear spring-damper model of contact force(Equation 4-20)

Figure 4-3 Comparisons between experimental phenomena and the simulated results with the different drag coefficient models ($U=2.0$ m/s, $H_0=0.08$ m, $L=6.0$ mm, $d=2.6$ mm, with gas-solid interaction force model from Di Felice [44]): (a) the experimental results from Zhong et al. [14]; (b) simulation with the Tran-Cong drag coefficient model [45], (c) simulation with the Holzer and Sommerfeld model [46], (d) simulation with the drag coefficient model from Ren et al. [47]

Figure 4-4 Different simulation results with the varying combinations of drag force coefficient models and gas-solid exchange coefficient models ($U=2.0$ m/s, $H_0=0.08$ m, $L=6.0$ mm, $d=2.6$ mm): (a) Di Felice model [44] & Holzer-Sommerfeld model [46], (b) Di Felice model [44] & Ren model [47], (c) Gidaspow model [83] & Holzer-Sommerfeld model [46], (d) Gidaspow model [83] & Ren model [47], (e) Syamlal-O'Brien model [81] & Holzer-Sommerfeld model[46], (f) Syamlal-O'Brien model [81]& Ren model [47]

Figure 4-5 Flow sheet for the numerical procedure of the CFD-DEM simulations on non-spherical particles

Figure 4-6 Comparisons between experimental results and CFD-DEM simulations in the fluidized bed with non-spherical particles [14]: (a) the structures and dimensional sizes of the fluidized bed and cylindroid particles; (b) $U=1.5$ m/s, (c) $U=2.0$ m/s

Figure 4-7 Geometry of the pseudo 2D rectangular spouted bed and the grid for gas phase

Figure 4-8 Macroscale flow patterns of cylindroid particles with varying aspect ratios ($u_g=6$ m/s, $H_0=0.21$ m, $\rho_p=1200$ kg/m³, $V_p=42.39$ mm³)

Figure 4-9 Fountain height of cylindroid particles with varying aspect ratios

($u_g=6$ m/s)

Figure 4-10 Spout shape of cylindroid particles with varying aspect ratios ($u_g=6$ m/s)

Figure 4-11 The time-averaged radial particle velocity distributions of three typical particles ($L/d=0.25, 1.0$ and 2.0) at the varying bed heights ($u_g=6$ m/s)

Figure 4-12 The radial time-averaged velocity distributions of particles with the varying L/d at the same bed height ($u_g=6$ m/s): (a) $h=0.06$ m; (b) $h=0.18$ m

Figure 4-13 The radial time-averaged velocity distributions of particles with the varying L/d ($u_g=6$ m/s)

Figure 4-14 The time-averaged radial orientation distributions of three kinds of cylindroid particles with varying shapes ($u_g=6$ m/s): (a) $L/d=0.25$; (b) $L/d=1.0$; (c) $L/d=2.0$

Figure 4-15 The time-averaged angle distributions of the particles with varying shapes in the spout region ($u_g=6$ m/s): (a) disc-like particles; (b) rod-like particles

Figure 4-16 The time-averaged angle distributions of the particles with varying shapes in the fountain region ($u_g=6$ m/s): (a) disc-like particles; (b) rod-like particles

Figure 4-17 The time-averaged angle distributions of the particles with varying shapes in the fountain region (left, $u_g=6$ m/s) and in the packing state (right) : (a) disc-like particles; (b) rod-like particles

Figure 4-18 The time-averaged radial CN distributions of three kinds of cylindroid particles with varying shapes ($u_g=6$ m/s): (a) $L/d=0.25$; (b) $L/d=1.0$; (c) $L/d=2.0$

Figure 4-19 The time-averaged CN distributions of the particles with varying shapes in the spout region ($u_g=6$ m/s) : (a) disc-like particles; (b) rod-like particles

Figure 4-20 The time-averaged CN distributions of the particles with varying shapes in the annulus region ($u_g=6$ m/s) : (a) disc-like particles; (b) rod-like particles

Figure 4-21 The time-averaged CN distributions of the particles with varying shapes in the fountain region ($u_g=6$ m/s)

Figure 5-1 Comparisons between the experiments [45,46] and simulations on the spouted bed with the diameter of 152 cm: (a) simulated spouting with $u=1.2u_{ms}$; (b) comparisons of particle velocity and voidage in the bed with $u=1.2u_{ms}$; (c) comparison of the boundary of the spout with $u=1.1u_{ms}$

Figure 5-2 Comparisons between experiments [28] and simulations for the multiple-spout bed (left: experiments, right: simulations): (a) $H_0/D_{t0}=1.0$, $Q_c/Q_{mf}=1.2$, $Q_a/Q_{mf}=3.03$; (b) $H_0/D_{t0}=1.5$, $Q_c/Q_{mf}=3.6$, $Q_a/Q_{mf}=1.65$

Figure 5-3 Flow patterns in different beds with $u=42$ m/s and $H_0=0.325$ m: (a) $\gamma=30^\circ$; (b) $\gamma=60^\circ$; (c) $\gamma=90^\circ$; (d) $\gamma=105^\circ$; (e) $\gamma=120^\circ$; (f) $\gamma=150^\circ$; (g) $\gamma=180^\circ$

Figure 5-4 Gas velocities in different beds with $u=42$ m/s and $H_0=0.325$ m: (a) $\gamma=30^\circ$; (b) $\gamma=60^\circ$; (c) $\gamma=90^\circ$; (d) $\gamma=105^\circ$; (e) $\gamma=120^\circ$; (f) $\gamma=150^\circ$; (g) $\gamma=180^\circ$

Figure 5-5 Particle velocities in different beds with $u=42$ m/s and $H_0=0.325$ m: (a) $\gamma=30^\circ$; (b) $\gamma=60^\circ$; (c) $\gamma=90^\circ$; (d) $\gamma=105^\circ$; (e) $\gamma=120^\circ$; (f) $\gamma=150^\circ$; (g) $\gamma=180^\circ$

Figure 5-6 Fountain heights in different spouted beds with $u=42$ m/s and $H_0=0.325$ m

Figure 5-7 Radical profiles of vertical particle velocity in the spout regions of different beds with $u=42$ m/s and $H_0=0.325$ m

Figure 5-8 The central axis profiles of the vertical particle velocity in different spouted beds with $u=42$ m/s and $H_0=0.325$ m

Figure 5-9 Radical profiles of vertical particle velocity in the annulus regions of different beds with $u=42$ m/s and $H_0=0.325$ m

Figure 5-10 Radical profiles of voidage in the spout regions of different beds with $u=42$ m/s and $H_0=0.325$ m

Figure 5-11 The distributions of diameters of spouts: (a) comparison of simulated and experimental results; (b) simulated results

Figure 5-12 Sketch of the simulated beds and corresponding physical parameters

Figure 5-13 Simulated flow patterns with different central gas flow rates ($H_0/D_{t0}=1.0$, $Q_a/Q_{mf}=3.03$): (a) $Q_c/Q_{mf}=1.0$, (b) $Q_c/Q_{mf}=1.5$, (c) $Q_c/Q_{mf}=2.0$, (d) $Q_c/Q_{mf}=2.5$, (e) $Q_c/Q_{mf}=3.03$

Figure 5-14 Simulated flow patterns with different lateral gas flow rates ($H_0/D_{t0}=1.5$, $Q_c/Q_{mf}=3.6$): (a) $Q_a/Q_{mf}=1.0$, (b) $Q_a/Q_{mf}=1.5$, (c) $Q_a/Q_{mf}=2.0$, (d) $Q_a/Q_{mf}=2.5$, (e) $Q_a/Q_{mf}=3.03$, (f) $Q_a/Q_{mf}=3.6$

Figure 5-15 Vector fields of particle velocities in the multi-spouted bed with double-spouting mode ($H_0/D_{t0}=1.0$, $Q_c/Q_{mf}=1.2$, $Q_a/Q_{mf}=3.03$): (a) no baffle; (b) $H_b=1/2$; (c) $H_b=H_0$

Figure 5-16 Vector fields of particle velocities in the multi-spouted bed with single-spouting mode ($H_0/D_{t0}=1.5$, $Q_c/Q_{mf}=3.6$, $Q_a/Q_{mf}=1.5$): (a) no baffle; (b) $H_b=1/2$; (c) $H_b=H_0$

Figure 5-17 Vector fields of particle velocities in the multi-spouted bed with triple-spouting mode ($H_0/D_{t0}=1.5$, $Q_c/Q_{mf}=3.03$, $Q_a/Q_{mf}=3.03$): (a) no baffle; (b) $H_b=1/2$; (c) $H_b=H_0$

Figure 5-18 Simulated distribution of solids volume fraction and particle vector field versus superficial gas velocity for conical-cylindrical spouted bed ($e=0.88$, $\alpha_{s,max}=0.63$,

$d_s=1.41$ mm, $H_0=325$ mm, $D_i=19$ mm, $D_c=152$ mm)

Figure 5-19 Flow sheet for identification of minimum spouting velocity u_{ms} in flow descending process

Figure 5-20 Comparisons of simulated variation of u_{ms} with d_s to predictions by empirical equations

Figure 5-21 Comparisons of simulated variation of u_{ms} with H_0 to predictions by empirical equations

Figure 5-22 Comparisons of simulated variation of u_{ms} with D_c/D_i to predictions by empirical equations

Figure 5-23 Typical flow patterns in spouted beds of seven different scales, all with $H_0/D_c=2.0$, $d_s=2.8$ mm, $\rho_s=2503$ kg/m³, $D_c/D_i=8$): (a) $D_c=0.304$ m, $u=71$ m/s; (b) $D_c=0.456$ m, $u=66$ m/s; (c) $D_c=0.608$ m, $u=62$ m/s; (d) $D_c=0.760$ m, $u=59$ m/s; (e) $D_c=0.912$ m, $u=58$ m/s; (f) $D_c=1.064$ m, $u=57$ m/s; (g) $D_c=1.216$ m, $u=54$ m/s.

Figure 5-24 Changes of u_{ms} with varying d_s for columns of different diameter

Figure 5-25 Changes of u_{ms} with varying ρ_s for columns of different diameter

Figure 5-26 Changes of u_{ms} with varying H_0/D_c for columns of different diameter

Figure 5-27 Changes of u_{ms} with varying D_c/D_i for columns of different diameter

Figure 5-28 Comparison of simulated data with: (a) correlation between u_{ms} and d_s ; (b) correlation between u_{ms} and ρ_s ; (c) correlation between u_{ms} and H_0 ; (d) correlation between u_{ms} and D_c/D_i

Figure 5-29 Comparisons of predictions from correlations and experimental data: (a) the inlet minimum spouting velocity, u_{ms} , and Equation (1); (b) the superficial minimum spouting velocity, U_{ms} , and Equation (3)

Figure 6-1 Industrial-scale spout-fluid bed mixing system: (a) materials in the given industrial process; (b) schematic of the proposed mixer and its main parts and sizes

Figure 6-2 Comparison of simulation results with experimental data reported by Sun et al. [38]

Figure 6-3 Typical flow behaviors of heat-carrier and biomass particles with $Q_s=0.067$ kg/s and $Q_f=0.035$ kg/s: (a) volume fraction of heat-carrier particles; (b) volume fraction of biomass particles. (left: 3D view; middle: $z=0$ section; right: $x=0$ section)

Figure 6-4 Typical velocity fields and motion paths of biomass particles with $Q_s=0.067$ kg/s and $Q_f=0.035$ kg/s. (left: $z=0$ section; middle: $z=x$ section; right: $x=0$ section)

Figure 6-5 Monitoring results of the flowrates of heat-carrier and biomass at four outlets and the corresponding particle behaviors in the mixer with $T_s=10.2$ s, $\Delta t_s=0.3s$,

$Q_s=0.067$ kg/s and $Q_f=0.035$ kg/s

Figure 6-6 Evaluation of mixing effectiveness: (a) monitoring results of mass ratio of carrier and biomass at four outlets; (b) statistical analysis to sampling data. ($Q_s=0.067$ kg/s and $Q_f=0.035$ kg/s)

Figure 6-7 Effects of spouting gas flowrate on the flow behaviors in mixer with $Q_f=0.044$ kg/s: (a) $Q_s/Q_f=0.8$; (b) $Q_s/Q_f=1.2$; (c) $Q_s/Q_f=1.6$; (d) $Q_s/Q_f=2.0$. (The contour is for the volume fraction of carrier particles. left: $x=0$ section, right: $z=0$ section)

Figure 6-8 Monitoring results of mass ratio of carrier and biomass at four outlets under the conditions of $Q_f=0.044$ kg/s and: (a) $Q_s/Q_f=0.8$; (b) $Q_s/Q_f=1.2$; (c) $Q_s/Q_f=1.6$; (d) $Q_s/Q_f=2.0$

Figure 6-9 Effects of spouting gas flowrate on mixing effectiveness with $Q_f=0.044$ kg/s: (1) statistical analysis to sampling data; (2) Change of M_e with varying Q_s/Q_f

Figure 6-10 Effects of fluidizing gas flowrate on the flow behaviors in mixer with $Q_s=0.058$ kg/s: (a) $Q_f/Q_s=0.5$; (b) $Q_f/Q_s=1.0$; (c) $Q_f/Q_s=1.5$ (The contour is for the volume fraction of carrier particles. left: $x=0$ section, right: $z=0$ section)

Figure 6-11 Monitoring results of mass ratio of carrier and biomass at four outlets under the conditions of $Q_s=0.058$ kg/s and: (a) $Q_f/Q_s=0.5$; (b) $Q_f/Q_s=1.0$; (c) $Q_f/Q_s=1.5$

Figure 6-12 Effects of fluidizing gas flowrate on mixing effectiveness with $Q_s=0.058$ kg/s: (1) statistical analysis to sampling data; (2) Change of M_e with varying Q_f/Q_s

LIST OF TABLES

- Table 3-1 The Properties of particles used in experiments
- Table 4-1 Cylinder-cylinder contact scenario and criteria [32,33,34]
- Table 4-2 Equations of the drag force coefficient C_D for individual non-spherical particle and gas-solid exchange coefficient β for the gas-solid system
- Table 4-3 Properties of cylindroid particles
- Table 4-4 The main physical and numerical parameters for simulations
- Table 5-1 Main equations and models for CFD (TFM) for spouted beds
- Table 5-2 General initial conditions and boundary conditions adopted for spouted beds [39,44]
- Table 5-3 Properties of the spouted bed system and main numerical parameters [39, 45, 46]
- Table 5-4 Physical properties of the objects and numerical parameters [28]
- Table 5-5 Physical properties of the objects and numerical parameters
- Table 5-6 Empirical equations for U_{ms} in conical-cylindrical spouted bed
- Table 6-1 Models for the interactions between phases
- Table 6-2 Properties of materials for the mixer and numerical parameters

CHAPETER 1 INTRODUCTION

1.1 Background and research gaps

Spouted bed is a typical fluidization device with the superior ability to handle the nonconventional particles with larger size, non-spherical shape or cohesive texture, and provide good particle circulation, effective fluid-particle contact, and high rates of heat and mass transfer. After more than 60 years' development, it has been widely used in agriculture, food, pharmacy, energy, environment, chemical industry and many other fields, showing the commercial successes in a variety of physical operations such as drying, blending, granulation, cooling, coating, as well as the attractive prospects in the thermochemical processes including coal gasification, resource utilization of biomass, oil shale pyrolysis, petroleum catalytic cracking, etc. As more than 70% of particles involved in these processes are non-spherical, seen in [Figure 1-1](#), understanding the fundamentals generally governing the spouting behaviors and dynamics of non-spherical particles is of great importance for the development and improvement of spouted bed technology.



[Figure 1-1](#) Typical non-spherical particles in spouted bed applications

In a spouted bed, non-spherical particles like ellipsoidal, cylindroid, polyhedral, plate-shaped, tablet-shaped, or ring like particles and so on, have significant differences from

spherical particles in the gas-solid flow behaviors, mass and heat transfers and reaction mechanisms. Non-spherical particles usually consist of complicated vertexes, edges and surfaces, forming diverse geometrical contact scenarios and interactions when they contact with neighboring particles or surrounding fluids, and thus perform different macroscopic spouting behaviors from conventional spherical particles. For example, angular particles (e.g., elongated and flatted ones) are likely to interlock each other and form solid-like assemblies, exhibiting stronger resistance to shear than smooth spheres, which make them more difficult to fluidize. On the other hand, the shape heterogeneousness and orientation in fluids usually also intensify the complication of interactions between non-spherical particles and turbulent fluids. Such influences of non-spherical particle shapes on flow behaviors inevitably will further affect the mass/heat transfer and reaction processes of particle-particle or particle-fluid.

Up to now, most studies on spouted beds still limit to handling spherical particles. Existing researches referring to non-spherical particles usually focus on the specific particles (e.g., grains, diced fruits, biomass and solid waste particles, etc.) that are involved in some particular practical processes such as drying, coating, blending, cooling, thermal reaction and so on. The emphases were often on exploring the feasibility and effectiveness of using spouted beds as the gas-solid device to deal with such unconventional particles in above processes, and the corresponding improvements or optimizations in spouted bed structures or operations, and some other aspects. Nevertheless, our knowledge for non-spherical particles in spouted beds are still significantly lacking even on the most fundamental and general spouting dynamics and mass/heat transfer mechanisms. Many issues, for example, what are the detailed motion modes of non-spherical particles in spouted beds, how to characterize their spouting behaviors and key parameters and so on, have not yet been clearly understood. The lack of effective measurement and simulation methods brings more difficulties and challenges to the researches on spouting non-spherical particles.

Another technological gap in the design and application of spouted bed is the scale-up of the units. Despite the inclusion of words such as “scaleup” and “scaling” in the title

of a number of articles dealing with spouted beds, there are no established procedures for scale-up and considerable uncertainty about how best to achieve it. As the gas and solid flow behaviors in spouted beds are closely related to many factors including the gas and particles properties, column geometry and operating conditions, traditional dimensional similitude methodology for scaling spouted bed often has to simultaneously nearly match a large group of dimensionless parameters (e.g., $\frac{gd_p}{U^2}$, $\frac{\rho d_p U}{\mu}$, $\frac{\rho_p}{\rho}$, $\frac{H}{d_p}$, $\frac{D_i}{d_p}$, ϕ_s , ε_0 , φ , PSD, e , etc.) to achieve the identical dimensionless hydrodynamic behaviors in columns of different sizes. Deliberately mismatching the dimensionless groups, one or two at a time, led to significant lack of agreement between original and the upscaled ones. In practice, however, it is clearly difficult to match so many dimensionless groups, or to carry out tests in which similitude is ensured by strict adherence to matching of all important independent dimensionless groups. The task of matching will be obviously more difficult if other variables, such as those related to pressurization, heat transfer and chemical reaction, also need to be considered in the particular application. Another powerful way for scaling spouted bed is to establish the “slot-rectangular spouted bed” by stretching spouted bed only in one dimension, or the “multiple-spouted bed” by merging several small units into one larger column. However, the gas-solid hydrodynamics in these two new spouted beds are still very far from being clearly understood. Numerous challenges, for example, the more complicated flow patterns and frequently occurring instabilities due to the three-dimensionality of slot-rectangular spouted bed or the strong interactions of spout jets in the multiple-spouted beds, are requiring solutions. Overall, scale-up is an important and difficult aspect in the design and operation of spouted bed units. It is of essential significance for the engineering applications of spouted beds to develop useful scaling theories, experiments and simulations and seek effective scaling methodologies.

In addition to above research gaps in fundamentals and engineering applications of spouted bed, the current study was also proposed against a particular background: our research group has been studying spouted bed (or spout-fluidized bed) for more than

20 years and obtained rich and significant findings by developing a series of powerful research methods including experimental studies and numerical simulations. The spouted bed was one of typical gas-solid reactors being emphatically studied in our National Natural Science Foundation Project (NNSFP) (No. 51325601) and the Natural Science Foundation Project of Jiangsu Province (No. BK20130022) that aim to make breakthroughs in the theories and methodologies about the interaction mechanisms of gas-solid flow and reactions, the reactors scale-up and the process design and optimization. On the other hand, the key engineering project we undertook to design a spouted bed mixer for biomass and heat-carrier with the capacity of treating 150,000 tons biomass per year also made an urgent demand to realize the scale-up and practical application of spouted bed, especially with non-spherical particles.

1.2 Thesis outline

Based on the above analysis about the requirements and deficiencies on spouted bed technology in fundamental and practical engineering, the main objective of this project is to reveal the complex spouting characteristics of non-spherical particles and the scaling relationships of spouted beds by experiments and simulations. The key focuses are:

1. To develop a specific understanding of the gas-solid dynamics of binary mixtures involving non-spherical particles in the spouted beds, including the spouting and mixing characteristics and the effects of particle shapes.
2. To explore the amplification law and develop a new method for the scale-up of spouted beds under the motivation to design a large-scale spouted bed mixer to heat the non-spherical biomass particles in real industries.

The novelty of this research project derives from the exploration on the spouting behaviors and mechanisms of non-spherical particles as opposed to that of spherical-particles which has been well-understood currently, as well as from the development and application of a new numerical amplification method to design a new spouted bed reactor with continuous operation on non-spherical biomass particles for practical

processes. Overall, this research project is expected to deliver significant contributions in accelerating the development and application of spouted bed technology.

With the research route as shown in [Figure 1-2](#), the thesis is structured into seven chapters and the outline of each chapter is given in the following:

[Chapter 1](#) introduce some research gaps for spouted bed in fundamentals and engineering applications and the background and purpose of the present research.

[Chapter 2](#) provides a literature survey on experimental and simulated researches on spouted beds with non-spherical particles, and the scaling studies of spouted beds.

[Chapter 3](#) experimentally studies the spouting behaviors of the mixtures of cylindroid particles and spherical bed materials. It mainly includes the evolutions of the spouting, mixing and pressure drop in the bed, and the detailed relationships between spouting characteristics and operating conditions. In this section, two different dynamic modes, namely the systems dominated by bed materials and that dominated by non-spherical particles would be identified.

[Chapter 4](#) develops the CFD-DEM method to model the spouting systems dominated by non-spherical particles. The micro-scale mechanisms of spouting cylindroid particles are studied and the flow pattern, particle velocity, particle orientation and coordination number are investigated to find out the effects of particle shape on spouting behaviors.

[Chapter 5](#) develops the numerical scaling and design method for spouted beds dominated by the bed materials. The effects of particle properties, bed structures and operational conditions on the dynamic behaviors in spouted beds with different scales are systematically studied. A new correlation is proposed to predict the minimum spouting velocity in both small and large spouted beds. Hydrodynamic behaviors in spouted beds with different structures also are investigated.

[Chapter 6](#) designs an industrial scale spout-fluid bed mixer to mix the non-spherical biomass particles (18.75 t/h) and spherical heat-carrier particles. A new spout-fluid mixer geometry is proposed for the practical process with continuous operation, and its

performance and the effects of operating parameters are numerically investigated.

Chapter 7 concludes the whole work conducted so far, outlines the main findings and recommends some further studies in this research direction.

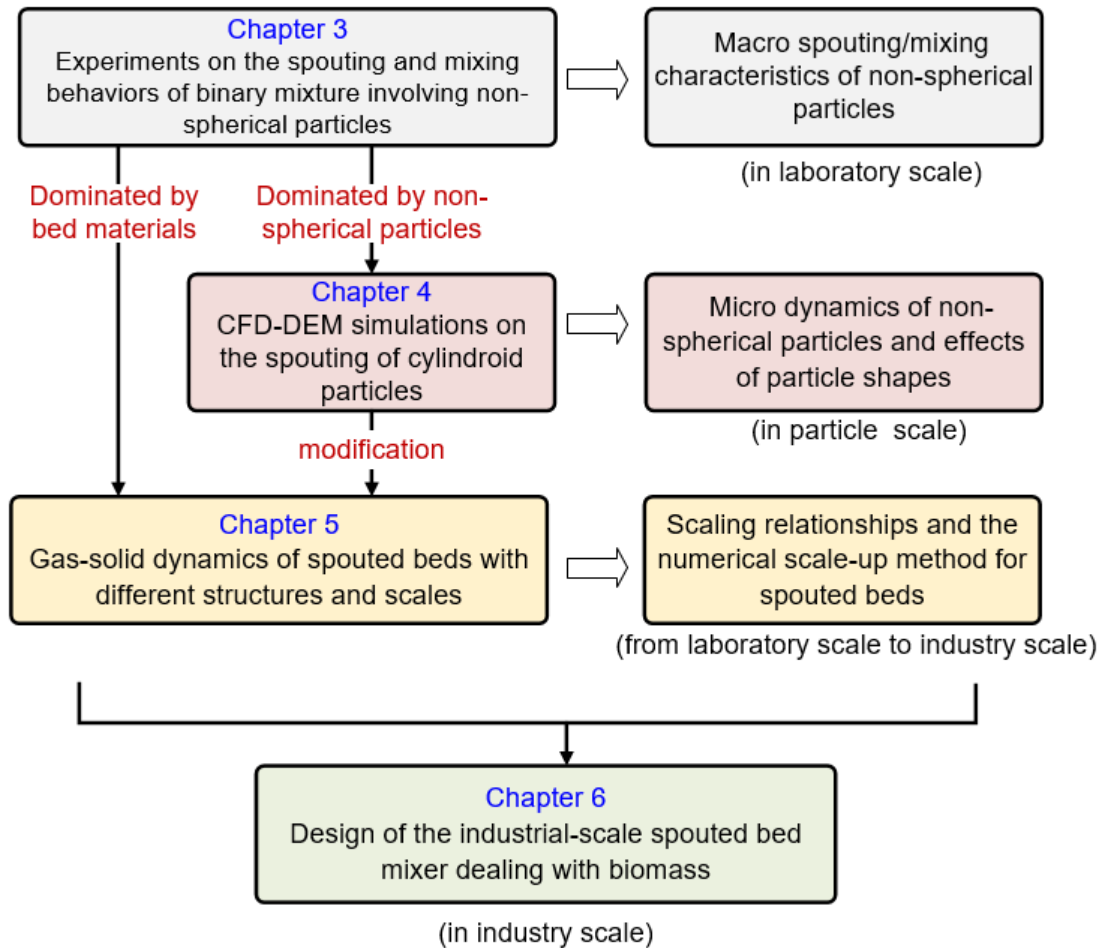


Figure 1-2 The research route of the project and the relationships of main components

CHAPTER 2 LITERATURE REVIEW

Spouted beds have been widely studied and applied for more than 60 years with a large number of research outputs including two books [1,2] being published and seven international symposia dedicated solely to spouted beds. The spouting behaviors of spherical particles in the laboratory-scale or pilot-scale spouted beds for agriculture-related and industrial operations have been comprehensively studied and understood. However, researches on the spouting dynamics and mass and heat transfers that involve non-spherical particles, as well as the attempts to scale up the spouted bed reactors for chemical engineering processes are significantly limited up to now. This chapter will review the studies on the spouted beds with non-spherical particles from the aspects of experiments, modellings and the scale-up theory and methodology.

2.1 Experiments

Experimental studies on the spouting non-spherical particles usually follow with some specific operation processes in industries such as drying [3-11], coating [12-16], thermal chemical reactions [17-38], and focus on the feasibility and effectiveness of spouted beds applied as the device to handle the specific particles with fluids and the possible optimizations in bed geometric structures or operations.

2.1.1 Drying

The strong abilities of spouted bed in dealing with particles with larger sizes and providing the good particle circulation, effective fluid-particle contact and heat/mass transfers result it becoming one of the most attractive dryer which has been applied widely in drying of particulate solids, as well as in combined operations, such as drying-granulation, drying-coating, drying-blending and so on. Because the rapid solid circulation and moving in spouted beds can prevent the particles from the heat damage when the hot gas is used as the drying fluid, spouted beds are especially suitable for drying the thermal-sensitive particles in agriculture, food, pharmaceutical industries such as grains [11], fruit pulp dices [3,5,10], seeds[7], solid wastes like peels[6,8], and food additives [9]. Most of the particles involved in these processes are of non-spherical shapes. The typical examples are as follows:

Almeida et al. [5] studied the fluid-dynamic characteristics, mainly including the stability and flow regime transition, of the deformable dice pieces of red guava dried in the spouted beds. Results showed that due to the water loss and inter-particle attritions during the drying process, the particles shrunk and deformed with the remarkable changes in size and density, which obviously affected the stability, as well as led to the flow regime transition in the spouted beds. The detailed stability was investigated by exploring the correlation between fountain height and the normalized Archimedes number in the dynamic conditions. They believed the dynamic stability in the spouted bed dryer requiring adequate loading and moisture content conditions of the products. Additionally, the Littman parameter and the Archimedes number are influenced especially by the particle diameter, which suffers great reduction along the drying process, where abrupt variation can explain the instability of the spouted-bed fluid dynamic behavior.

Wang et al. [4] investigated the effects of novel Pulse-Spouted Bed Microwave Freeze Drying (PSMFD) technology on the dielectric properties and quality characteristics (moisture content, porosity, color, flavor, texture and so on) of apple cuboids. Compared with the conventional air drying and freeze drying, the hybrid PSMFD technology could provide better preservation of apple color and volatile compounds and thus produce premium quality dried fruits. Cárdenas-Bailón et al. [10] evaluated the drying behaviors of carrot cubes (0.9×0.9 cm) shown in [Figure 2-1 \(a\)](#) in a spout-fluid bed dryer with the temperature in bed being 60 70 and 80 °C, respectively. The main product quality parameters, including β carotene content, the peroxidase (POD) residual activity and the pectin methyl esterase (PME) residual activity were also estimated. Results showed that the spout-fluid drying can effectively maintain the β carotene content in products and the values are similar to that produced by freeze drying. For drying carrot cubes spout-fluid bed is an effective alternative to the traditional tray dryer, vacuum drying or fluidized bed drying with the average drying temperature of 70 °C being recommended as a compromise between the drying time and the quality of the products.

Freire et al. [8] used the spouted bed with diameter of 0.36 m to dry the waste pulps which is massively generated by the citrus industry especially in Brazil and United States are the key orange juice producers. After crushed into particles with irregular shapes and dried properly, these orange juice solid wastes that correspond to 50% of the weight of the fruit could be used as the valuable commercial energy. In this study, the authors built the dynamic model of orange waste drying in a conical spouted bed with overall energy and mass balances under the temperatures of 70, 80 90 °C and the spouting flow rate of $1.7u_{ms}$, and a two-phase perfectly stirred tank reactor model was derived and used in a cascade configuration with time-varying parameter update.



Figure 2-1 Drying and deformation of non-spherical particles in spouted beds:(a) carrot cubes [10], (b) carrageenan gel particles [9]

Serowik et al. [9] used the spouted bed as the dryer to obtain the dried carrageenan gels, as shown in [Figure 2-1 \(b\)](#), which then could be conveniently grinded into the powder products. The functional properties of the powder products such as density, water activity color parameters, rheological properties, and solubility were employed to assess the dry effectiveness of the spouted bed. Results showed that the drying behaviors of carrageenan gels K12, K73 and their mixtures in spouted bed can be described with the Page model, while the decrease of spouted bed volume ratio and moisture content are found in a linear relationship depending significantly on the kind of material. With the temperature of hot air rising from 60 to 150 °C, the drying time for all types of carrageenan gels will decrease about 50% with the products presenting the lighter color (apart from the K73+ iota samples) and the lower equilibrium moisture content and water activity, while dried at 100 °C, the products are of the best solubility

and high gelling ability. Therefore, the authors recommended using K12 as the best raw material with the spouted bed drying at 100 °C to produce the carrageenan powders.

2.1.2 Coating

Benefiting from the regular particle circulation, effective solid-fluid contact, as well as the high rates of heat and mass transfer, spouted beds have been extensively used for the film coating of particles in many industrial sectors, such as the chemical, food, pharmaceutical, agricultural, iron ore and nuclear industries [12-16]. The suspension or solution can be introduced into spouted beds with top, bottom, or tangential atomization and perform film coating on the surface of particles to modify their physical and physicochemical properties. The properties of the final product are determined by the equipment geometry, operating conditions, characteristics of the material to be coated and coating material formulation. Spouted beds also offer possibility of the process automation and use of the same equipment for other applications such as granulation, drying, and coating of other products. As most of the products, like vegetables, seeds, fertilizers, sweets and candies, drugs and so on are non-spherical particles, many researchers are focusing on the spouting and coating behaviors of non-spherical particles in spouted beds with the aim of improving the process performance.

Pissinati et al. [13] analyzed the viability of the spouted bed process applying to add a gastric-resistant coating on soft gelatin capsules. By assessing the product quality with disintegration tests, traction×deformation tests and image analysis, and evaluating the coating mass distribution and shape factor, the effects of variables being investigated, including the conical base angle of the spouted bed, the relation between the feed mass flow rate of the coating suspension and that of spouting gas (W_s/W_g), the ratio between the flow rate of the spouting gas and that at minimum spouting condition (Q/Q_{ms}), the mass of capsules in the bed, and the capsule size. Results showed that, coating efficiency tended to increase with an increasing W_s/W_g . However, too large W_s/W_g might lead to the cracks or agglomeration of capsules during the coating process. The size of the capsule has no obvious effect on the coating efficiency. The mass of capsule

particles linearly increases with the coating time and when the ratio between coating mass and the surface area of soft gelatin capsules achieves 3.86 mg/cm^2 , capsules obtain the sufficient gastric-resistant effect. From their analysis, the authors believed the spouted bed is a fast and efficient method for the enteric coating of the soft gelatin capsules.

Similarly, Publio and Oliveira [14] studied the effects of spouted bed configuration and operating conditions on the coating process of Placebo tablets. They confirmed the growth kinetics of the tablets during spouted bed coating can be estimated by the equation obtained from mass balance:

$$\frac{d_p}{d_{p0}} = \left(1 + \rho_p / \rho_{\text{coat}} \frac{\eta W_s C_s \theta}{n_0 m_{p0}} \right) \quad (2-1)$$

where d_p and d_{p0} respectively are the current and initial particle diameters, mm; ρ_p and ρ_{coat} respectively are particle density and coating density, g/mL; η is the adhesion coefficient; W_s is the feed flow rate of the coating suspension, mL/min; C_s is the solid content, g/g; θ is the processing time, min; n_0 is the initial number of tablets in the bed and m_{p0} is the initial particle mass, kg.

Kfuri and Freitas [15] compared the performances of three different devices, namely the conventional spouted bed, the spouted bed with auxiliary air supply and spout-fluid beds for coating tablets by investigating the flow regimes, suspension feed rate and tablet load in the beds, as well as the coat quality indexes such as tablet surface appearance, hardness, moisture content and gastric resistance. Results indicated that all three systems studied presented good quality coating without problems of agglomeration, picking, or any other factor related to poor drying conditions. Since conventional spouted beds have a simpler design, there is no need to use auxiliary air supply in the coating of large particles under the conditions under investigation within this study. The gas-solid regimes in the beds or the tablet load do not affect coating performance obviously, while the increasing suspension feed rate could significantly raise the coating efficiencies and weight gain. Thus it is possible to operate at column

loads close to the maximum spoutable bed height and the coating times may be reduced by increasing suspension feed rates. These operations were not found to affect the coat quality, e.g., tablet moisture content, hardness, friability, and gastric resistance, according to pharmaceutical standards.

2.1.4 Combustion, gasification and pyrolyzation

Spouted beds began to be used as the reactors for the combustion of the low-calorific fuels and solid wastes in 1980s. H. A. Arbib and A. Lewy (1982) [37] carried out the combustion experiments of the low-calorific coals and solid wastes in the laboratory-scale spouted beds and indicated that the spouted bed was able to obtain high hydrocarbon conversion rate and combustion efficiency when dealing with low grade fuels, and was a very promising gas-solid reactors.

In the 1960s and 1970s, there was a boom in pyrolyzing or distilling oil shales to produce petroleum. Spouted beds were then extensively studied as one of the most potential reactors for petroleum productions from the oil shale. Lisboa et al. [38] conducted experiments to pyrolyze oil shale in a spouted bed reactor (ID=300 mm) with the capacity of 110~240 kg/h. Most of the oil shale particles in the experiments were less than 6.35 mm and about 40% of the particles were less than 0.84 mm in diameter. Experiments were carried out under the atmospheric conditions with the temperature inside the bed reaching 450~600 °C and that of the spouting gas varying from 20 to 565 °C. Results indicated that spouted beds could provide stable spouting in a wide range of operating conditions, with which the oil shale obtained the high quality and efficient pyrolysis. The effects of the bed temperature, oil shale particle size, feed rate and the properties of bed materials on the yield of shale oil were systematically figured out.

Prof. Olazar leading his team has made important contributions to the study and application of conical spouted beds in dealing with biomass and solid wastes. Since 1990s, Olazar et al. kept on performing researches on the utilization of spouted beds as reactors to reuse the wood chips and residues [18-20]. Over the years, they continually

extended the application of spouted beds to a series of fluidizing processes that usually involved various irregular or non-spherical particles, such as biomass, plastic particles, plant residues, waste tire particles and so on and mainly focused on the gas and solid flow characteristics in the conical spouted beds with the normal atmospheric temperature and pressure [24-27, 29-31, 33]. On the other hand, the effects of operating conditions and catalysts on the reaction (pyrolysis or gasification) products of biomass and solid waste were also studied under the high pressure and temperature. For example, Olazar et al. [25] investigated the different pyrolysis processes of two kinds of waste tire particles, whose particle size distributions respectively are in the range of 0.1~0.8 mm and 0.8~4.0 mm, at the temperature of 450~600 °C, and results indicated that the conical spouted beds were particularly suitable for the aerodynamic behaviors and reactions of waste tire particles by providing the remarkably good contact and strong heat and mass transfers between gas and solid phases. In 2010, Olazar and his team established a spouted bed plant and further studied the pyrolysis characteristics of waste tires in a conical spouted bed (425~600 °C) in the pilot scale [29]. Currently, the Olazar team is still working on the pyrolysis and combustion of biomass, solid waste particles and sludge particles in conical spouted beds [33-36] (Figure 2-2).

In the meantime, many other scholars were also conducting researches on the treating biomass or solid wastes in spouted beds. For example, Hoque et al. [21] used a spouted bed to carry out the gasification of coconut shells, and figured out the effect of gasification temperature on the products. Researchers from the Chinese Academy of Sciences [22] and Imperial College London [17, 23] applied spouted beds to sludge combustion reactions. Bernocco et al. [32] performed and demonstrated the feasibility of a biomass gasification plant using their innovative spouted bed reactors and provided a preliminary design of main plant apparatus for a nominal total power capacity of 100 kW.

Jun Liu [28] conducted the experimental studies on the spouting and mixing behaviors of the crushed rice straw particles and coal particles in three different spouted beds. By carefully investigating the effects of the mixing parameters of two materials and bed

structures on the gas-solid flow behaviors (including the pressure drop in beds, solid circulation rate and so on), he improved the co-gasification process of biomass and coal in spouted beds. However, all experiments were completed in the “cold states”, while the relevant thermal tests have not been carried out.



Figure 2-2 Picture of Ikerlan IK-4 pyrolysis pilot plant with the conical spouted bed reactor designed by the Olazar’s team [33]

2.1.5 Studies on the dynamic characteristics of spouting non-spherical particles

Apart from the application studies that focus on the specific particles or processes, several researchers also carried out some experiments to study the fundamental gas-solid flow characteristics and interaction mechanisms of the non-spherical particles in spouted beds, mainly including:

Morgan [40] proposed a prediction equation for the maximum spoutable height of spouted beds with non-spherical particles by introducing the particle sphericity to characterize the effects of particle shapes. They found with the same equal volume diameter (the diameter of a sphere of the same volume as the given particle), particles that deviated from the spherical shape more seriously would achieve the higher maximum spoutable bed height in spouted beds. However, when particle size is reduced,

the particle shape became less effective to the maximum spoutable bed height.

Liu et al. [41] studied the spout behavior of non-spherical particles in a cylindrical conical spouted bed with a diameter of 150 mm. The study involved 13 different particles with the sphericity (ϕ) varying from 0.39 to 1 and investigated the effects of particle shape on the minimum spouting velocities (U_{ms}) and fountain height (H_f). They found that for the particles with the sphericity being 0.75~1, with simply replacing the particle diameter d_p for spheres with the equal volume diameter d_v for non-spherical particles, the well-known Mathur-Gishler (M-G) equation can be effectively modified to predict their U_{ms} in spouted beds with the errors roughly within $\pm 20\%$. However, for the particle with the sphericity less than 0.75, the above simple modification usually overestimated their U_{ms} and the equivalent particle diameter ϕd_v is preferred to replace the particle diameter in M-G equation. Additionally, they proposed that when the particle sphericity is 0.65~1, using the Souter average sieve diameter in the M-G equation can also lead to better predictions.

Shao et al. [43] also studied the U_{ms} of non-spherical particles in a spouted bed with a diameter of 200 mm. Their experiments involved six different particles with the equal volume diameter varying from 1.9 mm to 6.2 mm and the sphericity being 0.73~0.95, as shown in [Figure 2-3](#). Studies have shown the effects of static bed height and nozzle diameter of the U_{ms} for non-spherical particles are very similar to that for spherical particles. However, as the sphericity decreases, the change amplitudes of U_{ms} would increase, and this increase would become more obvious with the increasing particle size. The researchers believed that the classical Mathur-Gishler equation itself can effectively predict the U_{ms} of non-spherical particles, and replacing the particle diameter d_p in M-G with $(\phi^{-0.5} d_v)$ usually results in a more accurate prediction.

$$U_{ms} = \left(\frac{\phi^{-0.5} d_v}{D} \right) \left(\frac{D_i}{D} \right)^{1/3} \left(\frac{2gH_0 (\rho_p - \rho_g)}{\rho_g} \right)^{0.5} \quad (2-2)$$

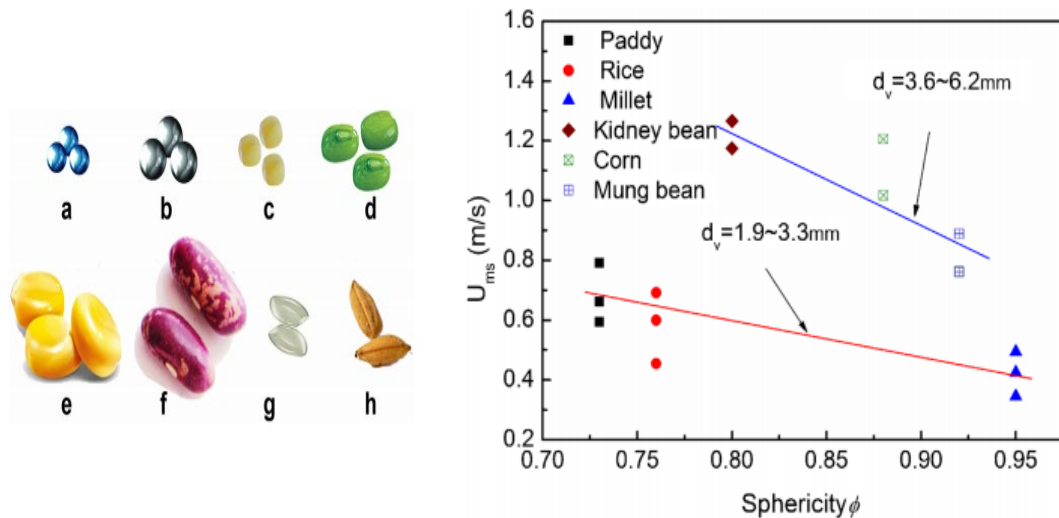


Figure 2-3 Changes of minimum spouting velocity U_{ms} with particle sphericity ϕ [43]

Saldarriaga et al. [44] studied the peak and spouting pressure drops of five biomass materials. They found that both peak and spouting pressure drops increase with the increasing particle size and density and the decreasing shape factor. The influence of particle size and density of irregular biomass materials is more pronounced than that of regular ones, especially on the peak pressure drop. Shape factor would obviously influence the static bed height of irregular materials and thus affect the spouting pressure drop.

2.2 Modeling of spouted beds with non-spherical particles

Numerical simulation has been generally accepted as a powerful tool for gas-solid two-phase flows. A large number of literatures have been involved in the numerical simulations of spouted beds [2]. However, most of these simulation works treated the non-spherical particles as spherical ones for the sake of simplicity [45]. In fact, for the particles whose shapes seriously deviate from spheres, their dynamics in gas-solid flow systems are usually complicated, because the geometrical contact scenarios between non-spherical particles and the interactions between particles and surrounding fluid are far more diverse. Using the force and motion models for spherical particles to model these non-spherical particulate systems was not often able to obtain the satisfactory predictions. It is necessary and urgent to explore more accurate numerical models and

methods for the non-spherical particles. As the spouted bed is one of the most complex dense gas-solid reactors, to accurately model the spouting of the non-spherical particles is faced with great challenges due to the lack of clear descriptions on the intricate gas-solid interactions as well as the huge computational cost.

In recent years, the Discrete Element Method coupling with the Computational fluid Dynamics (DEM-CFD) has achieved great success in the simulation of the fluidizing processes. DEM was first proposed by Cundall et al. in 1979 to model the rock movements in geology [46]. In 1992, Tsuji et al. applied this method to study the horizontal pipeline pneumatic conveying issues for the first time [47], and then successfully model the dense gas-solid flows in fluidized bed by combining DEM with Computational Fluid Dynamics (CFD) [48]. The combination of DEM and CFD is able to efficiently unite the macroscopic fluidization phenomena and the mesoscopic gas and solid interactions by considering the shapes and properties of individual particles and forces acting on them, and has been attracting the increasing attention since it was proposed. In the past decades, many research institutes around the world have been continuously working on the development and application of CFD-DEM in the gas-solid multiphase flow processes such as in fluidized bed, spouted bed, etc., and have achieved fruitful results [49-51].

However, most of the existing CFD-DEM studies were focused on spherical particles, while the simulation works on the gas-solid flow behaviors of non-spherical particles are still quite limited, and that involving spouted beds are even rarer [52]. The main CFD-DEM studies on the dense gas-solid flow systems with non-spherical particles are as follows:

Cleary and his team developed the CFD-DEM to investigate the effects of particle shape on particle motions and stress distribution in the gas-solid pipeline flow [53]. Hilton et al. [54] studied the dynamic behaviors of the cube and ellipsoidal particles in a three dimensional (3D) fluidized bed, by constructing the non-spherical particles with the hyperquad method in DEM and adopting the drag force model that was proposed by

Holzer and Sommerfeld [55] for non-spherical particles to calculate the interactions between laminar gas flow and solid particles. Their studies in particle scale found that the non-spherical particles usually receive larger drag force than the equal-volume spherical particles, thus the bed performs the higher pressure drop and could be fluidized at the lower gas velocity.

Professor Aibing Yu and his team also constructed the non-spherical particles like ellipsoidal particles with super-quadratic surfaces and carried out a series of CFD-DEM studies about the gas-solid flow characteristics in fluidized beds [56-60] (see [Figure 2-4 \(a\)](#)), including the flow regime features of the ellipsoidal particles with varying shapes and sizes in the fluidized beds, mathematical relationships between the pressure drops in bed and the fluidizing gas velocity and so on. They specially brought insight into the explicit particle information in fluidized beds, such as the contact numbers and orientations of the ellipsoidal particles and the detailed forces exerting on them. In addition, this team also obtained many outstanding achievements in the DEM studies on the fluidization of ultrafine particles [59], the heat transfer characteristics and mechanisms of ellipsoidal particles [58] and the drying behaviors with particle shrinkage [60].

Professor Kruggel-Emden and his team have made great progress in the CFD-DEM developments and mechanism studies for the dense non-spherical particulate systems in recent years [61-65]. In their CFD-DEM scheme, the non-spherical particles such as the cylinders (cylindroid particles), cubes, cuboids, plate-shaped particles and so on were usually constructed by the combined geometric element method, with their contact forces being calculated with the linear spring-damping model; the fluid phase was usually assumed as the laminar flow and the interaction between the fluid and the non-spherical particles was estimated with the Holzer-Sommerfeld drag model. Based on the above CFD-DEM scheme, they comprehensively studied not only the gas and solid dynamic behaviors of the homogeneous non-spherical particles, but also the mixing behavior of heterogeneous non-spherical particles in the dense pneumatic conveying of pipelines and the fluidization of fluidized beds as shown in [Figure 2-4\(b\)](#).

At the same time, researchers in China have made a series of important contributions for the CFD-DEM modeling on the dense gas-solid systems with non-spherical particles [66-72]. Their works mainly used the multi-sphere model to construct non-spherical particles by combining a certain number of spheres with various amounts of overlaps, meanwhile introduced the k- ϵ model to describe the turbulent gas phase. Based on the above approach, Zhong et al. [66] successfully performed the CFD-DEM simulations of the fluidization of cylindroid particles in a fluidized bed. The important hydrodynamic characteristics including bed pressure drop, particle collision probability, voidage of bed, particle velocity etc. and the mixing behaviors and mechanisms of the binary mixture of cylinders and spherical particles were studied in the macro and mesoscale scales [67, 73]. In addition, they have made earlier contributions to the CFD-DEM simulations of spouting the cylindroid particles, corn-shape particles and the mixtures of them and spherical particles in spouted beds [68-70, 73] (see [Figure 2-4\(c\)](#)) with the spouting characteristics and mixing mechanisms, as well as the effects of particle shapes on the above dynamic behaviors being thoroughly obtained.

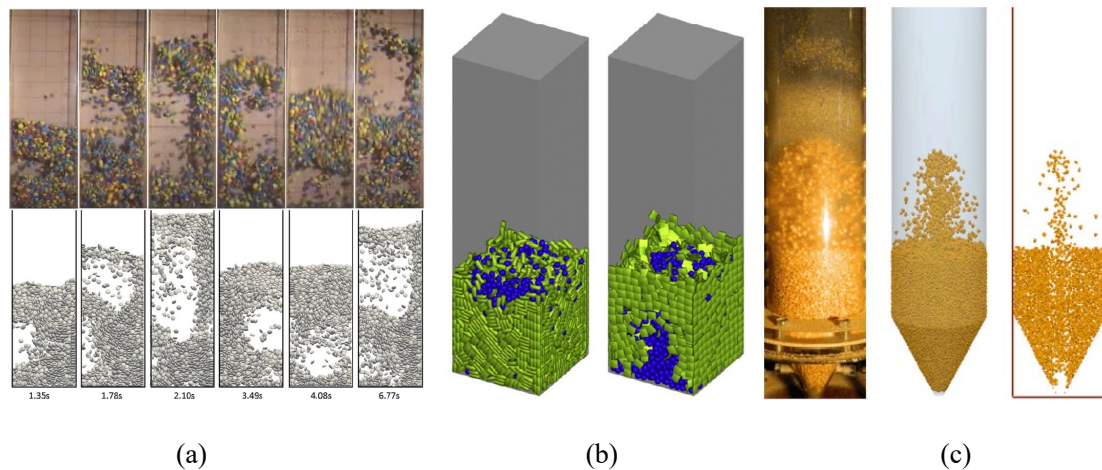


Figure 2-4 Typical CFD-DEM studies on the non-spherical particles: (a) the fluidizing behaviors of ellipsoidal particles [57], (b) the mixing behaviors of spherical particles and cuboid particles in the fluidized bed [65], (c) spouting of corn-shape particles [68]

On the other hand, scholars from Xi'an Jiaotong University, Zhejiang University, East China Agricultural University and so on are also conducting CFD-DEM researches on the non-spherical particulate systems. For example, Nan et al. [74] and Ma et al. [75] respectively constructed the cylindroid particles by the multi-sphere model and the

hyperquadric surface method, and studied the effects of particle aspect ratio on their fluidization characteristics in dense gas-solid flows. Lei et al. [76] used the multi-sphere model to construct the accurate ellipsoidal wheat seeds, and studied the dynamic behaviors of seed particles in pneumatic seeding device.

2.3 Scale-up of spouted beds

The design and operation of full-scale spouted bed units for the practical physical and chemical processes is one of the most important and difficult aspect in the field of spouted beds. The three main strategies that are available now to design the large spouted beds are as follows [2]: 1) Scaling up the test results obtained on smaller units by the dimensional similitude methodology to achieve the large spouted beds; 2) extending the small-scale spouted bed in a certain single dimension (for example, the thickness) to construct the slot-rectangular spouted bed; 3) parallel merging the small-sized spout units to assemble spouted beds with multiple-spout geometries, as shown in [Figures 2-5](#).

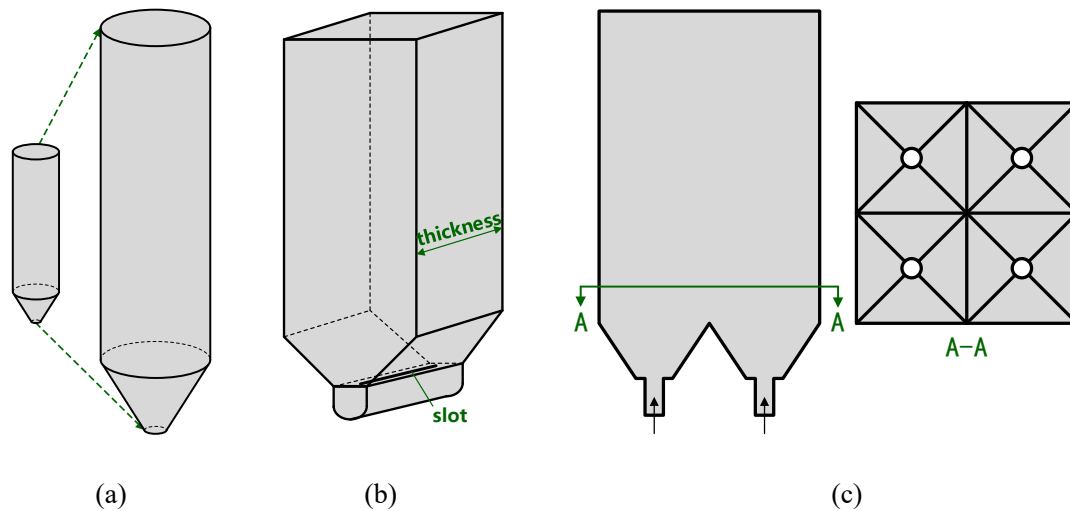


Figure 2-5 Three typical scaling modes of spouted beds: (a) scaling up with the dimensional similitude methodology, (b) extending the small-scale spouted bed in a certain single dimension to construct the slot-rectangular spouted bed, (c) parallel merging the small-sized spout units to assemble spouted beds with multiple-spout geometries

Regarding the first strategy of scaling up, He et al. [77] proposed the following dimensionless groups according to the dimensional similitude methodology to scale up

the hydrodynamics of spouted beds:

$$\frac{gd_p}{U^2}, \frac{\rho d_p U}{\mu}, \frac{\rho_p}{\rho}, \frac{H}{d_p}, \frac{D_i}{d_p}, \phi_s, \varepsilon_0, \varphi, \text{PSD} \quad (2-3)$$

where ϕ_s denotes the particle sphericity, φ is the angle of internal friction of the particulate material, and PSD is a dimensionless parameter describing the particle size distribution. They experimentally tested the sufficiency of these relations in four semicylindrical columns of different diameters operated at varying temperatures and pressures with narrow size distributions of regular particles. By comparing the hydrodynamic parameters such as the maximum spoutable bed depth, fountain height, spout diameter, axial pressure profiles, and dead zone boundaries, they concluded that all the dimensionless parameter groups in (2-3) are critical for the scaling of spouted beds: when all of them were very nearly matched, the dimensionless hydrodynamic behavior was nearly identical; the mismatching of even only one or two dimensionless groups would highly possibly cause the significant lack of agreement. The findings from the studies of Costa and Taranto [78] and Béttega et al. [79] reinforced these claims. On the other hand, Lu et al. [80-82] found through a series of numerical simulations that the contact collisions between particles play an important role in the fountain and annulus, and the coefficient of restitution for particle-particle collisions e should also be considered as one of the dimensionless parameters for scaling up the spouted beds. The above studies indicated that it is feasible to scale up the structure and hydrodynamics of spouted beds in principle by building a geometrical similar physical “cold” model with all the important independent dimensionless groups being closely matched. However, the rigorous dimensional similitude is usually hindered when applied in practice. For example, the properties of particles and fluids that are handled in spouted beds are often determined according to the practical processes and thus cannot be changed to match the dimensional groups; the dimensions of spouted beds and the particle sizes have also to follow some special criteria for the stable operations in spouted beds [2]. Studies indicated that the optimum range of D/D_i should be 6 to 10, and the maximum is likely to be ~ 12 to avoid substantial dead regions [83],

and meanwhile D_i/d_p should not exceed 25 for the stable spouting [84]. Therefore, it is usually very difficult to simultaneously meet the consistencies of so many dimensionless groups in practice. In fact, there is even not a clear conclusion on what dimensionless groups are the decisive factors in the scaling up of spouted beds up to today [77, 85-88].

The slot-rectangular spouted bed is the second scaling type developed from the planar symmetrical two-dimensional spouted bed (2DSB) [89], as shown in [Figure 2-5\(b\)](#). The volumetric capacity of 2DSB can be easily increased by extending the bed thickness to form a slot-rectangular spouted bed [2,89-91]. However, studies found that when the thickness of the 2DSB increases, the spouting behaviors in the bed would show the clear three-dimensional feathers. That is, the spouting pattern did not develop as expected to keep its original shape in the 2DSB just with the extension in the direction of thickness, but two or more discrete jets or spouts usually formed along the slot length causing the unstable spouting in beds [92, 93]. Due to the three-dimensionality of the geometry with the greater number of additional independent variables such as the column thickness, slot length, width and depth and so on, the slot-rectangular spouted beds often showed the remarkably more complicated flow patterns than the conventional conical-cylindrical beds. With the varying operating conditions, up to eight or nine flow regimes have been identified in the slot-rectangular spouted beds [93, 94]. Some works have led to a series of separate empirical and semi-empirical correlations for the intricate gas and solid hydrodynamics in the slot-rectangular columns such as minimum spouting velocity, maximum spoutable bed depth, maximum pressure drop, and flow regions [93]. However, these studies usually lack enough generality given the limited number of independent variables covered in individual experiments. Up to now, there is any general conclusion obtained on the spouting stability or other dynamic characteristics of slot-rectangular spouted beds [2].

Another possible way to scale up spouted beds is to arrange two or more discrete nozzles for the incoming spouting gas at the bottom of the bed column to form the multiple-spout beds, essentially dividing the overall system into several parallel

modular spouted beds [1, 2, 95]. With the multiple orifices, the ratio between bed diameter and orifice diameter and that between orifice diameter and particle diameter could be more easily kept in the proper ranges, which is favorable for the formation of stable spoutings in the enlarged columns. On the other hand, the gas incoming from the multiple entry points could also obtain a better contact with the solid particles. However, the special structure of multiple orifices also brings some particular problems. The uneven flows through the various orifices [93] and the strong interactions between adjacent jets such as merging, repelling, suppression, entrainment and so on [96-99], would easily cause the serious instability of the gas-solid flows in the spouted beds.

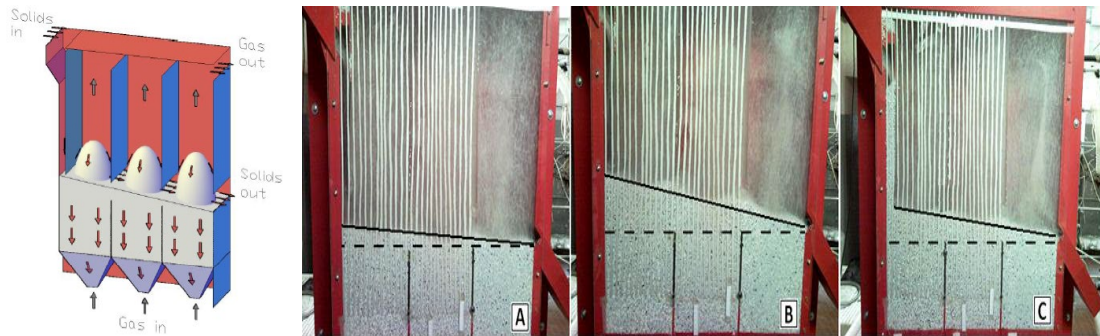


Figure 2-6 Experiments on the multiple-spout bed with continuous operations [99]

Installing the full or partial vertical partitions at the boundaries between adjacent geometrically similar compartments is one of the common methods to improve the stability of spouting in the beds [93, 97, 98]. However, up to now, many fundamental issues about the partitions have not been resolved. For example, whether the baffles are effective or not, how to determine the positions and sizes of the baffles, and how the baffles affect the dynamic characteristics of the gas and solid in the spouted beds, and so on.

2.4 Summary

This chapter has provided a comprehensive literature review on the studies of spouted beds with non-spherical particles from the aspects of experiments, modellings, scale-up theory and methodology. Based on the review, several gaps and challenges that

require urgent researches have been identified, listed below, which will be focused on throughout this program.

- Up to now, most studies on spouted beds still focus on handling spherical particles. Existing researches referring to non-spherical particles usually limit to some specific particles (e.g., grains, diced fruits, biomass and solid waste particles, etc.) involved in particular practical processes with the emphases often being laid on validating the feasibility and effectiveness of using spouted beds to deal with such unconventional particles, and the corresponding improvements or optimizations in spouted bed structures or operations. When referring to spouting non-spherical particles, the knowledge is still significantly lacking even on the most fundamental and general spouting dynamics and mass/heat transfer mechanisms. Many essential issues, for example, the detailed motion modes of non-spherical particles in spouted beds, how to characterize their spouting behaviors and key parameters and so on, the effects of particle shapes and so on, have not yet been clearly understood. The lack of effective measurement and simulation methods is one of the most crucial obstacles in studies of spouting non-spherical particles.
- Despite a number of articles focusing on the scaling up of spouted beds, it is still one of the most important technological gaps limiting the applications of spouted beds at large industrial processes. The scaling up of spouted beds faces many challenges such as the insufficient understanding on the gas-solid flow characteristics in the large scale spouted bed, the unclear scaling law and the lack of reliable methods and means to scale up the spouted bed and so on. Therefore, in-depth studies are urgently required to figure out the hydrodynamics characteristics of spouted beds with different structures and different sizes, explore the amplification laws of key parameters, and seek for new methods for the scale-up of spouted beds.

Reference

- 1 Mathur K B, Epstein N. Spouted beds. New York: Academic Press Inc., 1974.

- 2 Epstein N, Grace J R. Spouted and spout-fluid beds: fundamentals and applications. Cambridge: Cambridge University Press, 2010.
- 3 Lv W Q, Dong L, Lv H, et al. Recent development of microwave fluidization technology for drying of fresh fruits and vegetables. *Trends Food Sci Tech*, 2019, 86: 59-67.
- 4 Wang D D, Zhang M, Wang Y C, et al. Effect of pulsed-spouted bed microwave freeze drying on quality of apple cuboids. 2018, 11: 941-952
- 5 Almeida M M, Silva O S, Alsina O L S. Fluid-dynamic study of deformable materials in spouted-bed dryer. *Dry Technol*, 2006, 24: 499-508
- 6 Berghel J, Nilsson L, Renström R. Particle mixing and residence time when drying sawdust in a continuous spouted bed. *Chemical Engineering and Processing: Process Intensification*, 2008, 47(8): 1246-1251
- 7 Balakrishnan M, Raghavan G S V, Sreenarayanan V V, et al. Batch drying kinetics of cardamom in a two-dimensional spouted bed. 2011, 29(11): 1283-1290
- 8 Freire F B, Atxutegi A, Freire F B, et al. An adaptive lumped parameter cascade model for orange juice solid waste drying in spouted bed. 2017, 35(5): 577-584
- 9 Serowik M, Figiel A, Nejman M, et al. Drying characteristics and some properties of spouted bed dried semi-refined carrageenan. *J Food Eng*, 2017, 194: 46-57
- 10 Cárdenas-Bailón F, Osorio-Revilla G, Gallardo-Velázquez T. Evaluation of quality parameters of dried carrot cubes in a spout-fluidized-bed dryer with and without draft tube. *J Food Meas Charact*, 2017, 11(1): 245-255
- 11 Rajashekhara S, Murthy D. Drying of agricultural Grains in a multiple porous draft tube spouted bed. *Chem Eng Commun*, 2017, 204: 942-950
- 12 Freitas L A P. Pharmaceutical applications of spouted beds: A review on solid dosage forms. *Particuology*, 2019, 42:126-136
- 13 Pissinati R, Oliveira W P. Enteric coating of soft gelatin capsules by spouted bed: effect of operating conditions on coating efficiency and on product quality. *Eur J Pharm Biopharm*, 2003, 55(3): 313-321
- 14 Publio M C P, Oliveira W P. Effect of the equipment configuration and operating conditions on process performance and on physical characteristics of the product during coating in spouted bed. *Can J Chem Eng*, 2004, 82(1): 122-133
- 15 Kfuri C R, Freitas L A P. A comparative study of spouted and spout-fluid beds for tablet coating. *Dry Technol*, 2005, 23: 2369-2387
- 16 Neto J L V, Borges J E, Duarte C R, et al. Coating of particles in spouted bed: flow regime and stability. *Material Science Forum*, 2010, 660-661:573-579
- 17 Adegoroye A, Paterson N, Li X, et al. The characterisation of tars produced during the gasification of sewage sludge in a spouted bed reactor. *Fuel*, 1949, 83(14): 1949-

1960

18 Olazar M, Jose M J S, Llamosas R, et al. Hydrodynamics of Sawdust and Mixtures of Wood Residues in Conical Spouted Beds. *Ind Eng Chem Res*, 1994, 33(4): 993-1000

19 Olazar M, Aguado R, Bilbao J. Pyrolysis of sawdust in a conical spouted-bed reactor with a HZSM-5 catalyst. *AIChE J*, 2000, 46(5): 1025-1033

20 Aguado R, Olazar M, José M J S, et al. Pyrolysis of Sawdust in a Conical Spouted Bed Reactor. Yields and Product Composition. *Ind Eng Chem Res*, 2000, 39(6): 1925-1933

21 Hoque M M, Bhattacharya S C. Fuel characteristics of gasified coconut shell in a fluidized and a spouted bed reactor. *Energy*, 2001, 26(1): 101-110

22 MirkoBarz. Sewage sludge combustion in a spouted bed cascade system. *Particuology*, 2003, 1(5): 223-228

23 Paterson N, Zhuo Y, Reed G P, et al. Pyrolysis and gasification of sewage sludge in a spouted-bed reactor. *Water Environ J*, 2004, 18(2): 90-95

24 Atutxa A, Aguado R, Gayubo A G, et al. Kinetic description of the catalytic pyrolysis of biomass in a conical spouted Bed Reactor. *Energ Fuel*, 2005, 19(3): 765-774

25 Olazar M, Aguado R, Vélez D, et al. Kinetics of Scrap Tire Pyrolysis in a Conical Spouted Bed Reactor. *Ind Eng Chem Res*, 2005, 44(11): 3918-3924

26 Jose M S, Alvarez S, Alvaro O, et al. Treatment of cork wastes in a conical spouted bed reactor. *International Journal of Chemical Engineering*, 2006, 4(1): 80-80

27 Thamavithya M, Dutta A. An investigation of MSW gasification in a spout-fluid bed reactor. *Fuel Process Technol*, 2008, 89(10): 949-957

28 Liu J. Studies on hydrodynamics of straw with coal in three types of spouted bed and gasification flow test. Doctor dissertation, Jiangsu University, Zhenjiang, 2009

29 Lopez G, Aguado R, Olazar M, et al. Continuous pyrolysis of waste tyres in a conical spouted bed reactor. *Fuel*, 2010, 89(8): 1946-1952

30 Amutio M, Lopez G, Artetxe M, et al. Valorisation of Waste Tires by Pyrolysis over a FCC Catalyst in a Conical Spouted Bed Reactor [Conference Proceedings]. 2012. 817-822

31 Erkiaga A, Lopez G, Amutio M, et al. Steam gasification of biomass in a conical spouted bed reactor with olivine and γ -alumina as primary catalysts. *Fuel Process Technol*, 2013, 116: 292-299

32 Bernocco D, Bosio B, Arato E. Feasibility study of a spouted bed gasification plant. *Chem Eng Res Des*, 2013, 91(5): 843-855

33 Fernandez-Akarregi A R, Makibar J, Lopez G, et al. Design and operation of a

conical spouted bed reactor pilot plant (25 kg/h) for biomass fast pyrolysis. *Fuel Process Technol*, 2013, 112: 48-56

34 Alvarz J, Hooshdaran B, Cortazar M et al., Valorization of citrus wastes by fast pyrolysis in a conical spouted bed reactor. *Fuel*, 2018, 224: 111-120

35 Makibar J, Fernandez-Akarregi A R, Amutio M, et al. Performance of a conical spouted bed pilot plant for bio-oil production by poplar flash pyrolysis. *Fuel Process Technol*, 2015, 137: 283-289

36 Saldarriaga J F, Aguado R, Atxutegi A, et al. Kinetic modelling of pine sawdust combustion in a conical spouted bed reactor. *Fuel*, 2018, 227: 256-266

37 Arbib H A, Levy A. Combustion of low heating value fuels and wastes in the spouted bed. *Can J Chem Eng*, 1982, 60(4): 528-531

38 Lisbôa A C L, Watkinson A P. Pyrolysis with partial combustion of oil shale fines in a spouted bed. *Can J Chem Eng*, 2010, 70(5): 983-990

39 Tam S M, Pyrolysis of oil shale in a spouted bed pyrolyser. Doctor Dissertation, University of British Columbia, 1987

40 Morgan I M H, Littman H. Predicting the maximum spoutable height in spouted beds of irregularly shaped particles. *Ind Eng Chem Fund*, 1982, 21(1): 23-26

41 Liu L X, Litster J D. The effect of particle shape on the spouting properties of non-spherical particles. *Powder Technol*, 1991, 66(1): 59-67

42 Zhang Y, Zhong W, Jin B. Experimental Investigation on the Translational and Rotational Motion of Biomass Particle in a Spout-Fluid Bed. *Int J Chem React Eng*, 2013, 11(1): 453-468

43 Shao Y, Zhong W, Chen X, et al. Spouting of non-spherical particles in conical-cylindrical spouted bed. *Can J Chem Eng*, 2014, 92(4): 742-746

44 Saldarriaga J F, Atxutegi A, Aguado R. Correlations for calculating peak and spouting pressure drops in conical spouted beds of biomass. *J Taiwan Inst Chem E*, 2017, 80:678-685

45 Ullah A, Hong K, Gao Y N, et al. An overview of Eulerian CFD modeling and simulation of non-spherical biomass particles. *Renew Energ*, 2019, 141: 1054-1066

46 Cundall P A, Strack O D L. A discrete numerical model for granular assemblies. *Géotechnique*, 1979, 30(30): 331-336

47 Tsuji Y, Tanaka T, Ishida T. Lagrangian numerical simulation of plug flow of cohesionless particles in a horizontal pipe. *Powder Technol*, 1992, 71(3): 239-250

48 Tsuji Y, Kawaguchi T, Tanaka T. Discrete particle simulation of two-dimensional fluidized bed. *Powder Technol*, 1993, 77(1): 79-87

49 Favier J F, Abbaspour-Fard M H, Kremmer M. Modeling non-spherical particles

- using Multisphere Discrete Elements. *J Eng Mech*, 2001, 127(10): 971-977
- 50 Deen N G, Van Sint Annaland M, Van der Hoef M A, et al. Review of discrete particle modeling of fluidized beds. *Chem Eng Sci*, 2007, 62(1-2): 28-44
- 51a Zhu H P, Zhou Z Y, Yang R Y, et al. Discrete particle simulation of particulate systems: Theoretical developments. *Chem Eng Sci*, 2007, 62(13): 3378-3396
- 51b Zhu H P, Zhou Z Y, Yang R Y, et al. Discrete particle simulation of particulate systems: A review of major applications and findings. *Chem Eng Sci*, 2008, 63(23): 5728-5770
- 52 Zhong W, Yu A, Liu X, et al. DEM/CFD-DEM Modelling of Non-spherical Particulate Systems: Theoretical Developments and Applications. *Powder Technol*, 2016, 302: 108-152
- 53 Cleary P W. The effect of particle shape on simple shear flows. *Powder Technol*, 2008, 179(3): 144-163
- 54 Hilton J E, Mason L R, Cleary P W. Dynamics of gas-solid fluidized beds with non-spherical particle geometry, *Chem Eng Sci*, 2010, 65: 1584-1596
- 55 Hölzer A, Sommerfeld M. New simple correlation formula for the drag coefficient of non-spherical particles. *Powder Technol*, 2008, 184(3): 361-365
- 56 Shrestha S, Kuang S B, Yu A B, et al. Particle shape effect on bubble dynamics in central air jet pseudo-2D fluidized beds: A CFD-DEM study. *Chem Eng Sci*, 2019, 201: 448-446
- 57 Zhou Z Y, Pinson D, Zou R P, et al. Discrete particle simulation of gas fluidization of ellipsoidal particles. *Chem Eng Sci*, 2011, 66(23): 6128-6145
- 58 Gan J, Zhou Z, Yu A. Particle scale study of heat transfer in packed and fluidized beds of ellipsoidal particles. *Chem Eng Sci*, 2016, 144: 201-215
- 59 Gan J, Zhou Z, Yu A. CFD-DEM modeling of gas fluidization of fine ellipsoidal particles. *AIChE J*, 2016, 62(1): 62-77
- 60 Azmir J, Hou Q F, Yu A B. CFD-DEM simulation of drying of food grains with particle shrinkage. *Powder Technol*, 2019, 343: 792-802
- 61 Kruggel-Emden H, Oschmann T. Numerical study of rope formation and dispersion of non-spherical particles during pneumatic conveying in a pipe bend. *Powder Technol*, 2014, 268: 219-236
- 62 Oschmann T, Hold J, Kruggel-Emden H. Numerical investigation of mixing and orientation of non-spherical particles in a model type fluidized bed. *Powder Technol*, 2014, 258: 304-323
- 63 Oschmann T, Vollmari K, Kruggel-Emden H, et al. Numerical investigation of the mixing of non-spherical particles in fluidized beds and during pneumatic conveying. *Procedia Engineering*, 2015, 102: 976-985

- 64 Vollmari K, Jasevičius R, Kruggel-Emden H. Experimental and numerical study of fluidization and pressure drop of spherical and non-spherical particles in a model scale fluidized bed. *Powder Technol*, 2016, 291: 506-521
- 65 Vollmari K, Oschmann T, Kruggel-Emden H. Mixing quality in mono-and bidisperse systems under the influence of particle shape: A numerical and experimental study. *Powder Technol*, 2017, 308: 101-113
- 66 Zhong W Q, Zhang Y, Jin B S, et al. Discrete Element Method simulation of cylinder-shaped particle flow in a gas-solid fluidized bed. 2009, 32(3): 386-391
- 67 Zhang Y. Experimental investigation and 3D DEM simulation on particle mixing characteristic in gas-solid fluidized bed. Doctor Dissertation, Southeast University, Nanjing, 2010
- 68 Ren B, Zhong W, Chen Y, et al. CFD-DEM simulation of spouting of corn-shaped particles. *Particuology*, 2012, 10(5): 562-572
- 69 Ren B, Zhong W, Jin B, et al. Numerical simulation on the mixing behavior of corn-shaped particles in a spouted bed. *Powder Technol*, 2013, 234: 58-66
- 70 Ren B, Zhong W, Jiang X, et al. Numerical simulation of spouting of cylindroid particles in a spouted bed. *Can J Chem Eng*, 2014, 92(5): 928-934
- 71 Zhu L, Zhong Z, Wang H, et al. Simulation of large biomass pellets in fluidized bed by DEM-CFD. *Korean J Chem Eng*, 2016, 33(10): 3021-3028
- 72 Zhong W Q. Study on the hydrodynamic characteristics and scaling of the spout-fluid bed. Doctor Dissertation, Southeast University, Nanjing, 2007
- 73 Ren B. Experimental investigation and CFD-DEM simulation of gas-solid flow mechanisms of non-spherical particles in dense gas-solid system. Doctor Dissertation, Southeast University, Nanjing, 2013
- 74 Nan W, Wang Y, Wang J. Numerical analysis on the fluidization dynamics of rodlike particles. *Adv Powder Technol*, 2016, 27(5): 2265-2276
- 75 Ma H, Xu L, Zhao Y. CFD-DEM simulation of fluidization of rod-like particles in a fluidized bed. *Powder Technol*, 2017, 314: 355-366
- 76 Lei X, Liao Y, Liao Q. Simulation of seed motion in seed feeding device with DEM-CFD coupling approach for rapeseed and wheat. *Comput Electron Agr*, 2016, 131: 29-39
- 77 He Y L, Lim C J, Grace J R. Scale-up studies of spouted beds. *Chem Eng Sci*, 1997, 52(2): 329-339
- 78 Costa M D A, Taranto O P. Scale-up and Spouting of Two-Dimensional Beds. *Can J Chem Eng*, 2003, 81(2): 264-267
- 79 Béttega R, Freire J T. Scale-up study of spouted beds using computational fluid dynamics. *Can J Chem Eng*, 2010, 87(2): 193-203

- 80 Lu H, He Y, Liu W, et al. Computer simulations of gas-solid flow in spouted beds using kinetic-frictional stress model of granular flow. *Chem Eng Sci*, 2004, 59(4): 865-878
- 81 Shirvanian P A, Calo J M. Hydrodynamic scaling of a rectangular spouted vessel with a draft duct. *Chem Eng J*, 2004, 103(1-3): 29-34
- 82 Wei D, Xu J, Ye J, et al. Scale-up relationships of spouted beds by solid stress analyses. *Powder Technol*, 2009, 192(3): 273-278
- 83 Németh J, Pallai E, Aradi E. Scale-up examination of spouted bed dryers. *Can J Chem Eng*, 1983, 61(3): 419-425
- 84 Chandnani P P, Epstein N. Spoutability and spout destabilization of fine particles with a gas. In: Ostergaard K, Sorensen K eds. *Fluidization V*. New York: Engineering Foundation, 1986. 233-240
- 85 Aradhya S, Taofeeq H, Al-Dahhan M. A new mechanistic scale-up methodology for gas-solid spouted beds. *Chem Eng Proces*, 2016, 110: 146-159
- 86 Ali N, Al-Juwaya T, Al-Dahhan M. An advanced evaluation of spouted beds scale-up for coating TRISO nuclear fuel particles using Radioactive Particle Tracking (RPT). *Exp Therm Fluid Sci*, 2017, 80: 90-104
- 87 Ali N, Al-Juwaya T, Al-Dahhan M. An advanced evaluation of the mechanistic scale-up methodology of gas-solid spouted beds using radioactive particle tracking. *Particuology*, 2017, 34: 48-60
- 88 Wang Q, Zhang K, Brandani S, et al. Scale-up strategy for the jetting fluidized bed using a CFD model based on two-fluid theory. *Can J Chem Eng*, 2009, 87(2): 204-210
- 89 Mujumdar A S. Spouted bed technology- a brief review. In: Mujumdar A S ed., *In Drying'* 84, 1984. 151-157
- 90 Passos M L, Mujumdar A S, Raghavan V S G. Prediction of the maximum spoutable bed height in two-dimensional spouted beds. *Powder Technol*, 1993, 74(2): 97-105
- 91 Kalwar M I, Raghavan G S V, Mujumdar A S. Circulation of particles in two-dimensional spouted beds with draft plates. *Powder Technol*, 1993, 77(3): 233-242
- 92 Freitas L A P, Dogan O M, Lim C J, et al. Hydrodynamics and stability of slot-rectangular spouted beds. II. Increasing bed thickness. *Chem Eng Commun*, 2000, 181: 243-258
- 93 Chen Z W Stability and scale-up of slot-rectangular spouted beds: [Doctor Dissertation] University of British Columbia, 2007
- 94 Dogan O M, Freitas L A P, Lim C J, et al. Hydrodynamics and stability of slot-rectangular spouted beds. Part I : thin bed. *Chem Eng Commun*, 2000, 181(1): 225-242
- 95 Murthy D V R, Singh P N. Minimum spouting velocity in multiple spouted beds. *Can J Chem Eng*, 2010, 72(2): 235-239

96 Ren B, Zhong W, Zhang Y, et al. Investigation on flow patterns and transitions in a multiple-spouted bed. *Energ Fuel*, 2010, 24(3): 1941-1947

97 Chen D, Liu X, Zhong W, et al. Interactions of spout jets in a multiple-spouted bed. *Can J Chem Eng*, 2014, 92(6): 1150-1159

98 Foong S K, Barton P K, Ratcliffe J S. Characteristics of multiple spouted beds. *Mech. and Chem. Eng., Trans. Instn. Engrs. Aust.*, 1975, 11: 7-12

99 Curti M Solids and gas hydrodynamic characteristics in square-based spouted beds for thermal applications. PhD thesis, Torino: Politecnico di Torino, Department of Applied Science and Technology, 2015

**CHAPTER 3 EXPERIMENTAL STUDY ON THE SPOUTING
AND MIXING BEHAVIORS OF CYLINDROID PARTICLES**

3.1 Introduction

Biomass is considered as the most promising renewable energy source to contribute to the energy requirement in modern society, benefiting from its greenhouse gas neutral and the feasibility to reuse forestry and agricultural wastes [1-3]. A wide variety of efforts have been made worldwide to develop the biomass utilization technology, and three main thermal-chemical processes, i.e., combustion, gasification and pyrolysis, usually based on fluidization, show significant prospects to convert wood, energy crops, agricultural and forestry wastes to liquid, solid, and gaseous fuels [2-5]. Many typical fluidization process equipment, e.g., fluidized beds, spouted beds and spout-fluid beds have been employed to handle the biomass particles in many attempts [1, 5-8]. The spouted bed reactors are proved to be of great potential to treat biomass particles due to their ability to deal with particles with larger sizes or larger size distributions and to provide good particle circulation, effective fluid-particle contact, and high rates of heat and mass transfer [9-11]. Especially, the decouple residence times of gas and solids in spouted beds, which effectively reduce the gas residence time and unwanted secondary biomass reactions, increase the interest to use the spouted bed reactors to carry out catalytic pyrolysis of biomass.

In practice, biomass particles always are of special properties, and they are usually large in size, long and thin in shape and low in density [1]. Direct spouting the nonstandard biomass particles in spouted beds is quite difficult, thus inert material is often required in the reactors [1, 5, 7, 12]. The inert particles, mixing with the biomass in beds, not only effectively improve the flow behaviors of biomass, but also act as high-efficient heat transfer medium [5,7]. Compared with handling homogeneous spherical particles, the hydrodynamic characteristics of spouting a mixture of long and thin non-spherical biomass particles and fine spherical inert particles in spouted beds inevitably become more complicated. Understanding the spouting behaviors of the mixture is of fundamental importance to develop spouted bed reactors in biomass thermal-chemical processes.

Research on this aspect is very limited, and many essential issues are still unknown, for example, what spouting characteristics the mixture presents in the spouted bed? How the shape and size of biomass particles affect the spouting behaviors, and what size can achieve the satisfactory spouting state in the spouted bed? What is the optimal proportion of biomass particle that the unit can handle? Answers to these questions are of the essence to the application of spouted beds in biomass technology. However, the complicated properties of biomass particles bring too many coupled factors, for instance, particle shape, size and texture, to affect the spouting and mixing results in spouted beds. Unraveling and figuring out influence rules of these factors is of great challenge and requires a huge effort. Relevant research is urgently required.

In this project, cylindroid bamboo particles, wood particles and polyformaldehyde (POM) particles are selected to characterize biomass or waste particles and the glass beads are adopted as inert particles. The spouting and mixing mechanism of cylindroid particles and spherical particles in spouted bed were experimentally investigated. The characteristics of flow pattern and pressure drop of the binary mixture are figured out and cylindroid particles with different sizes and shapes are involved in experiments to reveal the effects of particle size and shape on the spouting and mixing behaviors in beds. In addition, influence of the volume fraction of cylindroid particles on the spouting phenomena, including the total pressure drop, the minimum spouting velocity, fountain height, is emphatically discussed.

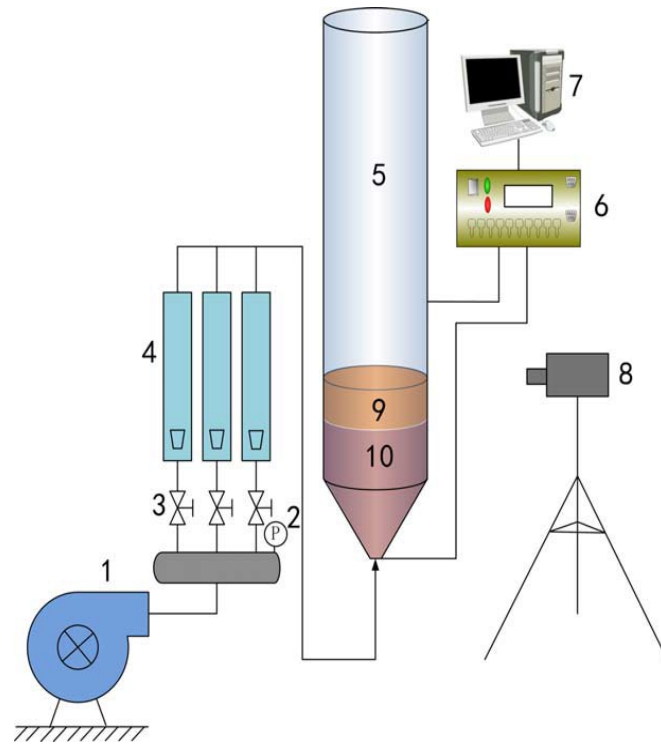
3.2 Experiments

The experimental apparatus used in the current study includes a cone-based cylindrical Plexiglas column, a gas supply system, an imaging system and a multi-channel differential pressure signal sampling system, which has been well shown in our previous work [13]. [Figure 3-1](#) gives the schematic diagram of the experimental setup. In [Figure 3-1](#), the internal diameter of cylindrical column, D , is 200 mm and the height is 1500 mm. The included angle of the conical base is 60° , and the diameter of the gas inlet orifice, D_i , is 20 mm. The spouting gas supplied by a Roots blower is introduced

Chapter 3 Experimental study on spouting and mixing behaviors of cylindroid particles into the column through the inlet orifice and the gas flow can be manually controlled by a valve and the flow rates are obtained by rotor flow meters. Two holes were drilled as the pressure measuring points on the side of column and the distances from the bed bottom are 0 and 640 mm, respectively. A multi-channel differential pressure signal transmitter with a scale of 0-50 kPa is used to measure the pressure drops of bed and converts them into voltage signals which are finally sent to computer through an A/D converter.

Table 3-1 The Properties of particles used in experiments

particles	$d \times L(\text{mm} \cdot \text{mm})$	d_v (mm)	ρ (kg/m ³)	ϕ	Asr (l/d)	α_0	
Cylindroid particles							
A		8×10	9.9	590	0.87	1.25	0.32
B		4×10	6.2	590	0.8	2.50	0.35
C		4×20	7.8	590	0.69	5.00	0.42
D0		—	9.0	741	1.0	—	0.46
D1		6×13.5	9.0	741	0.82	2.25	0.46
D2		5×19.4	9.0	741	0.74	3.88	0.51
D3		4×30.4	9.0	741	0.63	7.60	0.64
E1		6×13.5	9.0	1,407	0.82	2.25	0.43
E2		5×19.4	9.0	1,407	0.74	3.88	0.40
E3		4×30.4	9.0	1,407	0.63	7.60	0.59
Glass bead particles (bed material)							
G1		—	1.4	2,600	1.0		0.42
G2		—	2.6	2,600	1.0		0.42
G3		—	3.4	2,600	1.0		0.42



(a)



(b)

(1) Roots blower; (2) Pressure gauge; (3) Control valve; (4) Rotameter; (5) Spouted bed; (6) Differential pressure sensor; (7) Computer; (8) Digital CCD; (9) Cylindroid particles; (10) Glass beads.

Figure 3-1 Experiment setup of the spouted bed: (a) diagram scheme; (b) scene photograph

Chapter 3 Experimental study on spouting and mixing behaviors of cylindroid particles

The spouting and mixing processes are recorded with a high speed digital camera (Nikon Coolpix L200) which is set up in front of the spouted bed. A graduated paper tape is vertically pasted on the surface of column to indicate the heights of bed levels and fountains.

Closely sized spherical glass beads with the mean diameters varying from 1.4 mm to 2.6 mm, density of 2600 kg/m³ were employed as inert particles in present study, for the reason that the glass bead is one of the most common particles used in the spouting experiments and its excellent spouting characteristics have been well known by researchers [9]. The spouting characteristics of the bamboo particles with different shapes and densities mixing with the inert particles were examined, respectively. The non-spherical particles are cylinders and their detailed properties are shown in [Table 3-1](#). The densities in [Table 3-1](#) refers to the densities of materials. They were obtained by the following procedure: The total mass of 50 particles with the same material and shape were firstly weighed on a balance with precision of $\pm 0.001\text{g}$, then the density of this material is the averaged mass of one particle divided by its volume. In experiments, for each kind of cylindroid particles, their volume fraction in mixture, X_c , is varied from 0 to 1.0, and the spouting behaviors of the mixtures with different volume ratios of bamboo particles and glass bead are investigated.

In each experiment, the total volume, V , inside the spouted bed under the specified static bed height were calculated firstly. The corresponding volume of bamboo particles was $V_c=X_c*V$, while the volume of glass beads was $V_s=(1-X_c)*V$. At the beginning of the experiment, these two kinds of particles were respectively added into the spouted beds with the given volumes. The initial bed was loosely packed and completely layered: the bottom layer was glass bead, while the upper layer is bamboo particle, which specific distribution is one of the very likely starting states in the potential biomass thermal conversion processes [7, 14]. And more importantly, this separated distribution is simpler and easier to control in each run, and starting from the extreme initial state, more typical operational parameters will be obtained, for example, the maximum pressure drop. In addition, taking the completely separation of the biomass and inert

particles as the initial distribution can facilitate the more effective and convincing evaluation on the mix ability of spouted beds.

The ambient air was introduced through the gas inlet orifice with the gradually increasing flow rate, until stable external spouting is reached. During this flow ascending process, spouting information including pressure drops, flow patterns and fountain heights, were respectively recorded by the multi-channel differential pressure signal sampling system and the imaging system. Next, the air flow rate was gradually decreased until it was close to zero. The inlet-based minimum spouting velocity, u_{ms} , or the superficial minimum spouting velocity, U , was captured at the point when stable external spouting collapses in the flow descending process. In current system, the relationship between inlet-based gas velocity and the superficial gas velocity is $U=u/(D/D_i)^2$, i.e., $U=u/100$. Valuable information about pressure drops and flow patterns was also acquired.

3.3 Evolution of the spouting process

For the binary mixture of bamboo particles of Cylinder A ($d \times l = 8 \text{ mm} \times 10 \text{ mm}$) and the glass beads as an example, the typical process of spouting the cylindroid and spherical particles and the evolution of total pressure drop are illustrated in [Figure 3-2](#). The volume fraction of Cylinders A is $X_c = 0.4$ and the initial static bed height is $H_0 = 300 \text{ mm}$. The total transitions of flow pattern and evolution of pressure drop are generally similar to that of spouting homogenous spherical particles, but the additional mixing and segregating behaviors bring some unique features.

The experiment starts with a loosely packed bed, in which two kinds of particles are completely segregated. The glass beads are in the bottom of the bed, while the Cylinder A particles are in the upper layer. When the gas is introduced into the column through the nozzle with low gas flow rate, only the glass beads near the nozzle starts to circulate, while the glass beads in upper bed level and the Cylinder A particles are still static. Further increase in gas flow rate expands the regime where glass beads are in motion and more glass beads are involved in circulation. The internal spout is established and

grows with the increasing gas velocity. At the same time, the bed surface moves upward visibly. During this period, the total pressure drop increases with the increasing gas velocity, and reaches a peak value (point b) as $u=39$ m/s ($U=0.39$ m/s). This peak value is defined as the maximum pressure drop, Δp_{max} . Further increase in the gas velocity leads to the decreasing total pressure drop before the curve reaches the point c. This regime during which the internal spout expands within the layer of glass beads and the glass beads and cylindroid particles are completely segregated is labeled as the regime of complete segregation in Figure 3-2.

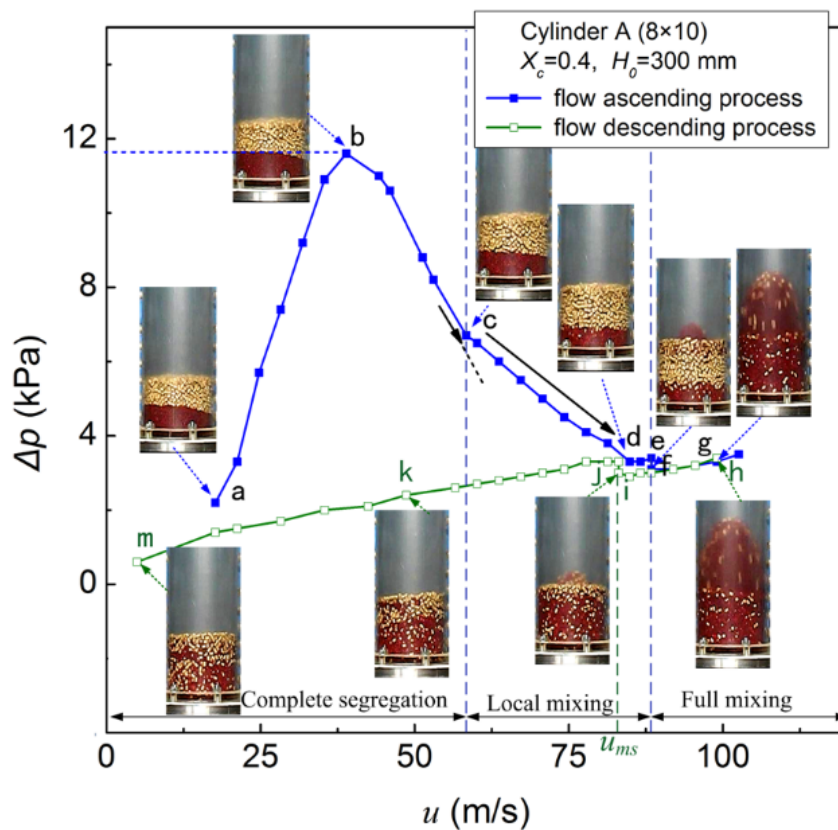


Figure 3-2 Evolutions of flow patterns and total pressure drops in gas flow ascending and descending processes with Cylinders A and glass beads ($H_0=300$ mm, $X_c=0.4$)

When the inlet gas velocity increases to $u=58$ m/s ($U=0.58$ m/s, point c in pressure drop curve), the internal spout just reaches the interface between glass beads and Cylinder A particles. The packed cylinder particles suddenly become more loosely, and the surface of the bed consequently rises. Initial local mixing behaviors occur from this moment.

When the gas flow rate continues to increase, the Cylinder A particles start to be

Chapter 3 Experimental study on spouting and mixing behaviors of cylindroid particles

involved in the internal spout and the mixture of Cylinder A particles and glass beads together move to the bottom of the bed and join in the circulation of internal spout. This process is corresponding to the regime from point c to point d in the pressure drop curve. From the point c ($u=58$ m/s, or $U=0.58$ m/s) to point d ($u=85$ m/s, or $U=0.85$ m/s), the pressure drop continues to decrease with the increasing u , but with a different trend from that between point b and c. Point c is one of the important turning points on the pressure drop curve in the flow ascending process. When the gas velocity exceeds 85 m/s, the pressure drop rises slightly with the increasing u before it meets an obvious decrease at the point e. The regime from point c to point e is labeled as local mixing in [Figure 3-2](#).

At point e ($u=88$ m/s, $U=0.88$ m/s), the internal spout suddenly breaks through the layer of Cylinder A particles and throws some glass beads on the bed surface. This state is quite unstable with a quite small fountain intermittently appearing and disappearing, and correspondingly the pressure drop still jumps between 3.1 kPa (point f) and 3.4 kPa (point e). It should be noted that, the term of “a small fountain” not only refers to that the height of fountain is very low, but also the scope covered by the fountain is very narrow in the bed surface. Only the cylindroid particles within the central region of the column are involved into the spouting, while the cylindroid particles near the wall only slightly vibrate at their respective positions or even remain stagnant. The poor flowability and larger size of cylindroid particles make them difficult to entrain for a small fountain, which means that the first cycle in the spouted bed is very local. This small fountain holds for only several seconds and then collapses. When the fountain disappears, all of the visible bamboo particles are stagnant or only slight vibrate, and a degree of segregation is obviously observed between the bamboo particles and glass beads which have mixed together during the previous cycle. After several seconds, the internal jet re-breaks through the bed surface and forms an external fountain. This state that fountain intermittently appears and disappears reflects the hysteresis effect of the current system.

Once the gas flow rate exceeds 88 m/s (i.e, the superficial gas velocity exceeds 0.88

m/s), a continuous and obviously higher fountain quickly forms and all particles in beds start to move. The cylindroid particles and glass beads are perfectly mixed and circularly move together in the bed. After stable external spouting forms, the increase in gas velocity still brings out a slowly rising pressure drop, as shown as the regime labeled as full mixing in [Figure 3-2](#). This phenomenon is somewhat different from that in the spouted bed handling a single kind of fine spherical particles, in which the pressure drop is usually reported as a roughly constant value with further increase in gas velocity.

In the total flow ascending process, the regime of local mixing is the peculiar stage for spouting the binary system which is initially layered. At point c, the internal spout just reaches the interface between glass beads and cylindroid particles, while it has extended through the layer of bamboo particles and near to the upper bed surface at point d. The difference in properties and compaction states of particles under and above the interface is believed to be responsible for the change in pressure drop trends before and after point c. The pressure drop in the flow ascending process is ascribed to the weight and compaction of the curvature region right above the roof of the internal spout [9]. Before the point c, the internal jet is within the layer of glass bead. With the increasing gas flow rate, the jet gradually expands, resulting in the gradual decrease of the glass beads above the roof of the inter spout. This decrease of glass beads with large density leads to the rapidly decreasing pressure drop in [Figure 3-2](#). However, after point c, it is the lighter bamboo particles above the roof of internal jet that gradually decrease with the increasing gas flow rate, which results in the obviously less rapid decrease in pressure drop. For the small growth in pressure drop from point d and e, the possible reason is that when the top of spout is approaching the upper bed surface, the fine glass beads are thrown upward into the space between the bamboo particles, which decreases the void fraction between particles and increases the mass above the roof of the internal spout, resulting in the slight increase in the pressure drop.

The similar distribution of pressure drop vs. superficial gas velocity was reported in a spouted bed equipped with a nonporous draft tube by Altzibar et al. [15, 16]. On

pressure drop curve of the bed with a nonporous draft tube, there is also a special turning point during the pressure drop decreases from the maximum value to the value of fountain formation with the increasing air velocity. Before and after this point, the pressure drop trends are different. Unfortunately, the authors [15, 16] did not provide the detailed information on the turning point. However, it is worth noting that both in the spouted bed with nonporous draft tube and in the current one handling the two kinds of particles that are initially layered, the spouts will go through two different regions. In the spouted bed with nonporous draft tube, the two regions are entrainment zone and tube zone, while in the current bed the spout will go through the layer of glass beads and the layer of bamboo particles. Zhao et al. [17] proposed a promising approach to calculate the pressure drop of fixed beds in which only a part of the cross section of the bed is passed by the injected gas. They introduced a factor k for the superficial gas velocity to account for the uneven gas distribution in the cross section of their tapered fluidized bed without a gas distributor, as shown in Equation 3-1:

$$\Delta P_f = C_1 H_0 \frac{D_0}{D_1} U^* + C_2 H_0 \frac{D_0(D_0^2 + D_0 D_1 + D_1^2)}{3D_1^3} U^* + \frac{1}{2} \left(\frac{U^*}{\varepsilon_0} \right)^2 \left[\left(\frac{D_0}{D_1} \right)^4 - 1 \right] \rho \quad (3-1)$$

where $U^* = kU = 3.5U$, $C_1 = (150(1-\varepsilon_0)^2/\varepsilon_0^3)(\mu/(\phi d_p)^2)$ and $C_2 = (1.75(1-\varepsilon_0)/\varepsilon_0^3)(\rho/(\phi d_p))$

In the current study, for the binary system of Cylinder A particles and glass beads with $H_0 = 300$ mm, $X_c = 0.4$ and $U = 0.389$ m/s, the calculated peak pressure drop based on Equation 3-1 is $\Delta p_{max,cal} = 1.9$ kPa, while the experimental result is $\Delta p_{max,exp} = 11.6$ Kpa. The significant deviation between the calculated and experimental results mainly relies on several reasons. Equation 3-1 was derived from a tapered fluidized bed¹⁷, while here it is used in a spouted bed. The gas-solid flow in a cylindrical-conical spouted bed is quite different from that in a tapered fluidized bed, even though they are both in apparently fixed state. Additionally, the current system contains two kinds of initially segregated particles, which makes the definition of parameters in Equation 3-1 somewhat doubtful. It should be pointed that, Equation 3-1 is still a quite promising prediction for the pressure drop in fluidized beds, but necessary validation or

modification is required when it is applied in spouted beds.

The spouting behaviors of binary mixture with cylinder A particles and glass beads in the gas flow descending process also have been investigated in the present work and the detailed information is revealed in [Figure 3-2](#). When gas velocity decreases from 95 m/s to 86 m/s, one can observe that the fountain in the bed becomes shorter, and the rate of particle circulation is slower. Particles in annulus consequently move down very slowly. A few of bamboo particles even stagnate on the edge of the bed surface. Slight local segregation can be first observed on the bed surface. During this process, the total pressure drop decreases slowly, following the similar path to that in the ascending process, until it suddenly elevates at $u=84$ m/s ($U=0.84$ m/s). With $u=84$ m/s ($U=0.84$ m/s), stable external spouting disappears. Only a very small fountain intermittently occurs with the pressure drop correspondingly jumping between points i and j. Obvious local segregation also happens in the annulus, which will become more significant when the fountain collapses. External spouting can be maintained at a considerably lower gas velocity in the gas flow descending process. In current study, the inlet gas velocity corresponding to point i and j is defined as the inlet-based minimum spouting velocity, u_{ms} . The superficial minimum spouting velocity is $U_{ms} = u_{ms}/100$.

With the further decreasing gas flow rate, the fountain disappears completely, and more bamboo particles are elevated to the upper bed level, resulting in the increasingly obvious local segregation. The total pressure drop decreases, following a quite different path, with a much lower pressure drop than for the ascending process. When the inlet gas velocity decreases to approximately zero, the cylindroid bamboo particles tend to distribute in the upper part of the bed. From the bed surface to the bottom, the concentration of bamboo particles declines, while the glass beads show the completely different distribution. There is no clear interface between these two kinds of particles.

In conclusion, in the spouted bed handling the binary system of cylindroid bamboo particles and glass beads with the proper particle properties and volume ratio, once the gas velocity exceeds the minimum spouting velocity and the resulting stable external

spouting takes place, the cylindroid particles and glass beads will fully mix with each other and stably circulate together through the spout region, fountain region and annulus region. During the stable spouting, i.e., the normal operating status in a spouted bed reactor, segregation phenomenon never happens. The segregation only appears when gas velocity is lower than the minimum spouting velocity, which is an apparently improper operating condition. The proper volume ratio and the minimum spouting velocity are the key parameters that directly determine both the stable spouting and full mixing. This is quite different from the observation in the fluidized beds which is characterized with the complicated and indistinct relationships between the fluidization regimes and the mixing and segregation phenomena [5, 18, 19]. The minimum spouting velocity in a spouted bed has been found to depend on various factors, such as the reactor configuration, the properties of particles and gas, and the operating conditions [9]. However, the current study is focused on the treatment on the binary system of cylinders and spheres in a spouted bed, and therefore the proper volumetric ratio and the effect of volume ratio on the minimum spouting velocity will be emphatically discussed in the following sections.

3.4 Characteristics of pressure drops

3.4.1 Effects of volume fraction of cylindroid particles on the pressure drop

The volume fraction of cylindroid particles, X_c , in the spouted bed, reflecting the biomass ratio that the unit handles in practical applications, is one of the important design parameters. The volume fraction of Cylinder A particles is varied from 0 to 1.0 in current study to investigate the effects of X_c on the total pressure drop in the bed, while the total static bed height is kept as $H_0=300$ mm. Typical curves of pressure drop in the flow ascending process are illustrated in [Figure 3-3](#).

In [Figure 3-3](#), the increase in X_c leads to the decreasing total pressure drop in their ascending processes. The pressure drop in the flow ascending process is ascribed to the weight and compaction of the curvature region right above the roof of the internal spout [9], and properties of particles above the roof of the internal spout significantly affect

the pressure drop. When X_c increases, the amount of bamboo particles with lower density increases, while the amount of glass beads with higher density decreases, which effectively reduces the weight of particles above the roof of the internal spout. When stable spouting forms in the bed with perfect mixing taking place, the increase in X_c effectively reduces the bulk density in the column, which needs lower pressure drop to support the spouting.

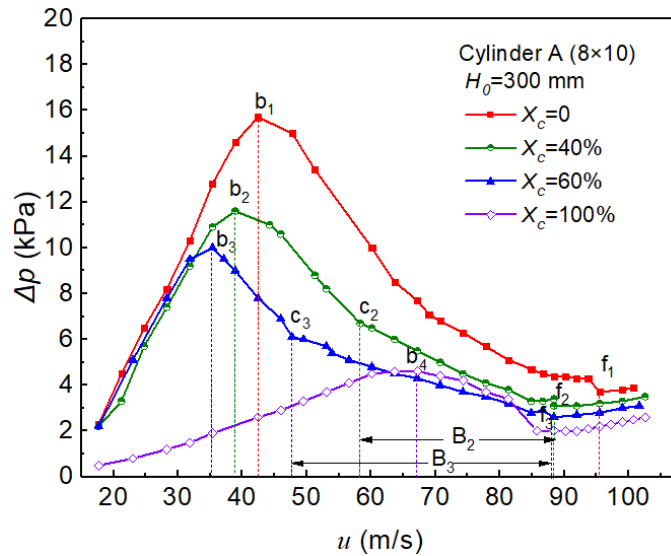


Figure 3-3 Evolutions of total pressure drop in the gas flow ascending when handling Cylinders A and glass beads with varying X_c ($H_0=300$ mm)

Figure 3-3 also shows the obvious difference in the distribution trends of pressure drops with different X_c . For the binary systems with $X_c=0.4$ and 0.6 , in which bamboo particles and glass beads initially layered in the bed, the regime of local mixing of $X_c=0.6$ (labeled as B_3) is obviously wider than that of $X_c=0.4$ (B_2). Δp_{max} always comes out in the regimes of complete segregation, and the bed with larger X_c encounters its smaller maximum pressure drop at the lower gas velocity. When X_c increases from 0.4 to 0.6 , the layer of glass beads becomes thinner, causing that the turning point c_3 comes at the lower gas velocity than c_2 dose.

Above phenomenon, however, never happens when spouting pure glass beads ($X_c=0$) or pure bamboo particles ($X_c=1.0$). Compared with aforementioned evolutions of pressure drop, there are many other unique and interesting phenomena in spouting the pure non-spherical bamboo particles with larger size and lower density ($X_c=1.0$ in

Figure 3-3), which will be discuss in detail in our another work.

3.4.2 Effects of particle size on the pressure drop

In the thermo-chemical conversion of biomass, the size and shape of biomass particles is another important factor to affect the operational efficiency of the spouted beds. Therefore, three kinds of bamboo particles, i.e., Cylinder A ($d \times l = 8 \text{ mm} \times 10 \text{ mm}$), Cylinder B ($4 \text{ mm} \times 10 \text{ mm}$) and Cylinder C ($4 \text{ mm} \times 20 \text{ mm}$), are adopted to preliminarily investigate the effects of particle size and shape on the flow behaviors in the bed under the condition that $X_c = 0.4$ and $H_0 = 300 \text{ mm}$. Detailed properties of these three kinds of particles are shown in Table 3-1.

The pressure drop distributions of three kinds of bamboo particles respectively mixing with glass beads are illustrated in Figure 3-4. Three curves are in similar trends, and three regimes, as well as the key points, defined in Figure 3-2 can be explicitly distinguished in each curve.

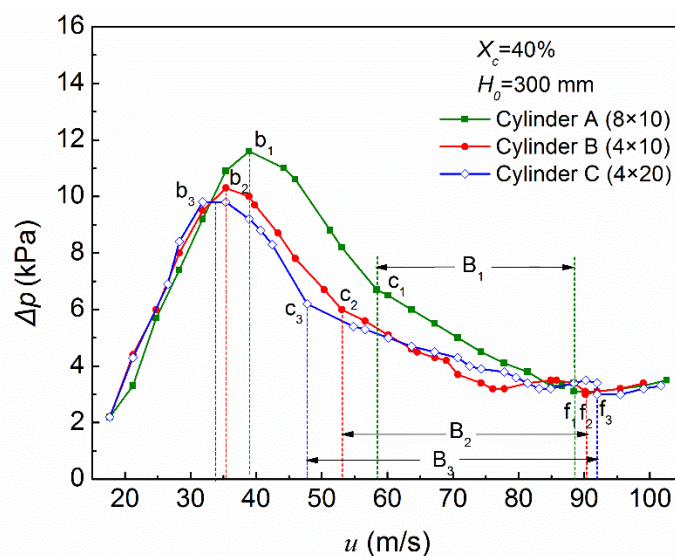


Figure 3-4 Evolutions of total pressure drop in the gas flow ascending when handling glass beads and different cylindroid particles ($H_0 = 300 \text{ mm}$, $X_c = 0.4$)

However, the differences in diameter and height of cylinders cause their differences in packing void fraction, equi-volume sphere diameter, aspect ratio (or sphericity), and these complicated features combined with the special structure of the bed, lead to obvious differences in the three pressure drop curves. The curve corresponding to

Cylinder C with the largest aspect ratio is the first to encounter its peak value (point b_3), followed by the curve of Cylinder B and the curve of Cylinder A, while the values of Δp_{max} are successively larger. The curve of Cylinder C also encounters its turning point c_3 at a lowest gas velocity, while the curve of Cylinder A encounters its turning point c_1 at the highest gas velocity.

The maximum pressure drops of these binary systems take place before their internal spout extend into the layer of bamboo particles, and therefore the shape and size of bamboo particles are not able to directly affect the evolution of the internal spouts. But the Cylinder A particles have a lowest packing void fraction, which means, with the same packing volume, this kind of particles will have the greatest mass compared to the other kinds of cylinders. The greatest mass right above the roof of internal spout most seriously suppresses the development of the internal spout and the system needs highest gas velocity to reach its largest Δp_{max} and to expand through the layer of glass beads. For the Cylinder C with high aspect ratio, its highest packing void fraction leads to the fastest growing internal spout in the bed, and therefore the corresponding curves reaches its Δp_{max} at the lowest gas velocity. The packing void fraction is considered as the main factor to affect the evolution of pressure drop in the layer of glass beads.

When the internal spout extends into the layer of bamboo particles, the shape and size of bamboo particles, determining their flowability, will directly influence the flow behaviors in beds, which results in the complicated pressure drop distributions in regimes of local mixing. Cylinder A particles have the highest sphericity and thus the best flowability, which leads to that curve of Cylinder A in Regime B_1 is smooth and the pressure drop decreases near linearly with the increasing gas velocity, while the lower sphericities of Cylinder B and C (or the higher aspect ratio), causing the worse flowability, make their curves in Regime B_2 and Regime B_3 more fluctuant. In addition, the worse flowability is bad for the development of internal spout and thus the curve of Cylinder C goes through the widest Regime B_3 , finally obtaining the stable spouting (point f_3) at the highest gas velocity, while the curve of Cylinder A goes through the narrowest Regime B_1 , obtaining its stable spouting (point f_1) at the lowest gas velocity.

After the stable spouting forms, the pressure drops of three curves are very similar both in value and trend and the possible reason is that when stable spouting takes place, the bamboo particles well mix with the glass beads and the flowability of this mixture mainly depends on the glass beads, which is in majority in beds.

In addition, the maximum pressure drop, Δp_{max} , in the beds with varying volume fractions of Cylinder A, as well as Cylinder B and C, are illustrated in Figure 3-5. It reveals that X_c obviously influences Δp_{max} , and for each kind of bamboo particles, Δp_{max} always near linearly decreases with the increasing X_c ; for different cylindroid particles with the same X_c , the particles with larger packing void fraction will be of the lower Δp_{max} .

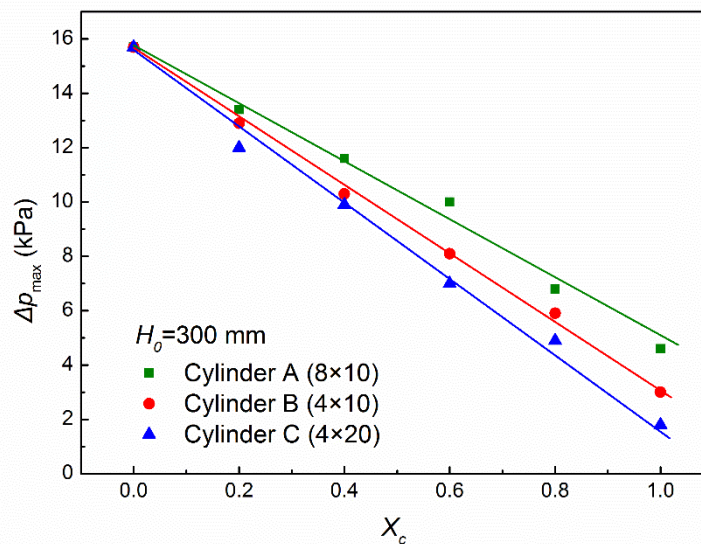


Figure 3-5 The maximum pressure drop when handling glass beads and different cylindroid particles with varying X_c ($H_0=300$ mm)

Δp_{max} is recommended to be proportion to the bulk density of bed, ρ_b , in the system of spouting homogenous particles[20-22]. However, for the binary systems with larger cylindroid particles and fine spherical particles which are initially layered, influences on Δp_{max} become more complicated. Here, with the increasing X_c , the decreasing mass in the region directly above the internal spout mainly contributes to the decrease of Δp_{max} . At the same static bed height, the increasing X_c , thickening the layer of bamboo particles in the initial bed, causes the linearly decrease in the mass above the internal

Chapter 3 Experimental study on spouting and mixing behaviors of cylindroid particles spout, leading to the decreasing Δp_{max} . The larger packing void fraction in the layer of cylindroid particles will also reduce the mass above the internal spout, and then result in the decrease in Δp_{max} .

3.5 Characteristics of stable spouting

To more directly investigate and comprehend the spouting and mixing phenomenon in spouted beds, the snapshots of spouted beds with different particles and varying X_c are shown in [Figure 3-6](#), and the corresponding fountain heights are illustrated in [Figure 3-7](#). In all cases, the gas velocity is $u=106$ m/s.

3.5.1 The maximum volume fraction of bamboo particles, $X_{c,max}$ in mixture

In [Figure 3-6](#), when X_c of Cylinder A particles varies from 0 to 1.0, stable spouting can successfully forms in every case and in the cases of $X_c=0.2, 0.4, 0.6$ and 0.8 , the particles of Cylinder A mix very well with the glass beads. For Cylinder B particles, stable spouting and well mixing can take place under the conditions of $X_c \leq 0.6$ with the gas velocity of 106 m/s. When X_c is increased from 0.8 to 1.0, the fountain becomes unstable and leans towards the bed wall with increasingly high probability.

For Cylinder C particles, stable spouting and well mixing only can take place under the conditions of $X_c=0, 0.2$ and 0.4 . When $X_c=0.6$, the fountain starts to lean toward the bed wall intermittently; when $X_c=0.8$, the fountain always leans so that it is difficult to capture its height. When $X_c=1.0$, external spouting even fails to form with the inlet gas velocity of 106 m/s in the flow ascending process. The high aspect ratio of Cylinder C particles results in their bad flowability, and mixing them with the fine spherical glass beads can effectively improve the flowability of the mixture. With increasing X_c , the volume fraction of glass beads decreases and the flowability of mixture in the bed become worse, which cause the fountain increasingly leaning. With continuously taking multiple shots, the instantaneously upright fountain was captured in the [Figure 3-6](#).

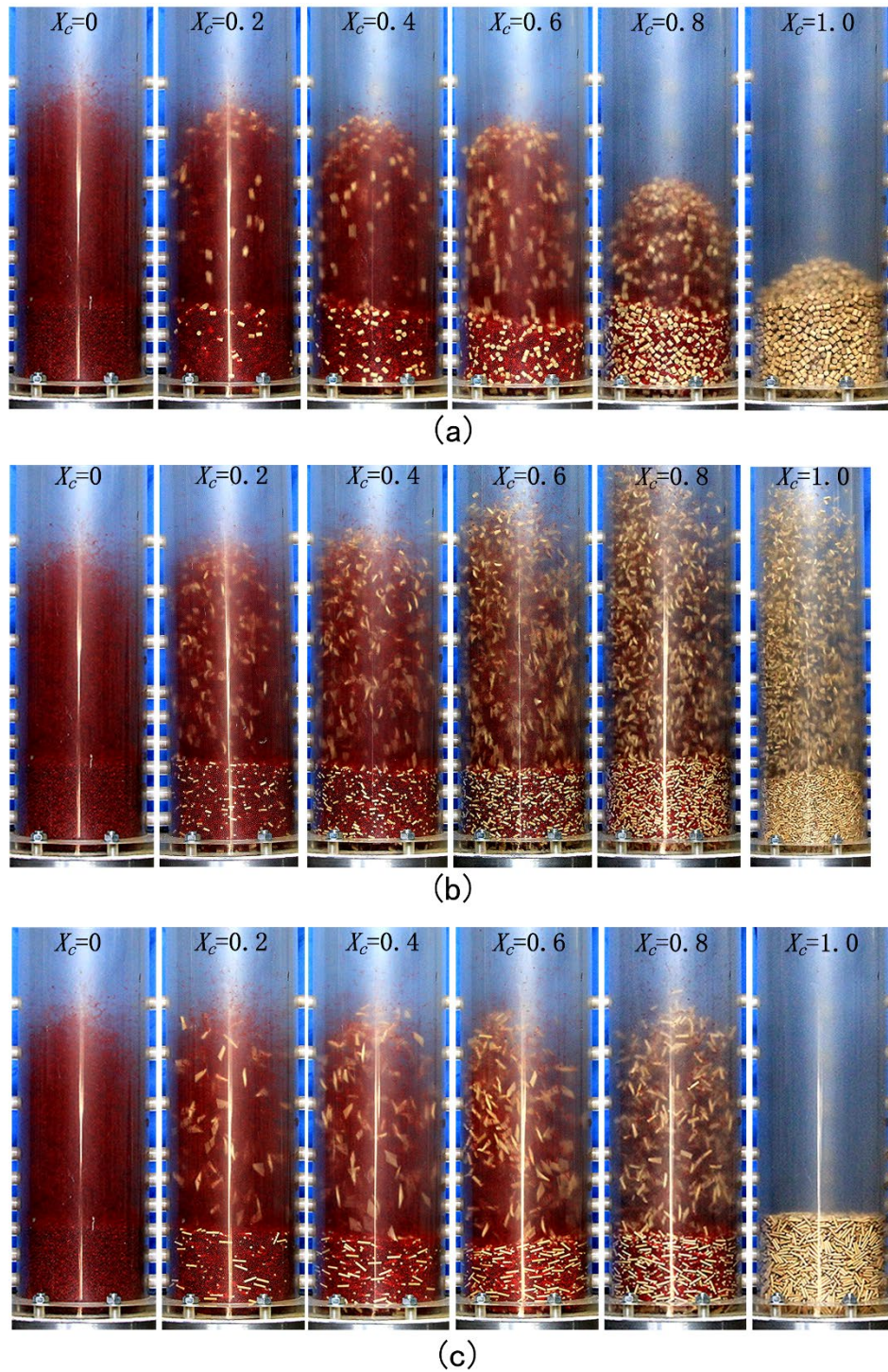


Figure 3-6 Snapshots of external spouting states handling the mixtures of glass beads and different cylindroid particles with varying X_c ($H_0=300$ mm, $u=106$ m/s): (a) Cylinder A with $d_v=9.9$ mm and $l/d=1.25$; (b) Cylinder B with $d_v=6.8$ mm and $l/d=2.5$; (c) Cylinder C with $d_v=7.2$ mm and $l/d=5$.

For each kind of the bamboo particles, there is a maximum volume fraction of bamboo particles, $X_{c,max}$, to maintain the stable spouting with a certain gas velocity. $X_{c,max}$ is considered to be related to the flowability of bamboo particles, which depends on the

aspect ratio of cylinders in current study. With the gas velocity of 106 m/s, $X_{c,max}$ of Cylinder A is 1.0, and for Cylinder B and C, $X_{c,max}$ is 0.6 and 0.4, respectively, which means that the cylindroid particles with larger aspect ratio will be of the less $X_{c,max}$ when they are mixed with the bed materials in spouted beds.

3.5.2 Fountain height

The fountain height, h_f , is defined as the distance from the surface of the annulus to the top of the fountain in current study, and the detailed values under different conditions are revealed in Figure 3-7.

These three kinds of particles show the entirely different changes of fountain height with varying X_c , as gas velocity is kept as 106 m/s, i.e., $U=1.06$ m/s. For Cylinder A particles, the fountain height decreases with the increasing X_c , while fountain height of Cylinder B obviously increases when X_c is increased. Different from both the situations of Cylinder A and Cylinder B, the fountain height of Cylinder C only presents a quite slight increase with the increasing X_c . In addition, with the same X_c (except for the cases of $X_c=0$ and 1.0), the mixture including Cylinders B always achieves the highest fountain, while the mixtures including Cylinders A obtains the lowest fountain.

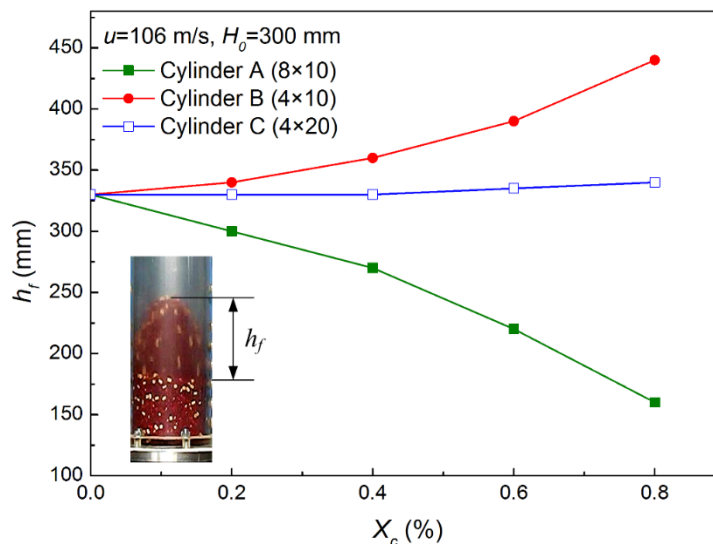


Figure 3-7 Fountain heights when spouting the mixtures of glass beads and different cylindroid particles with varying X_c ($H_0=300$ mm, $u=106$ m/s)

3.6 Key parameters and their influence on the mixing behaviors

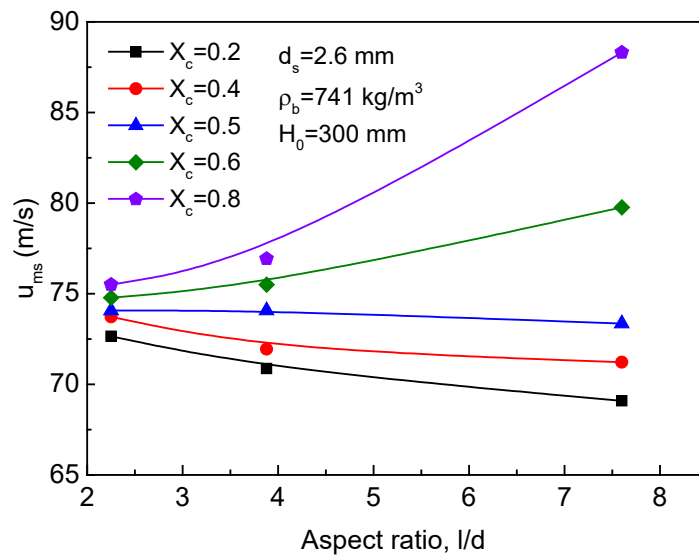
The minimum spouting velocity, u_{ms} , is one of the most important parameters in the design and operation of spouted beds [9,23]. It is the minimum gas velocity required to establish the external spouting, and generally presents the different values when the spouted bed is operated respectively followed the velocity ascending process and descending process. The minimum spouting velocity that obtained in the velocity ascending process is usually higher than that from the velocity descending process, and in this study, the latter value is adopted to discuss as the characteristic parameter of spouted beds. The minimum spouting velocity are closely related to various factors such as material properties, bed structure and operating conditions [9] with the complicated influence mechanisms. Many researchers have conducted enormous in-depth researches and proposed a large number of reliable u_{ms} prediction correlations including the well-known Mathur-Gisshler correlation (M-G correlation, 1955) [24], however, of which most for the small scale spouted beds with spherical particles [24-30]. To date, the studies on the characteristics of the minimum spouting velocity in large industrial spouted beds are very limited [31-35], and that involving the non-spherical particles or their mixtures are even more rare. Compared with in the spouting systems with only the spherical particles, the influence factors of u_{ms} in that including the mixtures of the non-spherical particle and spherical particles are more complicated [13]. It is not only closely related to the various sizes and densities of the constituent particles, but also largely affected by their shapes and the proportions. The detailed influences of these factors on u_{ms} in the spouted beds with multi kinds particles are significantly unclear, and relevant research is urgently required.

3.6.1 Effects of particle shapes

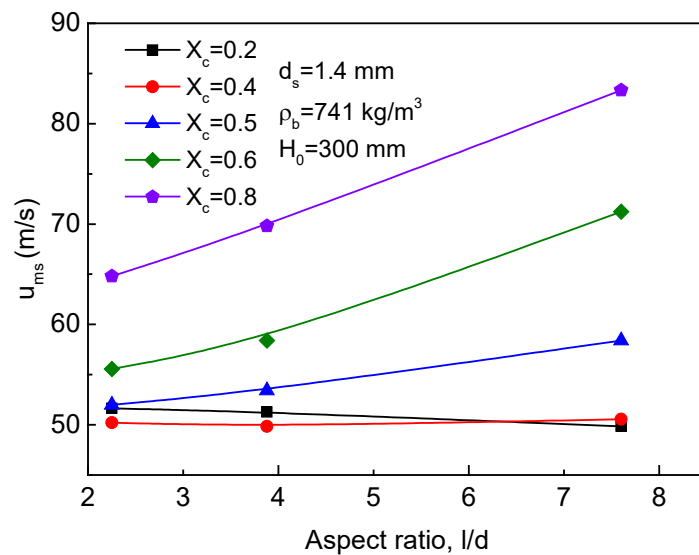
The effects of particle shapes of cylinders on the minimum spouting velocity of the spouting systems with binary particles were shown in [Figure 3-8](#) under the conditions that the diameters of spherical glass beads (bed material), d_s , were 2.6 mm and 1.4 mm. Three kinds of cylindroid particles with the equivalent volume diameter of $d_v=9.0$ mm

Chapter 3 Experimental study on spouting and mixing behaviors of cylindroid particles were involved in the experiments with their aspect ratios being $L/d= 2.25, 3.88$ and 7.6 , respectively.

For the cases with the bed materials of $d_s= 2.6$ mm, when the volume fraction of cylindroid particles in the spouted bed was less than 0.5, namely $X_c \leq 0.5$, the u_{ms} of the system decreased slightly with the increase of the aspect ratio of the cylindroid particles, while when $X_c > 0.5$, the u_{ms} started to increased significantly with the increasing aspect ratio.



(a)



(b)

Figure 3-8 u_{ms} of the mixing system including the cylinders with varying shape: (a) $d_s=2.6$ mm; (b) $d_s=1.4$ mm

This was because for the binary particle system with the small volume fraction of the cylindroid particles and the large volume fraction of bed material, the spherical glass bead particles are decisive for the spouting behaviors of this system. The cylindroid particles are uniformly dispersed in the large amount of bed material particles which could be easily spouted stably and effectively in the bed, and the effects of their shape become not obvious. However, the cylinders with the increasing aspect ratio perform the increasing voidage when loosely stacked in the bed (see [Table 3-1](#)). Thus with the same bulk volume in the bed, the mass of cylinders, as well as the total mass in the bed, will decrease, and the minimum gas velocity required to spout them also slightly decreases.

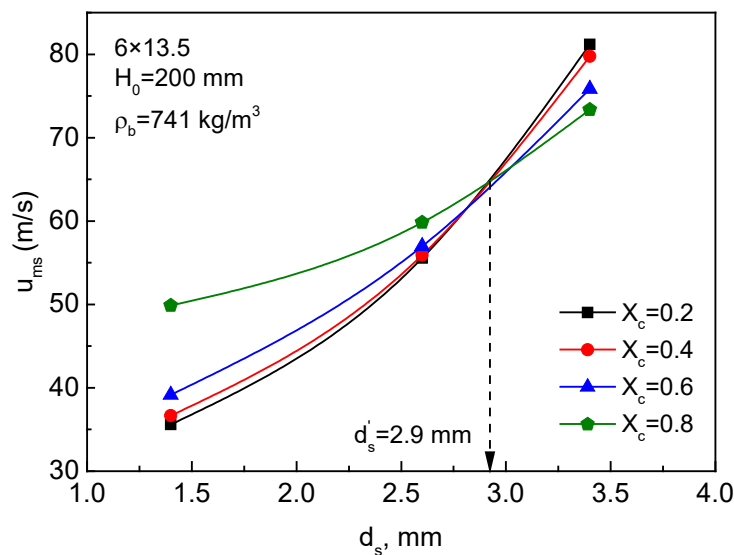
When the volume fraction of cylindroid particles in the bed become large, for example, $X_c \geq 0.6$, seen in [Figure 3-8\(a\)](#), the properties of the cylindroid particles begin to play a decisive role in the spouting behaviors, with their shape showing the obvious influence on the minimum spouting velocity in the bed with the binary particles. With the larger aspect ratio, the cylindroid particles become longer and thinner and their interactions like collision, friction and inter-locking will intensify. This leads to the poor fluidization in the bed and the increasing gas velocity to support the spouting. Therefore, when the volume fraction of cylindroid particles in the bed is larger than 0.5, the minimum spouting velocity of the mixing system increases significantly with the increasing particle aspect ratio; This increasing trend becomes more significant as X_c is larger.

For the system with the bed material particles of 1.4 mm, the minimum spouting velocity shows the similar trend when the aspect ratio of cylinder increases, as shown in [Figure 3-8\(b\)](#). Compared to the case that the glass bead has a size of 2.6 mm, the minimum spouting velocity shows the obvious decrease as the size of bed material particles becomes smaller. The smaller bed material particles perform a lower ability to carry the cylindroid particles especially at the lower spouting velocity. Therefore, when $X_c=0.5$, the overall flow behavior in the bed with the bed material of $d_s=1.4$ mm already begun to be dominated by cylindroid particles, and the minimum spout velocity of the system turns to increase with the increase of the aspect ratio of cylinders, while in the

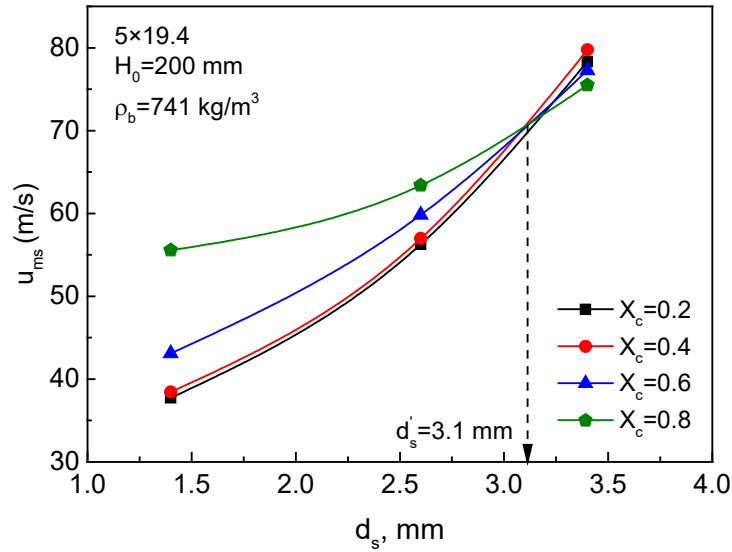
Chapter 3 Experimental study on spouting and mixing behaviors of cylindroid particles mixed system with the bed material (glass bead) of $d_s=2.6$ mm, the spouting behavior in the bed is still mainly dominated by the bed material as $X_c=0.5$.

3.6.2 Effects of the size of bed materials

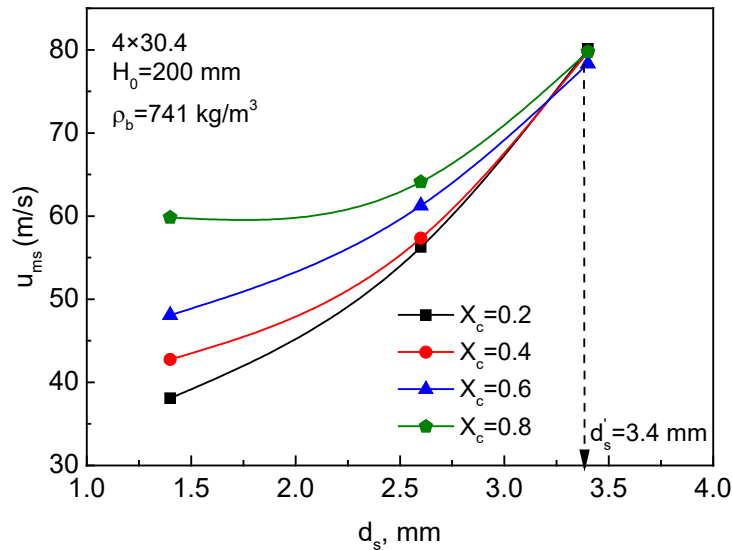
Under the condition that the static bed height is $H_0=200$ mm, the densities of cylindroid particle and bed material are $\rho_b=741$ kg/m³ and $\rho_s=2600$ kg/m³, respectively, the minimum spouting velocities of the mixing system are shown in Figure 3-9 with the particle size of the bed material, d_s , increasing from 1.4 mm to 3.6 mm. When mixing with three kinds of cylinders with different aspect ratios, the u_{ms} of the system always increases with the increasing particle size of the bed material. At the condition that the volume fraction of cylinders in the bed is lower, namely the volume fraction of the bed material particles is higher, this increasing tendency of u_{ms} is more obvious. This is because when the particle size of the bed material increases with its specific surface area decreasing, the fluid force acting on the particles of the unit mass will reduce. Therefore, the higher gas velocity is required to support the spouting in the bed. With the higher volume fraction of bed material particles in the bed, this effect become more obvious.



(a)



(b)



(c)

Figure 3-9 The change of u_{ms} in the spouted bed with the particle sizes of bed material varying from 1.41 mm to 3.4 mm: (a) cylinder E1 6x13.5; (b) cylinder D2 5x19.4; (c) cylinder D3 4x30.4

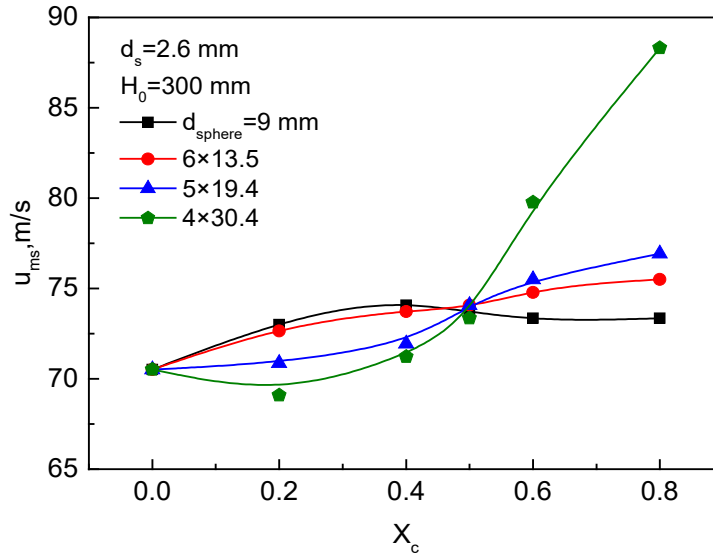
For one kind of cylinder particle, for example, the D1 particle in Figure 3-9 (a) ($d \times L = 6 \text{ mm} \times 13.5 \text{ mm}$), when the particle size of the bed material is very small, like $d_s < 2.9$ mm, u_{ms} in the bed increases significantly with the increasing X_c , while if $d_s > 2.9$ mm, u_{ms} turns to decrease with the increase of X_c . When d_s is around 2.9 mm, u_{ms} of the system remains almost the same as X_c changes in the range of 0.2 to 0.8. That is, in the current spouting system with the binary particles, when the particles with the diameter of $d'_s \approx 2.9$ mm are used as bed material, u_{ms} in the bed is nearly independent of the

volume fraction of cylinders and the cylindroid particles ($d_v=9.0$ mm) and bed material seem to be equivalent regarding u_{ms} . For the growingly elongated particles D2 (Figure 3-9(b), $d \times L = 5$ mm \times 19.4 mm) and the particles D3 (Figure 3-9 (c), $d \times L = 4$ mm \times 30.4 mm), the equivalent d_s' are approximately 3.1 mm and 3.4 mm, respectively. Obviously, as the aspect ratio of the cylindroid particles increases, the equivalent bed diameter d_s' in the mixing system gradually increases. This increase in the diameter d_s' of the equivalent bed material can reflect to some extent the effects of the change in the shape of cylindroid particles.

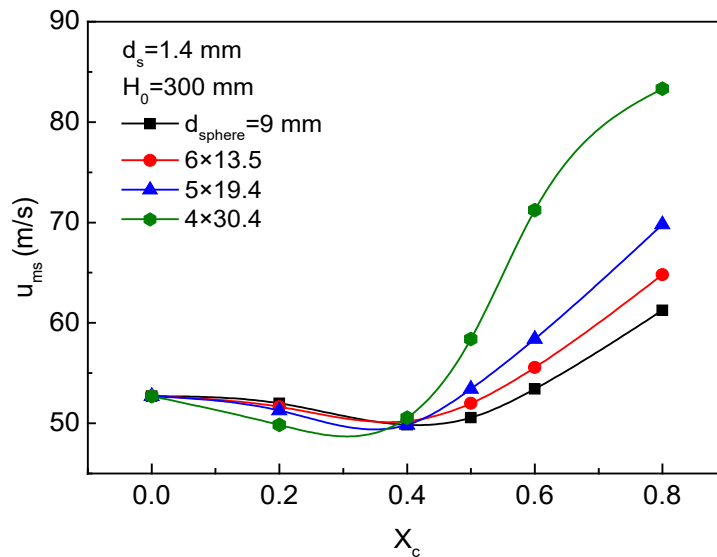
3.6.3 Effects of the volume fraction of cylindroid particles

Figure 3-10 shows the minimum spouting velocities of the systems that three kinds of cylinders and the sphere which have the same particle volume respectively mix with the bed material with the different X_c . Compared with the Figure 3-8, Figure 3-10 more clearly shows that when the cylindroid particles mix with certain a kind of bed material, the cylindroid particle has a special critical volume fraction, X_{cc} . When $X_c < X_{cc}$, the spouting behavior in the bed is mainly dominated by bed material, and the influence of the shapes of cylinders on u_{ms} is relatively limited. The minimum spouting velocities of the systems with the same bed material and different cylindroid particles show the limited difference. The main reason for the difference is that cylindroid particles with the larger aspect ratio are usually of the smaller particle packing density (Table 3-1). This will lead to the lighter bed mass when packed in the spouted bed with the same volume fraction, and thus the smaller minimum gas velocity required to support the spouting.

When $X_c > X_{cc}$, the spouting behavior of the mixing system turns to be dominated by cylindroid particles, and the differences in the shapes of cylindroid particles begin to bring significant changes in the minimum spouting velocity in the bed. With the same volume fraction, the cylindroid particles that have the larger aspect ratio will perform the stronger interaction, which will result in the worse particle fluidity and thus the higher minimum spouting velocity for the mixing systems.



(a)



(b)

Figure 3-10 The effects of volume fraction of cylindroid particles on u_{ms} in the spouted bed with binary particles: (a) $d_s=2.6 \text{ mm}$, (b) $d_s=1.4 \text{ mm}$

Under the condition that the static bed height is $H_0=300 \text{ mm}$ with the density and equal volume fraction of the cylindroid particle being $\rho_b=741 \text{ kg/m}^3$ and $d_v=9.0 \text{ mm}$, and that of the bed material particle being $\rho_s=2600 \text{ kg/m}^3$ and $d_s=2.6 \text{ mm}$, the critical volume fraction of cylindroid particles in the spouting system is about $X_{cc} = 0.5$ as seen in [Figure 3-10\(a\)](#). Under this critical operating condition, the minimum spout velocity of the mixing system is nearly unaffected by the shape of the material particles. It can be considered that under this condition, the bed material particles have a relatively large carrying capacity, and can effectively mask the influence of the shape of cylindroid

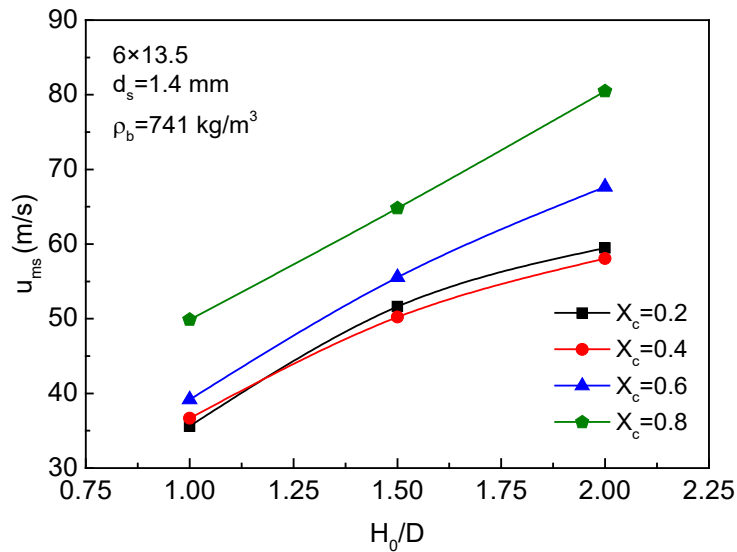
particles on the minimum spouting velocity of the system. When the particle size of the bed material d_s reduces to 1.4 mm, the volume fraction of the bed material with the maximum carrying capacity under the current system is about $X_{sc}=1-X_{cc}=1-0.4=0.6$, as shown in [Figure 3-10\(b\)](#), and the corresponding volume fraction of cylindroid particles is $X_{cc}=0.4$. In general, when the volume fraction of cylindroid particles in the spouting system is less than X_{cc} , the minimum spout velocity in the bed can be roughly determined by the properties of the bed material, and the influences of the volume fraction and shape of cylindroid particles are limited.

3.6.4 Effects of the static bed height

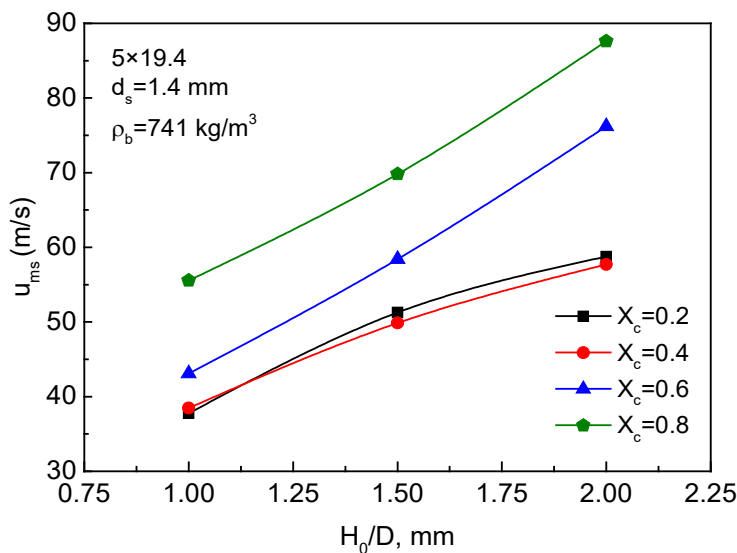
When cylindroid particle D1 ($d \times L = 6 \text{ mm} \times 13.5 \text{ mm}$) and D2 ($d \times L = 5 \text{ mm} \times 19.4 \text{ mm}$) are respectively mixed with the bed material of $d_s = 1.4 \text{ mm}$, the effects of the static bed height on the minimum spouting velocity are shown in [Figure 3-11](#). Results show that the minimum spouting velocity of the system obviously increase with the increasing static bed height. This is because the increasing static bed height results in an increase in the resistance that the gas needs to overcome as it penetrates the bed, thus a larger spouting gas velocity is required to support external spouting.

The tendency of the minimum spouting velocity in the bed increasing with the static bed height varies with the volume fraction of the cylindroid particles. When the volume fraction of the cylindroid particles is small, such as $X_c=0.2$ or 0.4 , the increase rate of u_{ms} shows a gradual decrease with the increasing static bed height, while with the larger volume fraction of cylindroid particles, the increase tendency of u_{ms} with the increasing static bed height becomes more obvious.

In addition, when the volume fraction of the cylindroid particles is small, the shape of the particles has little effect on the minimum spouting velocity. Only when the volume fractions of the cylindroid particles are large, the minimum spouting velocities in [Figure 3-11\(a\)](#) and [\(b\)](#) shows the significant differences.



(a)



(b)

Figure 3-11 Effects of static bed height on u_{ms} in the spouted bed with binary particles ($d_s=1.4$ mm): (a) D1 ($d \times L = 6$ mm \times 13.5 mm), (b) D2 ($d \times L = 5$ mm \times 19.4 mm)

3.7 Summaries

In this chapter, taking the cylindroid particles as a typically representative objects, the spouting and mixing characteristics of non-spherical particles and spherical particles (bed material) in the spouted bed were experimentally studied, and the spouting behaviors and mechanisms of the binary-particle systems were obtained. The main findings had been published in AICHE J. 2014 (61) 58-67. Summaries are as follows:

(1) The synchronous development of the spouting and the mixing of the binary-particle

system in the spouted bed is found. The spouting behaviors of the two kinds of particles in the spouted bed is synchronously coupled with the mixing behavior. As long as the stable external spouting is established, particles can thoroughly mix with each other, and once the external spouting collapses, these two kinds of particles show the partial separation immediately. Such coupled spouting and mixing in the spouted bed can significantly simplify the studies of mixing behaviors in the spouted beds to the problem regarding the stable spouting which have been understood relatively more comprehensively.

(2) The factors influencing the key parameters of the spouting and their change rules were figured out. The effects of particle properties (cylindroid particles and spherical bed material) and operating conditions on the minimum spouting velocity of the mixing system were studied and these effects were found closely related to the volume fraction of non-spherical particles. In general, when the volume fraction of cylindroid particles is small, the minimum spouting velocity increases with the increasing particle size of bed material and static bed height, while the effect of non-spherical particle shape on the minimum spouting velocity of the system is not obvious; When the volume fraction of the non-spherical particles is large, the minimum spouting velocity of the system increases obviously with the increasing aspect ratio of the cylindroid particles, as well as the static bed height, and the tendency of the minimum spouting velocity to increase with the increasing sizes of bed material obviously slow down.

(3) Two different system types that dominated by non-spherical particles and dominated by spherical bed material were proposed. Generally speaking, when the volume fraction of non-spherical particles is greater than 40%~50%, the spouting system with binary particles is dominated by non-spherical particles with the non-spherical particle properties showing significant influences on the characteristics and key parameters of spouting and the particle shape effects cannot be negligible; On the contrary, the mixing system is dominated by the spherical bed material, and the spouting characteristics and key parameters of the system mainly depend on the properties of bed material.

Reference:

- 1 Cui H P, Grace J R. Fluidization of biomass particles: A review of experimental multiphase flow aspects. *Chem Eng Sci*, 2007, 62(1-2):45-55
- 2 Bridgwater A V. Renewable fuels and chemicals by thermal processing of biomass. *Chem Eng J*, 2003, 91(2-3): 87-102
- 3 Mohan D, Pittman C U, Steele P H. Pyrolysis of Wood/Biomass for Bio-oil: A Critical Review. *Energy Fuel*, 2006, 20(3):848-889
- 4 Bridgwater A V, Peacocke G V C. Fast pyrolysis processes for biomass. *Renew Sust Energ Rev*, 2000, 4(1):1-73
- 5 Zhang Y, Jin B S, Zhong W Q. Experimental investigation on mixing and segregation behavior of biomass particle in fluidized bed. *Chem Eng Process (Process Intensification)*, 2009, 48(3):745-754
- 6 Bridgwater A V. Review of fast pyrolysis of biomass and product upgrading. *Biomass Bioenerg*, 2012, 38(0):68-94
- 7 Ren B, Zhong W Q, Jin B S, Shao Y J, Yuan Z L. Numerical simulation on the mixing behavior of corn-shaped particles in a spouted bed. *Powder Technol*, 2013, 234(0):58-66
- 8 Lathouwers D, Bellan J. Modeling of dense gas-solid reactive mixtures applied to biomass pyrolysis in a fluidized bed. *Int J Multiphas Flow*, 2001, 27(12): 2155-2187.
- 9 Epstein N, Grace J R. *Spouted and Spout-Fluid Beds: Fundamentals and Applications*. England: Cambridge University Press, 2011
- 10 Olazar M, San Jose M J, Penas F J, Aguayo A T, Bilbao J. Stability and hydrodynamics of conical spouted beds with binary mixtures. *Ind Eng Chem Res*, 1993, 32(11): 2826-2834
- 11 Olazar M, San Jose M J, Lamosas R L, Bilbao J. Hydrodynamics of Sawdust and Mixtures of Wood Residues in Conical Spouted Beds. *Ind Eng Chem Res*, 1994, 33(4):993-1000
- 12 Zhong W Q, Jin B S, Zhang Y, Wang X F, Xiao R. Fluidization of Biomass Particles in a Gas-Solid Fluidized Bed. *Energy Fuel*, 2008, 22(6): 4170-4176
- 13 Shao Y J, Zhong W Q, Chen X, Chen Y, Jin B S. Spouting of non-spherical particles in conical-cylindrical spouted bed. *Can J Chem Eng*, 2014, 92(4):742-746
- 14 Devahastin S, Mujumdar A S. Some hydrodynamic and mixing characteristics of a pulsed spouted bed dryer. *Powder Technol*, 2001, 117:189-197
- 15 Altzibar H, Lopez G, Bilbao J, Olazar M. Operating and peak pressure drops in conical spouted beds equipped with draft tubes of different configuration. *Ind Eng*

16 Altzibar H, Lopez G, Bilbao J, Olazar M. Minimum spouting velocity of conical spouted beds provided with draft tubes of different configuration. *Ind Eng Chem Res*, 2013, 52:2995-3006

17 Zhao Z G, Zhang J W, Zhang G Y, Zeng X, Liu X X, Xu G W. Hydrodynamic characterization of a tapered gas-solid bed without a gas distributor. *Powder Technol*, 2014, 256:300-309

18 Olivieri G, Marzocchilla A, Salatino P. A fluid-bed continuous classifier of polydisperse granular solids. *J Taiwan Inst Chem Eng*, 2009, 40:638-644

19 Marzocchella A, Salatino P, Di Pastena V, Lirer L. Transient fluidization and segregation of binary mixtures of particles. *AIChE J*, 2000, 46(11): 2175-2182

20 Asenjo J A, Muñoz R, Pyle D L. On the transition from a fixed to a spouted bed. *Chem Eng Sci*, 1977, 32(2): 109-117

21 Kmiec A. Hydrodynamics of Flows and Heat Transfer in Spouted Beds. *Chem Eng J*, 1980, 19(3):189-200

22 Rocha S C S, Taranto O P, Ayub G E. Aerodynamics and heat transfer during coating of tablets in two-dimensional spouted bed. *Can J Chem Eng*, 1995, 73(3):308-312

23 Mathur K B, Epstein N. Spouted beds. New York: Academic Press Inc., 1974

24 Mathur K B, Gishler P E. A technique for contacting gases with coarse solid particles. *AIChE J*, 1955, 1(2): 157-164

25 Choi M, Meisen A. Hydrodynamics of shallow, conical spouted beds. *Can J Chem Eng*, 1992, 70: 916-924

26 Anabtawi M Z, Uysal B Z, Jumah R Y. Flow characteristics in a rectangular spout-fluid bed. *Powder Technol*, 1992, 69(3): 205-211

27 Olazar M, José M J S, Aguayo A T, et al. Hydrodynamics of nearly flat base spouted beds. *Chem Eng J Biochem Eng J*, 1994, 55(1-2): 27-37

28 Du W, Bi X, Epstein N. Exploring a non-dimensional varying exponent equation relating minimum spouting velocity to maximum spoutable bed depth. *Can J Chem Eng*, 2009, 87(2): 157-162

29 Uemaki O, Yamada R, Kugo M. Particle segregation in a spouted bed of binary mixtures of particles. *Can J Chem Eng*, 1983, 61(3): 303-307

30 Zhong W, Liu X, Grace J R, et al. Prediction of minimum spouting velocity of spouted bed by CFD-TFM: Scale-up. *Can J Chem Eng*, 2013, 91(11): 1809-1814

31 He Y L, Lim C J, Grace J R. Spouted bed and spout-fluid bed behaviour in a column of diameter 0.91 m. *Can J Chem Eng*, 1992, 70(5): 848-857

32 Fane A G, Mitchell R A. Minimum spouting velocity of scaled-up beds. *Can J Chem*

33 Zhang H Q. The present status of study on hydrodynamics in larger-diameter spouted beds. Journal of Shenyang institute of chemical technology, 1991, 5(2): 105-114 (In Chinese)

34 Zhong W, Chen X, Grace J R, et al. Intelligent prediction of minimum spouting velocity of spouted bed by back propagation neural network. Int J Chem React Eng, 2015, 247(3): 197-203

35 Hosseini S H, Karami M, Olazar M, et al. Prediction of the minimum spouting velocity by genetic programming approach. Ind Eng Chem Res, 2014, 53(32): 12639-12643

**CHAPTER 4 CFD-DEM SIMULATIONS ON THE SPOUTING
BEHAVIORS OF CYLINDROID PARTICLES**

4.1 Introduction

The dynamics of non-spherical particles are significantly more complicated than those of spherical particles in many processes such as packing, compaction, conveying or fluidization, because the geometrical contact scenarios are far more diverse between a non-spherical particle and its neighbors or walls, as well as the interactions between particles and surrounding fluid. For example, angular particles (e.g., elongated and flatted biomass particles, solid waste particles or others) are likely to interlock each other to form solid-like assemblies, exhibiting stronger resistance to shear than smooth spheres [1], which will affect their spouting in the spouted beds. On the other hand, the various orientations of non-spherical particles also remarkably increase the complexity of the dynamic behaviors of the non-spherical particle flow systems. However, up to now studies on the spouting behaviors of non-spherical particles in spouted beds is very limited, mostly focusing on the mesoscale and macroscale gas-solid flow characteristics including spouting patterns, pressure drops, minimum spouting velocity, mixing behaviors and so on [2-6]. The in-depth understanding in the particle scale is significantly insufficient, and many important issues, for example, how the particle shape affects the spouting behaviors, still have no clear answers.

One of the main difficulties in the studies of the complex dense gas-solid systems with non-spherical particles lies in the lack of effective methods to obtain the detailed information in the particle scale, making it difficult to fully understand the dynamic characteristics and motion mechanisms of non-spherical particles. With the rapid developments of computer technology, numerical simulation has become an important approach to study the dense gas-solid two-phase flow to effectively make up for the shortcomings of experiment and theoretical analysis. Many advanced numerical techniques, such as Computational Fluid Dynamics (CFD), Monte Carlo Method, Cellular Automata Model, Discrete Element Method (DEM) and so on have been developed and widely applied as powerful tools [7]. Among them the DEM method, which can describe the relationships between micro- and macro-scopic properties of particulate matter by considering the shapes and properties of individual particles and

forces acting on them, has attracted increasing attention becoming one of the most promising approaches in the study of gas-solid flows with non-spherical particles [8]. DEM modellings of gas-solid systems with non-spherical particles have its own particular characteristics and difficulties. Many key problems are still under exploration, mainly including how to accurately characterize the non-spherical particle shapes and efficiently detect their contacts, how to calculate the contact forces of non-spherical particles and describe the gas-solid interaction and how to achieve the efficient coupling calculation of gas-solid two phases, and so on [8]. Southeast University had begun to focus on the DEM numerical simulations in 1999. After more than ten years of continuous development and optimization on theories and models [9-15], we successfully established the CFD-DEM parallel numerical simulation platform for the dense gas-solid systems with non-spherical particles, and took the lead to realize the CFD-DEM simulations of the fluidization or spouting behaviors of the corn-shaped particles, cylindroid particles and so on [8, 16-18]. For the previous works in Southeast University, the non-spherical particles were usually constructed with the Multi-Sphere Method. This method can explicitly and flexibly construct particles with arbitrary shapes, and converts the complicated contact detections and parameter calculations between the non-spherical particles into the simple problems between spheres, which remarkably increases the computational efficiency of non-spherical particle simulations, showing significant advantages in the simulations of industrial progresses involving the particles with large quantities or diverse shapes. However, the Multi-Sphere Method introduces some artificial roughness when depicting the particle shapes, which inevitably affects the microscopic forces and motions of the particles, and this has limited its applications in the fundamental studies dealing with the motion mechanisms of the non-spherical particles [18,19].

Based on the years of research works of Southeast University and closely cooperating with the group of Professor Aibing Yu from Monash University, this chapter developed the CFD-DEM models for the dense gas-solid systems with cylindroid particles. Different from our previous work in Southeast University with the non-spherical

particles usually being represented by the Multi-Sphere Method, in the current study, the real cylindroid particles including rod-like particles and disc-like particles, were accurately constructed by combining the two circular planes and one cylindrical curved surface, and the various different contact criteria including edge-edge, face-face, band-band, edge-face, edge-band, face-band and so on were comprehensively involved. With the more accurate and detailed particle shape representation and forces calculations, spouting features of cylindroid particles with varying shapes were investigated and the gas and solid dynamic mechanisms, as well as the effects of particles shapes on the spouting behaviors were comprehensively figured out in particle scale.

4.2 CFD-DEM models for the gas-solid flows with cylindroid particles

4.2.1 Turbulence model of gas phase

The k - ε model was adopted to simulate the turbulence of gas phase motions in the non-spherical particulate systems, with the detailed continuity equation, momentum conservation equation and k - ε equations are as follows:

(1) Continuity equation:

$$\frac{\partial}{\partial t}(\alpha\rho_g) + \nabla \cdot (\alpha\rho_g \mathbf{u}_g) = 0 \quad (4-1)$$

(2) Momentum conservation equation:

$$\frac{\partial}{\partial t}(\alpha\rho_g \mathbf{u}_g) + \nabla \cdot (\alpha\rho_g \mathbf{u}_g \mathbf{u}_g) = -\nabla p + \nabla \cdot (\alpha\boldsymbol{\tau}) + \alpha\rho_g \mathbf{g} - \mathbf{R}_{gs} \quad (4-2)$$

with

$$\boldsymbol{\tau} = (\mu + \mu_t) \left[\nabla \mathbf{u}_g + (\nabla \mathbf{u}_g)^{-1} - \frac{2}{3} \nabla \mathbf{u}_g \mathbf{I} \right], \quad \mu_t = C_\mu \rho_g k^2 / \varepsilon$$

where t is time, s; ρ_g is the gas density, kg/m³; \mathbf{u}_g is gas velocities, m/s; α is the volume fraction of gas; p is the gas pressure, Pa; $\boldsymbol{\tau}$ is the fluid viscous stress tensor, Pa; μ and μ_t are the gas kinetic viscosity and turbulent viscosity, respectively, Pa·s; C_μ is the empirical coefficient and $C_\mu=0.09$ in the current simulations [18]; k is turbulent energy, m²/s²; ε is the turbulent dissipation rate, m²/s²; R_{gs} is the term of gas-solid interaction, N, of which the calculation method is shown in [section 4.2.4.2](#).

(3) Equations of the turbulence model

The governing transport equations for turbulent energy k and turbulent dissipation rate ε are:

$$\frac{\partial}{\partial t}(\rho_g \alpha k) + \nabla(\alpha \rho_g k \mathbf{u}_g) = \nabla \left[\alpha \left(\mu + \frac{\mu_t}{\varepsilon_k} \right) \nabla k \right] + \alpha G_k + \alpha \rho_g \varepsilon_k + S_d^k \quad (4-3)$$

$$\frac{\partial}{\partial t}(\rho_g \alpha \varepsilon) + \nabla(\alpha \rho_g \varepsilon \mathbf{u}_g) = \nabla \left[\alpha \left(\mu + \frac{\mu_t}{\varepsilon_\varepsilon} \right) \nabla \varepsilon \right] + \alpha \frac{\varepsilon}{k} (C_1 G_k - C_2 \rho_g \varepsilon) + S_d^\varepsilon \quad (4-4)$$

G_k represents the generation of turbulence kinetic energy due to the mean velocity gradients with

$$G_k = \frac{\mu_t}{\rho_g} \left\{ 2 \left[\left(\frac{\partial u}{\partial x} \right)^2 + \left(\frac{\partial v}{\partial y} \right)^2 \right] + \left(\frac{\partial u}{\partial y} + \frac{\partial v}{\partial x} \right)^2 \right\} \quad (4-5)$$

$\varepsilon_k=1.0$ and $\varepsilon_\varepsilon=1.33$ are the turbulent Prandtl constant [18, 20]; S_d^k and S_d^ε give the influence of the particle to the fluid, calculated by:

$$S_d^k = \beta |\mathbf{u} - \mathbf{v}_p|^2 + \beta (\Delta v \Delta v - \Delta u \Delta v) \quad (4-6)$$

$$S_d^\varepsilon = C_3 \frac{\varepsilon_\varepsilon}{k} S_d^k \quad (4-7)$$

where Δu and Δv are the instantaneous velocity pulsations of gas phase and solid phase, respectively; the first term on the right of the Equation 4-6 is the solid particle resistance production term, and the second is the redistribution term to describe the transformation relationship of kinetic energies between the solid particles and gas phase with the below equations:

$$\beta (\Delta v \Delta v - \Delta u \Delta v) = -2\beta k \left(1 - \frac{\tau_1}{\tau_1 + \tau_d} \right) \frac{\tau_1}{\tau_1 + \tau_d} \quad (4-8)$$

$$\tau_d = \frac{4d_p \rho_p}{3C_D \rho_g |\mathbf{u}_g - \mathbf{v}_p|} \quad (4-9)$$

$$\tau_1 = 0.35 \frac{k}{\varepsilon} \quad (4-10)$$

where τ_1 is the Lagrange time scale of gas phase, and τ_d is the solid particle response time.

In these equations, the related empirical constants are set as: $C_1=0.09$, $C_2=1.44$, $C_3=1.92$ [18,20].

(5) State equation of Gas

$$p = \rho_g R_m T \quad (4-11)$$

where $R_m=8.314 \text{ J}/(\text{mol}\cdot\text{K})$, $T=(273.15+t) \text{ K}$

4.2.2 Representation of cylindroid particles

The representation of particle shape is fundamentally important for accurately describing particles behaviors, because DEM requires detailed information of individual particle-to-particle contacts for the evaluation of contact forces and torques. The existing approaches to construct particles in DEM generally fall into two categories: the single-particle approach and the composite-particle approach. The single-particle approach mainly includes the polygons and polyhedrons, continuous function representation, discrete function representation, virtual space method, combined geometric element method etc., and the composite-particle approach mainly refers to the multi-sphere model and the bonded model. Our review article [8] has detailed discussed and summarized the above representation methods for non-spherical particles. Generally, each of such methods has its own distinct advantages and disadvantages regarding the accuracy, flexibility, numerical stability and efficiency. For example, the continuous function representation (CFR) tends to be strongly targeted for regular shape particles with smooth and continuous surfaces, but it is unsuitable for particles with sharp edges or flat surfaces which are specifically targeted by the polygon/polyhedron approach. The high order continuous functions or complicated polygon/polyhedron has a challenge in the numerical efficiency. Despite discrete function representation (DFR) being quite simple and versatile to construct arbitrary particle shapes, its application is limited by the requirement of extraordinary computational resources. The composite approaches, especially the most popular multi-sphere method, have significant advantages to describe arbitrary particle shapes with flexibility. However, the multi-sphere method faces the remarkable problems mainly in determining the time step, the number and positions of element-spheres. The introduction of the artificial roughness would also inevitably affect the microscopic forces and motions of the particles and thus limit its applications in the fundamental studies dealing with the microscopic motion mechanisms of the non-spherical particles.

In the current study, the real cylindroid particles are constructed with the combined

geometric element method by combining the two circular planes and one cylindrical curved surface. Two typical kinds of cylindroid particles, namely the disk-like particles and rod-like particles, were respectively constructed as shown in Figure 4-1 with three main geometric factors, viz. the planes, curved surface and their intersecting lines. The location of each particle in the space is defined as the position of particle centroid, O' , and the particle shape is characterized by the length of the cylindrical surface, L , and the diameter of the circular plane, d , as shown in Figure 4-1. The particle orientation is described with the vector $O'A$.

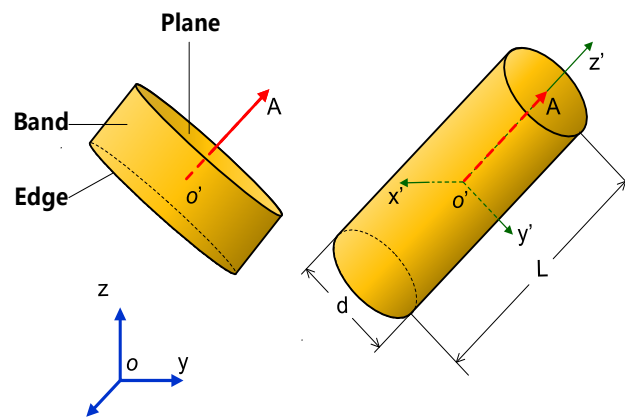


Figure 4-1 Representation of the realistic cylindroid particles in DEM

4.2.3 Motion equations of cylindroid particles

A particle in a granular flow can have two motion types, viz translational and rotational, which are governed by Newton's second law of motion as given below:

$$m_i \frac{d^2 \mathbf{x}_i}{dt^2} = m_i \mathbf{a}_i = \mathbf{F}_i \quad (4-12)$$

$$\mathbf{v}_i = \frac{d\mathbf{x}_i}{dt} \quad (4-13)$$

$$I_i \frac{d^2 \boldsymbol{\theta}_i}{dt^2} = I_i \boldsymbol{\alpha}_i = \mathbf{T}_i \quad (4-14)$$

$$\boldsymbol{\omega}_i = \frac{d\boldsymbol{\theta}_i}{dt} \quad (4-15)$$

where, m_i , \mathbf{v}_i , \mathbf{a}_i and \mathbf{x}_i are the mass (kg), velocity (m/s), acceleration (m/s^2), and position (m) of the particle, respectively and I_i , $\boldsymbol{\theta}_i$, $\boldsymbol{\omega}_i$ and $\boldsymbol{\alpha}_i$ are the moment of inertia (kg/m^2), orientation vector (i.e., the angle between the principle axis of the particle and the

inertial coordinate system, ω), angular velocity (rad/s) and angular acceleration (rad/s²), respectively. \mathbf{F}_i and \mathbf{T}_i are the sum of all the forces and torques which are respectively given by:

$$\mathbf{F}_i = \mathbf{F}_{i,\text{contact}} + \mathbf{F}_{i,\text{gravity}} + \mathbf{F}_{i,\text{fluid}} + \mathbf{F}_{i,\text{external}} \quad (4-16)$$

$$\mathbf{T}_i = \mathbf{T}_{i,\text{contact}} + \mathbf{T}_{i,\text{fluid}} + \mathbf{T}_{i,\text{external}} \quad (4-17)$$

However, the motion Equations 4-12 and 4-14 are strictly correct only for a particle which is symmetric around its center of mass. For a generic non-spherical particle, the moment of inertia always changes with the new spatial orientation of a particle at each time step. To address the change of the inertia moment for a particle with large aspect ratios and determine the orientation of this particle, the space-fixed and body-fixed coordinate systems are usually introduced to conveniently describe the rotation of non-spherical particles. The space-fixed (or laboratory) coordinate system is fixed in a laboratory space, while the body-fixed (or local) coordinate system is a moving Cartesian coordinate system fixed to the particle. The axes of the latter coordinate system are chosen as the principle axes of inertia of particle. In the body-fixed frame, the rotation motion of non-spherical particles can be described as:

$$\mathbf{I}_i' \frac{d\mathbf{W}_i}{dt} + \mathbf{W}_i \times (\mathbf{I}_i' \mathbf{W}_i) = \Lambda_i^{-1} \mathbf{T}_i \quad (4-18)$$

where, \mathbf{W}_i is the angular velocity in the body fixed frame, and \mathbf{T}_i is external moment in the initial frame. \mathbf{I}_i is the inertia tensor along the principle axis and Λ_i^{-1} is the transformation matrix converting a vector from the inertia frame into the body fixed frame.

For the particles constructed by the single-particle approach, the orientation of the particle's principal axes can be described by three Euler angles, (φ, θ, ψ) [7,21-24]. At each time step, for convenience the inertia tensor \mathbf{I}_i in Equation 4-14 in the space-fixed coordinate system (x, y, z) is converted to \mathbf{I}_i' in the body-fixed coordinate system (x', y', z') by the transformation matrix Λ_i^{-1} determined by the three Euler angles. The angular velocity \mathbf{W}_i of particles in body-fixed frame can be calculated by Equation 4-

18. As angular velocity is closely related to the changed of Euler angles, three new Euler angles can be calculated and then the spatial orientation of particles can be determined on the basis of the so-called quaternion method [25-27], as well as by other methods [28,29]. More details about this approach can be found in references [7,23].

4.2.4 Calculations of forces on cylindroid particles

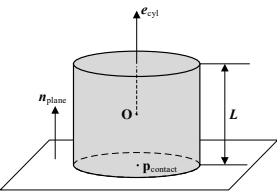
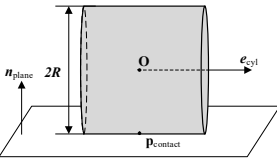
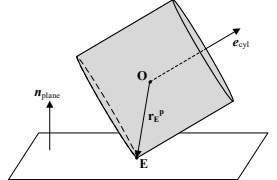
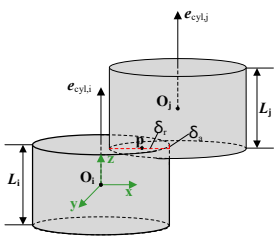
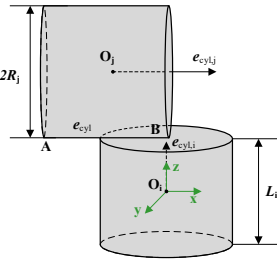
In [Equations 4-12-4-15](#), the forces on the particles mainly includes gravity, contact force, particle-fluid interaction force, and non-contact force. In the complex dense gas-solid two-phase flow systems like spouted beds, apart from the gravity, the contact forces between the particles and the interaction forces between the particle and fluid are significantly essential for the dynamic behaviors of gas and solids in the bed. To accurately calculate these forces that are closely related to the detailed shapes of particles are of fundamental importance to the CFD-DEM simulations with the cylindroid particles.

4.2.4.1 Contact detection of cylindroid particles and the contact forces

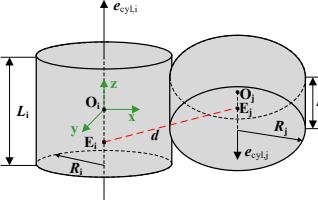
Although few attempts have been made to explore a general contact detection algorithm independent of the object representation, until now, particle representation and contact detection have been considered to be inextricably linked. Particles constructed by a certain approach usually have the corresponding specific method to detect their contacts. Researchers have proposed several methods to detect the contacts between cylindroid particles [15,30-34]. For example, Eberly projected the cylinder axes onto a line or plane, and used the method of separating axis to determine if overlap occurs by testing with set of directions related to the axes of cylinders [30]; Ketchel and Larochelle defined the cylinders with the finite and infinite lengths, and determine whether they contacted or not by check for the intersecting points between the axis of each cylinder and the common normal between two cylinders. These methods have obvious advantages in the computing speeds and resource costs. However, they are not able to provide the accurate expressions for contact locations, overlaps, or normal directions, all of which are essentially important for DEM simulations. Aiming at these issues, Kodam et al. [32,

33] and Guo et al. [34] comprehensively considered the varying contact situations between the real-shaped cylinders and proposed the detailed detection criteria for each possible contact situation and the corresponding calculation methods for the contact information, such as location, overlap, or normal direction and so on. This approach can obviously improve the calculating accuracy of contact forces between cylinders. With some corrections and further development to the algorithms of Kodam et al. [32, 33] and Guo et al. [34], the current study established the comprehensive contact detection criteria for the particles with realistic cylindroid shapes. The detailed information is listed in Table 4-1.

Table 4-1 Cylinder-cylinder contact scenario and criteria [32,33,34]

Contact scenario		Contact criteria
Cylinder Wall	Face - wall	 $\begin{cases} \mathbf{e}_{cyl} \cdot \mathbf{n}_{plane} = 1 \\ z(O) < \frac{1}{2}L \end{cases}$
	Band - wall	 $\begin{cases} \mathbf{e}_{cyl} \cdot \mathbf{n}_{plane} = 0 \\ z(O) < R \end{cases}$
	Edge - wall	 $\text{sign}(z(E)) = -\text{sign}(z(O))$
Cylinder cylinder	Face - face	 $\begin{cases} \mathbf{e}_{cyl,i} \cdot \mathbf{e}_{cyl,j} = 1 \\ z(O_j) < \frac{1}{2}(L_i + L_j) \\ x^2(O_j) + y^2(O_j) < (R_i + R_j)^2 \\ \delta_a < \delta_r \end{cases}$
	Face - band	 $\begin{cases} \mathbf{e}_{cyl,i} \cdot \mathbf{e}_{cyl,j} = 0 \\ z(O_j) < \frac{1}{2}L_i + R_j \\ x^2(A) + y^2(A) < R_1^2 \text{ OR } x^2(B) + y^2(B) < R_1^2 \end{cases}$

<p>Face - Edge</p>		$\begin{cases} z(E) < \frac{1}{2}L_i \\ x^2(E) + y^2(E) < R_i^2 \\ \overrightarrow{E'O_i'} \cdot \overrightarrow{E'O_j'} \geq 0 \end{cases}$ <p>or</p> $\begin{cases} z(E) < \frac{1}{2}L_i \\ x^2(E) + y^2(E) < R_i^2 \\ \overrightarrow{E'O_i'} \cdot \overrightarrow{E'O_j'} < 0 \delta_a < \delta_r \end{cases}$
<p>Special contact</p>		<p>If (not face-edge contact)</p> $\begin{cases} z(P) < \frac{1}{2}L_i \\ x^2(P) + y^2(P) < R_i^2 \\ \text{sign}(z(P)) = \text{sign}(z(O_j)) \\ z(O_j) > \frac{1}{2}L_i \\ \delta_a < \delta_r \end{cases}$
<p>Band - Edge</p>		<p>If (not face-edge contact) and (not special contact)</p> $\begin{cases} z(P) < \frac{1}{2}L_i \\ x^2(P) + y^2(P) < R_i^2 \end{cases}$
<p>Edge - Edge</p>		$\begin{cases} z(A) < \frac{1}{2}L_i \\ x^2(B) + y^2(B) < R_i^2 \end{cases}$
<p>Band - Band (parallel)</p>		$\begin{cases} \mathbf{e}_{\text{cyl},i} \cdot \mathbf{e}_{\text{cyl},j} = 1 \\ z(O_j) < \frac{1}{2}(L_i + L_j) \\ x^2(O_j) + y^2(O_j) < (R_i + R_j)^2 \\ \delta_a > \delta_r \end{cases}$

	<p>Band - Band (skewed)</p>		$\left\{ \begin{array}{l} \overline{EO_i} \times \overline{EO_j} \neq 0 \\ d < R_i + R_j \\ O_i E_i < \frac{1}{2} L_i \\ O_j E_j < \frac{1}{2} L_j \\ R_i + R_j - d < \min \left(\begin{array}{l} \left(\frac{1}{2} L_i - O_i E_i \right) \\ \left(\frac{1}{2} L_j - O_j E_j \right) \end{array} \right) \end{array} \right.$
--	---	---	--

After the contacts between particles are detected, another important mission of DEM is to evaluate the contact forces. In general, the contact between particles is not at a single point but rather on a finite area due to the deformation of the particle surface and this deformation is numerically described by the overlap between rigid bodies in DEM. As the overlaps between non-spherical particles usually have irregular shapes, the geometry of contact overlap, in addition to the overlap distance and relative velocity particles, will undoubtedly affect the contact forces. For example, a cylinder end face-to-plane wall contact and cylinder band-to-plane wall contact will generally have different contact forces because of their different overlap volumes at the same overlap. Feng and Owen [35] proposed an attempt to include the influence of the contact geometry into the contact force model based on the assumptions that the elastic strain energy stored in the contact of particles increases monotonically with the overlap area, and the normal force is applied in the direction along which the contact energy reduces at a maximum rate. However, it is very difficult to decide on a specific relationship between contact energy and overlap, because the contact geometry always varies depending on the particle orientation, contact location, magnitude of the overlap, as well as the material physical parameters. Furthermore, issues may arise as this concept is extended to 3D cylindroid particles in [Table 1](#), because of the significant difficulties in analytically determining the relationships between the contact energies and the complex and various overlap volumes between particles. Generally, there has not been a common and efficient algorithm to calculate the contact forces for the non-spherical particles with irregular contact geometries. Nowadays, most of the researchers tend to use the spring-damping theory to model the contact forces of particles. The linear

spring-damping model (Equation 4-19) proposed Cundall and Strack [36] and the Hertz-Mindlin model (Equation 4-20) are two most widely used models to calculate the contact forces in DEM. Relatively, the linear model is more simple and universal and it is usually preferred by many researchers when dealing with the non-hertzian contact between non-spherical particles [37-43].

$$\mathbf{F}_n = -(K_n \delta_n + C_n \mathbf{v}_r \cdot \mathbf{n}_c) \mathbf{n}_c \quad (4-19)$$

$$\mathbf{F}_n = -4/3 E^* \sqrt{R^*} \delta_n^{3/2} \mathbf{n}_c - C_n \left(8m^* E^* \sqrt{R^*} \delta_n \right)^{1/2} (\mathbf{v}_r \cdot \mathbf{n}_c) \mathbf{n}_c \quad (4-20)$$

In this study, the linear model of Equation 4-19 and the nonlinear model of Equation 4-20 were respectively applied to calculate the contact force of cylindroid particles in a fluidized bed. In the meantime, the gas-solid interaction was described by combining Syamlal-O'Brien model [81] with Holzer-Sommerfeld model [46], which will be discussed in detail in the next section. The simulated results were compared with the experimental phenomena of Zhong et al. [14] aiming to choose the suitable contact force model for the fluidization of cylindroid particles.

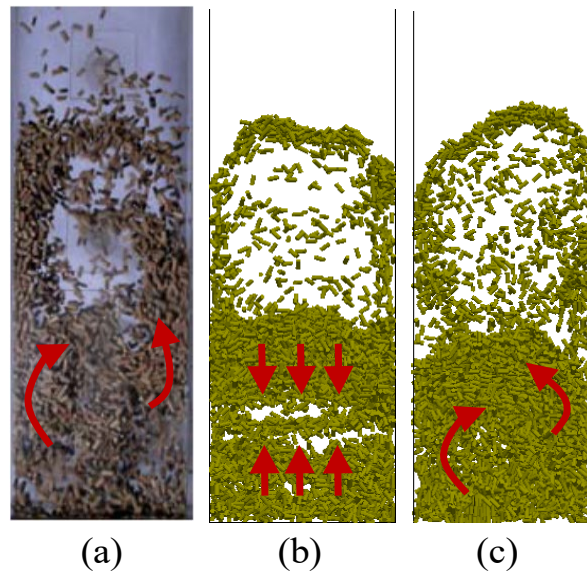


Figure 4-2 Comparisons between experimental phenomena and the simulated results with the different contact force models ($U=2.0$ m/s, $H_0=0.08$ m, $L=6.0$ mm, $d=2.6$ mm): (a) the experimental results from Zhong et al (2009)[14] ; (b) simulation with the Hertz-Mindlin contact force model (Equation 4-19); (c) simulation with the linear spring-damper model of contact force(Equation 4-20)

Comparisons in Figure 4-2 show that when the nonlinear Hertz-Mindlin model was

used to calculate the contact force, as shown in Figure 4-2(b), the cylindroid particles in the bed took on the layered surges under the action of the airflow. At the same time the horizontal strip bubbles formed and slowly moved up from the bottom of the bed. Only the particles in the limited region near the bubbles were obviously disturbed, while in other areas of the bed the particles were almost immobile. These phenomena were clearly different from the experimental results in Figure 4-2(a) that the particles exhibited the drastically turbulent movements in the entire bed region. When the linear contact force model of Equation 4-19 was used to calculate the particle contact force, the irregular turbulent movements of cylindroid particles shown in Figure 4-2(a) were very similar to the experimental results. It indicated that the linear contact force model could obtain a relatively closer results to the actual phenomena than the nonlinear model when describing the contact of the cylindroid particles. Therefore, the linear contact force model was used in this study with the model equations as follows:

$$\mathbf{F}_c = \mathbf{F}_n + \mathbf{F}_t \quad (4-21)$$

$$\mathbf{F}_n = -(K_n \delta_n + C_n \mathbf{v}_r \cdot \mathbf{n}_c) \mathbf{n}_c \quad (4-22)$$

$$\mathbf{F}_t = -K_t \delta_t - C_t \mathbf{v}_{r,t} \quad (4-23)$$

When $|\mathbf{F}_t| > \mu_f |\mathbf{F}_n|$, the slip motions of particles near the contact point should be considered with the slip velocity is described as

$$\mathbf{v}_t = \mathbf{v}_r - (\mathbf{v}_r \cdot \mathbf{n}_c) \mathbf{n}_c + d_c (\boldsymbol{\omega}_i - \boldsymbol{\omega}_j) \times \mathbf{n}_c \quad (4-24)$$

The tangential force resulting from the slip motion is calculated as

$$\mathbf{F}_t = \mu_f |\mathbf{F}_n| \frac{\mathbf{v}_t}{|\mathbf{v}_t|} \quad (4-25)$$

In above equations, \mathbf{F}_n and \mathbf{F}_t are the normal contact force and tangential contact force, respectively, N; \mathbf{n}_c is the unit normal vector; C_n and C_t are the damping coefficients in the normal direction and tangential direction, respectively, kg/s; K_n is the elasticity coefficient in the normal direction, N/m; δ_n , and δ_t are the deformations of particle in the contact normal and tangential directions and $\delta_{t, \max}$ is the maximum deformation

that could occur in the contact tangential direction, m ; \mathbf{v}_r is the relative velocity between particles, m/s ; d_c is the distance between the contact point and the axis of a particle, m ; \mathbf{v}_t is the slip velocity between particles at the contact point, m/s ; μ_f is the coefficient of sliding friction between particles.

4.2.4.2 Interaction forces between fluid and cylindroid particles

The drag force is the main fluid force acting on the particles in the gas-solid systems. A bulk of early investigations focused on the drag force experienced by spheres moving through a fluid, and the resulting empirical correlations for the drag coefficient, C_D , which have been comprehensively reviewed in our publication [8], provide sufficient information to estimate the drag force of spheres. Comparisons between most of these correlations for spheres showed relatively small deviations. However, for non-spherical particles, the problem of the drag force becomes much more complicated. The terminal falling velocity (and hence the drag coefficient) for a typical non-spherical particle is strongly influenced by its size, shape, and orientation in addition to the physical and rheological properties of the fluid medium, wall effects and so on.

Currently available methodologies to deal with the drag force on a non-spherical particle fall into two distinct categories: the first approach is to develop the exclusive drag expressions for particles with fixed shape and orientation, such as spheroidal particles [48-50], polyhedrons [51,52], cubes [53-56], cylinders [47,57-66], disks [67-69], hemispheroidal particles [70], parallelepiped [71], cones [72], and flat annular rings [73], to name a few. In the second approach, efforts are made to provide a single general correlation on the drag coefficient for non-spherical particles covering as many shapes and orientations as possible. The attempts by Haider and Levenspiel [74], Thompson and Clark [75], Ganser [76], Chien [77], and Hartman et al. [78] and so on illustrate the applicability of this approach. Obviously, for a particle with a certain specific shape, the general expressions derived from the second approach tends to be less accurate than the specialized one for that shape, but the feasible interpolations/extrapolations to the various shapes provide the general expressions an attractive on engineering applications. Aforementioned expressions of the drag force are generally obtained theoretically or

semi-empirically for an isolated particle or for particles in dilute gas-solid systems. When considering practical concentrated particulate flows, especially the dense gas-solid or liquid-solid multiphase systems in industrial processes, the particle drag force may deviate significantly from that of an isolated particle. For flows through a packed bed of particles, the most commonly used approach to determine the particle drag force is to measure the bed pressure drop or bed expansion, which can then be used to find an average drag force for a single particle. The resulting correlations developed for the drag force F_D can be classified into two categories. The first category is usually formed by F_{D0} , which is the drag force around a single particle, and a correlation function f , which includes the parameters, such as the local voidage and particle Reynolds number in order to take into account the effect and interaction of surrounding particles. The most popular examples for the composed F_D are from Di Felice [44] and Wen and Yu [79] (see Table 4-2). This approach is very promising to develop the drag force relationships for multiphase systems with non-spherical particles, due to the abundance of reports on the drag coefficients of isolated non-spherical particles. In the second form, F_D is expressed in one formula of the averaged force acted on the particle, which includes the solid holdup derived from the pressure drop or bed expansion to characterize the particle-particle interactions. Typical and well-known examples of this form are expressions developed by Ergun [80], Syamlal and O'Brien [81] and so on. However, as the most of the existing expressions of the gas-solid interaction forces were proposed for spherical particles, their accuracies will be obviously affected when applied to the non-spherical particulate systems. On the other hand, these expressions are often difficult to clarify the effects of particle shapes.

Given the lack of feasible or reliable drag force expressions for dense gas-solid systems with non-spherical particles, the popular equations of Ergun, Wen and Yu and Di Felice for spherical particles and their modifications are usually directly used to calculate the drag force for non-spherical particles. Actually, there is no consensus at present as to the most suitable correlation for accurately predicting the fluid force even in a spherical particulate system at a given Reynolds number and packing fraction, let alone in a non-

spherical particulate system. Thus, it is necessary to validate the existing drag force correlations to choose an appropriate one for simulation works.

As the Di Felice model [44], the Gidaspow model [83] and the Syamlal-O'Brien model [81] (see Table 4-2) had all been effectively used as the gas-solid interaction models for the spherical particles in dense gas-solid reactors like fluidized beds and spouted beds [6, 17, 21, 82], their usability for non-spherical particulate systems were emphatically investigated in the current study. Differently, the drag coefficient, C_D , in the above three models would be replaced with the results for non-spherical particles, as seen in Table 4-2. The one-to-one combination study of C_D and gas-solid exchange coefficient β was conducted and the optimal computation for the gas-solid interactions between gas and cylindroid particles would be obtained by comparing with the experimental results from Zhong et al. [14]. It should be mentioned that when using the Di Felice model to calculate the gas-solid interaction, it is the force acting on the individual particle that is obtained, and the opposite reaction acting on the calculation unit of the fluid phase requires the conversion equation:

$$\mathbf{F}_{d,f} = \frac{\sum_{i=1}^k \mathbf{F}_{d,i}}{\Delta V} \quad (4-26)$$

On the other hand, the Gidaspow model and Syamlal-O'Brien model is to obtain the force acting on the calculation unit of the fluid phase, and the opposite reaction forces that act on the particles inside this calculation unit would be calculated as:

$$\mathbf{F}_{d,i} = \mathbf{F}_{d,f} \frac{V_p}{\Delta V(1-\alpha_f)} \quad (4-27)$$

where $\mathbf{F}_{d,f}$ and $\mathbf{F}_{d,i}$ are the forces respectively acting on a calculation unit of the fluid phase and the individual particle, N; ΔV and V_p are the volume of calculation unit of the fluid and the volume of a particle, respectively, m^3 ; α_f is the voidage in the calculation unit of the fluid.

Table 4-2 Equations of the drag force coefficient C_D for individual non-spherical particle and gas-solid exchange coefficient β for the gas-solid system

Equations of the drag force coefficient C_D for individual non-spherical particle

Tran-Cong[45]
$$C_D = \frac{24}{Re} \frac{d_a}{d_p} \left[1 + \frac{0.15}{\sqrt{c}} \left(\frac{d_a}{d_p} Re \right)^{0.687} \right] + \frac{0.42 \left(\frac{d_a}{d_p} \right)^2}{\left[1 + 4.25 \cdot 10^4 \left(\frac{d_a}{d_p} Re \right)^{-1.16} \right] \sqrt{c}}$$

Holzer and Sommerfeld[46]
$$C_D = \frac{8}{Re} \frac{1}{\sqrt{\phi_{\parallel}}} + \frac{16}{Re} \frac{1}{\sqrt{\phi}} + \frac{3}{\sqrt{Re}} \frac{1}{\phi^{3/4}} + 0.4210^{0.4(-\log\phi)^{0.2}} \frac{1}{\phi_{\perp}}$$

Ren et al.[47]
$$C_D = \frac{24}{Re} (1 + C_1 Re^{C_2}) + \frac{C_3}{1 + C_4/Re}$$

$$C_1 = 2.3545 \left(\frac{\rho_p - \rho_f}{\rho_f} \right)^{-0.4519} \phi^{-4.8155} \left(\frac{d_a}{d_v} \right)^{0.3407}$$

$$C_2 = -1.2429 \left(\frac{\rho_p - \rho_f}{\rho_f} \right)^{0.0699} \phi^{-5.4294} \left(\frac{d_a}{d_v} \right)^{-0.796}$$

$$C_3 = 0.8716 \left(\frac{\rho_p - \rho_f}{\rho_f} \right)^{0.01755} \phi^{-1.0301} \left(\frac{d_a}{d_v} \right)^{-1.5628}$$

$$C_4 = -0.3424 \left(\frac{\rho_p - \rho_f}{\rho_f} \right)^{0.7290} \phi^{-1.6319} \left(\frac{d_a}{d_v} \right)^{-1.2486}$$

Equations of gas-solid exchange coefficient β for the gas-solid system

Di Felice[44]
$$F_D = F_{D0} \alpha_f^{-(\chi+1)}$$

$$F_{D0} = \frac{1}{8} \pi C_D \rho_f |\mathbf{u}-\mathbf{v}| (\mathbf{u}-\mathbf{v})$$

$$\chi = 3.7 - 0.65 \exp \left[-\frac{(1.5 - \log_{10} Re)^2}{2} \right]$$

$$F_D = \beta (\mathbf{u}-\mathbf{v})$$

Gidaspow[83]
$$\beta = \begin{cases} \frac{\mu_f (1 - \alpha_f)}{d_p^2 \alpha_f} [150(1 - \alpha_f) + 1.75 Re] & \alpha_f \leq 0.8 \\ 0.75 C_D \frac{\mu_f (1 - \alpha_f)}{d_p^2} \alpha_f^{-2.7} Re & \alpha_f > 0.85 \end{cases}$$

Syamlal- O'Brien[81]
$$Re = \frac{\rho_f \alpha_f |\mathbf{u}-\mathbf{v}| d_p}{\mu_f}$$

$$F_D = \beta (\mathbf{u}-\mathbf{v})$$

$$\beta = \frac{3 \rho_f \alpha_f \alpha_s}{4 v_r^2 d_p} |\mathbf{u}-\mathbf{v}| C_D \frac{Re}{v_r}$$

$$Re = \frac{\rho_f \alpha_f |\mathbf{u}-\mathbf{v}| d_p}{\mu_f}$$

$$v_r = 0.5 \left(A - 0.06 Re + \sqrt{(0.06 Re)^2 + 0.12 Re (2B - A) + A^2} \right)$$

$$A = \alpha_f^{4.14}, \quad B = \begin{cases} 0.8 \alpha_f^{1.28} & \alpha_f \leq 0.85 \\ \alpha_f^{2.65} & \alpha_f > 0.85 \end{cases}$$

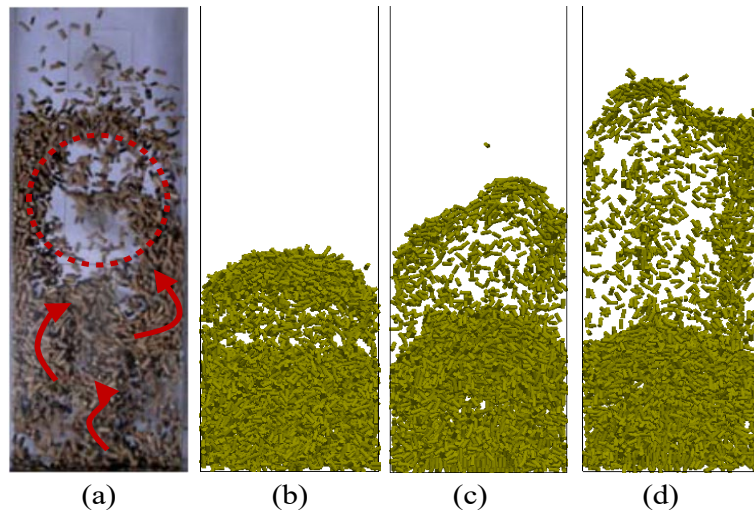


Figure 4-3 Comparisons between experimental phenomena and the simulated results with the different drag coefficient models ($U=2.0$ m/s, $H_0=0.08$ m, $L=6.0$ mm, $d=2.6$ mm, with gas-solid interaction force model from Di Felice [44]): (a) the experimental results from Zhong et al [14]; (b) simulation with the Tran-Cong drag coefficient model [45], (c) simulation with the Holzer and Sommerfeld model [46], (d) simulation with the drag coefficient model from Ren et al. [47]

Figure 4-3 showed the simulated results with C_D being calculated by the Tran-Cong model, Holzer-Sommerfeld model and the empirical equation from Ren et al. respectively, while the gas-solid exchange coefficient β being calculated by the Di Felice model. Under the conditions of $U=2.0$ m/s, $H_0=0.08$ m, $L=6.0$ mm and $D=2.6$ mm, when the gas and solid motions in the fluidized bed reached the relatively stable states, the simulation using the equation of Ren et al. obtained the higher bed height, while the bed heights simulated with the Holzer-Sommerfeld model and Tran-Cong model were relatively lower. This meant that under the same conditions, the drag coefficient calculated by the model proposed by Ren et al. is larger than that by the other models, and the results calculated by Tran-Cong model is the smallest. In addition, when using the Di Felice model to calculate the gas-solid exchange coefficient, there would be no obvious bubble appearing in the fluidized bed no matter which drag coefficient model is used, resulting in the significantly different gas and solid flow behaviors from the experiments.

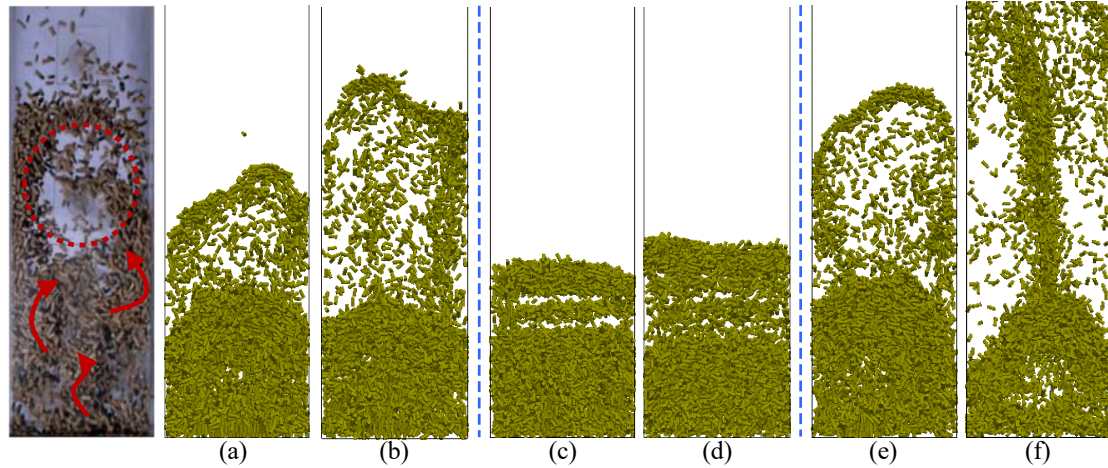


Figure 4-4 Different simulation results with the varying combinations of drag force coefficient models and gas-solid exchange coefficient models ($U=2.0$ m/s, $H_0=0.08$ m, $L=6.0$ mm, $d=2.6$ mm): (a) Di Felice model [44] & Holzer-Sommerfeld model [46], (b) Di Felice model [44] & Ren model [47], (c) Gidaspow model [83] & Holzer-Sommerfeld model [46], (d) Gidaspow model [83] & Ren model [47], (e) Syamlal-O'Brien model [81] & Holzer-Sommerfeld model [46], (f) Syamlal-O'Brien model [81] & Ren model [47]

The simulation results of the flow patterns in the fluidized bed with different combinations of C_D and β were shown in Figure 4-4. When β was calculated by Gidaspow model, no matter which drag coefficient model was used, the simulated bed heights were always remarkably lower than the experimental result and only fluctuated at a certain height as shown in Figure 4-4. When β was calculated by Di Felice model or Syamlal-O'Brien model, the simulation could obtain the reasonable bed height by combining with the proper drag force model, as seen in Figure 4-4(b) (the combination of Di Felice model and Ren's model) or Figure 4-4(e) (the combination of Syamlal-O'Brien model and Holzer-Sommerfeld model). However, the combination of Di Felice model and Ren's model failed to form obvious bubbles. Comparatively, the simulation with the combination of Syamlal-O'Brien model and Holzer-Sommerfeld model could obtain the most similar flow patterns to experiments. Therefore, the drag coefficient for cylindroid particles will be calculated with Holzer-Sommerfeld model, and the gas-solid exchange coefficient will adopt Syamlal-O'Brien model in this study.

4.2.5 Initial conditions and boundary conditions

At the fluid inlet (nozzle) of the spouted bed, the velocity components, kinetic energy

of turbulence and energy dissipation rate of the gas phase were assumed to be uniformly distributed. The gas was injected normal to the entrance with a velocity:

$$u_{x0}=0, u_{y0}=Q_s/A_s=u_s \quad (4-28)$$

where Q_s is the flowrate of spouting gas, m^3/s , and A_s is sectional area of the nozzle.

The kinetic energy of turbulence and energy dissipation rate of the gas phase at the fluid inlet were respectively set as:

$$k_0=(0.5-1.5\%) \frac{u_s^2}{2} \quad (4-29)$$

$$\varepsilon_0 = \frac{C_\mu \rho_g k_0^2}{\mu_t} \quad (4-30)$$

where $\rho_g u_s L / \mu_t = 100 \sim 1000$.

The solid velocity at the fluid inlet was zero.

A no-slip boundary condition was assumed for both gas and solid phases, and thus the gas velocity components at the x and y directions were:

$$u_{wx} = u_{wy} = 0 \quad (4-31)$$

The diffusion coefficient of the gas velocity component u_z (parallel with the wall) was calculated as follows:

$$\mu_t = \left[\frac{y_p C_\mu^{0.25} k_p^{0.5}}{\nu} \right] \frac{\mu_g}{\ln(y_p^+ E) / \kappa} \quad (4-32)$$

$$y_p^+ = \frac{y_p C_\mu^{0.25} k_p^{0.5}}{\nu} \quad (4-33)$$

where κ was Von Karman number and $\kappa=0.4 \sim 0.42$; y_p is the distance between the wall and the first node; E is obtained with $\ln(E) / \kappa = B$ and the constant $B=5.0 \sim 5.5$.

The energy dissipation rate of the gas phase at the wall was calculated with:

$$\varepsilon_p = \frac{C_\mu^{0.75} k_p^{1.5}}{\kappa y_p} \quad (4-34)$$

In the region that is near the wall and beyond the viscous flow region, the dimensionless velocity and temperature were assumed to follow the logarithmic distribution, namely:

$$u^+ = \frac{1}{\kappa} \ln y^+ + B \quad (4-35)$$

$$y^+ = \frac{y C_\mu^{0.25} k^{0.5}}{\nu} \quad (4-36)$$

$$u^+ = \frac{u C_\mu^{0.25} k^{0.5}}{\tau_w / \rho_g} = \frac{1}{\kappa} \ln(Ey^+) \quad (4-37)$$

In the mesh generation, the first node P near the wall was located within the logarithmic region where the flow was intensively turbulent, and then the equivalent viscosity coefficient between the node P and wall was:

$$\mu_t = \left[\frac{y_p C_\mu^{0.25} k_p^{0.5}}{\nu} \right] \frac{\mu_g}{\ln(y_p^+ E) / \kappa} = \frac{y_p^+ \mu_g}{u_p^+} \quad (4-38)$$

The kinetic energy of turbulence at the node P was calculated by Equation 4-38 with the modified boundary condition being:

$$\left(\frac{\partial k}{\partial x} \right)_w = 0 \quad (4-39)$$

Energy dissipation rate of the gas phase at the node P was calculated with Equation 4-34.

The front and back boundaries of the bed were set as the periodic boundary condition. The outlet at the top of bed was set as pressure outlet.

4.2.6 Numerical solutions

The flow sheet for the numerical procedure of the CFD-DEM simulations on non-spherical particles in this study was shown in Figure 4-5. The gas phase was firstly solved and particle trajectories were then obtained by revolving the equations of motion. Specifically, a finite volume method was implemented to solve the set of conservative and constitutive equations of gas phase with the first-order upwind discretization being used to convert the partial differential equations to algebraic ones. The SIMPLE algorithm was adopted for the pressure-velocity coupling and correlation, and a convergence criterion of 10^{-4} for each scaled residual component is specified for the relative error between successive iterations. For the particle phase, the contact force of particle-particle (wall) and the interaction force of particle-fluid and gravity were mainly considered to predict the particle motions. The grid element method was used

to detect the contacts between particles. In this method, the space occupied by the particle system was divided into regular grids, and only those particles located in the same grid unit or adjacent units would be detected for contacts.

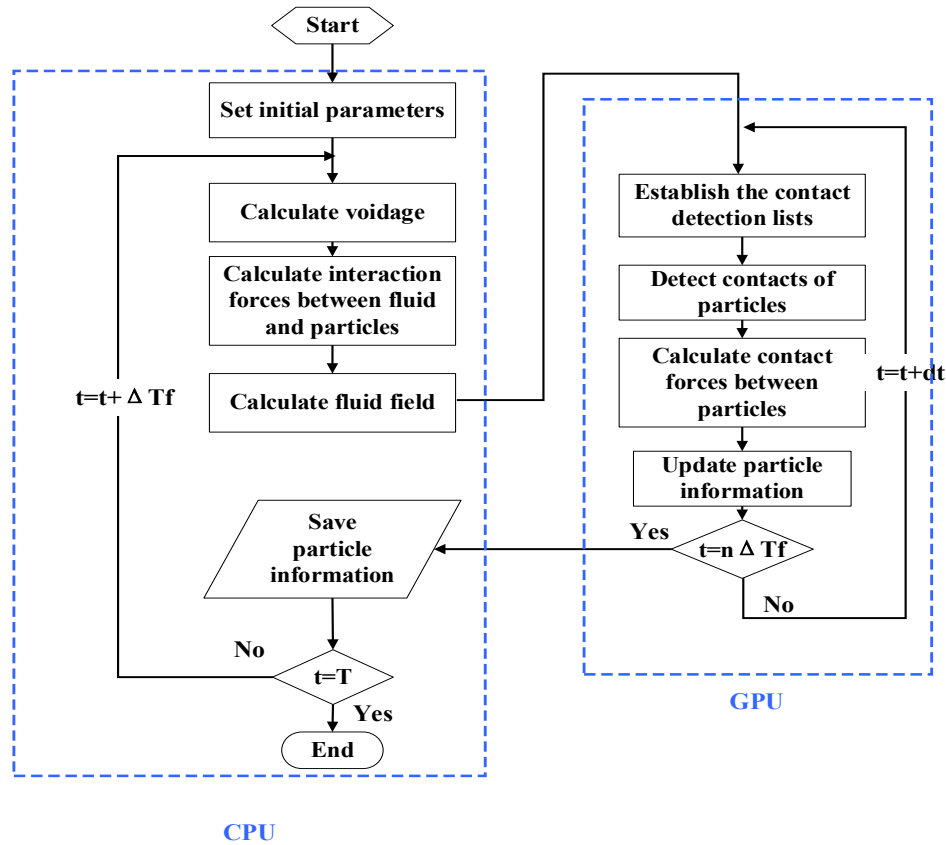


Figure 4-5 Flow sheet for the numerical procedure of the CFD-DEM simulations of non-spherical particles

The gas phase and particle phase were two-way coupled by the Averaged volume method (AVM). In the AVM, the grid size of gas phase is usually larger than the size of particle. The information of particles is firstly mapped into the corresponding CFD grid according to their locations and then the contact forces of particles and the interaction force of particle-fluid could be calculated according to the particle information and fluid information within the current CFD grid. In a CFD grid cell, the gas-solid interaction force exerting on the fluid is equal to the sum of that acting on all particles within this grid cell. The voidage needed in the calculation of gas-solid interaction force was obtained with the sampling statistical method. A certain number of sampling points were uniformly set in a CFD grid cell and the voidage in this cell would be figured out by calculating the ratio between the number of sampling points that were outside the

particle bodies to the total number of sampling points. The time step of particle phase was determined according to the Rayleigh wave theory, and it was taken to be 5% of the critical Rayleigh time step T_R , which was given as:

$$T_R = \frac{1}{2} \pi d_p \left(\frac{\rho_p}{G} \right)^{1/2} (0.1631\gamma + 0.8766)^{-1} \quad (4-40)$$

The performance of GPU-based DEM code for the gas-solid flow system with cylindroid particles is evaluated on a NVIDIA Tesla K20M GPU cluster at the University of New South Wales. It consists of 33 compute nodes, each of which has 12 CPU (Inter[®] Xeon[®] E5-2603) cores (24 hyperthreaded cores) and 4 GPUs with 2496 CUDA cores each. The specification parameters of GPU cluster are: Memory clock 2.6 GHz, maximum band width 208 GB/sec, Peak performance of double precision (FMA) 1.17 TFlops.

4.2.7 Validation of models

Figure 4-6 showed the typical comparisons on flow patterns of a fluidized bed with cylindroid particles between experimental results from the literature [14] and the simulations with the above CFD-DEM models and numerical solutions. The structures and dimensional sizes of the fluidized bed and cylindroid particles were illustrated in Figure 4-6(a) with the particle density and static bed height respectively being 850 kg/m³ and 0.08 m. The linear spring-damper model was adopted to calculate the contact force between particles and the friction coefficient between particle and particle (wall), Poisson ratio, elasticity coefficient and damped coefficient were set as 0.4, 0.4, 10⁴, 100, respectively according to the sensitivity analysis. The drag force coefficient of cylindroid particles was obtained with the Holzer-Sommerfeld correlation [46], and the interaction exchange coefficient between gas phase and solid phase were described with the Syamlal-O'Brien model [81]. Figure 4-6(b) and (c) showed the simulation results and experimental results with the fluidizing gas velocity being $U=1.5$ m/s and $U=2.0$ m/s, respectively. The satisfactory agreements indicated that the above CFD-DEM models and numerical solutions were able to successfully predict the flow behaviors of gas and cylindroid particles in the dense gas-solid two-phase turbulent

flows.

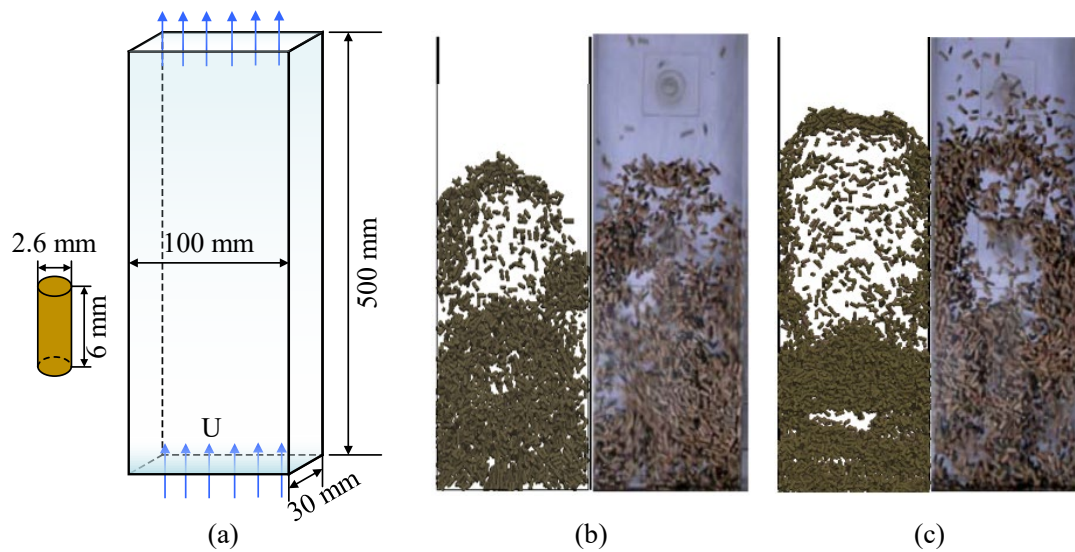


Figure 4-6 Comparisons between experimental results and CFD-DEM simulations in the fluidized bed with non-spherical particles [14]: (a) the structures and dimensional sizes of the fluidized bed and cylindroid particles; (b) $U=1.5$ m/s, (c) $U=2.0$ m/s

4.3 CFD-DEM study on the spouting of cylindroid particles in a spouted bed

In this section, numerical simulations were carried out based on the developed CFD-DEM models to study the spouting behaviors of cylindroid particles. The effects of particle shape on the spouting characteristics including flow pattern, particle velocity, orientation and contact details were emphatically investigated from the particle scale and the microscale gas and solid motion mechanisms were figured out.

4.3.1 Computational conditions

The Geometry of the pseudo 2D rectangular spouted bed and its grid for the gas phase were shown in [Figure 4-7](#). The dimensional sizes of the spouted bed were 200 mm×24 mm×1000 mm. The finer grid size, namely 6.67 mm×10 mm, was adopted in the middle zone of the bed for spout region where the gas is of relatively higher velocity and intensive turbulence, while in the other zone, the grid size was 10 mm×10 mm. Seven kind of cylindroid particles with the aspect ratios varying from 0.25 to 3.0 were involved in the current study, and their detailed properties were shown in [Table 4-3](#). [Table 4-4](#) listed the main physical and numerical parameters chosen in this simulation.

Table 4-3 Properties of cylindroid particles

Particles	ρ_p (kg/m ³)	V (mm ³)	L (mm)	d (mm)	L/d	Sphericity	
1		1200	42.39	1.5	6.0	0.25	0.693
2		1200	42.39	2.38	4.76	0.5	0.825
3		1200	42.39	3.78	3.78	1.0	0.874
4		1200	42.39	4.95	3.30	1.5	0.859
5		1200	42.39	6.0	3.0	2.0	0.832
6		1200	42.39	6.96	2.78	2.5	0.804
7		1200	42.39	7.86	2.62	3.0	0.779

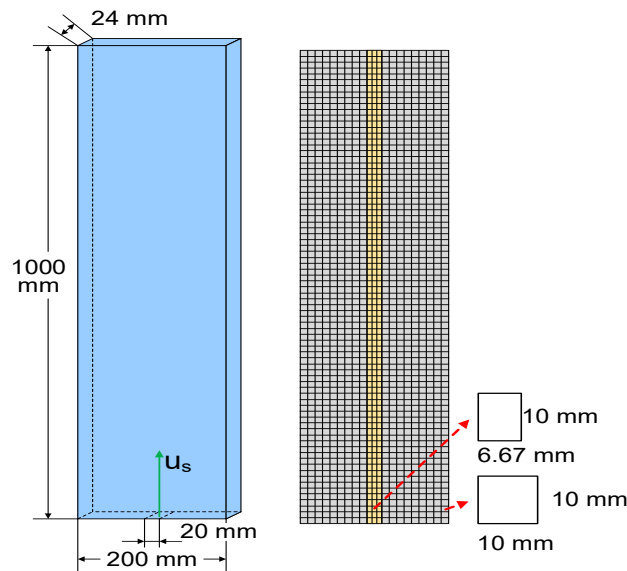


Figure 4-7 Geometry of the pseudo 2D rectangular spouted bed and grid for gas phase

Table 4-4 The main physical and numerical parameters for simulations

Properties	values
Section dimensions of spouted bed, A	0.2 m × 0.024 m
Bed height, H_b	1.0 m
Grid size ($\Delta x \times \Delta y \times \Delta z$)	See Figure 4-7
Gas density, ρ_g	1.205 kg/m ³
Gas viscosity, μ_g	1.8×10^{-5} Pa/s
Static bed height, H_0	0.21 m
Number of particle, N	15000~17000
Friction coefficient:	

Particle-particle, μ_p	0.4
Particle-wall, μ_w	0.4
Poisson's ratio:	
Particle-particle, γ_p	0.4
Particle-wall, γ_w	0.4
Elasticity coefficient:	
Particle-particle, K_p	10^4
Particle-wall, K_w	10^4
Damped coefficient :	
Particle-particle, C_p	100
Particle-wall, C_w	100

4.3.2 Macroscale flow patterns

The different spouting patterns of seven particles with different shapes were shown in [Figure 4-8](#) with the static bed height $H_0=0.21$ m and spouting gas velocity $u_s=6.0$ m/s. All these seven kinds of particles were able to form typical external spouting with the distinct spout, fountain and annular region in the bed. When the aspect ratio L/d of the particles is around 1.0, such as $L/d=0.5\sim 1.5$, the spouting was relatively more stable with the central stream being vertical in spout and fountain. When L/d gradually deviated from 1.0, with the particle shape becoming more flat or long, the stability of the spouting was gradually deteriorated, and the upward flow in the center region of bed obviously twisted with the fountain continuously wagging. With the increasing deviation of L/d from 1.0, the non-spherical features of particles became more obvious, and their increasingly strong interactions, for example, collision, friction and interlocking would damage the fluidity of particle assemblies causing the increasing instability of spouting in the bed. On the other hand, the particles with $L/d=1.0$ reached the highest fountain height; as the L/d of particles gradually deviated from 1.0, the fountain height in the bed also decreased, as shown in [Figure 4-9](#). The effect of the aspect ratio of the particles on the fountain height was very remarkable when the L/d is around 1.0, and when $L/d>2.0$, it significantly weakened.

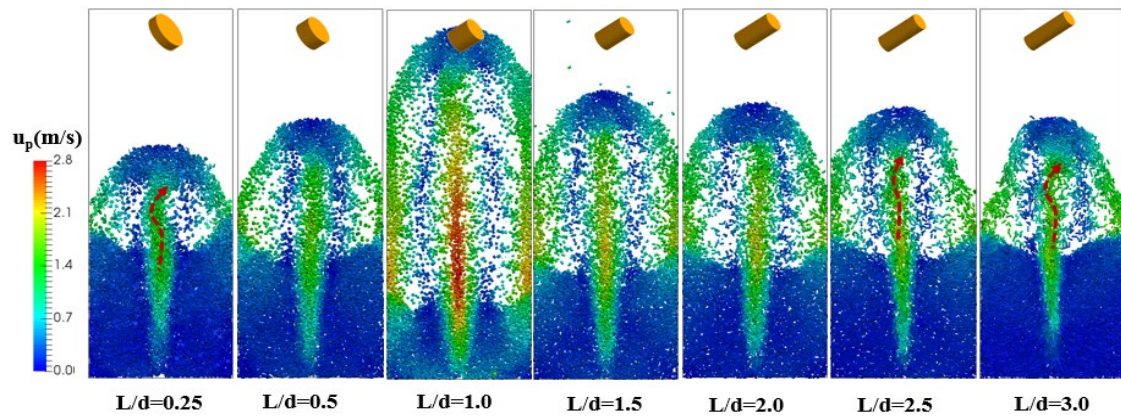


Figure 4-8 Macroscale flow patterns of cylindroid particles with varying aspect ratios ($u_g=6$ m/s, $H_0=0.21$ m, $\rho_p=1200$ kg/m³, $V_p=42.39$ mm³)

Under the bed surface, particles with the aspect ratio of $L/d = 1.0$ performed the widest spout region, as well as the maximum jet radius, as seen in Figure 4-8 and Figure 4-10. This larger jet radius or the wider spout meant more particles were moving upward in the rapid spout, and the bed had the higher solid circulation rate. When the aspect ratio of particles gradually deviated from 1.0, becoming larger or smaller, the width of the spout region thereupon decreased. Above the bed surface, the width of central stream in fountain as a whole showed the similar trend with that in spout. A difference was that when the aspect ratio of the particle was quite large, such as $L/d=3.0$, the time-averaged width of the central stream in the fountain would increase to a certain extent. This is because when the particle aspect ratio was large, the fountain becomes unstable and constantly swayed around, resulting in the larger average-width over a period of time. In addition, when the particle aspect ratio was relatively larger, for example, $L/d = 2.5$ or 3.0, the spout width near the bottom of the bed showed a remarkable increase, because the stronger interaction between the elongated particles led to more particles being entrained into the spout near the nozzle. In general, for the particle with the smaller aspect ratio, the boundaries of central stream in the bed were relatively flatter, and when the aspect ratio increased, the boundaries of central stream became more winding. For particles with $L/d=1.0$, the highest fountain height and the widest spout width meant more particles in the spout and fountain region, resulting in an obviously lower bed surface in the annulus.

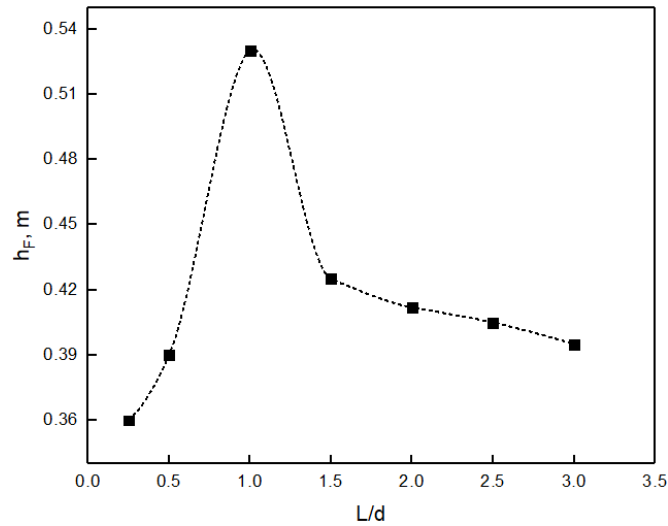


Figure 4-9 Fountain height of cylindroid particles with varying aspect ratios ($u_g=6$ m/s)

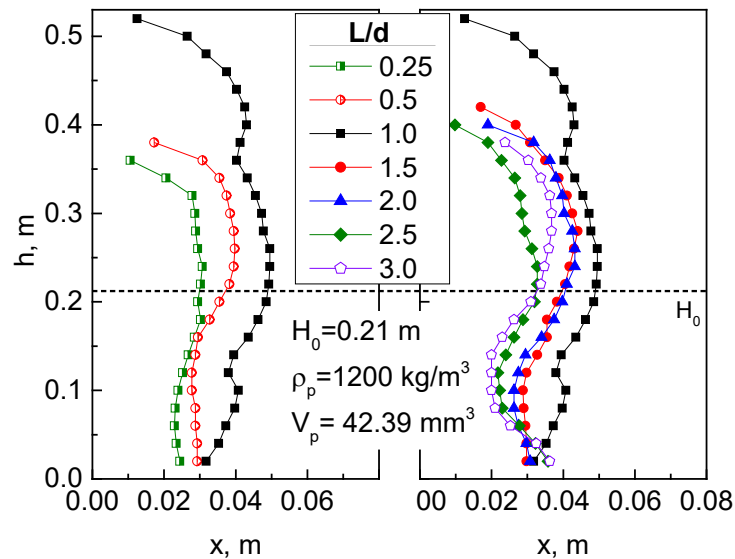


Figure 4-10 Spout shape of cylindroid particles with varying aspect ratios ($u_g=6$ m/s)

4.3.3 Particle velocity

The time-averaged radial particle velocity distributions of three typical particles ($L/d=0.25, 1.0$ and 2.0) at the bed heights of $h=0.06, 0.12, 0.18$ and 0.24 m were shown in Figure 4-11 under the conditions of $H_0=0.21$ m and $u_g=6$ m/s. These three kinds of particles with different shapes showed the similar velocity distribution characteristics when spouted in the rectangular spouted bed. Specifically, under the bed surface, the particles in the spout moved upward with the relatively higher velocities, while that in the annulus moved downward with the lower velocities. As a whole, along the rising

bed height, both the particle velocities in the spout and annulus increased. Only an exception appeared in the velocity distributions of the particles with $L/d=1.0$ at the heights of $h=0.18$ m and $h=0.24$ m. In this case the bed surface was under $h=0.18$ m, particles at the heights of $h=0.18$ m and $h=0.24$ m were already located in the fountain, and thus the particles moving upward in the central stream started to decelerate, while that in the lateral region were falling with increasing velocities.

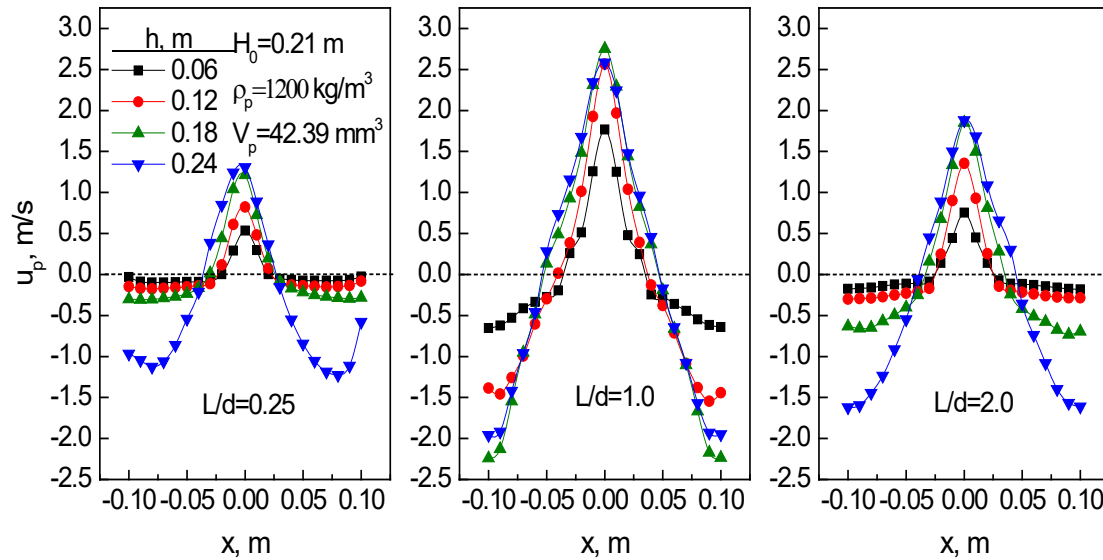


Figure 4-11 The time-averaged radial particle velocity distributions of three typical particles ($L/d=0.25$, 1.0 and 2.0) at the varying bed heights ($u_g=6$ m/s)

Although the velocity distributions of particles with varying shapes shared the similar trend, the values of their velocities performed remarkable differences. The specific velocity values of different particles at the same bed heights, for example, $h=0.06$ m and $h=0.18$ m, were shown in Figure 4-12. For the disk-like particles ($L/d \leq 1.0$), with the increasing L/d , their velocities in the spout and annulus obviously increased both at the bottom of the bed ($h=0.06$ m) or at the upper part of the bed ($h = 0.18$ m), and meanwhile the width of the spout widened, as shown in the left parts of Figure 4-12(a) and (b). That meant the particles with the flatter shape performed the smaller velocities and formed the narrower spout when spouted in the spouted bed.

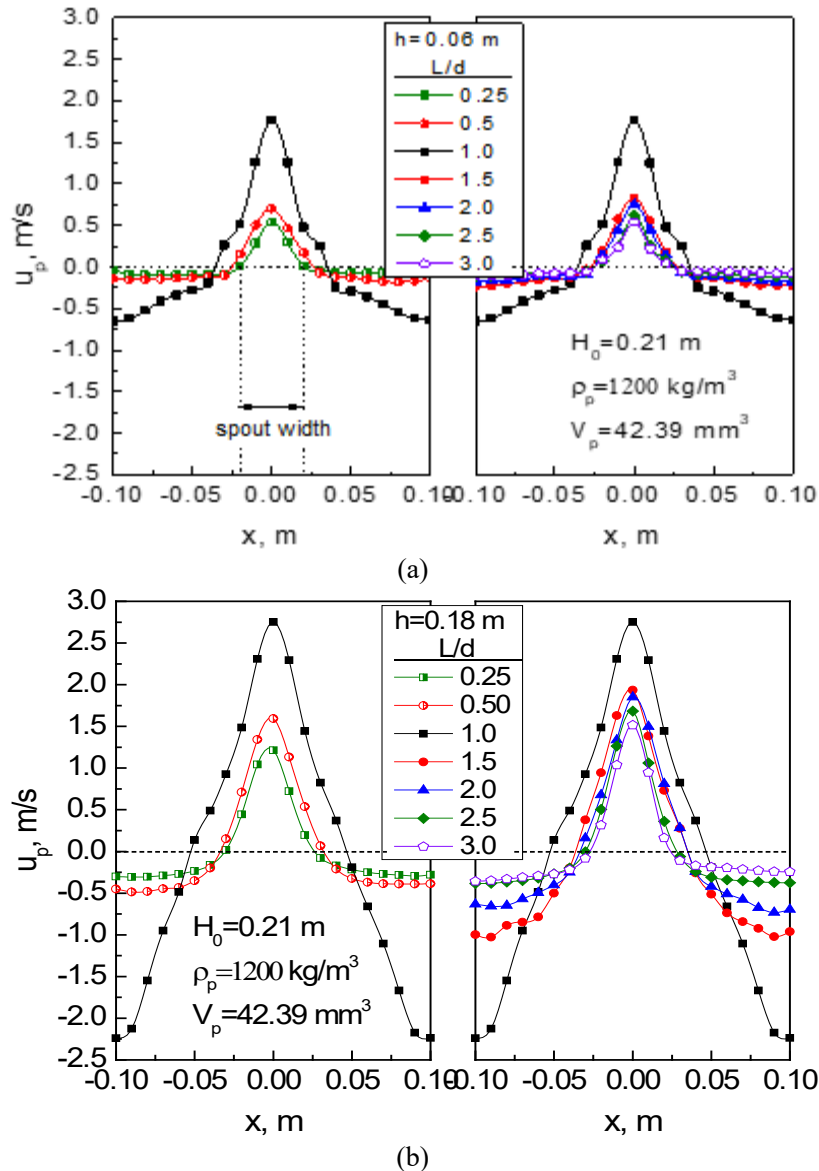


Figure 4-12 The radial time-averaged velocity distributions of particles with the varying L/d at the same bed height ($u_g=6 \text{ m/s}$): (a) $h=0.06 \text{ m}$; (b) $h=0.18 \text{ m}$

However, the rod-like particles ($L/d \geq 1.0$) showed the opposite variation trend in particle velocities. With the increasing L/d , the particle velocities in the spout and annulus decreased and the spout in the bed became narrower, as seen in the right parts of Figure 4-12(a) and (b). That was to say, for rod-like particles, if the particle shape became thinner and longer, they would perform the smaller velocities and formed the narrower spout when spouted in the bed.

Figure 4-13 showed the time-averaged axial velocity distributions of the seven kinds of particles spouting in the bed. Along the central axis of the spouted bed, the seven kinds of particles showed the similar variation trend: the particle velocities firstly increased

from zero to the peak values, and then gradually reduced to zero. For the disc-like particles, when L/d decreased with the particle shape becoming flatter, the particle velocity ascended slowly along the central axis of the bed and the velocity peak decreased; for the rod-like particles, the similar trend occurred when the L/d increased with the particle shape being thinner and longer. When $L/d=1.0$, the particle velocity showed the fastest raise and the highest peak along the central axis of the bed.

In general, the spouting of the particle with $L/d=1.0$ has the largest particle velocities in the spout and the annulus, the widest spout width, and thus the largest particle circulation rate. When the particle aspect ratio gradually deviated from 1.0 with the particle shape becoming more flat or long and further deviating from the sphere, their velocities in the bed reduced and the spout width also narrowed resulting in the decreasing particle circulation rate in the spouted bed.

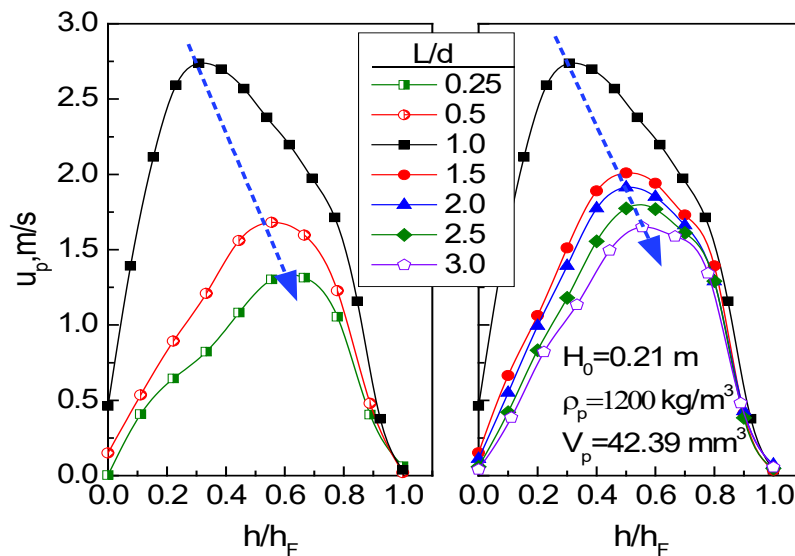


Figure 4-13 The radial time-averaged velocity distributions of particles with the varying L/d ($u_g=6$ m/s)

4.3.4 Orientations of cylindroid particles in the spouted bed

Different from the usual isotropic nature of spherical particles, non-spherical particles tend to show distinct orientations in the particulate systems, which not only determines the forces and motions of particles, but also significantly affects the mass and heat transfer between the particle and particle, or particle and fluid. For the cylindroid particles such as the disc-like particles or rod-like particles, the effects of orientations

are particularly pronounced. As the cylindroid particles are centrally symmetric, in this study the angle between the principal axis of a particle and the vertical direction was defined as the direction angle of this particle, α . A series of evenly distributed sampling points were respectively set at the heights of $h=0.06, 0.12, 0.18, 0.24$ m in the spouted bed and at a certain time the averaged value of the direction angles of all particles that were inside the neighborhood of a sampling point were counted as the particle angle of this sampling point at the current moment. The time-averaged particle angles at sampling points in a period time of stable spouting were finally adopted to characterize the particle orientations in the spouted bed.

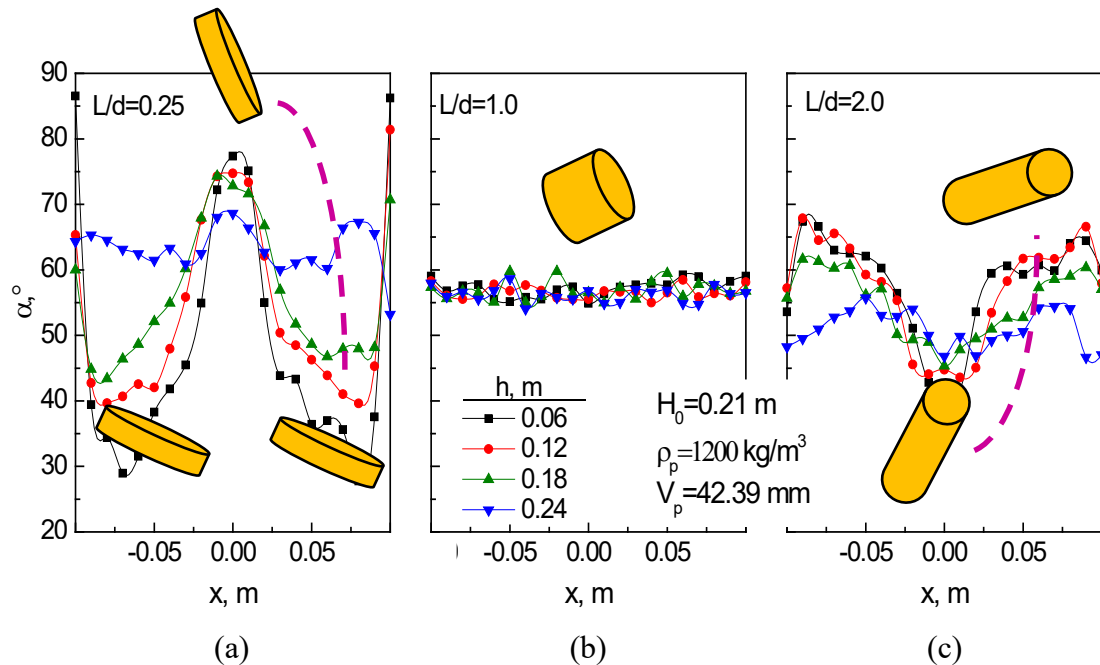


Figure 4-14 The time-averaged radial orientation distributions of three kinds of cylindroid particles with varying shapes ($u_g=6$ m/s): (a) $L/d=0.25$; (b) $L/d=1.0$; (c) $L/d=2.0$

Based on the above definition, the time-averaged radial particle angle distributions of three typical cylindroid particles with $L/d=0.25, 1.0$ and 2.0 at the different bed heights ($h=0.06, 0.12, 0.18, 0.24$ m) were shown in [Figure 4-14](#). Particles with different shapes demonstrated the completely different orientation distributions characteristics in the spouted bed. For the disc-like particle, namely $L/d=0.25$, the particle angles varied significantly in the bottom and middle parts of the bed: in the spout the angles between the principal axes of the particles and the vertical direction were more than 70° ,

indicating the disc-like particles tended to “stand” on their side in the spout as shown in [Figure 4-14\(a\)](#), while in the lateral annulus, the particle angles were obviously smaller, only about 30~40° and the particles mainly “lay flat” on their ends in this region; however, the particles near the wall usually stood on their sides against the wall with the particle angles of 90°. Generally, the angle of disc-like particle showed the defined “W” –shaped radial distributions in the bottom and middle parts of the spouted bed as shown in [Figure 4-14\(a\)](#). This variation of particle angles in the radial direction obviously weakened with the increase of the bed height. At the height that above the bed surface, for example $h=0.24$ m, the radial particle orientations became uniform and only slightly fluctuated in the range of 60~70°.

For the rod-like particle, such as $L/d=2.0$, their orientation distributions in the radial direction also showed the obvious variations: in the bottom and middle regions of the bed the particles tended to “stand upright” on their ends in the spout with the particle angle being quite small (about 40°), while in the annulus the particles preferred to “lay” on their sides with the particle angle being larger (60~70°); the angles of particles near the wall were also relatively smaller (about 55°). The angle of rod-like particle generally showed the “M” –shaped distributions in the radial direction in the bottom and middle regions of the spouted bed as shown in [Figure 4-14\(c\)](#). Similar to that of disc-like particles, this angle variation of rod-like particles in the radial direction also weakened with the increase of bed height.

In summary, the typical cylindroid particles have the distinct orientation variations in the spouted bed, especially in the bottom and middle regions of the bed. In the vertical upward stream of the spout, the particles tend to put their larger dimension parallel to the stream direction, while in the annulus where the particles are slowly falling, the particles tend to put their larger dimension perpendicular to the steam direction. When $L/d=1.0$, the particle angles were fairly evenly distributed in the bed as shown in [Figure 4-14\(b\)](#), and the averaged angle of the particles in the entire bed level only slightly fluctuated between 55 and 60°.

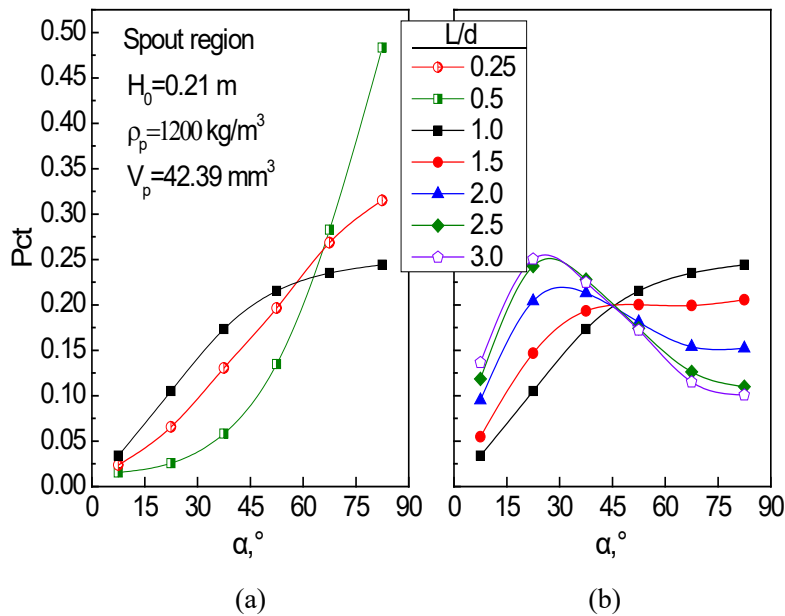


Figure 4-15 The time-averaged angle distributions of the particles with varying shapes in the spout region ($u_g=6$ m/s): (a) disc-like particles; (b) rod-like particles (“Pct” in Y-axis represents “percentage”. This will be consistent across following figures)

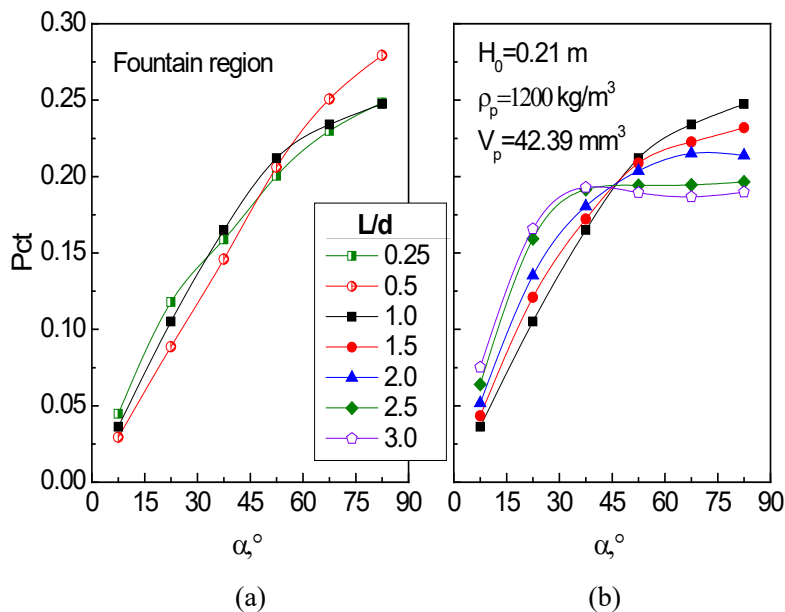


Figure 4-16 The time-averaged angle distributions of the particles with varying shapes in the fountain region ($u_g=6$ m/s): (a) disc-like particles; (b) rod-like particles

Figures 4-15, 4-16, and 4-17 showed the detailed orientation differences of the particles with the different shapes in the spout, fountain, and annulus regions, respectively. In the spout region, for the three kinds of disc-shaped particles, the number of particle with the angles between 75~90° accounted for the highest proportion when spouting, indicating in the spout region the particles that tended to “stand on the side” occupied

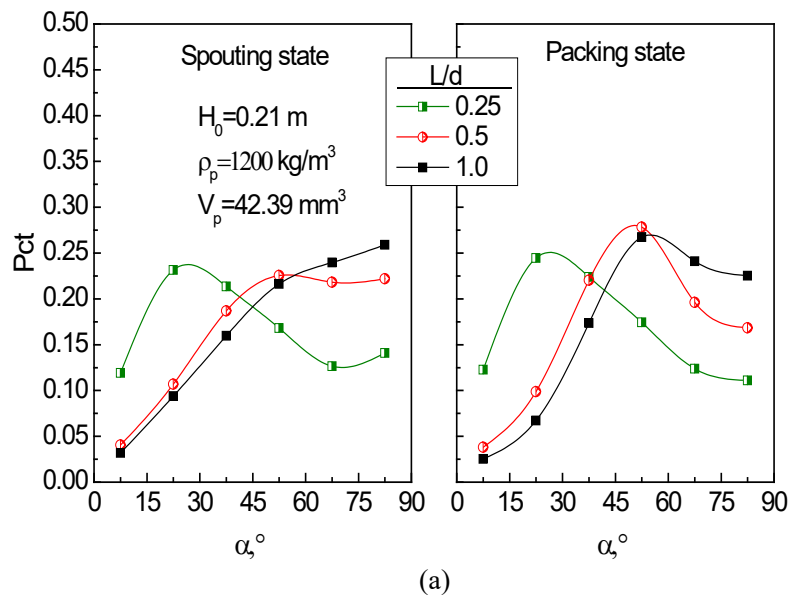
the largest proportion among all the particles with various orientations. The proportions of the particles that had the smaller angle were accordingly lower in this region, as shown in [Figure 4-15\(a\)](#). The [Figure 4-15\(a\)](#) also showed that for different particles, the particles with the larger L/d had the higher probabilities to perform the larger angles, which meant if the particle shape was flatter, there would be more particles tending to “stand on the side” in the spout. Regarding the rod-shaped particles, for the particle with the larger L/d , the proportion of the particles with the angles less than 45° were higher, and that with the angles larger than 45° were accordingly lower in the spout, as shown in [Figure 4-15\(b\)](#). That was if the particle was thinner and longer, there would be more particles in the spout tending to “stand on the end” with the angles less than 45° . In summary, in the spout, both the particles with the flatter shaper or the thinner and longer shape tended to place their larger dimensions in the vertical direction.

In the fountain region, for the disc-like particles, the particles with the larger angles accounted for the higher proportions and the particles with the angles of $75\sim 90^\circ$ had the highest proportion. That was the particles that tended to “stand on the side” had the largest number among all the particles with various orientations in the fountain region. Different in the spout region, the effects of particle shapes on their orientations became very less obviously in the fountain region, and three kinds of disc-like particles showed the very similar orientation distribution in the fountain region as shown in [Figure 4-16\(a\)](#). Regarding the rod-like particles, particles with the larger angles generally accounted for the higher proportions in the fountain and the highest proportion of particles preferred to “lay on the side” among all the particles with various orientations. With the larger L/d , the proportion of particles with the angles less than 45° would increase, indicating that for the particles with the thinner and longer shape, the proportion of particles that “stands on the end” would slightly increase, as shown in [Figure 4-16\(b\)](#).

In the annulus region, for the disc-shaped particles, when $L/d=0.25$, the angles of the most of particles were less than 45° , as shown in the left of [Figure 4-17\(a\)](#), which meant the most of particles tended to “lay on the end” in the annulus when spouting in the

spouted bed. When the particles became longer and thinner, the proportion of particles with the angles larger than 45° increased and more particles tended to “stand on the side”. Compared with the situations of naturally loose packing (see the right part of Figure 4-17(a)), the proportions of particles with the large angles (more than 60°) obviously increased in the annulus region at spouting states. The downward movements of the particles in the annulus region made more particles convert from the state of “lay on the end” to the state of “stand on the side”.

For the rod-like particles, in the annulus region, the proportions of particles with the larger angles were obviously larger, and the particles with the angles of $75\sim 90^\circ$ had the largest proportion, as shown in the left of Figure 4-17(b), which indicated that most of the particles tended to “lay on the side” in the annulus. When L/d increased with the particle being thinner and longer, the proportions of the particles that tended to “lay on the side” also increased. Compared with the situations of naturally loose packing (see the right part of Figure 4-17(b)), the proportions of the particles with the large angles showed a slight decrease in the annulus at spouting states. That was the downward movements made more particles convert from the state of “lay on the side” to the state of “stand on the end”.



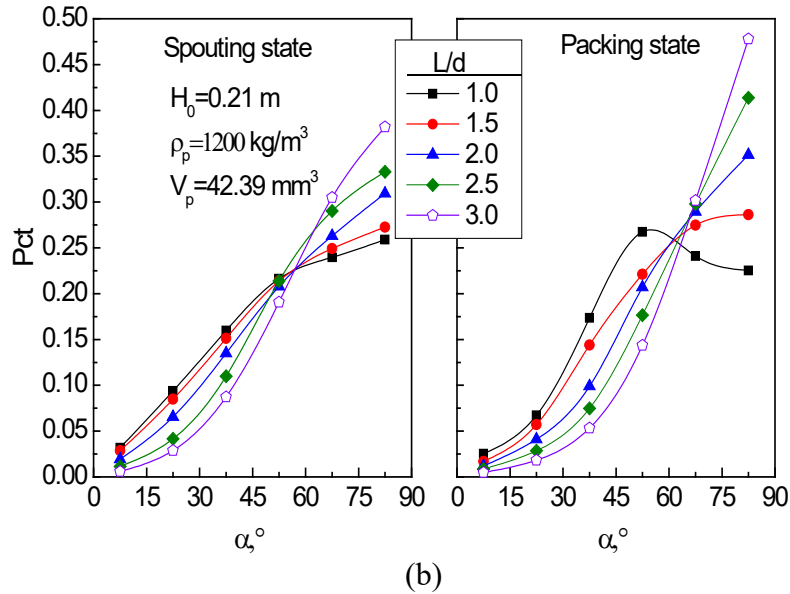


Figure 4-17 The time-averaged angle distributions of the particles with varying shapes in the fountain region (left, $u_g=6$ m/s) and in the packing state (right) : (a) disc-like particles; (b) rod-like particles

4.3.5 Coordination number (CN) of cylindroid particles in the spouted bed

Coordination number (CN) of a given particle is defined as the total number of contacts between this particle and other objects such as particles, walls and so on at a moment. The distributions of coordination numbers can effectively characterize the contacts and collisions between particles in the bed. The larger CN usually indicates the more frequent contacts and closer interactions between particles; from the mass and heat transfer point of view, this may result in more intense mass and heat transfer between particles. For the systems in which conductivity between particles plays an important role, the CN is of the remarkable significance to analyze the thermal behaviors.

The CN may vary with the definition of critical separation less than which two particles are defined in contact. The critical separation should be zero in theory when a real contact occurs between particles. But in practical computation, it is often defined as a small value slightly larger than zero. This treatment does not affect the analysis as long as the definition is consistent. In this work, the critical separation is set to $1\%d_v$ (equivalent volume diameter of particle).

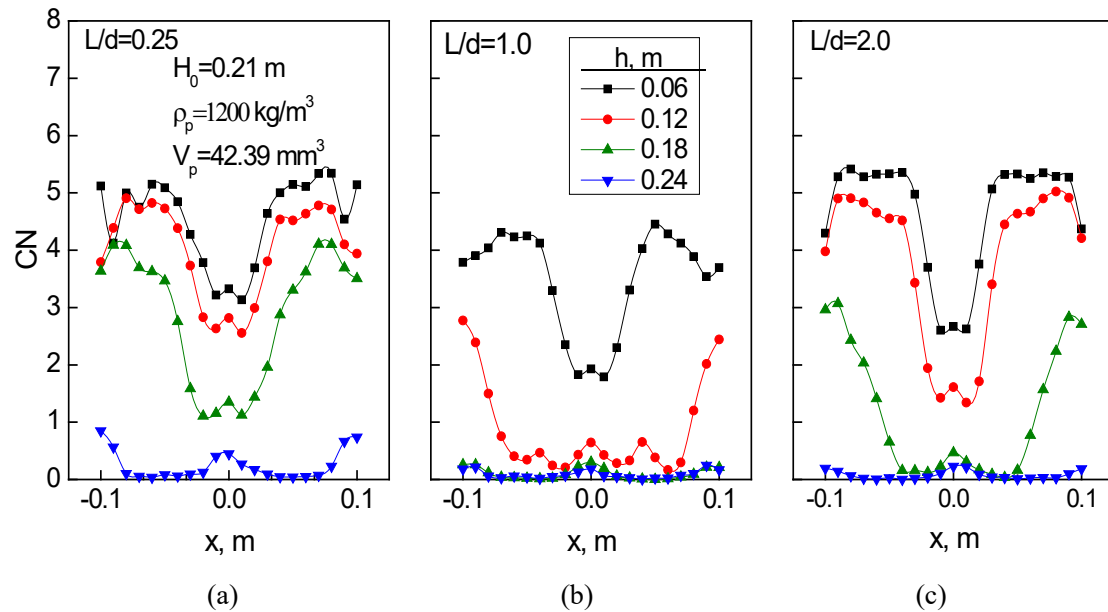
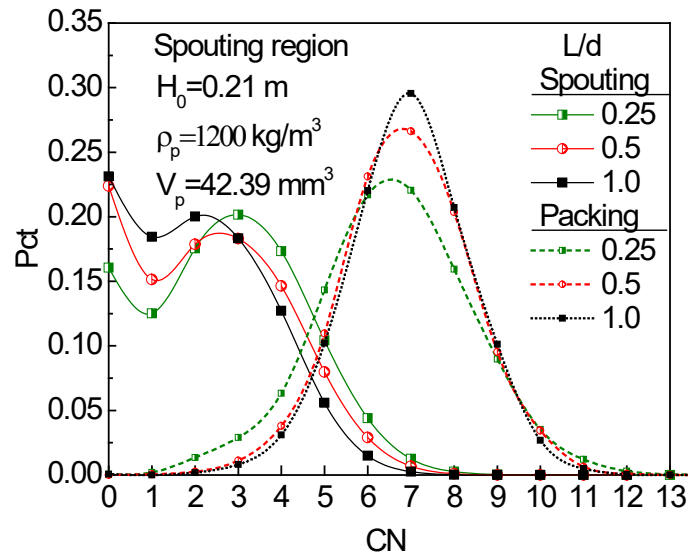


Figure 4-18 The time-averaged radial CN distributions of three kinds of cylindroid particles with varying shapes ($u_g = 6$ m/s): (a) $L/d = 0.25$; (b) $L/d = 1.0$; (c) $L/d = 2.0$

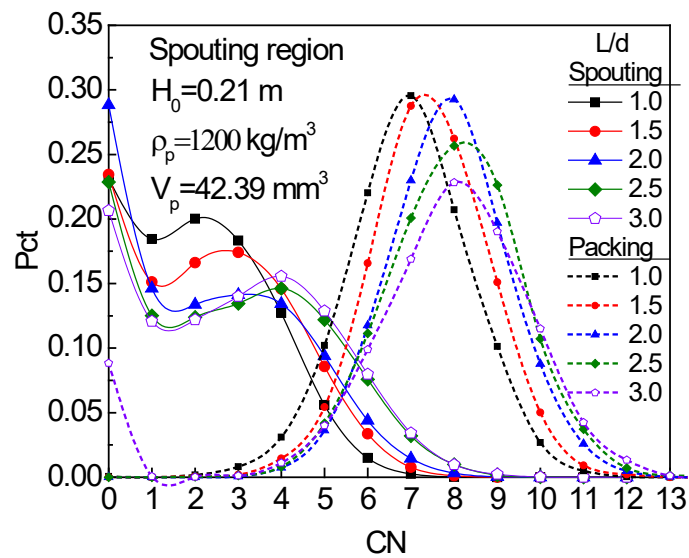
Figure 4-18 showed the time-averaged radial CN distributions of the three typical cylindroid particles ($L/d = 0.25, 1.0$ and 2.0) at different bed heights ($h = 0.06, 0.12, 0.18, 0.24$ m) in the spouted bed. In the bed level, the three particles presented the similar distribution with the lower CNs in the central spout region and the higher in the lateral annulus region, namely, the particle contacts in the spout were obviously less than that in the lateral annulus. With the bed height increasing from 0.06 m to 0.12 or 0.18 m, the CNs both in the spout and annulus decreased indicating that the particle contacts obviously reduced in the upper part of the bed level. In the fountain region outside the bed (such as $h = 0.24$ m), CN showed little difference in the radial direction, and the time-averaged CN was less than 1. This meant there was almost no contact between the particles in the fountain region. It could also be seen from Figures 4-18 that for the particles with different shapes, their CN distributions under the same conditions showed significant differences in value.

Figures 4-19, 4-20 and 4-21 showed the detailed CN distributions of particles with different shapes in the spout, annulus and fountain regions, respectively. When the spouted bed was in the spouting state, in the spout region, the cylindroid particles with $CN = 0$, VIZ, that did not contact with other particles, usually accounted for the largest proportion; particles with the CN between $0 \sim 4$ were in the majority and that with CN

larger than 6 only accounted for the very small proportion (<5%).



(a)



(b)

Figure 4-19 The time-averaged CN distributions of the particles with varying shapes in the spout region ($u_g = 6$ m/s) : (a) disc-like particles; (b) rod-like particles

For different particles, as L/d deviated from 1.0, the CN curves would shift to the right gradually, that was the proportions of particles with the smaller CN decreased and that with the larger CN increased, as shown in Figure 4-19. This indicated that when particles tended to be flatter or to be longer and thinner, the contacts between particles would increase generally. Compared to the situations of packing, the probability distribution curves of CN in the spout region of spouting states showed the very different configurations with the main bodies of curves obviously shifting to the left

and proportions of CN=0 rapidly increasing. This revealed the remarkable less particle contacts in the spout region under the spouting states than that under the packing states.

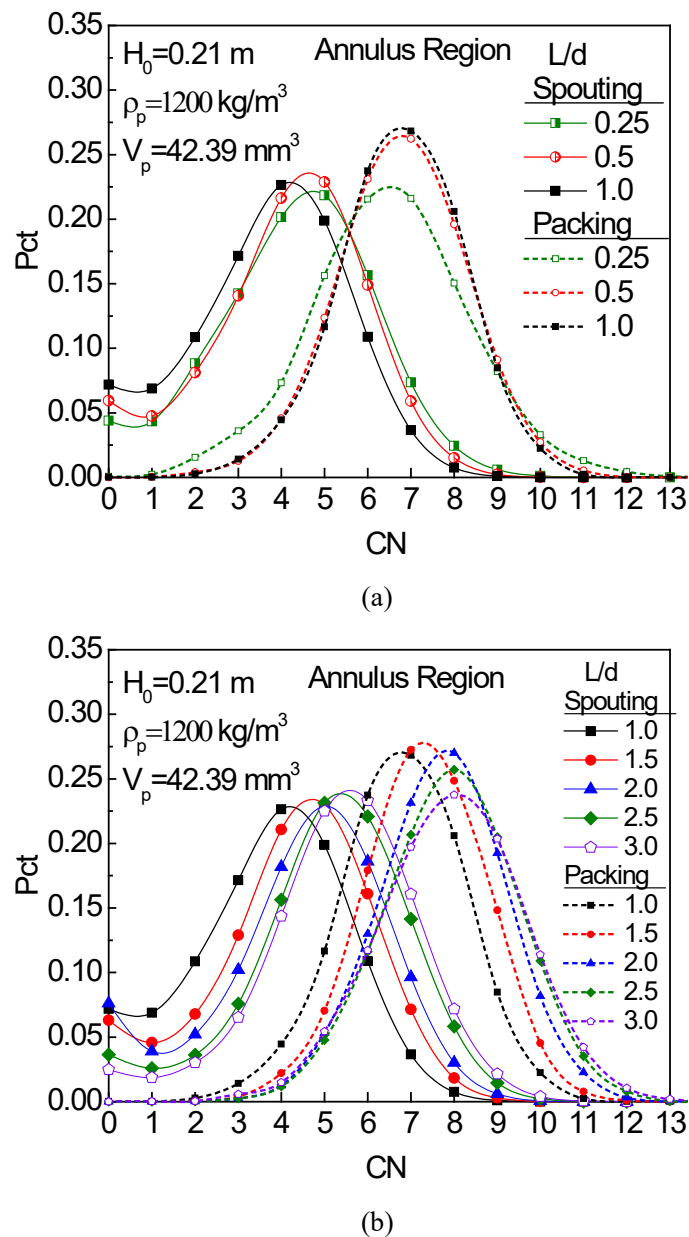


Figure 4-20 The time-averaged CN distributions of the particles with varying shapes in the annulus region ($u_g=6$ m/s) : (a) disc-like particles; (b) rod-like particles

Differently, the probability distribution curves of CN in the annulus region presented the very similar configurations to that under the packing states, as shown in Figure 4-20, but the positions of the former curves also shifted to the left obviously in the coordinate system. Under the spouting states, the proportions of particles with CN between 3~6 were highest in the annulus and that with CN exceeding 7 were very low, while under the packing states, it is the particles with CN between 5~9 that usually

accounted for the highest proportions. The downward movements of particles reduced the contacts between them to some extent in the annulus.

Additionally, for different particles, as L/d deviated from 1.0, their CN curves would shift to right with the proportions of particles with the large CN slightly increasing both in the spout and annulus region. This was to say with the shapes of particles becoming flatter or longer, their contacts in the spouted would increase.

In the fountain region, the majority of the particles (about 70%) were not in contact with any other particles ($CN = 0$). The proportion of particles with $CN > 1$ was quite small as shown in Figure 4-21. This determined that the shapes of the particles had little effect on the CN distributions in the fountain region, and all of the particles had the similar probability distribution curves of CN.

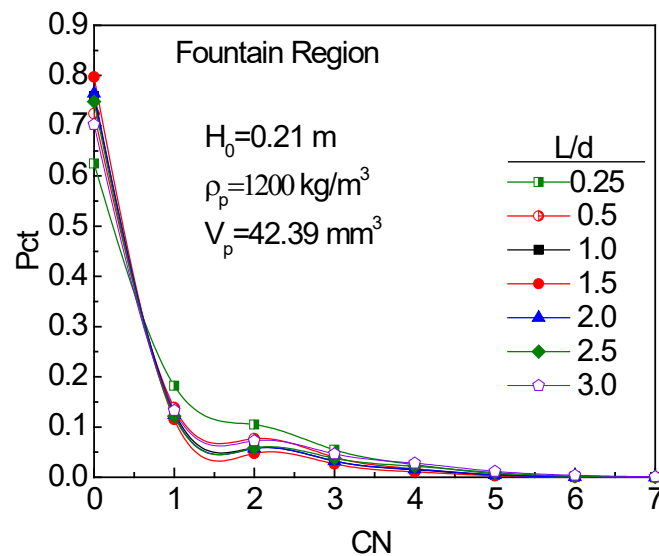


Figure 4-21 The time-averaged CN distributions of the particles with varying shapes in the fountain region ($u_g = 6$ m/s)

4.4 Summaries

The CFD-DEM models for the dense gas-solid flow systems with real cylindroid particles were developed in this chapter. The spouting features of cylindroid particles with varying shapes were studied in a spouted bed and the gas and solid dynamic characteristics and mechanisms, as well as the effects of particles shapes on the spouting behaviors were comprehensively figured out in particle scale. The main contents and conclusions are as follows:

(1) The CFD-DEM models for the dense gas-solid flow systems with real cylindroid particles were developed: the gas motion was modelled with $k-\varepsilon$ turbulent model, and the particles were represented with realistic cylindroid shapes by the combined geometric element method; with comprehensively analyzing the various contact scenario and contact force calculations and improving the interactions models for gas and cylindroid particles, the CFD-DEM modelling on “turbulent gas flow + real cylindroid particles + spouting” were successfully achieved in a CPU+GPU computing platform.

(2) In the macro scale, cylindroid particles had the similar gas and solid flow patterns with that of spherical particles in the spouted bed and three distinct three regions, namely the spout, annulus and fountain regions would form when the stable external spouting was established. The particle shapes have the obvious effects on the spouting characteristics: under the same conditions, the particles with a $L/d \sim 1$ formed the highest fountain and largest spout radius and thus the largest particles circulation rate in the spouted bed. As the cylindroid particles became flatter or longer with their shapes increasingly deviating from the sphere, the stability of the fountain would decrease and its height reduced; at the same time, the spout width, as well as the particle circulation rate also decreased.

(3) In the particle scale, the particle velocity, orientation and coordination number were investigated to discuss the effects of particle shapes on the spouting behaviors. Results showed that the cylindroid particles had the obvious orientations in the spouted bed: in the spout region, particles with remarkable difference in length and diameter tended to put their larger dimension parallel to the (vertical) flow direction, and obtained the minimum projected areas in the flow direction and thus the minimum drag forces; while, in the annulus region, these particles tended to put their larger dimension perpendicular to their falling direction (vertical). When particles were flatter or longer, such difference in orientation would be more obvious, and this would be increasingly unfavorable for the particle circulation motions in the spouted bed. On the other hand, when the particles increasingly deviated from the sphere, their contacts obviously increased and

the interactions including collision, friction, inter-locking, etc., became stronger. This also led to the worse flowability in the bed.

Reference

- 1 Guo Y, Wassgren C, Ketterhagen W, et al. A numerical study of granular shear flows of rod-like particles using the Discrete Element Method. *J Fluid Mech*, 2012, 713(6): 1-26
- 2 Morgan I M H, Littman H. Predicting the maximum spoutable height in spouted beds of irregularly shaped particles. *Ind Eng Chem Fund*, 1982, 21(1): 23-26
- 3 Liu L X, Litster J D. The effect of particle shape on the spouting properties of non-spherical particles. *Powder Technol*, 1991, 66(1): 59-67
- 4 Zhang Y, Zhong W, Jin B. Experimental investigation on the translational and rotational motion of biomass particle in a spout-fluid bed. *Int J Chem React Eng*, 2013, 11(1): 453-468
- 5 Shao Y, Zhong W, Chen X, et al. Spouting of non-spherical particles in conical-cylindrical spouted bed. *Can J Chem Eng*, 2014, 92(4): 742-746
- 6 Ren B, Zhong W, Jiang X, et al. Numerical simulation of spouting of cylindroid particles in a spouted bed. *Can J Chem Eng*, 2014, 92(5): 928-934
- 7 Džiugys A, Peters B. An approach to simulate the motion of spherical and non-spherical fuel particles in combustion chambers. *Granul Matter*, 2001, 3(4): 231-266
- 8 Zhong W Q, Yu A B, Liu X J, et al. DEM/CFD-DEM modelling of non-spherical Particulate Systems: Theoretical Developments and Applications. *Powder Technol*, 2016, 302: 108-152
- 9 Zhong W Q. Study on the hydrodynamic characteristics and scaling of the spout-fluid bed. Doctor Dissertation, Southeast University, Nanjing, 2007
- 10 Zhang Y. Experimental investigation and 3D DEM simulation on particle mixing characteristic in gas-solid fluidized bed. Doctor Dissertation, Southeast University, Nanjing, 2010
- 11 Yuan Z L. Direct numerical simulation on the dense gas-solid two-phase flow. *Thermal power engineering*, 1999, 14(6): 465-466 (in Chinese)
- 12 Xiong Y Q, Yuan Z L, Zhang M Y. Three-dimensional numerical simulation on conveying properties of gas-solid injector under pressurization. *Journal of Chemical Industry and Engineering (China)*, 2004, 55(10): 1638-1643
- 13 Zhong W Q, Xiong Y Q, Yuan Z L, et al. Three-dimensional numerical simulation of gas-solid flow behavior in spout-fluid bed. *Journal of Southeast University (Natural Science Edition)*, 2005, 35(5): 746-751

- 14 Zhong W Q, Zhang Y, Jin B S, et al. Discrete element method simulation of cylinder-shaped particle flow in a gas-solid fluidized bed. *Chem Eng Technol*, 2009, 32(3): 386-391
- 15 Geng F, Yuan Z, Yan Y, et al. Numerical simulation on mixing kinetics of slender particles in a rotary dryer. *Powder Technol*, 2009, 193(1): 50-58
- 16 Ren B, Zhong W, Chen Y, et al. CFD-DEM simulation of spouting of corn-shaped particles. *Particuology*, 2012, 10(5): 562-572
- 17 Ren B, Zhong W, Jin B, et al. Numerical simulation on the mixing behavior of corn-shaped particles in a spouted bed. *Powder Technol*, 2013, 234: 58-66
- 18 Ren B, Zhong W, Jin B, et al. Computational Fluid Dynamics (CFD)-Discrete Element Method (DEM) simulation of gas-solid turbulent flow in a cylindrical spouted bed with a conical base. *Energ Fuel*, 2011, 25(9): 4095-4105
- 19 Kruggel-Emden H, Rickelt S, Wirtz S, et al. A study on the validity of the multi-sphere Discrete Element Method. *Powder Technol*, 2008, 188(2): 153-165
- 20 Bertodano M L D, Lahey R T, Jones A O C. Development of a $k-\epsilon$ model for bubbly two-phase flow. *Journal of Fluids Engineering*, 1994, 116(1): 128-134
- 21 Zhou Z Y, Pinson D, Zou R P, et al. CFD-DEM simulation of gas fluidization of ellipsoidal particles. *Proceedings of the Seventh International Conference on CFD in the Minerals and Process Industries*, 2009, CSIRO, Melbourne, Australia
- 22 Zhan Z, Yaoming L, Zhenwei L, et al. DEM simulation and physical testing of rice seed impact against a grain loss sensor. *Biosyst Eng*, 2013, 116(4): 410-419
- 23 Zhou Z Y, Zou R P, Pinson D, et al. Dynamic Simulation of the Packing of Ellipsoidal Particles. *Ind Eng Chem Res*, 2011, 50(16): 9787-9798
- 24 Dong K, Wang C, Yu A. A novel method based on orientation discretization for discrete element modeling of non-spherical particles. *Chem Eng Sci*, 2015, 126: 500-516
- 25 Evans D J, Murad S. Singularity free algorithm for molecular dynamics simulation of rigid polyatomics. *Mol Phys*, 1977, 34(2): 327-331
- 26 Fincham D, Heyes M D. Recent advances in molecular-dynamics Computer simulation. New York: John Wiley & Sons, Inc, 1985, pp: 493-575
- 27 Kosenko I I. Intergration of the equations of a rotational motion of a rigid body in quaternion algebra. The Euler case. *J. Appl. Maths Mechs*, 1998, 2(62): 193-200
- 28 Rahman A, Stillinger F H. Molecular dynamics study of liquid water. *J Chem Phys*, 1971, 55(7): 3336-3359
- 29 Barojas J, Levesque D, Quentrec B. Simulation of diatomic homonuclear liquids. *Phys Rev A*, 1973, 7(3): 1092-1105

- 30 Eberly D. Intersection of cylinders, <http://www.geometrictools.com/Documentation/IntersectionOfCylinders>, 2009.
- 31 Ketchel J S, Larochelle P M. Collision detection of cylindrical rigid bodies using line geometry. In: Proceeding of IDETC/CIE 2005 - ASME 2005 International Design Engineering Technical Conference & Computers and Information in Engineering Conference. California, USA. 2005
- 32 Kodam M, Bharadwaj R, Curtis J, et al. Cylindrical object contact detection for use in discrete element method simulations, Part II–Experimental validation. *Chem Eng Sci*, 2010, 65(22): 5863-5871
- 33 Kodam M, Bharadwaj R, Curtis J, et al. Cylindrical object contact detection for use in discrete element method simulations. Part I–Contact detection algorithms. *Chem Eng Sci*, 2010, 65(22): 5852-5862
- 34 Guo Y, Wassgren C, Ketterhagen W, et al. Some computational considerations associated with discrete element modeling of cylindrical particles. *Powder Technol*, 2012, 228(3): 193-198
- 35 Feng Y T, Owen D R J. A 2D polygon/polygon contact model: algorithmic aspects. *Eng Computation*, 2004, 21(2/3/4): 265-277
- 36 Cundall P A, Strack O D L. A discrete numerical model for granular assemblies. *Géotechnique*, 1979, 30(30): 331-336
- 37 Wachs A, Girolami L, Vinay G, et al. Grains3D, a flexible DEM approach for particles of arbitrary convex shape– Part I: Numerical model and validations. *Powder Technol*, 2012, 224: 374-389
- 38 Kohring G A, Melin S, Puhl H, et al. Computer simulations of critical, non-stationary granular flow through a hopper. *Comput Method Appl M*, 1995, 124(3): 273-281
- 39 Fraige F Y, Langston P A, Chen G Z. Distinct element modelling of cubic particle packing and flow. *Powder Technol*, 2008, 186(3): 224-240
- 40 Höhner D, Wirtz S, Scherer V. Experimental and numerical investigation on the influence of particle shape and shape approximation on hopper discharge using the discrete element method. *Powder Technol*, 2013, 235: 614-627
- 41 Kruggel-Emden H, Oschmann T. Numerical study of rope formation and dispersion of non-spherical particles during pneumatic conveying in a pipe bend. *Powder Technol*, 2014, 268: 219-236
- 42 Höhner D, Wirtz S, Scherer V. A study on the influence of particle shape on the mechanical interactions of granular media in a hopper using the Discrete Element Method. *Powder Technol*, 2015, 278: 286-305
- 43 Oschmann T, Vollmari K, Kruggel-Emden H, et al. Numerical investigation of the mixing of non-spherical particles in fluidized beds and during pneumatic conveying. *Procedia Engineering*, 2015, 102: 976-985

- 44 Di Felice R. The Voidage function for fluid-particle interaction systems. *Int J Multiphas Flow*, 1994, 20(1): 153-159
- 45 Tran-Cong S, Gay M, Michaelides E E. Drag coefficients of irregularly shaped particles. *Powder Technol*, 2004, 139(1): 21-32
- 46 Hölzer A, Sommerfeld M. New simple correlation formula for the drag coefficient of non-spherical particles. *Powder Technol*, 2008, 184(3): 361-365
- 47 Ren B, Zhong W, Jin B, et al. Study on the drag of a cylinder-shaped particle in steady upward gas flow. *Ind Eng Chem Res*, 2011, 50(12): 7593-7600
- 48 Bowen B D, Masliyah J H. Drag force on isolated axisymmetric particles in Stokes flow. *Can J Chem Eng*, 1973, 51(1): 8-15
- 49 Militzer J, Kan J M, Hamdullahpur F, et al. Drag coefficient for axisymmetric flow around individual spheroidal particles. *Powder Technol*, 1989, 57(3): 193-195
- 50 Tripathi A, Chhabra R P, Sundararajan T. Power law fluid flow over spheroidal particles. *Ind Eng Chem Res*, 1994, 32(2): 403-410
- 51 Pettyjohn E S, Christiansen E B. Effect of particle shape on free-settling rates of isometric particles. *Chem Eng Prog*, 1948, 44(2): 157-172
- 52 Haider A, Levenspiel O. Drag coefficient and terminal velocity of spherical and nonspherical particles. *Powder Technol*, 1989, 58(1): 63-70
- 53 Rodrigue D, Chhabra R P, De K D. Drag on non-spherical particles in non-newtonian fluids. *Can J Chem Eng*, 1994, 72(4): 588-593
- 54 Madhav G V, Chhabra R P. Drag on non-spherical particles in viscous fluids. *Int J Miner Process*, 1995, 43(1): 15-29
- 55 Agarwal N, Chhabra R P. Settling velocity of cubes in Newtonian and power law liquids. *Powder Technol*, 2007, 178(1): 17-21
- 56 Laskovski D, Stevenson P, Galvin K P. Lift and drag forces on an isolated cubic particle in pipe flow. *Chem Eng Res Des*, 2009, 87(12): 1573-1581
- 57 Marchildon E K, A C, Gauvin W H. Drag and oscillatory motion of freely falling cylindrical particles. *Can J Chem Eng*, 1964, 42(4): 178-182
- 58 Huner B, Hussey R G. Cylinder drag at low Reynolds number. *Physics of Fluids (1958-1988)*, 1977, 20(8): 1211-1218
- 59 Ui T J, Hussey R G, Roger R P. Stokes drag on a cylinder in axial motion. *Physics of Fluids (1958-1988)*, 1984, 27(4): 787-795
- 60 Unnikrishnan A, Chhabra R P. An experimental study of motion of cylinders in Newtonian fluids: wall effects and drag coefficient. *Can J Chem Eng*, 1991, 69(3): 729-735
- 61 Phan-Thien N, Dou H S. Viscoelastic flow past a cylinder: drag coefficient. *Comput*

Method Appl M, 1999, 180(3): 243-266

62 Chhabra R P, Rami K, Uhlherr P H T. Drag on cylinders in shear thinning viscoelastic liquids. *Chem Eng Sci*, 2001, 56(6): 2221-2227

63 Hsu J, Shie C, Tseng S. Sedimentation of a cylindrical particle in a Carreau fluid. *J Colloid Interf Sci*, 2005, 286(1): 392-399

64 Gabitto J, Tsouris C. Drag coefficient and settling velocity for particles of cylindrical shape. *Powder Technol*, 2008, 183(2): 314-322

65 Vakil A, Green S I. Drag and lift coefficients of inclined finite circular cylinders at moderate Reynolds numbers. *Comput Fluids*, 2009, 38(9): 1771-1781

66 Jossic L, Magnin A. Drag of an isolated cylinder and interactions between two cylinders in yield stress fluids. *J Non-Newton Fluid*, 2009, 164(1-3): 9-16

67 Willmarth W W, Hawk N E, Harvey R L. Steady and unsteady motions and wakes of freely falling disks. *Phys Fluids*. 1964, 7(2): 197-208

68 Shail R, Norton D J. On the slow broadside motion of a thin disc along the axis of a fluid-filled circular duct. In: *Mathematical Proceedings of the Cambridge Philosophical Society*. 65, Cambridge University Press, 1969, 65(3): 793-802

69 Davis P. Application of optical chaos to temporal pattern search in a nonlinear optical resonator. *Jpn J Appl Phys*, 1990, 29(7A): L1238-1240

70 Wang J, Qi H, You C. Experimental study of sedimentation characteristics of spheroidal particles. *Particuology*, 2009, 7(4): 264-268

71 Heiss J F, Coull J. The effect of orientation and shape on the settling velocity of non-isometric particles in a viscous medium. *Chem Eng Prog*, 1952, 48(3): 133-140

72 Jayaweera K, Mason B J. The behavior of freely falling cylinders and cones in a viscous fluid. *J Fluid Mech*, 1965, 22(04): 709-720

73 Roger R P, Hussey R G. Stokes drag on a flat annular ring. *Phys Fluids*, 1982, 25(6): 915-922

74 Haider A, Levenspiel O. Drag coefficient and terminal velocity of spherical and nonspherical particles. *Powder Technol*, 1989, 58(1): 63-70

75 Thompson T L, Clark N N. A holistic approach to particle drag prediction. *Powder Technol*, 1991, 67(1): 57-66

76 Ganser G H. A rational approach to drag prediction of spherical and nonspherical particles. *Powder Technol*, 1993, 77(2): 143-152

77 Chien S F. Settling Velocity of Irregularly Shaped Particles. *Spe Drill Completion*, 1994, 9(04): 281-289

78 Hartman M, Trnka O, Svoboda K, et al. Influence of particle shape on the drag coefficient for isometric particles. *Collection of Czechoslovak*, 1994, 59(12): 2583-

2594

79 Wen C Y, Yu Y H. A generalized method for predicting the minimum fluidization velocity. *AIChE J*, 1966, 12(3): 610-612

80 Ergun S. Fluid flow through packed columns. *Chem Eng Prog*, 1952, 48: 89-94

81 Syamlal M, O'Brien T J. Computer simulation of bubbles in a fluidized bed. *AIChE Symp Ser*, 1989, 85(270): 22-31

82 Liu X, Shao Y, Zhong W, et al. Prediction of minimum spouting velocity by CFD-TFM: Approach development. *Can J Chem Eng*, 2013, 91(11): 1800-1808

83 Gidaspow D. *Multiphase Flow and Fluidization*. San Diego: Academic Press, 1994.

**CHAPTER 5 GAS-SOLID FLOW CHARACTERISTICS AND
SCALE-UP OF SPOUTED BEDS**

5.1 Introduction

The scale-up issues has always been the focus and difficulty in the field of spouted beds. It faces many problems such as the insufficient understanding on the gas-solid flow characteristics in the large scale spouted bed, the unclear scaling law, the lack of reliable methods and means to scale up the spouted bed and so on. Most of the existing researches on spouted beds have limited to the small scale bed ($D_c < 0.5$ m). Researches on spouted beds with the diameter of more than 0.61 m has only been reported in a few cases [1-11]. Studies have shown that the hydrodynamic characteristics of large-scale spouted beds are significantly different from those of small-scale spouted beds. The empirical correlation obtained from the small spouted beds ($D_c < 0.3$ m) showed the significant deviations when used in the spouted bed with large diameter ($D_c > 0.6$ m) [1,2,10,11]. Limited by the experimental methods and conditions, the current understanding on the flow characteristics and key parameters in the scaling process is very insufficient even for the simplest spouting systems with spherical particles, far from meeting the urgent demand in the practical industries.

On the other hand, the effective methods are deficient to scale up the spouted bed. The three main strategies available now to design the large spouted beds are as follows [1]: Scaling up the test results obtained on smaller units by the dimensional similitude methodology to achieve the large spouted beds; extending the small-scale spouted bed in a certain single dimension (for example, the thickness) to construct the slot-rectangular spouted bed; parallel merging the small-sized spout units to assemble spouted beds with multiple spout geometries. However, the rigorous dimensional similitude is usually hindered when applied in practice [1,6,12-16]. For example, the properties of particles and fluids that are handled in spouted beds are often determined according to the practical processes and thus cannot be changed to match the dimensional groups; the dimensions of spouted beds and the particle sizes have also to follow some special criterions for the stable operations in spouted beds. For example, the optimum range of D/D_i should be 6 to 10, and the maximum is likely to be ~ 12 [17]

to avoid substantial dead regions, and meanwhile D_i/d_p should not exceed 25 [18] for the stable spouting. Therefore, it is usually very difficult to simultaneously meet the consistencies of so many dimensionless groups in practice. In fact, there is even not a clear conclusion on what dimensionless groups are the decisive factors in the scaling up of spouted beds up to today [6,19-22]. The slot-rectangular spouted bed [1,4,23,24] and multiple-spout bed [1,2,25-29] also face the significantly insufficient understandings on their gas-solid flow characteristics, as well as their own particular challenges, for instance, the serious instabilities caused by the three-dimensionality of the geometry [30-32] regarding for slot-rectangular spouted beds or the strong interactions between jets for the multiple-spout beds [25-28].

In summary, to figure out the hydrodynamics characteristics of spouted beds with different structures and different sizes, explore the amplification law, and seek for the new methods are of great significance for the scale-up of spouted beds. In response to the limitations in the experimental methods and conditions, the enormous manpower, material resources, and time consumption faced in the test of the large-scale spouted beds, Professor Epstein N and Professor Grace J R clearly stated that computational simulation method would be one of the most effective means for the scaling research of spouted beds in their monograph on spouted beds [1]. However, due to the limitation of computational resources, most of the Eulerian-Lagrangian simulations still focus on laboratory-scale or pilot-scale systems today and especially when referring to the non-spherical particulate systems, only the range of 100 to 20000 particles has been achieved by DEM. The state-of-the-art DEM simulation technique is far from being perfect enough to deal with real systems in nature or industry in which the number of particles often surpasses 10^9 . On the other hand, based on the experimental results in Chapter 3, for the gas-solid systems containing only small amounts of non-spherical particles, the spouting characteristics and key parameters of the systems mainly depended on the properties of the spherical bed material. It would not be necessary to use the computationally expensive DEM-CFD developed in Chapter 4 to consider the shapes of non-spherical particles. Based on this, this chapter alternatively developed

the Euler-Euler two-fluid model to study the gas-solid flow behaviors of spouted beds and their scaling-up characteristics. By directly predicting the spouting behaviors in spouted beds with different structures and sizes, the gas-solid flow characteristics and the key parameters during the scaling process of the spouted bed could be analyzed and obtained.

5.2 TFM approach for spouted beds and model validations

With the rapid development of computer technology and improvement of numerical algorithms, computational modeling has become a powerful tool to explore the hydrodynamics of spouted beds. one useful approach is the Eulerian-Eulerian multiphase model (two-fluid model, TFM). The TFM approach deals with multiple-phase flow by treating the phases as the interpenetrating continua and incorporating the concept of phase volume fraction to represent the space occupied by each phase. On the basis of continuum theory, the conservation equations on mass, momentum and energy are respectively used to describe the gas and solid flows. The constitutive equations for the solid stress and the gas-solid interaction models are established to realize the closure of the above governing equation.

With the continuous development and improvement of researchers from worldwide in recent years, the TFM approach has been widely used in the in-depth studies of the spouted bed on the gas-solid flow characteristics and scale-up issues. For instance, Lu et al. [14] incorporated the hydrodynamic model with a kinetic-frictional constitutive model, which includes the particle phase stresses, to simulate gas-solids flow in spouted beds. Du et al. [33,34] and Lan et al. [35] investigated the influence of drag coefficient correlations, frictional stress, maximum packing limit, restitution coefficient and solid-phase wall boundary condition on the simulation of spouted beds. Other researchers, e.g. Béttega et al. [12], Duarte et al. [36,37] and Santos et al. [38], have verified the effectiveness of the TFM approach in exploring gas-solid spouted bed flow behavior and scale-up.

Based on the existing knowledge, this study developed and obtained a group of TFM

models and parameters for the gas-solid flow systems in spouted beds with different structure and sizes by the comprehensive sensibility analysis on the mesh independence, gas-solid drag model, friction stress model, maximum packing limit, coefficient of restitution, turbulence model, boundary conditions and so on, and used the above simulation method to study and solve some key issues in the design and application of spouted beds.

5.2.1 TFM models for spouted beds

In the current TFM approach, the gas motion is simulated by the $k-\varepsilon$ two-equation turbulent model, while the particle phase motion is estimated from the kinetic theory of granular flow. The Syamlal-O'Brien drag model [39,42] and Schaeffer frictional stress model [39-41] are respectively employed to deal with the drag force between phases and the friction stress for solid. The detailed governing equations, closure models and constitutive equations are shown in Table 5-1.

Table 5-1 Main equations and models for TFM for spouted beds

Governing equations	
Continuity equations	$\frac{\partial}{\partial t}(\rho_q \alpha_q) + \nabla \cdot (\rho_q \alpha_q \bar{v}_q) = 0 \quad q = g, s$ $\alpha_g + \alpha_s = 1$
Momentum equation	<p>Gas phase</p> $\frac{\partial}{\partial t}(\rho_g \alpha_g \bar{v}_g) + \nabla \cdot (\rho_g \alpha_g \bar{v}_g \bar{v}_g) = -\alpha_g \nabla p + \nabla \cdot \bar{\tau}_g + \alpha_g \rho_g \bar{g} + \bar{R}_{gs}$ $\bar{\tau}_g = \alpha_g \mu_g (\nabla \bar{v}_g + \nabla \bar{v}_g^T) - \frac{2}{3} \alpha_g \mu_g (\nabla \cdot \bar{v}_g) \bar{I}$ <p>Solid phase</p> $\frac{\partial}{\partial t}(\rho_s \alpha_s \bar{v}_s) + \nabla \cdot (\rho_s \alpha_s \bar{v}_s \bar{v}_s) = -\alpha_s \nabla p - \nabla p_s + \nabla \cdot \bar{\tau}_s + \alpha_s \rho_s \bar{g} - \bar{R}_{gs}$ $\bar{\tau}_s = \alpha_s \mu_s (\nabla \bar{v}_s + \nabla \bar{v}_s^T) - \alpha_s (\lambda_s - \frac{2}{3} \mu_s) (\nabla \cdot \bar{v}_s) \bar{I}$ $\bar{R}_{gs} = K_{gs} (\bar{v}_s - \bar{v}_g)$
Closure equations based on the kinetic theory of granular flow	
Solid phase pressure	$p_s = \alpha_s \rho_s \theta [1 + 2g_0 \alpha_s (1 + e)]$
Radial distribution function	$g_0 = \left[1 - \left(\frac{\alpha_s}{\alpha_{s,max}} \right)^{1/3} \right]^{-1}$
Particles bulk viscosity	$\lambda_s = \frac{4}{3} \alpha_s^2 \rho_s d_s g_0 (1 + e) \sqrt{\frac{\theta}{\pi}}$
Particles shear viscosity	$\mu_s = \frac{4}{5} \alpha_s \rho_s d_s g_0 (1 + e) \sqrt{\frac{\theta}{\pi}} + \frac{\alpha_s d_s \rho_s \sqrt{\pi \theta}}{6(3 - e)} \left[1 + \frac{2}{5} \alpha_s g_0 (1 + e)(3e - 1) \right] + \frac{p_s \sin \varphi}{2\sqrt{I_{2D}}}$

Chapter 5 Gas-solid flow characteristics and scale-up of spouted beds

Collision dissipation energy	$\gamma_s = 3(1 - e^2)\alpha_s^2\rho_s g_0 \Theta \left(\frac{4}{d_s} \sqrt{\frac{\Theta}{\pi}} - \nabla \cdot \mathbf{v}_s \right)$
Granular energy diffusion coefficient	$\Gamma_\Theta = \frac{150\rho_s d_s \sqrt{\pi\Theta}}{384(1+e)g_0} \left[1 + \frac{6}{5}(1+e)g_0\alpha_s \right]^2 + 2\alpha_s^2\rho_s d_s g_0 (1+e) \sqrt{\frac{\Theta}{\pi}}$
Transfer of the kinetic energy	$\phi_{gs} = -3\beta\Theta$
Interaction models between phases	
Gas-solid momentum exchange coefficient (Syamlal-O'Brien drag model [42])	$K_{gs} = \frac{3\alpha_g\alpha_s\rho_g}{4v_{r,s}^2 d_p} C_D \vec{v}_s - \vec{v}_g $ $C_D = (0.63 + \frac{4.8}{\sqrt{\text{Re}_s/v_{r,s}}})^2$ $\text{Re}_s = \frac{\rho_g\alpha_g \mathbf{v}_g - \mathbf{v}_s d_s}{\mu_g}$ $v_{r,s} = 0.5 \left(A - 0.06\text{Re}_s + \sqrt{(0.06\text{Re}_s)^2 + 0.12\text{Re}_s(2B - A) + A^2} \right)$ $A = \alpha_g^{4.14}, \quad B = \begin{cases} 0.8\alpha_g^{1.28}, & \alpha_g \leq 0.85 \\ \alpha_g^{2.65}, & \alpha_g > 0.85 \end{cases}$
The modified k-ε turbulence model	
Gas turbulent kinetic energy	$\frac{\partial}{\partial t}(\alpha_g\rho_g k_g) + \nabla \cdot (\alpha_g\rho_g \vec{U}_g k_g) = \nabla \cdot (\alpha_g \frac{\mu_{t,g}}{\sigma_k} \nabla k_g) + \alpha_g G_{k,g} - \alpha_g \rho_g \varepsilon_g + \alpha_g \rho_g \Pi_{k_g}$
Gas turbulent dissipation rate	$\frac{\partial}{\partial t}(\alpha_g\rho_g \varepsilon_g) + \nabla \cdot (\alpha_g\rho_g \vec{U}_g \varepsilon_g) = \nabla \cdot (\alpha_g \frac{\mu_{t,g}}{\sigma_k} \nabla \varepsilon_g) + \alpha_g \frac{\varepsilon_g}{k_g} (C_1 G_{k,g} - C_2 \rho_g \varepsilon_g) + \alpha_g \rho_g \Pi_{\varepsilon_g}$
	$\mu_{t,g} = \rho_g C_\mu \frac{k_g}{\varepsilon_g}$ $G_{k,g} = \mu_{t,g} (\nabla \vec{v}_g + (\nabla \vec{v}_g)^T) : \nabla \vec{v}_g$ $\Pi_{k_g} = \sum_{p=1}^M \frac{K_{gs}}{\alpha_g \rho_g} (k_{gs} - 2k_g + \vec{v}_{gs} \cdot \vec{v}_{dr})$ $\Pi_{\varepsilon_g} = C_{3\varepsilon} \frac{\varepsilon_g}{k_g} \Pi_{k_g}$
constant	$C_\mu = 0.09, \quad C_{1\varepsilon} = 1.42, \quad C_{2\varepsilon} = 1.92, \quad C_{3\varepsilon} = 1.2, \quad \sigma_k = 1, \quad \sigma_\varepsilon = 1.3$

The finite volume method is implemented to solve the above conservative and constitutive equations [39]. First-order upwind discretization is used to convert the partial different equations to algebraic ones. The SIMPLE algorithm is adopted for pressure-velocity coupling and correction, with the iterative convergence criterion being 10^{-4} .

The general initial conditions and boundary conditions adopted for spouted beds are shown in [Table 5-2](#).

Table 5-2 General initial conditions and boundary conditions adopted for spouted beds [39,44]

Initial conditons	
Gas phase	$u_{g,inlet}=(S_{column}/S_{inlet})U$, normal to enterance Gas phase turbulent kinetic energy: $k = \frac{3}{2}(uI)^2$ Turbulence intensity: $I = 0.16(Re_{Du})^{-\frac{1}{y}}$ Turbulence dissipation rate: $\varepsilon = C_{\mu}^{\frac{3}{4}} \frac{k^{3/2}}{l}$ $C_{\mu} = 0.09$, $l = 0.07L$ Initial velocity of gas in the other section: $u_g=0$
Solid phase	Inlet $u_{s,inlet}=0$, $\alpha_{s,inlet}=0$ The packing conditions of solid are set according to the specific objects
Boundary conditions	
Inlets	Gas phase: velocity-inlet, normal to enterance Gas phase turbulent kinetic energy $k = \frac{3}{2}(uI)^2$ Turbulence intensity: $I = 0.16(Re_{Du})^{-\frac{1}{y}}$ Turbulence dissipation rate: $\varepsilon = C_{\mu}^{\frac{3}{4}} \frac{k^{3/2}}{l}$ $C_{\mu} = 0.09$, $l = 0.07L$ Solid phase: $u_{s,y} = u_{s,x} = u_{s,z} = 0$, granular temperature: $\Theta_{s,inlet}=0.0001$, $\alpha_{s,inlet}=0$
outlets	Pressure out Gas phase turbulent kinetic energy for return flow $k = \frac{3}{2}(uI)^2$, $I = 0.16(Re_{Du})^{-\frac{1}{y}}$ Turbulence dissipation rate for return flow $\varepsilon = C_{\mu}^{\frac{3}{4}} \frac{k^{3/2}}{l}$, $C_{\mu} = 0.09$, $l = 0.07L$
Wall	No-slip bourdaries

5.2.2 Model validations

Experimental results from He et al. [45,46] on the spouted bed with the dimeter of 152 mm and that from Ren et al. [28] on the multiple-spout bed were used to validate the proposed CFD-DEM models.

(1) Validation for the spouted bed with inner diameter of 152 mm

The detailed bed structure, material properties, experimental conditions and the key parameters used in the simulation are shown in [Table 5-3](#). Among them, the collision restitution coefficient of particles, e , and the solid maximum packing limit, $\alpha_{s, \max}$ are the two most important parameters in the TFM based on particle kinetic theory. The restitution coefficient characterizes the degree of inelastic collision between particles. The maximum packing limit $\alpha_{s, \max}$ is the maximum volume fraction that can be achieved by the particle phase in the simulated system without exceeding the physical limit. Their values directly affect the kinetics, viscosity, pressure and dynamic energy dissipation of the solid phase in the TFM theory. Since these two parameters are closely related to the nature of the particles and gas-solid system, and always difficult to determine them directly, they are generally derived from the existing experiments [47].

Detailed comparisons of simulated radial distributions of particle velocity and voidage with experimental results are shown in [Figure 5-1](#). Results show that simulations with the adopted Syamlal-O'Brien drag model, Schaeffer frictional stress model, maximum packing limit $\alpha_{s, \max} = 0.63$ and restitution coefficient $e = 0.88$ achieve the best agreement with the experimental data.

[Table 5-3](#) Properties of spouted bed system and main numerical parameters [39, 45, 46]

properties	value
Diameter of the bed, D_c (mm)	152.0
Diameter of the gas inlet, D_i (mm)	19.0
Height of the bed, H (mm)	815
Angle of conical bottom, γ ($^\circ$)	60
Particle size, d_s (mm)	1.41
Particle density, ρ_s (kg/m^3)	2503
Particle sphericity, ϕ	1.0
Gas density, ρ_g (kg/m^3)	1.225
Gas viscosity, μ_g (Pa·s)	1.7894×10^{-5}

Static bed height, H_0 (mm)	300
Restitution coefficient, e	0.88
Maximum solid packing volume fraction, $\alpha_{s,max}$	0.63

(2) Validation for the multiple-spout bed

Figure 5-2 presents comparisons between experiments and simulations for the two typical flow patterns in the multiple-spout bed of which the dimensional sizes are $D_T=300$ mm, $B=30$ mm and $H=1000$ mm with the width of each spouting cell being $D_{T0}=100$ mm, gas inlet width $D_s=10$ mm, gas density $\rho_g=1.225$ kg/m³, gas viscosity $\mu_g=1.7894 \times 10^{-5}$ Pa·s, particle size $d_s=2.8$ mm, particle density $\rho_s=900$ kg/m³, and $e=0.90$, $\alpha_{s,max}=0.59$. For each flow pattern, an experimental image photographed by Ren et al. [28] is shown on the left side, while on the right side there is a corresponding simulated result under the same condition. The good agreements between the experimental and simulated flow patterns indicate that the present models are valid to predict the gas-solid two-phase flow behaviors in multiple spouted beds [27].

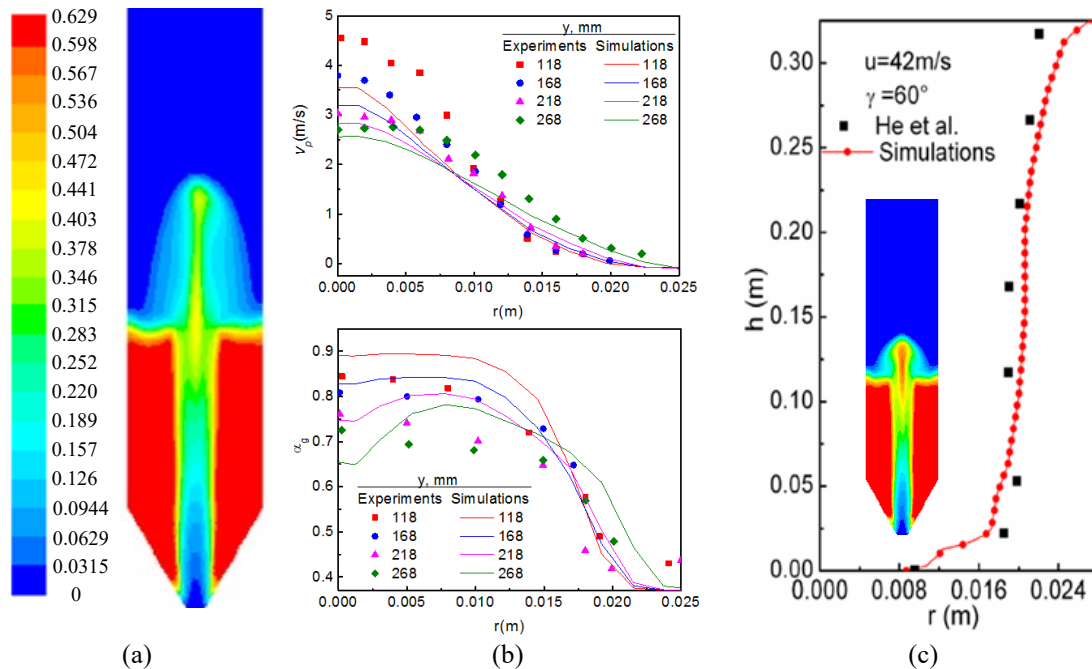


Figure 5-1 Comparisons between the experiments [45,46] and simulations on the spouted bed with the diameter of 152 cm: (a) simulated spouting with $u=1.2u_{ms}$; (b) comparisons of particle velocity and voidage in the bed with $u=1.2u_{ms}$; (c) comparison of the boundary of the spout with $u=1.1u_{ms}$

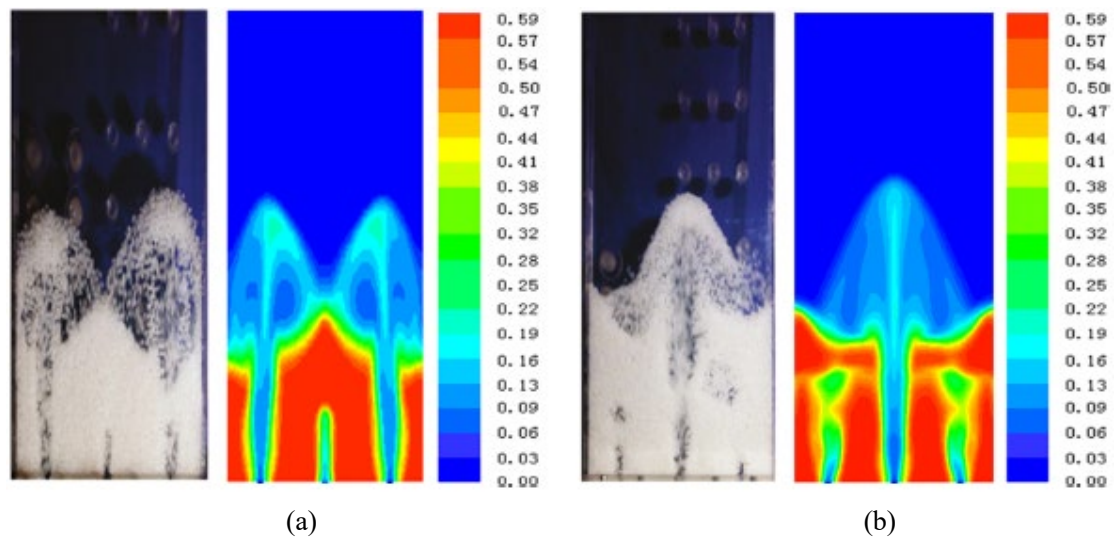


Figure 5-2 Comparisons between experiments [28] and simulations for the multiple-spout bed (left: experiments, right: simulations): (a) $H_0/D_{t0}=1.0$, $Q_c/Q_{mf}=1.2$, $Q_a/Q_{mf}=3.03$; (b) $H_0/D_{t0}=1.5$, $Q_c/Q_{mf}=3.6$, $Q_a/Q_{mf}=1.65$

5.3 Evaluation on the effect of conical geometry on flow behaviors in spouted beds

For the conventional conical-cylindrical spouted beds, one of the significant uncertainties is the influence of conical section geometry which proves to be essential to the gaseous reactants reacting time and residence time in the industrial processes. Since most previous studies have just focused on the columns with the conical angle of 60° , the fixed geometric condition questions to what extent the influence of the conical geometry of the spouted bed on the hydrodynamics of the whole beds. While somewhat differences in hydrodynamics have been observed of shallow spouted beds and nearly flat base spouted beds.

As a result, increasing interest has been taken in questions as follows: when the base conical angle changes, what happens in the hydrodynamic behaviors of spouted bed; how the conical angle affects the gas and solid motions in whole bed? And what conical angle will lead to the best gas-solid flow behaviors? Therefore, it is interesting to study the gas-solid flow behaviors of the conical-cylindrical spouted bed with different conical section geometries.

In this study, the TFM approach is adopted to study the gas-solid flow behaviors in the

conical-cylindrical spouted beds with different conical section geometries. The numerical computations are based on the operating conditions of He et al. [45, 46] while the conical angle ranges from 30° to 180° . The solid flow pattern, particle velocity in spout and annulus, fountain height and the diameter of the spout are investigated.

5.3.1 Gas and solid flow distributions

Under the operating condition of the static bed height $H_0=0.325$ m, gas inlet velocity $u=42$ m/s, the flow patterns in the spouted beds with different conical angles are shown in Figure 5-3, and the distributions of gas and solid velocity vector are illustrated in Figure 5-4 and Figure 5-5, respectively. According to these three figures, when conical angle, γ , is 30° , the conical-cylindrical spouted beds fails to form stable spouting. The internal spout slightly distorts. Olazar et al. [48] and Shan et al. [49] have also observed this unstable spouting in their experiments and they believed there was a minimum conical angle (28° according to Olazar et al. [48] and 40° according to Shan et al. [49]) below which stable spouting with cyclic solids down flow and stable fountain was not attainable. As γ is beyond 30° , three flow regions, i.e., the spout, annulus and fountain can be clearly visualized, with stable spouting taking place.

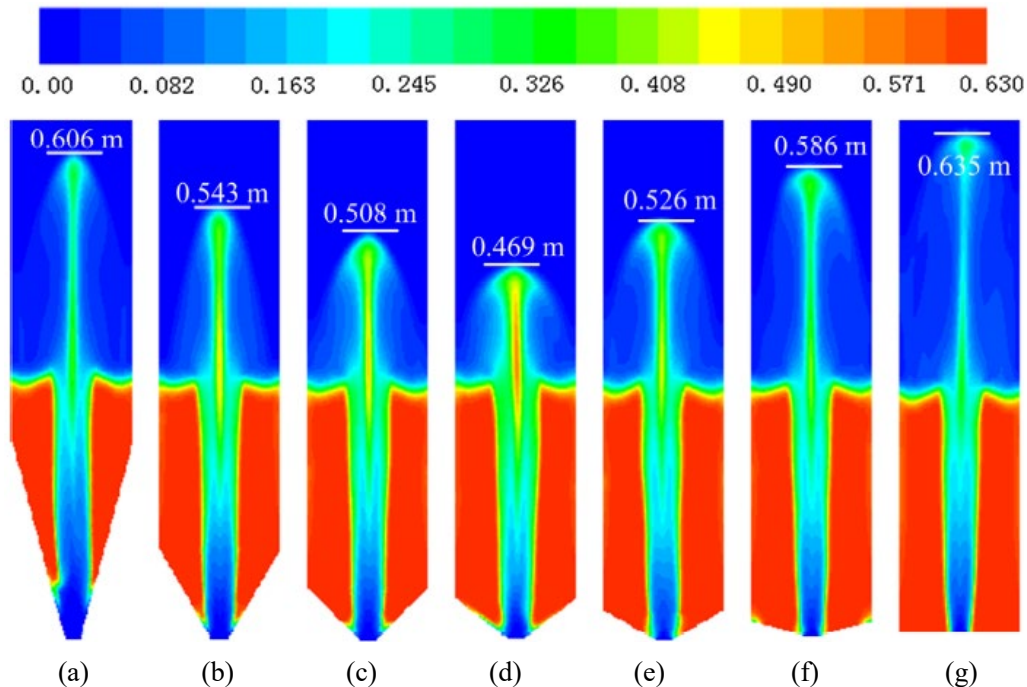


Figure 5-3 Flow patterns in different beds with $u=42$ m/s and $H_0=0.325$ m: (a) $\gamma=30^\circ$; (b) $\gamma=60^\circ$; (c) $\gamma=90^\circ$; (d) $\gamma=105^\circ$; (e) $\gamma=120^\circ$; (f) $\gamma=150^\circ$; (g) $\gamma=180^\circ$

The gas velocity distribution in Figure 5-4 shows that after entering into the nozzles, the gases carry out different diffusions due to the varying conical angles. When $\gamma=30^\circ$, the gas diffuses completely and occupies the whole conical space near the nozzles. If the diffusion angle, β , is introduced to represent the degree of gas diffusion, β equals to approximately 30° when $\gamma=30^\circ$. When the conical angle γ increases, β is found to increase and always tend to equal to γ when γ is within 105° . However, when γ is beyond 105° , with the increasing γ , β presents a reverse trend. This means with the growing γ , the gas diffusion reduces and thus gas flow near the nozzle possesses stronger concentration and larger velocity. The capability of the gas flow to carry the particles will strengthen.

In Figure 5-5, a slightly curved solid flow is demonstrated in the bed with 30° conical angle, since the small conical angle leads to a very narrow base space in bed, and thus the solid motions there pretty unstable. The increase in γ , leading to the growing inclination of the conical wall and consequently the increasing base space in the bottom of the column, brings the gentler particles motion in annulus and more stable internal spouting in the bottom region.

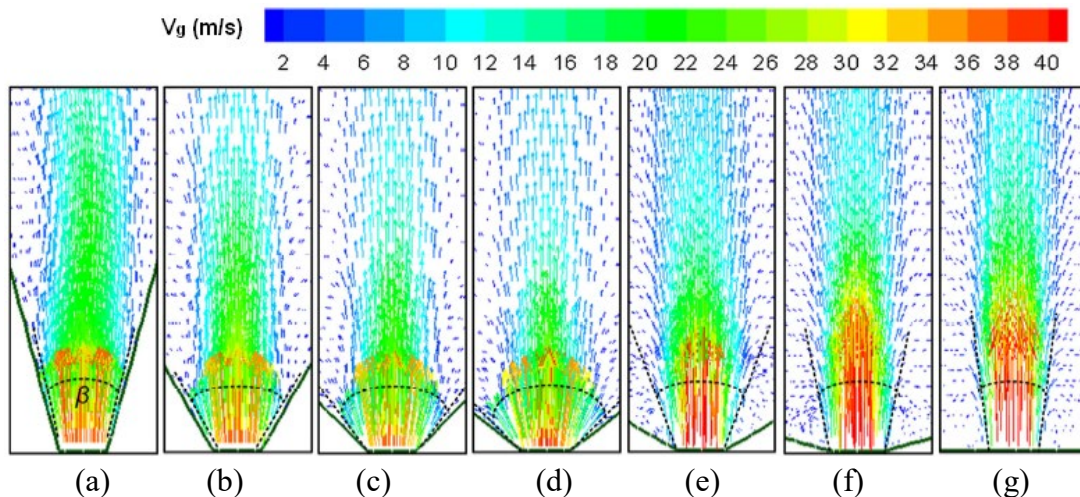


Figure 5-4 Gas velocities in different beds with $u=42$ m/s and $H_0=0.325$ m: (a) $\gamma=30^\circ$; (b) $\gamma=60^\circ$; (c) $\gamma=90^\circ$; (d) $\gamma=105^\circ$; (e) $\gamma=120^\circ$; (f) $\gamma=150^\circ$; (g) $\gamma=180^\circ$

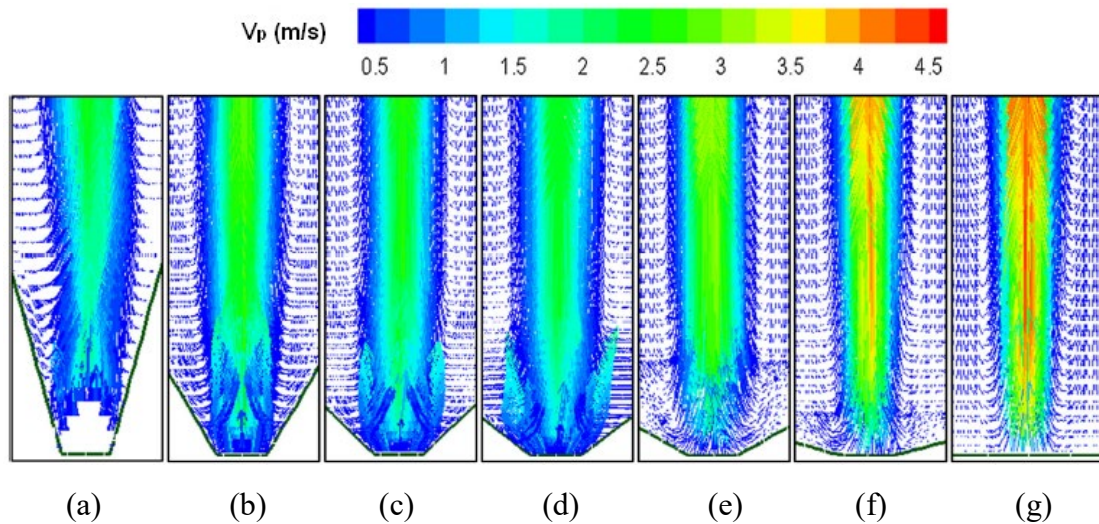


Figure 5-5 Particle velocities in different beds with $u=42$ m/s and $H_0=0.325$ m: (a) $\gamma=30^\circ$; (b) $\gamma=60^\circ$; (c) $\gamma=90^\circ$; (d) $\gamma=105^\circ$; (e) $\gamma=120^\circ$; (f) $\gamma=150^\circ$; (g) $\gamma=180^\circ$

Figure 5-6 shows the fountain heights in different spouted beds. At the identical operating conditions of $u=42$ m/s and $H_0=0.325$ m, the spouted bed with 105° conical angle has a lowest fountain height, while when the conical angle increases or decreases from 105° , the fountain height always increases.

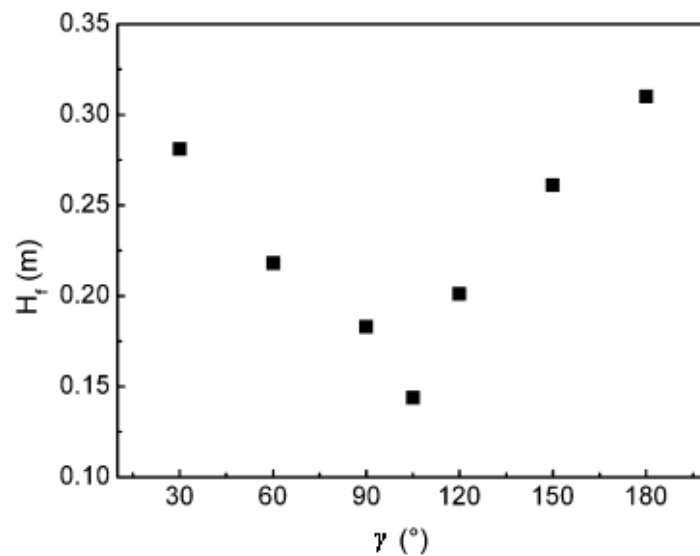


Figure 5-6 Fountain heights in different spouted beds with $u=42$ m/s and $H_0=0.325$ m

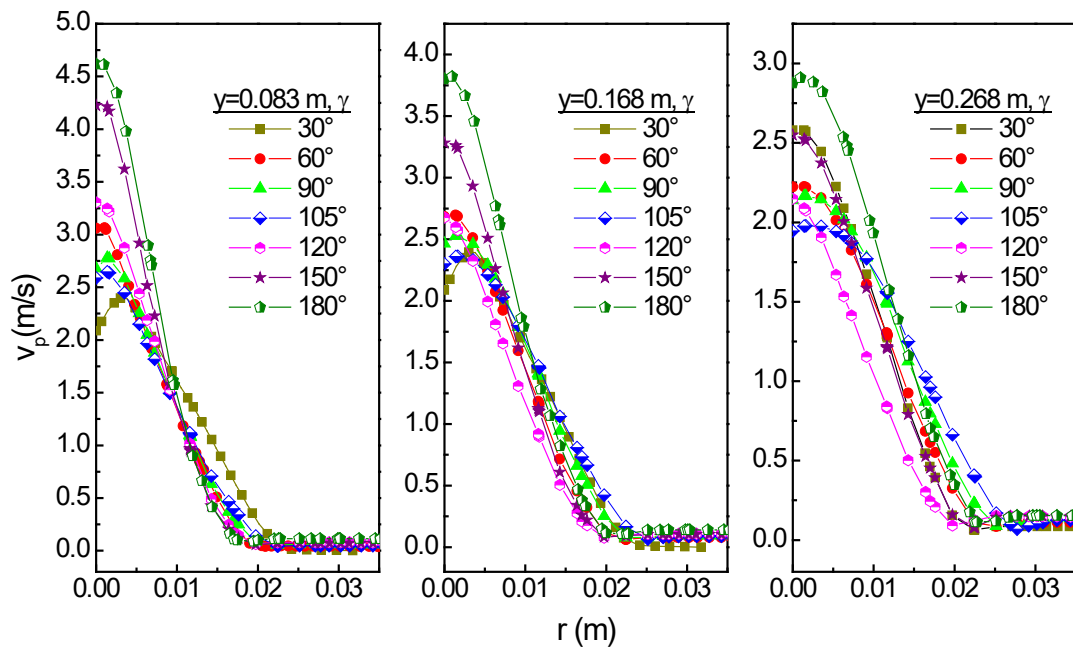


Figure 5-7 Radical profiles of vertical particle velocity in the spout regions of different beds with $u=42$ m/s and $H_0=0.325$ m

5.3.2 Particle velocity

Figure 5-7 shows the simulated radical profiles of vertical particle velocity in the spout regions of different beds under the identical conditions of $H_0=0.325$ m and $u=42$ m/s. At the identical bed levels, when the conical angle is less than 105° , the vertical particle velocities always decrease with the increasing γ ; while when $\gamma > 105^\circ$, the particle velocities become to increase when the conical angle continually increase.

In order to express the velocity differences more explicitly, Figure 5-8 provides the central axis profiles of the vertical particle velocity in different spouted beds. Except in the column with the 30° conical angle, the particle velocity profiles in other beds have a similar tendency along the axis: The local velocities first sharply increase to reach the maximums at the distance of about 0.07 m from the nozzles and then gradually decrease along the height, until it decreases to zero at the top of the fountains. At the same time, the differences in quantitative term are quite obvious. When the conical angle increases from 60° to 105° , the particle velocity along the entire axis always decreases, while when γ continues to increase from 105° to 180° , the velocity then turns to increase with the growing γ .

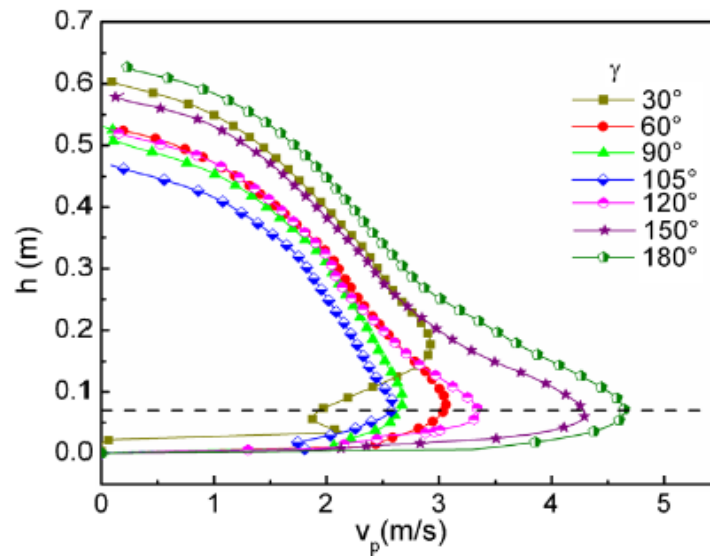


Figure 5-8 The central axis profiles of the vertical particle velocity in different spouted beds with $u=42$ m/s and $H_0=0.325$ m

On the other hand, in annulus at identical level of different beds, the particle velocities generally increase with the increasing conical as shown in Figure 5-9. At the level that more far from the conical region, the radical profile of particle velocity in annulus is more uniform. For example, for the two beds with 60° and 120° angle whose base heights are respectively 115.3 mm and 38.4 mm, the particle velocity in the bed with 120° distributes more uniformly in the identical levels.

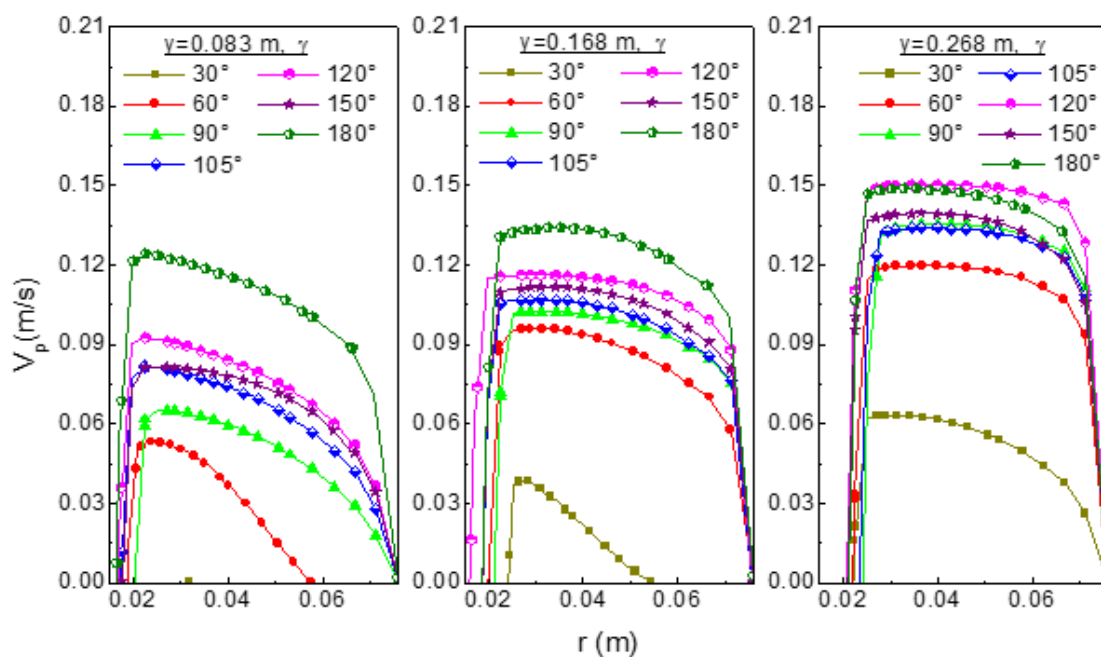


Figure 5-9 Radical profiles of vertical particle velocity in the annulus regions of different beds with $u=42$ m/s and $H_0=0.325$ m

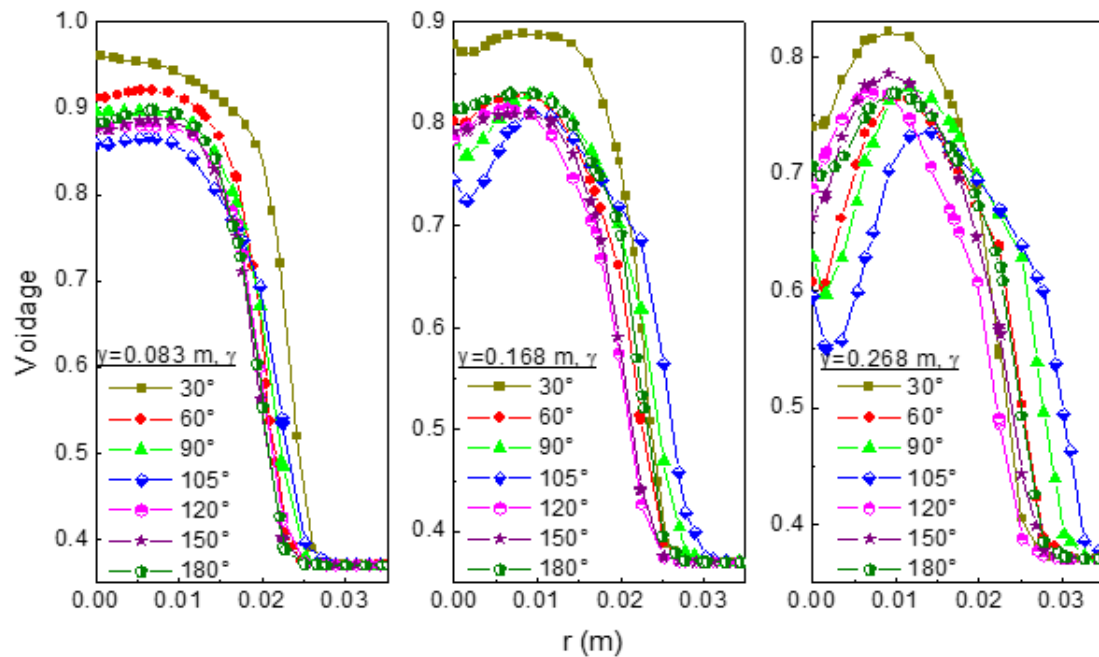


Figure 5-10 Radical profiles of voidage in the spout regions of different beds with $u=42$ m/s and $H_0=0.325$ m

5.3.3 Voidage in the spout

Figure 5-10 shows the simulated radical profiles of voidage in the spouts of different beds under the identical operating conditions of $u=42$ m/s and $H_0=0.325$ m. In every bed, the voidage always increases with decreasing bed level, which means that at the bed level closer to the base region, the local voidage is higher. However, in different spouted beds the degrees of voidage change with the bed level are different. The spouted bed with smaller conical angle meets a more rapid voidage decrease, which means in the spouted bed with wider base, the voidage is relatively more uniform. At identical heights, the spouted bed with 105° conical angle has the smallest voidage. When the conical angle increases or decreases from 105° , the voidage in spout always rises. It simply proves that the spouted bed with 105° angle has the largest particle concentration in the spout.

5.3.4 Diameter of the spout

The diameter of spout, representing the spout shape, is one of the important characteristics of spouted beds. The spout boundary is defined as the positions at which the vertical particle velocity is zero. Figure 5-11 (a) shows the comparison of the

simulated spout boundary with the experimental result of He et al. [45,46] the predicted and experimental spout diameters versus bed depth are in a satisfying agreement, confirming the prediction for spout shape is very reliable. Figure 5-11 (b) shows the predicted spout diameters of various spouted beds. When the conical angle increases from 30° to 105° , the spout diameter continually becomes wider, while when the conical angle is beyond 105° , the spout diameter turns to reduce with the increasing conical angle. When the angle is approximately 105° , the spouted bed has a widest spout diameter.

Combining the results about voidage in 5.3.3 that the spouted bed with 105° conical angle has the largest particle concentration in the spout, it is safe to infer that in the bed with 105° , most of the particles are involved and carried by the gas flow in the bed. With the same gas jetting into the each spouted bed, if more particles are involved and carried by the gas, each particle will receive less momentum from the gas and thus get the smaller velocity. Therefore, the spouted bed with 105° conical angle has the smallest particle velocities and thus the lowest fountain.

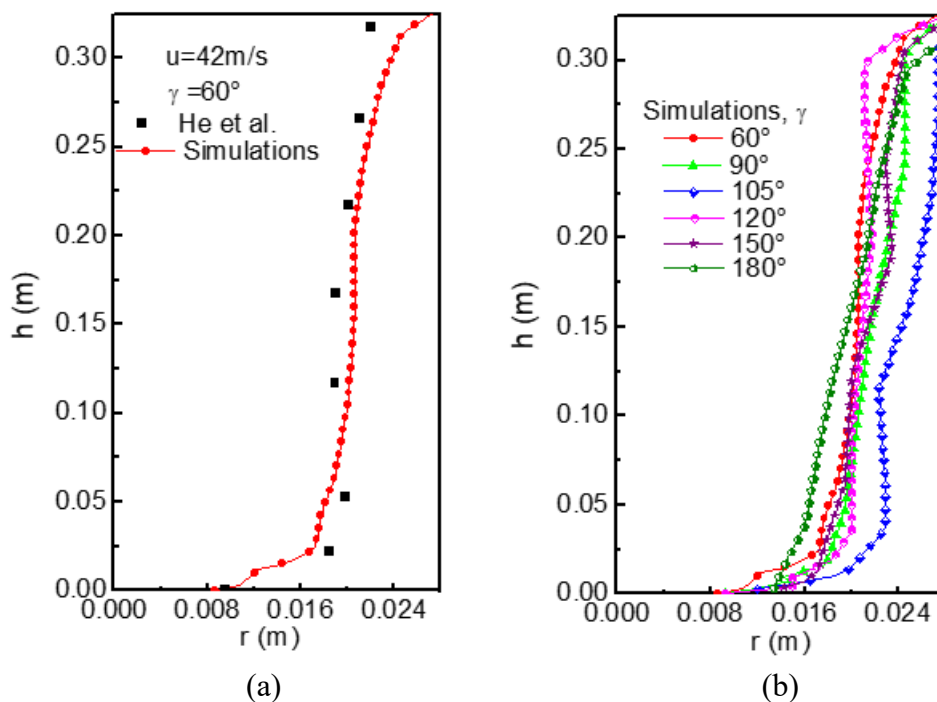


Figure 5-11 The distributions of diameters of spouts: (a) comparison of simulated and experimental results; (b) simulated results

5.4 Interactions of spout jets in a multiple-spouted bed

Multiple-spouted beds in laboratory scale have been proven to be quite effective for gas-solid contacting and mixing, as well as one promising method for the scale-up of spouted beds [1]. However, this spouted bed is still restricted on industrial scale since the interactions between adjacent spout jets may easily lead to serious operation problems [1]. Several studies have been carried out on multiple-spouted beds. For instance, Murthy et al. [29] investigated the minimum spouting velocities in rectangular column beds with different cells. Zhang et al. [51,52] investigated the minimum spouted velocity, maximum spouted pressure drop and maximum spouted height in a double-nozzles rectangular bed with a draft tube. Hu et al. [26] and Ren et al. [28] experimentally studied the flow patterns in multiple-spouted beds. However, as detailed information about flow characteristics in multiple-spouted beds is still unknown, further studies are required to be carried out, especially on the flow patterns and the interactions among spouts.

Furthermore, the interference among spouts, which may lead to the merging of spouts, is one of the problems encountered with multiple-spouted beds. Therefore, full or partial vertical baffles installed at the boundaries between modules are considered as helpful components to reduce short-circulating particles and avoid spouts merging. However, as very few investigations were made on the effects of baffles on flow behaviors in multiple spouted beds till now, the settings of baffles, that is position and height, still require further investigations.

Therefore, in this work, the proposed 3D TFM approach is adopted to study the interactions of spout jets in a multiple-spouted bed. The effects of baffles on the flow behaviors are investigated as well. Numerical computations of this paper are based on the experiments of Ren et al. [28]. The proposed multiple-spouted bed is composed of three spouted bed cells, while each cell has an independent spout nozzle. During the simulations, with varying flow rates through the spout nozzles, the flow patterns, particle velocity and voidage in the beds are investigated with and without baffles.

5.4.1 Properties of objects and numerical parameters

Simulations are based on the experiments of Ren et al. [28] Model structures and corresponding physical parameters are shown in Figure 5-12. The vessel has a cross-section of 300 mm×30 mm and a height of 1000 mm. Detailed descriptions of the experimental parameters can be found in the paper of Ren et al. [28]. Interactions of spout jets with varying central spouting gas flow rates, Q_c , lateral spouting gas flow rates, Q_a , and static spouted height, H_0 , are investigated under the proposed structural conditions. Furthermore, another case is also studied, in which two baffles are set in the bed dividing the bed into three cells (cross-section of 100 mm×30 mm each), as shown in Figure 5-12(b), to evaluate the effects of baffles on flow behaviors. The properties of the particles and fluid, as well as the key numerical parameters are listed in Table 5-4.

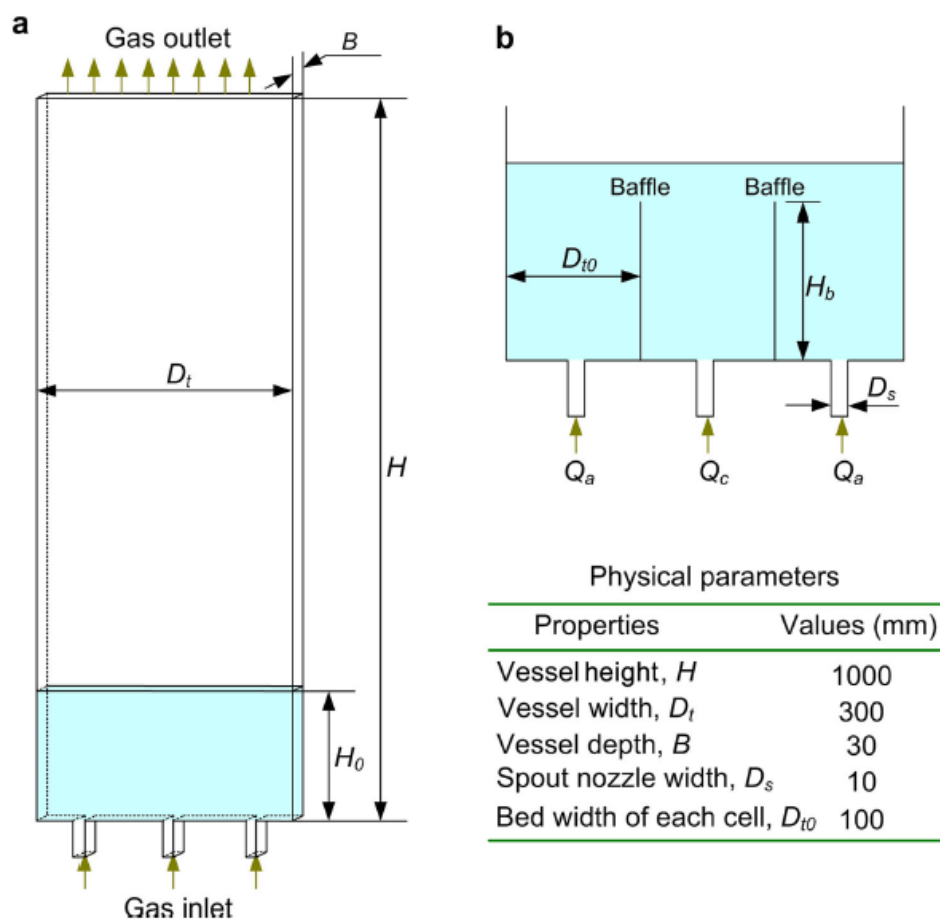


Figure 5-12 Sketch of the simulated beds and corresponding physical parameters

Table 5-4 Physical properties of the objects and numerical parameters [28]

Properties	Value
Particle diameter, d_s (mm)	2.8
Particle density, ρ_s (kg/m ³)	900
Particle bulk voidage, ε_p	0.42
Minimum fluidizing velocity, u_{mf} (m/s)	0.82
Gas density, ρ_g (kg/m ³)	1.225
Gas viscosity, μ_g (Pa/s)	1.7894×10^{-5}
Restitution coefficient, e	0.90
Maximum solid packing volume fraction, $\alpha_{s,max}$	0.59

5.4.2 Effects of central spouting gas flow rate

The effects of increasing the central gas flow rate on the lateral spouting are investigated in this paper when the central gas flow rate, Q_c , ranges from $Q_c/Q_{mf}=1$ to $Q_c/Q_{mf}=3.03$, while other conditions remain the same as $H_0/D_{t0}=1.5$, $Q_a/Q_{mf}=3.03$, where Q_{mf} is the minimum fluidizing flow rate for a cell.

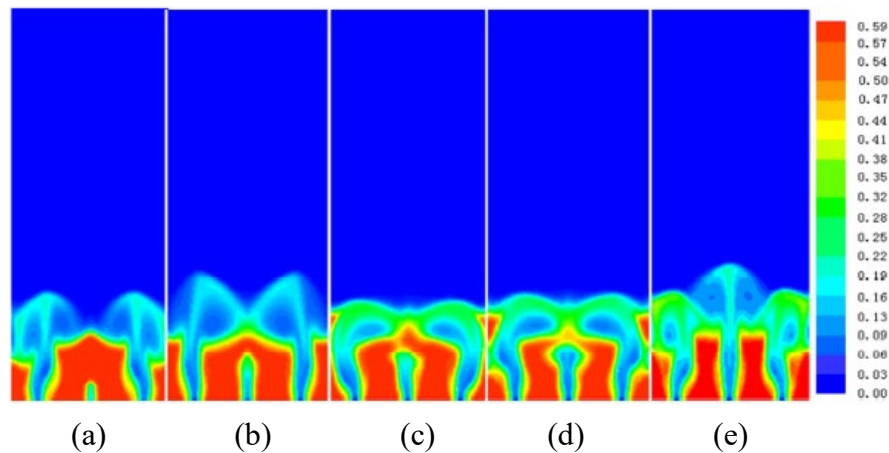


Figure 5-13 Simulated flow patterns with different central gas flow rates ($H_0/D_{t0}=1.0$, $Q_a/Q_{mf}=3.03$): (a) $Q_c/Q_{mf}=1.0$, (b) $Q_c/Q_{mf}=1.5$, (c) $Q_c/Q_{mf}=2.0$, (d) $Q_c/Q_{mf}=2.5$, (e) $Q_c/Q_{mf}=3.03$

Figure 5-13(a) shows the flow pattern in the multiple-spouted bed with the central gas flow rate $Q_c=Q_{mf}$. A void zone is formed above the central nozzle, and the central jet is low as the central gas flow rate is relatively low. Two fountains are generated by lateral

spouting gases, which penetrate the surface of the bed, and the spouts are vertical to the bed. The central spout exerts a very small influence on the development of lateral spouts. The lateral gas throws particles upward and then the particles fall into the central region, which restricts the development of the central jet. Also, the dense zone above the central nozzle exerts a big resistance on the particles, thus the turbulence intensity in the upper bed above the central nozzle is low.

Figure 5-13(b)–(d) indicate that the gradual increase in central gas flow rate attributes to the mutual effect. The lateral fountains bend slightly to the center, most of the particles are thrown towards the central surface of the bed by the lateral spouting gas, suppressing the development of the central spout. Meanwhile, with the increase of Q_c , which is still lower than Q_a , the central jet penetration depth increased. As shown in Figure 5-13(c) and d, when the central spout jet nearly reaches the bed surface, a vortex of particles in the top of the central spout can be seen. The vortex occupies more space in the bed, thus it exerts a push force on the lateral spouts. The lateral spouts tilt slightly towards the wall, with the fountains bending more to the center of the bed. The fountains throw more particles on the central surface of the bed, which in turn suppresses the development of the central jet.

Figure 5-13(e), when the central gas flow rate is high enough, a central fountain can be observed. Three distinct fountains form, respectively, and the central fountain is at its highest. The central fountain develops straight in a vertical direction, while the lateral fountains are somehow distorted. The lateral fountains are suppressed by the central fountain and are interfered with the central fountain, it is become somewhat unstable. The central gas throws particles into the air and some of the particles then fall down into the lateral fountains, restricting the growth of the lateral fountains. The existence of bed walls also exerts resistance on the lateral spouts.

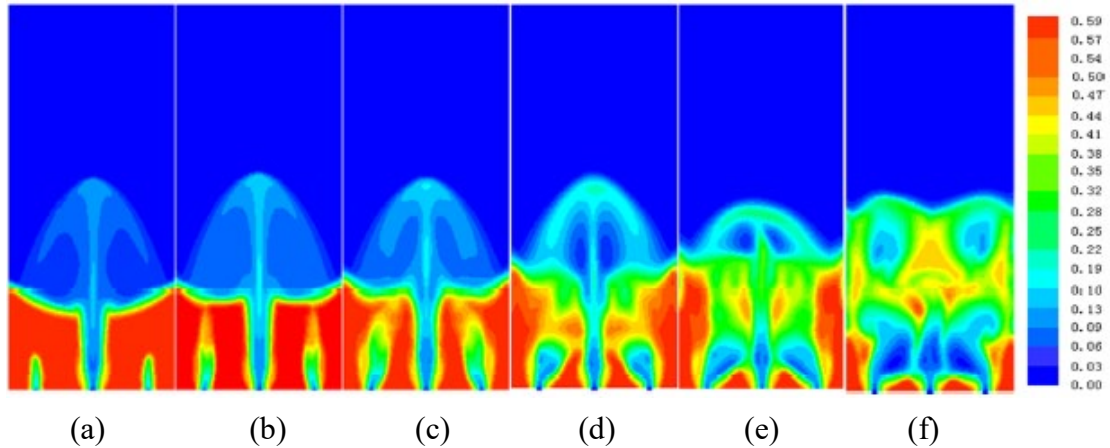


Figure 5-14 Simulated flow patterns with different lateral gas flow rates ($H_0/D_{t0}=1.5$, $Q_c/Q_{mf}=3.6$): (a) $Q_a/Q_{mf}=1.0$, (b) $Q_a/Q_{mf}=1.5$, (c) $Q_a/Q_{mf}=2.0$, (d) $Q_a/Q_{mf}=2.5$, (e) $Q_a/Q_{mf}=3.03$, (f) $Q_a/Q_{mf}=3.6$

5.4.3 Effects of lateral spouting gas flow rate

The effect of the increase of the lateral gas flow rates on the central spouting is investigated in this paper with the lateral gas flow rate, Q_a , ranging from $Q_a/Q_{mf}=1$ to $Q_a/Q_{mf}=3.6$, while other conditions remain the same as $H_0/D_{t0}=1.5$ and $Q_c/Q_{mf}=3.6$.

Figure 5-14 shows the simulated flow patterns with different lateral gas flow rates, which reveals that the variations of lateral flow rates significantly affect the central spout and fountain. When the lateral gas flow rate is low, that is $Q_a/Q_{mf}=1$ and 1.5 , shown in **Figure 5-14(a)** and **(b)**, the central spout is stable and non-pulsating, and the overall bed region can be divided into several parts: a central spout zone, a fountain zone and an annulus zone with two small jets above the lateral nozzles. The heights of the lateral jets increase with increasing lateral gas flow rate.

The increasing lateral spout gas rate exerts an increasing influence on the central spout, which changes the shape of the central spout as well as the flow pattern of the central fountain. With the increase of Q_a , the lateral jets grow and change their directions to merge with the central spout. At higher lateral gas flow rates, that is when $Q_a/Q_{mf}=3$ and 3.6 , the lateral jets reach the bed surface. The gas-solid flow in the bed becomes quite unstable. Small bubbles lift off from the jets because of acute momentum dissipation and then combine into larger bubbles in the middle and on the surface of the bed. When the bubbles grow and periodic slugging occurs, the particles of whole cross-

section start to move up and down, as shown in [Figure 5-14\(f\)](#), significant momentum dissipation is thus aroused.

5.4.4 Effects of the effects of baffles

To deal with flow instability caused by interference among spouts, vertical baffles may be installed in the multiple-spouted beds. In this section, the influences of baffles settled between modules are investigated. Typical flow regimes, that is single spouting (SS) and multi-spouting (MS) in a multiple-spouted bed are studied under conditions with and without baffles. The baffles are installed between modules, extending from the base to the bed surface, and the heights are set at $H_b=1/2H_0$ and $H_b=H_0$. Simulated particle vector field under the above conditions are shown in [Figures 5-15~5-17](#).

(1) double-spouting

[Figure 5-15](#) shows the simulated distribution of the particle vector field with and without baffles under the condition of $H_0/D_{t0}=1$, $Q_a/Q_{mf}=3.03$, $Q_c/Q_{mf}=1.2$. When no baffles are in the bed, as shown in [Figure 5-15\(a\)](#), two stable lateral fountains form. The particle in the lateral region are thrown into the air and then raining back on the annular region, where they slowly travel downward and inward to the lateral spouts. The particle circulations established by the lateral spouting definitely dominate the solid flow in the overall bed. The central spout is noticeably suppressed by the lateral ones, thus only a very small internal jet forms in the central zone.

When two baffles are installed, as shown in [Figures 5-15\(b\)](#) and [\(c\)](#), the bed space is divided into three parts. In [Figure 5-15\(b\)](#), the height of baffles is $H_b=1/2H_0$. Due to the baffles, the particle circulations caused by the lateral gas flows are restrained in the lateral parts of the bed, reducing their suppression on the central spouting. This leads to a better development of the central jet. The central jet penetration depth apparently increases. However, since the height of the baffles is only half the static bed height, the lateral particle circulations still dominate the upper part of the bed, and to some extent, suppress the central spouting. Meanwhile, the increasing central jet has some counter influence on the lateral solid flow, as explained in Flow Patterns Section, resulting in

the lateral spouts leaning slightly to the central spout. In addition, for the lateral spouting, the unbalanced resistances respectively from the bed wall and the shorter baffles are also responsible for the spout bend.

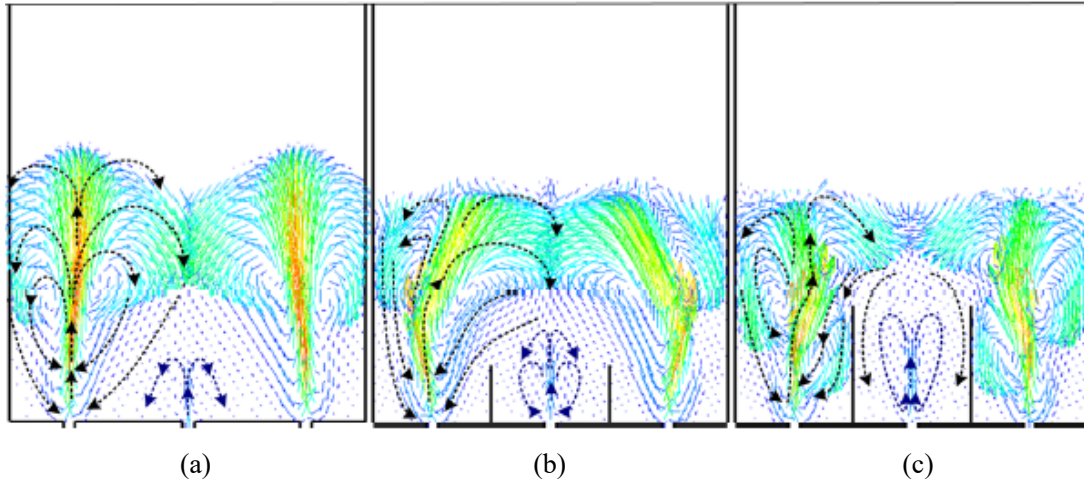


Figure 5-15 Vector fields of particle velocities in the multi-spouted bed with double-spouting mode ($H_0/D_{t0}=1.0$, $Q_c/Q_{mf}=1.2$, $Q_a/Q_{mf}=3.03$): (a) no baffle; (b) $H_b=1/2 H_0$; (c) $H_b=H_0$

In **Figure 5-15(c)**, the height of baffles is equal to the static bed height. Under this condition, the lateral particle circulation developments are restricted and mostly take place in the lateral parts of the bed, and they have a small effect on the central spouting. The central spouting achieves a longer jet penetration depth. Three distinct solid circulations, that is the two lateral external spoutings, and one central internal spout, can be observed in this figure. Comparing with the baffles in **Figure 5-15(b)**, the longer baffles in **Figure 9c** on one hand, avoid the counter influence from the central jet on the lateral spouting, on the other hand, they contribute to the balance of resistances respectively from the bed wall and the baffles. Therefore, the lateral spoutings bend less.

(2) Single-spouting

Figure 5-16 shows the simulated distribution of the particle vector field with and without baffles under the condition of $H_0/D_{t0}=1.5$, $Q_a/Q_{mf}=1.5$ and $Q_c/Q_{mf}=3.6$. When no baffle is installed, as shown in **Figure 5-16(a)**, a single stable central fountain can be observed. The high-velocity central gas flow causes a stream of particles to rise rapidly

in the central spout. These particles are thrown into the air and then rain back on to the annular region, which can be observed as a fountain. In the annular region, they slowly travel downward and inward. However, in the bottom region of the multiple-spouted bed, the particles in the lateral region are inevitably carried by the lateral gas flow and move upward, resulting in a small cavity forming above the lateral nozzle. After all almost all particles are entrained into the central spout. Thus, only one systematic cyclic pattern of the solids movement is established for the single spouting in the overall bed.

When baffles are installed, as shown in Figure 5-16(b) and (c), to complete a circle movement in the overall bed, the particles have to move upward to stride over the baffles. When the baffles are longer, as shown in Figure 5-16(c), the particles perform a longer distance to get back into the central spout, leading to more energy consumption in the overall circulation. In addition, the resistance of the baffles to the particles also increases the system energy consumption. The result is that the height of the central fountain reduces with the increasing of baffle length.

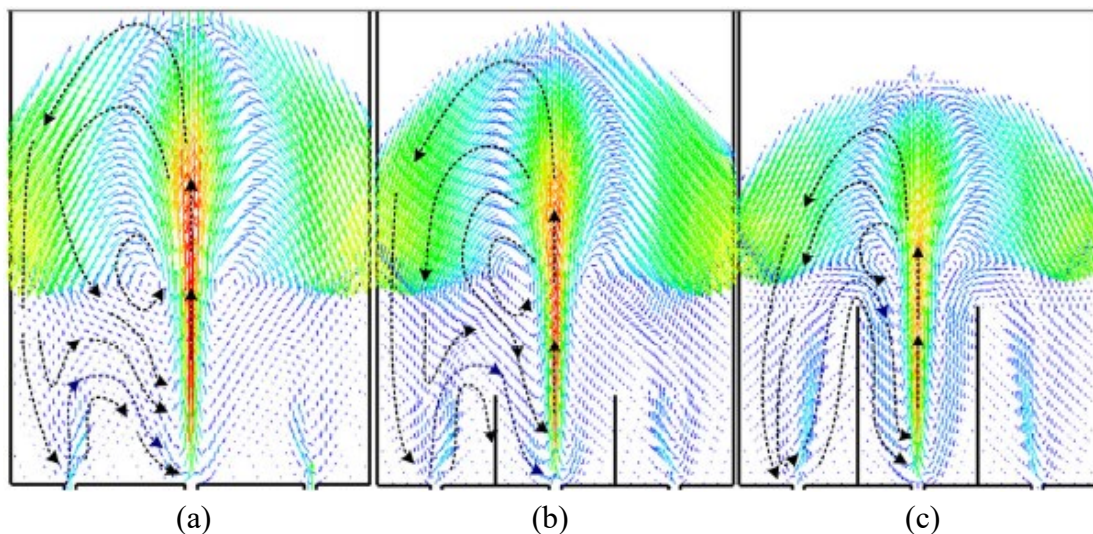


Figure 5-16 Vector fields of particle velocities in the multi-spouted bed with single-spouting mode ($H_0/D_{t0}=1.5$, $Q_c/Q_{mf}=3.6$, $Q_a/Q_{mf}=1.5$): (a) no baffle; (b) $H_b=1/2 H_0$; (c) $H_b=H_0$

(3) Triple-spouting

Figure 5-17 shows the simulated distribution of the particle vector field with and without baffles under the condition of $H_0/D_{t0}=1.0$, $Q_a/Q_{mf}=3.03$ and $Q_c/Q_{mf}=3.03$. When no baffles are installed, as shown in Figure 5-17(a), three stable spoutings can be

observed in the bed, but with the different fountain heights. The central fountain is obviously higher than the lateral ones, although the gas flow rate in the three cells are same. The resistance of the bed wall is considered to hinder the developments of the lateral spoutings, resulting in lower fountain heights. In addition, the particles raining down from the central fountain also suppress the lateral fountains, which further increase the difference of the height between the lateral fountain and the central one. In the overall bed, three distinct particle circulations take place, and the adjacent circulations encounter each other in the upper part of the bed, resulting in the obvious particle mixing in that region.

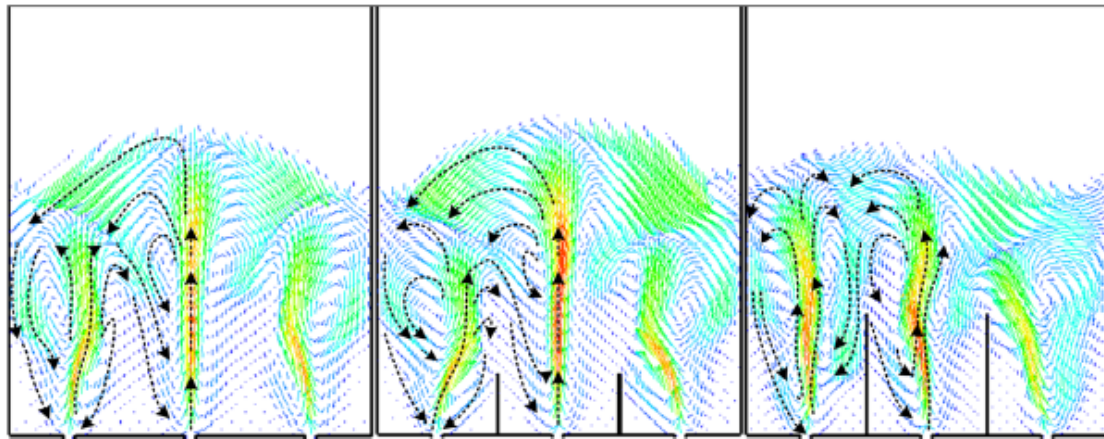


Figure 5-17 Vector fields of particle velocities in the multi-spouted bed with triple-spouting mode ($H_0/D_{t0}=1.5$, $Q_c/Q_{mf}=3.03$, $Q_a/Q_{mf}=3.03$): (a) no baffle; (b) $H_b=1/2 H_0$; (c) $H_b=H_0$

When the short baffles are installed in the bed, as shown in [Figure 5-17\(b\)](#), there is no obvious change in the flow pattern. That is because the short baffles are located in the bottom part of the bed, where the three spouts are independent and little particle mixing take place. Therefore, the short baffles have a small influence on the particle movement. When the longer baffles, with the height equal to H_0 , are installed in the bed, as shown in [Figure 5-17\(c\)](#), the baffle is long enough to affect the particle movement in the upper part of the bed, leading to apparent changes in the flow pattern. The baffles divide the bed into three equal spaces, and the central spouting also suffers the resistance from the wall as the lateral spoutings does. Thus three similar external spoutings take place in the bed and the difference in fountain heights almost disappear. However, the adjacent

fountains encounter in the region above the baffles and the interactions of fountains such as impacting and squeezing caused the fountains to be unstable.

5.5 Prediction of minimum spouting velocity by TFM

The minimum spouting velocity is a key hydrodynamic characteristic to design, operate and scale up spouted bed reactors. From previous studies [54-59] many experimental and theoretical methods have been applied to obtain a proper definition of the minimum spouting velocity, including the well-known Mathur and Gishler equation [54], as well as other empirical correlations. These correlations give approximate predictions of minimum spouting velocity based on experimental data from relatively small columns ($D < 0.5$ m). However, most existing correlations are restricted to a limited range of column dimensions and properties of gas and particles. Furthermore, almost all existing correlations fail to predict the minimum spouting velocity when spouted beds are scaled up. Accurate determination of the minimum spouting velocity is still one of the crucial unsolved problems in large spouted beds. The objective of the current study was to apply the TFM approach to predict the minimum spouting velocity of spouted beds. One group of three-dimensional models for simulating spouted beds is presented, and the determination of minimum spouting velocity is proposed based on TFM modeling.

5.5.1 Determination of minimum spouting velocity

The evolution of a spouted bed normally includes cavity formation, internal spout expansion and formation of an external spout with increasing fluid flow. According to previous work, compared with the process of increasing gas velocity, external spouting can be maintained at a significantly lower gas velocity when the superficial gas flow rate is decreased from stable spouting, that is, in the flow descending process where the “breakup” force does not exist. The gas velocity corresponding to the point at which stable external spouting collapses is used to demarcate minimum spouting and hence to determine the minimum spouting velocity. Thus, in the present work, the simulated minimum spouting state, solids distribution and particle vector field are obtained from visual observation with descending flow.

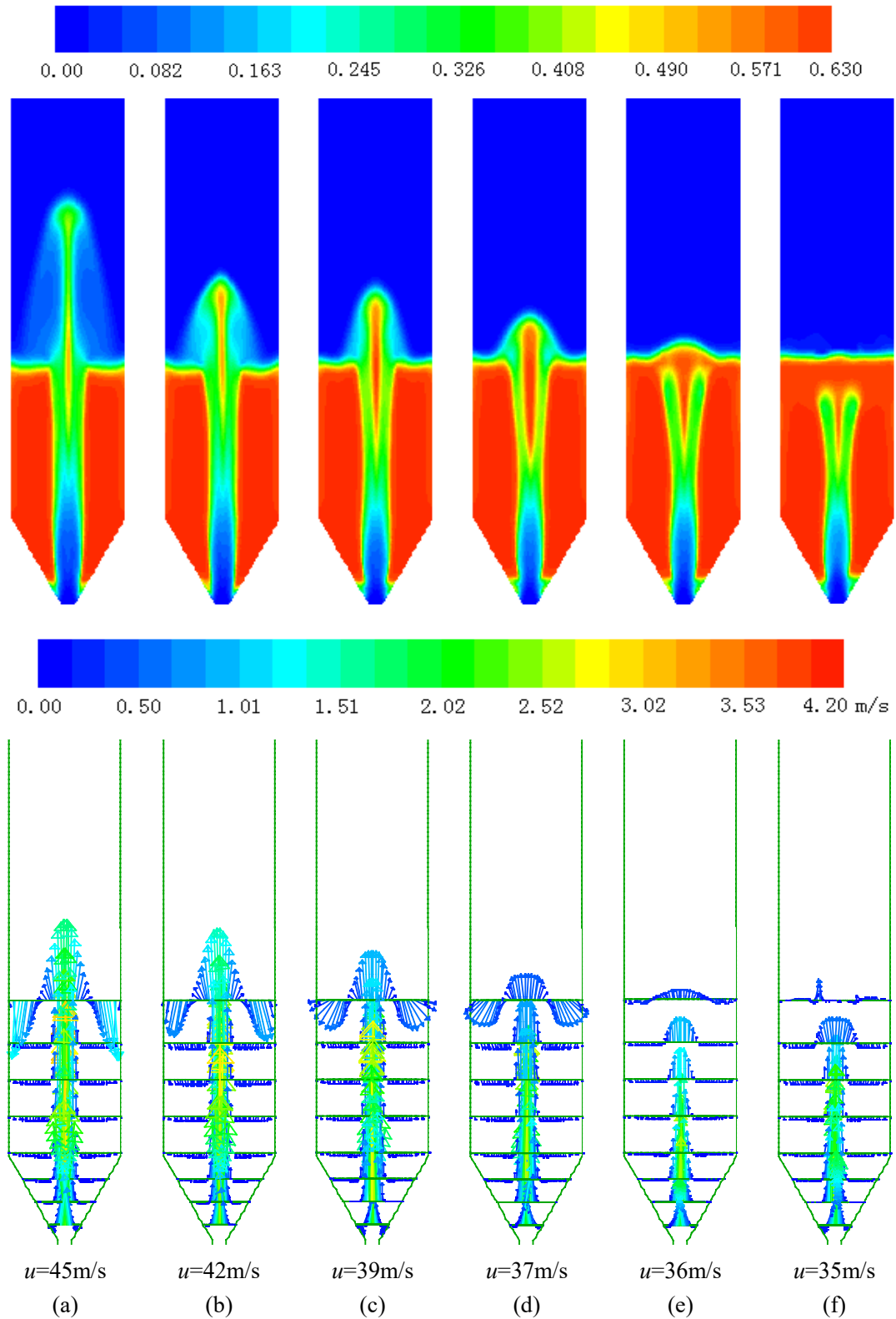


Figure 5-18 Simulated distribution of solids volume fraction and particle vector field versus superficial gas velocity for conical-cylindrical spouted bed ($e=0.88$, $\alpha_{s,\max}=0.63$, $d_s=1.41$ mm, $H_0=325$ mm, $D_i=19$ mm, $D_c=152$ mm)

Both the inlet minimum spouting velocity, u_{ms} , and the superficial minimum spouting velocity, U_{ms} , can describe the minimum spouting states. These two variables are related by $u_{ms} = (D_c/D_i)^2 U_{ms}$. In the present simulated work, u_{ms} values are directly obtained from the simulations, and hence most of the following discussion is based on u_{ms} .

Figure 5-18 reveals the patterns of the fixed solids volume fraction and particle vector fields for different inlet gas jetting velocities, u , leading to identification of the minimum spouting condition. In each case, $d_s = 1.41$ mm, $\rho_s = 2503$ kg/m³, $H_0 = 325$ mm, $D_i = 19$ mm and $D_c = 152$ mm, to match the experimental conditions of He et al. [45, 46]. In Figure 5-18, the steps to predict u_{ms} are as follows:

- (1) Firstly, the superficial minimum spouting velocity, U_{mse} , is estimated by the Mathur-Gishler equation [54]. In our case, $U_{mse} = 0.531$ m/s and the corresponding inlet minimum spouting velocity is $u_{mse} = 34$ m/s.
- (2) To ensure stable external spouting, $u = c \cdot u_{mse}$ is applied to start the simulation, and for the current small column $c = 1.2-1.5$. The resulting solids volume fraction and particle vector field are shown as event (a). There are some indications that for large spouted beds, $c = 1.5-2.0$ is required.
- (3) The gas jet velocity is gradually decreased until the external spouting totally collapses. The processes are described as events (b) to (f).
- (4) The gas velocity corresponding to the point at which stable external spouting collapses is defined as the simulated u_{ms} , represented by event (e).

The above steps are summarized in Figure 5-19. The same procedures were adopted to identify u_{ms} for the other conditions in Table 5-5.

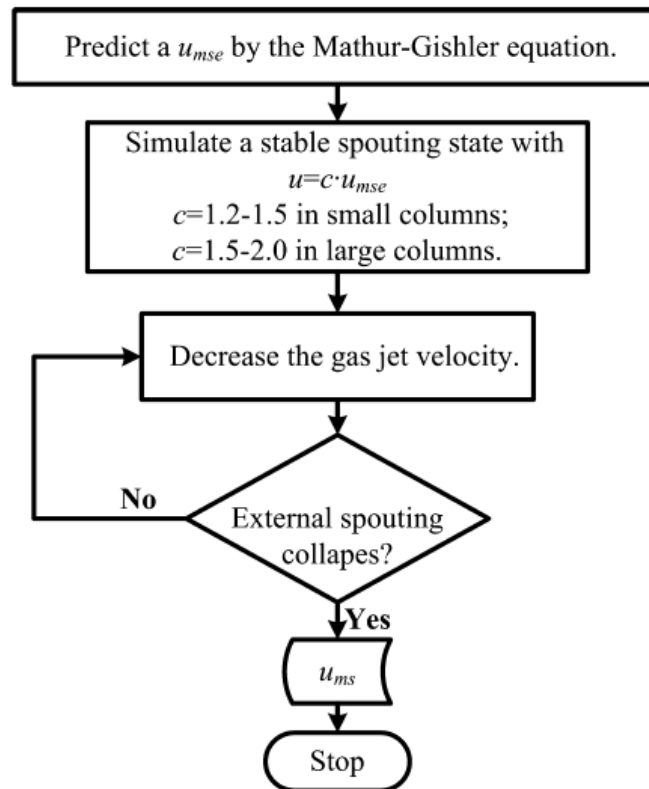


Figure 5-19 Flow sheet for identification of minimum spouting velocity u_{ms} in flow descending process

5.5.2 Approach evaluation

In a typical conical-cylindrical spouted bed, the minimum spouting velocity depends on the dimensions D_c , D_i , H_0 , as well as the gas and particle properties. Some equations [54,56,58,59] for U_{ms} based on experimental or theoretical efforts of previous researchers are listed in Table 5-6. Predictions of these equations are compared below with values predicted by the CFD technique.

Table 5-5 Physical properties of the objects and numerical parameters

properties	value
Particle diameter, d_s (mm)	1.0, 1.4, 1.8, 2.2, 2.6, 3.0, 3.4, 3.8, 4.2
Static bed height, H_0 (mm)	300, 350, 400, 450, 500, 550, 600
Diameter of the bed, D_c (mm)	152
Diameter of the spout gas inlet, D_i (mm)	25.33, 21.71, 19.00, 16.89, 15.20
Total bed height, H (mm)	815
Angle of conical bottom, γ ($^\circ$)	60

Particle density, ρ_s (kg/m ³)	2503
Gas density, ρ_g (kg/m ³)	1.225
Gas viscosity, μ_g (Pa/s)	1.7894×10^{-5}
Restitution coefficient, e	0.88
Maximum solid packing volume fraction, $\alpha_{s,max}$	0.63
Numerical time interval, Δt (s)	5×10^{-5}

Table 5-6 Empirical equations for U_{ms} in conical-cylindrical spouted bed

Authors	correlations
Mathur and Gishler ^[54]	$U_{ms} = \left(\frac{d_s}{D_c} \right) \left(\frac{D_i}{D_c} \right)^{1/3} \sqrt{\frac{2gH_0(\rho_s - \rho_g)}{\rho_g}}$
Choi and Meisen ^[58]	$U_{ms} = 18.5 \left(\frac{\rho_s - \rho_g}{\rho_g} \right)^{0.263} \left(\frac{H_0}{D_c} \right)^{-0.193} \left(\frac{d_s}{D_c} \right)^{1.19} \left(\frac{D_i}{D_c} \right)^{0.373} \sqrt{2gH_0}$
Anabtawi et al. ^[56]	$U_{ms} = 2.44 \left(\frac{d_s}{D_c} \right)^{0.7} \left(\frac{D_i}{D_c} \right)^{0.58} \left(\frac{H_0}{D_c} \right)^{0.5} \left(\frac{2gH_0(\rho_s - \rho_g)}{\rho_g} \right)^{0.28}$
Uemaki et al. ^[59]	$U_{ms} = 0.977 \left(\frac{d_s}{D_c} \right)^{0.615} \left(\frac{D_i}{D_c} \right)^{0.274} \left(\frac{2gH_0(\rho_s - \rho_g)}{\rho_g} \right)^{0.324}$

5.5.2.1 Effect of particle diameter, d_s

Detailed comparisons of the inlet minimum spouting velocities, u_{ms} , simulated by the CFD approach and calculated from empirical correlations are shown in Figure 5-20, with particle diameters varying from 1.0 to 4.2 mm. The physical parameters of the spouted bed are included cone angle $\gamma=60^\circ$, $H_0=325$ mm, $D_i=19$ mm and $D_c=152$ mm. In Figure 5-20, it is clear that u_{ms} increases with increasing particle diameter. The simulated values from the proposed CFD approach are in best agreement with the widely used equation of Mathur and Gishler [54], with an average absolute deviation (AAD) of only 4.2%. The equation of Choi and Meisen [58] shows a higher AAD of 10.7%.

Referring to Figure 5-20, it is noteworthy that in the particle diameter range from 1.0 mm to approximately 2.6 mm, the simulated u_{ms} agrees quite well with the results of

the Choi-Meisen equation. However, with further increase of d_s , the simulated inlet gas jetting velocities are in excellent agreement with the Mathur-Gishler equation, while deviations from the Choi-Meisen equation increase significantly. The equation of Uemaki et al. [59] is for binary mixtures of particles differing in size, with $u_{ms} \propto d_s^{0.615}$, where d_s is the Sauter mean diameter.

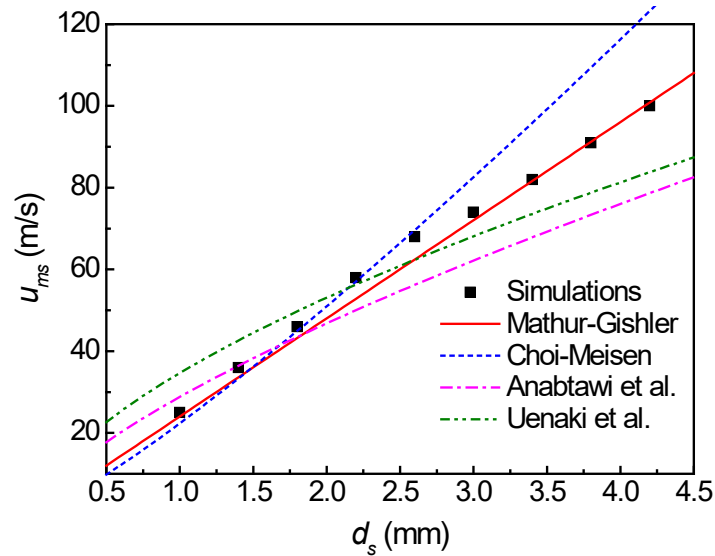


Figure 5-20 Comparisons of simulated variation of u_{ms} with d_s to predictions by empirical equations

Compared with Mathur-Gishler equation and Choi-Meisen equation, the u_{ms} values calculated by the equation of Uemaki et al. give values of d_s which are significantly higher than the simulated results for the smaller particles, and much lower for the larger particles, as shown in Figure 5-20. The AAD of the Uemaki equation is 14.9%. The correlation from Anabtawi et al. [56] for a spouted bed was developed by in conjunction with an experimental study on a square spout-fluid bed, resulting in $u_{ms} \propto d_s^{0.7}$. The Anabtawi equation displays a very similar tendency to the Uemaki equation, but with consistently smaller values of u_{ms} . Thus the Anabtawi equation also shows considerable deviation from the simulated results, with an AAD of 14.1%.

5.5.2.2 Effect of static bed height, H_0

The simulated and calculated results of u_{ms} are shown in Figure 5-21 as a function of

static bed height. The static bed heights simulated in this work varied from 0.30 to 0.60 m, while the other physical parameters of the spouted bed were kept constant at $d_s=1.41$ mm, $D_i=19$ mm and $D_c=152$ mm.

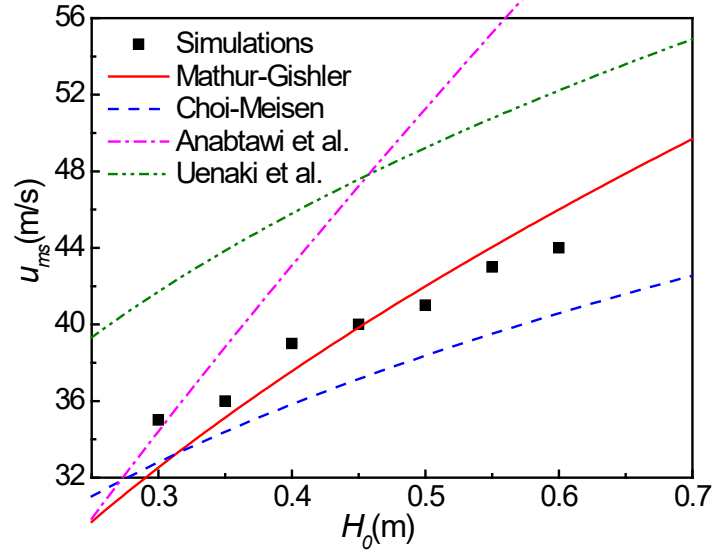


Figure 5-21 Comparisons of simulated variation of u_{ms} with H_0 to predictions by empirical equations

The simulated u_{ms} values are in good agreement with the Mathur-Gishler[54] predictions, the AAD between them being 3.3%. The simulated distribution trend of u_{ms} is similar to that of Choi and Meisen [58], but the simulated values are always higher than the predictions, with an AAD of 6.9%. The equations of Uemaki et al. [59] and Anabtawi et al. [56] show large differences from those of Mathur-Gishler and Choi-Meisen, as well as significant deviations from the simulation results. The average absolute deviation between the CFD simulated results and the Anabtawi equation is as large as 18.0%. Moreover, u_{ms} by the Anabtawi equation is proportional to $H_0^{0.78}$, which indicates a more rapid rise of u_{ms} with H_0 than any other predictions in Figure 5-21. This deviation may be due to the fact that the Anabtawi equation is based on a square spouted bed, whereas the current study is based on a conical-cylindrical bed. The Uemaki equation is primarily for binary mixtures of particles differing in size, and leads to an average, consistently positive deviation of 19.2% from the simulation results.

5.5.2.3 Effect of fluid inlet diameter, D_i

In order to reach the stable spouting state throughout the column, the optimum ratio of D_c/D_i is suggested to range from 6 to 10, with the maximum ratio less than 12 to avoid dead regions. Therefore, in the present simulation, u_{ms} has been obtained with D_c/D_i varied from 6 to 10, achieved by varying D_i from 25.33 to 15.20 mm, while keeping D_c constant at 152 mm. The other fixed parameters are $d_s=1.41$ mm and $H_0=325$ mm.

The simulated and empirical results are compared in Figure 5-22.

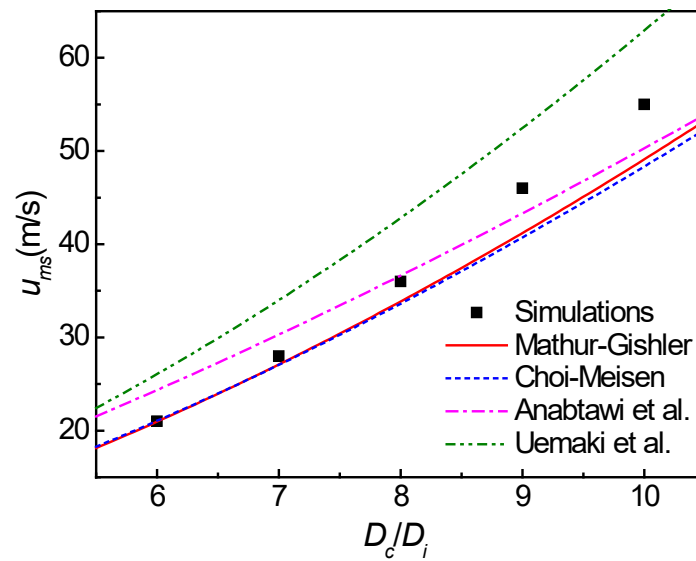


Figure 5-22 Comparisons of simulated variation of u_{ms} with D_c/D_i to predictions by empirical equations

The predictions from the Mathur-Gishler equation and Choi-Meisen equation show very little difference with varying D_c/D_i . Both are in good agreement with the simulations, with AADs of 6.1% and 6.8%, respectively. However, the simulated values of u_{ms} exceed the predictions from the two equations more and more as D_c/D_i increases. u_{ms} from the Mathur-Gishler equation is proportional to $(D_c/D_i)^{1.67}$ at constant D_c , while the Choi-Meisen, Anabtawi and Uemaki equations show $u_{ms} \propto (D_c/D_i)^{1.63}$, $u_{ms} \propto (D_c/D_i)^{1.42}$ and $u_{ms} \propto (D_c/D_i)^{1.73}$, respectively. Compared with the predictions by Mathur and Gishler, Choi and Meisen, and Anabtawi et al., the simulations reveal a more rapid rise with increasing D_c/D_i , which is qualitatively similar to the trend shown by the Uemaki et al. predictions, but with quantitatively smaller values of u_{ms} .

The above results indicated that the current CFD (TFM) approach can achieve the comparable accuracy with the well-recognized and widely used Mathur-Gishler correlation to predict the minimum spouting velocity of spouted beds with a wide range of operating conditions and particle properties, which shows the high reliability of TFM approach in the studies of spouted beds.

5.6 Hydrodynamic characteristics of the scaling spouted bed

Many experimental and theoretical investigations have been carried out on small-scale spouted beds in the past 50 years, providing many correlations and models to predict the hydrodynamic parameters in small-scale spouted bed vessels. However, existing correlations and models based on small-scale spouted bed vessels are unable to give accurate predictions when applied to large-scale spouted bed vessels. For example, the well-known minimum spouting velocity equation of Mathur and Gishler [54] was shown to become increasingly unsatisfactory as the vessel diameter exceeded about 0.4 m. Lim and Grace [8] also indicated that the equation gave poor predictions of the minimum spouting velocity for the 0.91 m diameter vessel tested in their work. There has been little hydrodynamic study on commercial-scale spouted beds until now. As a result, there are no reliable hydrodynamic models or correlations for large columns, nor are there any established procedures to scale up spouted beds. To apply spouted beds in industrial processes, scale-up studies are of great importance.

As discussed above, dimensional similitude is often employed to scale up spouted beds and obtain data on large-diameter vessels, but it works well only when all dimensionless groups are closely matched. Mismatching the dimensionless groups, even one or two of them, can lead to significant disagreement. However, the number of dimensionless groups to be matched is large enough that it is very difficult to match all of them. Moreover, in most industrial processes, the particle properties and fluid properties are almost fixed or can only be changed in narrow ranges, making it extremely difficult or impossible to match all important independent dimensionless groups. Given this situation, an alternative scale-up procedure, i.e., considering a series of columns of

identical geometry, but different scales, for spouting of the same material becomes promising for complex spouted bed processes. However, this approach does not appear to have received much attention in the spouted bed literature. In this case, scale-up based on numerical simulation is promising.

In the present work, numerical simulations based on the three-dimensional CFD (TFM) approach were carried out to study the minimum spouting velocities of spouted beds of different scale. The spouted bed with a diameter of 0.152 m from the experiments of He et al. [45,46] is scaled up from 0.304 to 1.216 m. The effects of static bed height, particle diameter and density, and fluid inlet diameter on the minimum spouting velocity in different size beds were investigated numerically. A new correlation is developed for the prediction of u_{ms} in both small and large beds.

5.6.1 Typical flow patterns

Figure 5-23 shows the typical instantaneous flow patterns in columns of seven different sizes for $H_0/D_c=2$, $d_s=2.8$ mm, $\rho_s=2503$ kg/m³ and $D_c/D_i=8$.

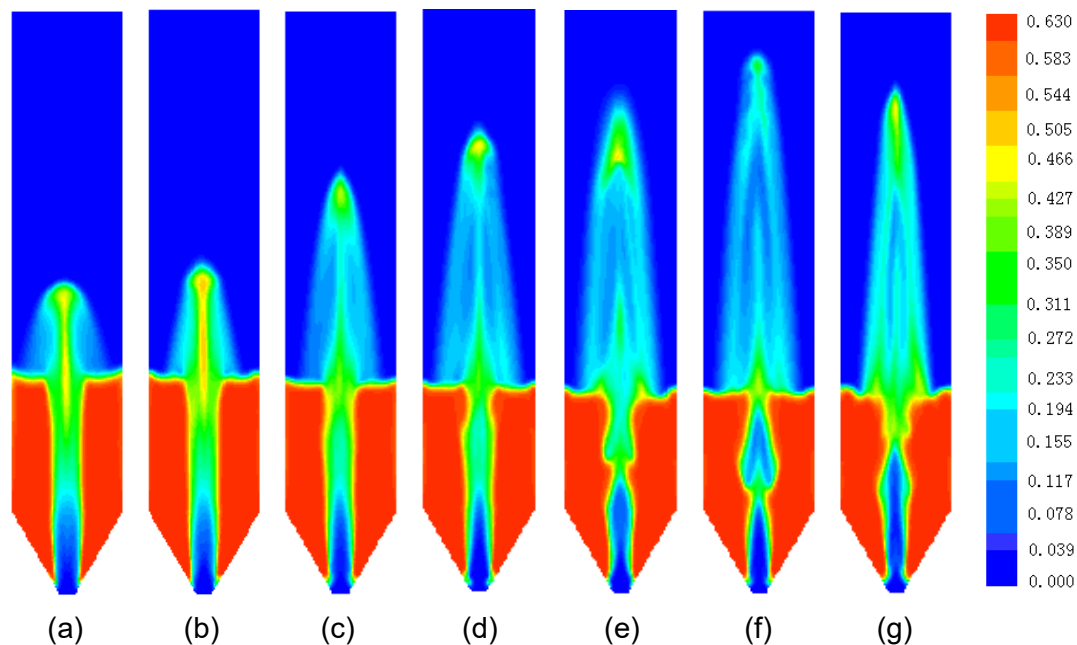


Figure 5-23 Typical flow patterns in spouted beds of seven different scales, all with $H_0/D_c=2.0$, $d_s=2.8$ mm, $\rho_s=2503$ kg/m³, $D_c/D_i=8$): (a) $D_c=0.304$ m, $u=71$ m/s; (b) $D_c=0.456$ m, $u=66$ m/s; (c) $D_c=0.608$ m, $u=62$ m/s; (d) $D_c=0.760$ m, $u=59$ m/s; (e) $D_c=0.912$ m, $u=58$ m/s; (f) $D_c=1.064$ m, $u=57$ m/s; (g) $D_c=1.216$ m, $u=54$ m/s.

In small columns ($D_c=0.304, 0.456, 0.608$ and 0.760 m) permanent and stable external spouting can be established, and the spout, annulus and fountain can be clearly observed when the gas flow rate is high enough, while stable spouting gradually becomes difficult when the column is enlarged. As a result, when the column size is larger than 760 mm, the spout becomes unstable, with variations in spout diameter as instabilities appear and grow at the interface between the spout and annulus. Corresponding values of D_i/d_p show that the instability appeared for this ratio greater than ~ 25 to 30 , consistent with earlier work by Chandnani and Epstein [18].

5.6.2 Effects of key parameters on the minimum spouting velocity in scaling

A series of numerical simulations was performed to determine the minimum spouting velocities in spouted beds of different sizes. The effects of particle properties, operating and geometric parameters on the minimum spouting velocity were investigated as the columns were scaled up at identical dimensionless conditions, i.e., constant $u/u_{ms}, H_0/D_c$ and D_c/D_i . The conditions for the simulations are specified in Table 5-7 for varying d_s .

(1) Effect of particle diameter

The simulated conditions with varying d_s are listed in Table 5-7. Changes of u_{ms} with varying d_s for column diameter ranging from 0.304 to 1.216 m are presented in Figure 5-24. Both simulated data and predictions derived from the Mathur and Gishler equation [54] (M-G equation) are given in this figure. For the spouted bed column with certain size, the diameter of particles varies from 2.8 to 4.0 mm while the other operating conditions are maintained as $H_0/D_c=2, \rho_s=2503$ kg/m³ and $D_c/D_i=8$.

The simulated results show that u_{ms} in each column always increases with increasing d_s . As the column diameter is scaled up, the increase of u_{ms} with increasing d_s is less obvious. The simulated effect of d_s on u_{ms} is similar to the predictions of the M-G equation, while the simulated u_{ms} values are always larger than the corresponding M-G predictions. Previous experiments [7,8] have also demonstrated that the M-G equation tends to underestimate the minimum spouting velocity in large-scale spouted beds.

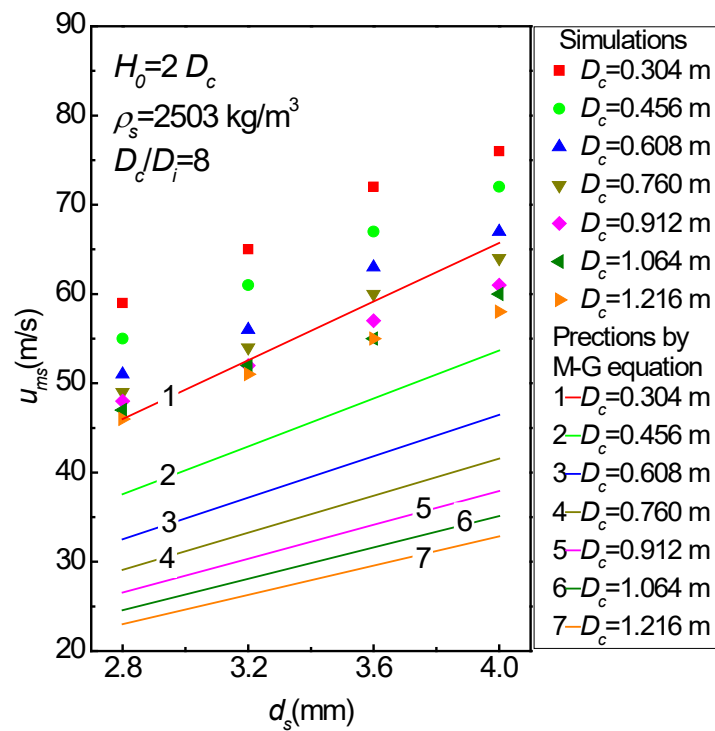


Figure 5-24 Changes of u_{ms} with varying d_s for columns of different diameter

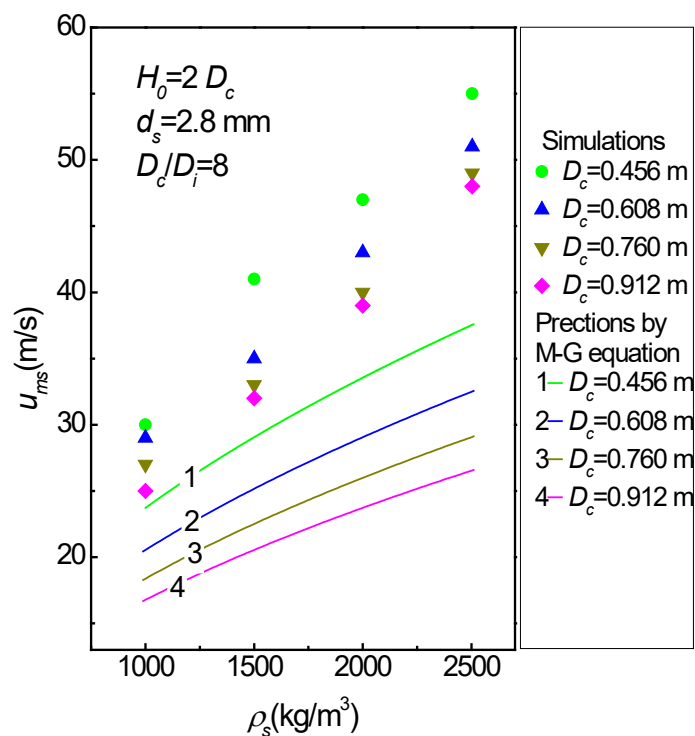


Figure 5-25 Changes of u_{ms} with varying ρ_s for columns of different diameter

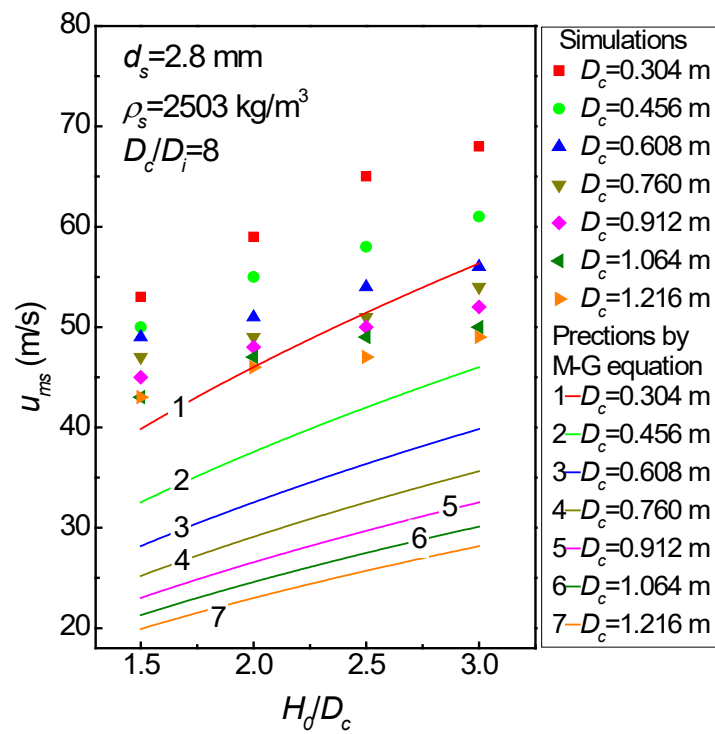


Figure 5-26 Changes of u_{ms} with varying H_0/D_c for columns of different diameter

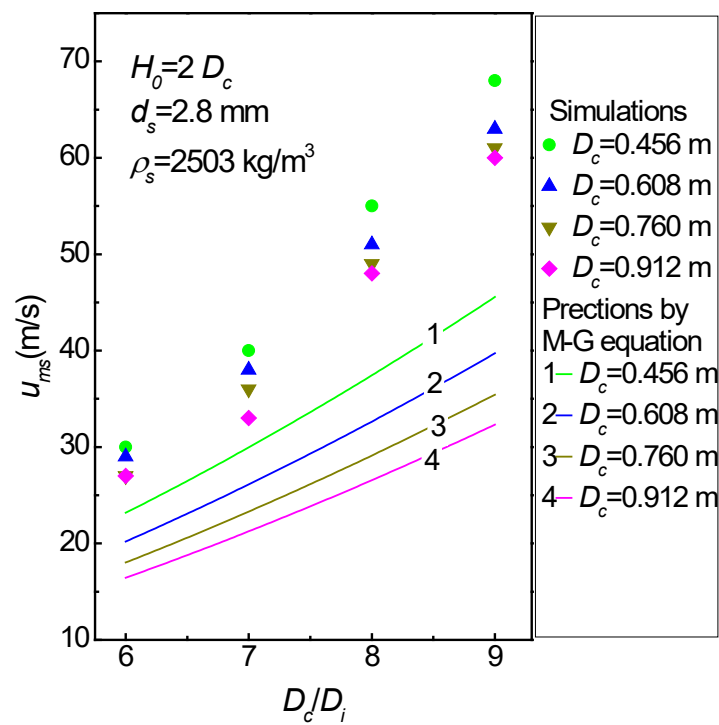


Figure 5-27 Changes of u_{ms} with varying D_c/D_i for columns of different diameter

(2) Effect of particle density

Figure 5-25 shows changes of u_{ms} with the particle density, ρ_s , varying from 1,000 to 2,503 kg/m³ and D_c from 0.456 to 0.912 m, while the other operating conditions remain $d_s=2.8$ mm, $H_0/D_c=2$, $D_c/D_i=8$. As the particles become denser, the minimum air velocity required to spout them is higher. In larger columns, ρ_s has a somewhat more significant effect on u_{ms} .

(3) Effect of static bed height on u_{ms}

Figure 5-26 shows changes of u_{ms} in seven columns of different diameters when the height-diameter ratio, H_0/D_c , varies from 1.5 to 3 in every column, while the other conditions are kept as $d_s=2.8$ mm, $\rho_s=2503$ kg/m³ and $D_c/D_i=8$. The simulations show that when $D_c \leq 0.760$ m, u_{ms} increases with increasing static bed height in each column, with the trend being similar to the predictions of the M-G equation. When D_c is further scaled up from 0.760 m, the change of u_{ms} with the increasing H_0 becomes less obvious, i.e., u_{ms} becomes less sensitive to H_0 in large spouted beds.

(4) Effect of fluid inlet diameter on u_{ms}

Changes of u_{ms} in four columns of different diameters are shown in Figure 5-27 with D_c/D_i varying from 6 to 9 and the other operating conditions unchanged at $d_s=2.8$ mm, $\rho_s=2503$ kg/m³ and $H_0/D_c=2$. In each column, as D_c/D_i increases, i.e., for smaller D_i , u_{ms} increases rapidly. In the larger spouted beds, this trend appears to become more obvious. However, the superficial minimum spouting velocity, U_{ms} , (equal to $(D_i/D_c)^2 u_{ms}$), changes little as D_i varies. That is to say, in larger-scale spouted beds, when D_c is fixed, D_i has a remarkable effect on the inlet minimum spouting velocity, but little effect on the superficial minimum spouting velocity.

5.6.3 Development of a new correlation

In order to find the dependency of u_{ms} on d_s , ρ_s , H_0 and D_i for all D_c , the simulated u_{ms} values were correlated in power law format of these parameters. The results are shown in Figure 5-28.

In Figure 5-28 (a), with the exponents on d_s and D_c of 0.8 and 0.23, respectively, all

simulated u_{ms} values for different size columns fall approximately on one line. Thus, during the process of spouted bed scale-up, with other operating parameters maintained constant, u_{ms} varies with $d_s^{0.8} / D_c^{0.23}$. Similarly, Figures 5-28 (b), (c) and (d) show that u_{ms} is respectively proportional to $[(\rho_s - \rho) / \rho]^{0.67} / D_c^{0.23}$, $(H_0 / D_c)^{0.3} / D_c^{0.23}$ and $(D_c / D_i)^{1.98} / D_c^{0.23}$, with other operating parameters held constant. With these correlation indices, a new dimensional correlation is:

$$u_{ms} = 0.40 \left(\frac{d_s^{3.48}}{D_c} \right)^{0.23} \left(\frac{H_0}{D_c} \right)^{0.3} \left(\frac{D_c}{D_i} \right)^{1.98} \left(\frac{\rho_s - \rho_g}{\rho_g} \right)^{0.67} \quad (5-1)$$

with d_s and D_i in meters and u_{ms} in m/s.

Substitution of $U_{ms} = u_{ms} (D_i / D_c)^2$, then gives:

$$U_{ms} = 0.40 \left(\frac{d_s^{3.48}}{D_c} \right)^{0.23} \left(\frac{H_0}{D_c} \right)^{0.3} \left(\frac{D_i}{D_c} \right)^{0.02} \left(\frac{\rho_s - \rho_g}{\rho_g} \right)^{0.67} \quad (5-2)$$

Note that the 0.02 index is so small that (D_i / D_c) term can be ignored in many cases.

Therefore, Equation (5-2) can be approximate to:

$$U_{ms} = 0.38 \left(\frac{d_s^{3.48}}{D_c} \right)^{0.23} \left(\frac{H_0}{D_c} \right)^{0.3} \left(\frac{\rho_s - \rho_g}{\rho_g} \right)^{0.67} \quad (5-3)$$

It must be emphasized again that H_0 / D_c in the current simulations only varies between 1.5 and 3. Simulations indicate that when H_0 / D_c is smaller than 1.5, the dependence of u_{ms} on H_0 changes significantly, as has been observed by He et al. [7]. Therefore, it is very difficult for a single correlation to describe such different dependences. Predictions for $H_0 / D_c < 1.5$ are currently unavailable and require further study in the future. In addition, the new correlation was developed for spouted beds with fixed conical base angle of 60° , and takes no account of the influence of variations in conical section geometry.

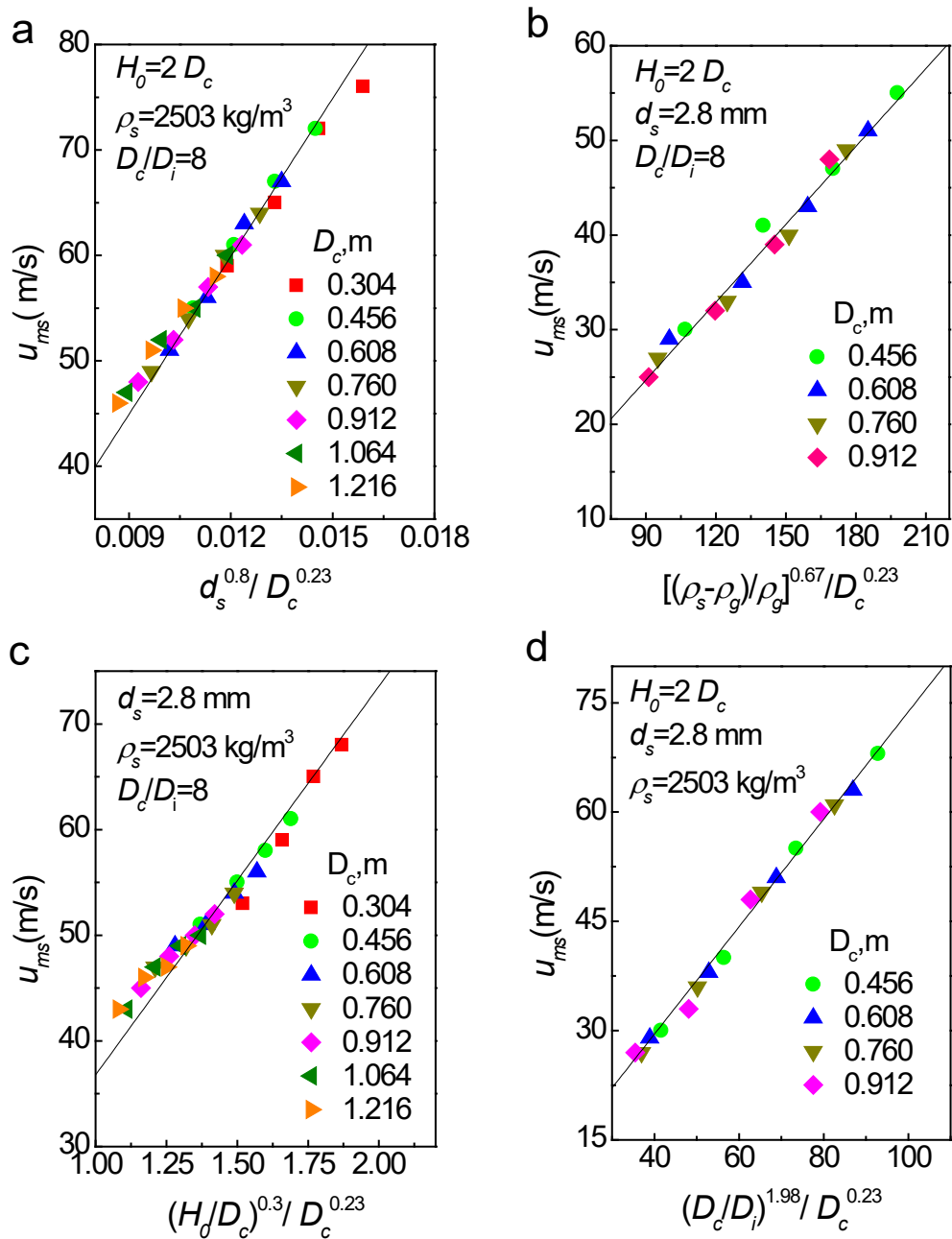


Figure 5-28 Comparison of simulated data with: (a) correlation between u_{ms} and d_s ; (b) correlation between u_{ms} and ρ_s ; (c) correlation between u_{ms} and H_0 ; (d) correlation between u_{ms} and D_c/D_i

Some experimental data were used to evaluate the new correlation. Figure 5-29(a) compares u_{ms} predicted by Equation (5-1) and the experimental data from several researches [5,8,56,58]. Favorable agreement is achieved in most cases, with most deviations $<20\%$ and almost all deviations within $\pm 35\%$. The average deviation is approximately 11.6% . Figure 5-29 (b) compares U_{ms} predicted by the Equation (5-3) and the experimental data. Good agreement is again observed.

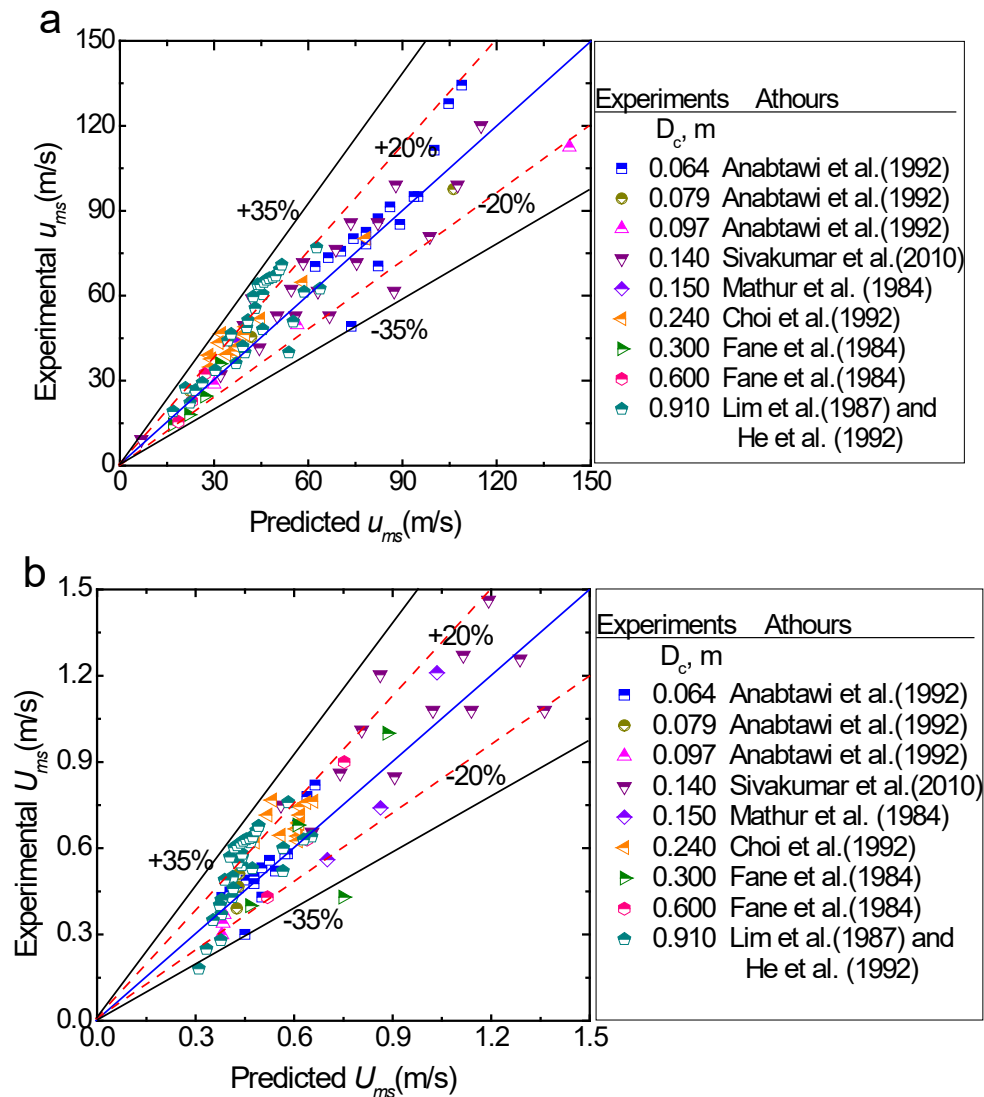


Figure 5-29 Comparisons of predictions from correlations and experimental data: (a) the inlet minimum spouting velocity, u_{ms} , and Equation (5-1); (b) the superficial minimum spouting velocity, U_{ms} , and Equation (5-3)

In the small columns ($D_c=0.064, 0.079, 0.097, 0.140$ and 0.150 m), the predicted u_{ms} are in very good agreement with the experimental results, with almost all the deviations within $\pm 20\%$. A number of the existing empirical correlations can also obtain similar predictions. However, when the columns are scaled up to $D_c=0.3, 0.6$ and 0.910 m, the new correlation can still give satisfactory predictions, with deviations within $\pm 35\%$, while previous correlations become much less accurate for large columns. In addition, the new correlation predicts that u_{ms} is $\propto H_0^{0.3}$ for $H_0/D_c > 1.5$, in agreement with the results reported by He et al. [7].

As there are limited experimental results for larger-scale spouted beds in the literature,

evaluation of the [correlation \(1\)](#) or [\(3\)](#) is rather limited. More work is required to test and improve the new correlation. Nevertheless, the new correlations appear able to provide quite good estimation of the minimum spouting velocity in different size beds, for the used cases when $H_0/D_c > 1.5$, and the cone angle is 60° , and air at atmospheric pressure and temperature is the motive fluid.

5.7 Summaries

The numerical scale-up and design method were developed in this chapter. By directly predicting the gas-solid flow behaviors in small- and large-scale spouted bed with the CFD approach, the effects of particle properties, bed structures and operating conditions on the dynamic behaviors in spouted beds with different scales were systematically studied. A series of findings have been published in Can J Chem Eng 2013 (91): 1800-1808, Can J Chem Eng 2013 (91): 1809-1814 and Can J Chem Eng 2014 (92): 768-774. The summaries are as follows:

(1) The angle of the conical bottom of spouted bed significantly influences the gas-solid flows in the bed. With the angle less than 30° , the stable external spout cannot form in the spouted bed. The gas-solid flow behavior in the spouting zone is bounded by the conical angle of 105° . When the conical angle is less than 105° , the particle velocity, voidage and fountain height in the spout decrease with the increasing conical bottom; when the conical angle is larger than 105° , the above parameters show the opposite trends.

(2) The gas-solid flow characteristics in the multiple-spout bed in different operating modes and the effects of the baffle structure were revealed. The significant interactions between the jets and between the jet and the wall make it difficult to form the stable and balanced three-spouting mode in a conventional three-spout bed. With the equal gas velocity in each spouting cell, the lateral spoutings may be subject to the wall resistance and pressed by the central spouting fountain to form the unstable single-spouting mode, or the three jets would strongly interact and merge with each other to form the unstable bubbling state in the bed. Setting baffles with the same height in the

bed can effectively balance the wall resistances on each jets and block the interactions between them, which is beneficial to the stable spoutings in the bed, but would at the same time increase the circulation resistance inside the bed and consume more system kinetic energy.

(3) The hydrodynamics characteristics in the spouted beds with varying scales were directly predicted and analyzed by the simulations. The key parameters for example the minimum spouting velocity in the process of scale-up are obtained with the effects of material properties, bed structure and operating parameters being figured out and a new correlation was proposed to predict the minimum spouting velocity in both small and large spouted beds. Lastly this developed numerical scale-up method and related conclusions were successfully used to design an industrial scale biomass-carrier mixer.

Reference

- 1 Epstein N, Grace J R. Spouted and spout-fluid beds: fundamentals and applications. New York: Cambridge University Press, 2010.
- 2 Mathur K B, Epstein N. Spouted beds. New York: Academic Press Inc., 1974.
- 3 Green M C, Bridgwater J. An experimental study of spouting in large sector beds. *Can J Chem Eng*, 1983, 61(3): 281-288
- 4 Kalwar M I, Raghavan G S V, Mujumdar A S. Circulation of particles in two-dimensional spouted beds with draft plates. *Powder Technol*, 1993, 77(3): 233-242
- 5 Fane A G, Mitchell R A. Minimum spouting velocity of scaled-up beds. *Can J Chem Eng*, 1984, 62(3): 437-439
- 6 He Y L, Lim C J, Grace J R. Scale-up studies of spouted beds. *Chem Eng Sci*, 1997, 52(2): 329-339
- 7 He Y L, Lim C J, Grace J R. Spouted bed and spout-fluid bed behaviour in a column of diameter 0.91 m. *Can J Chem Eng*, 1992, 70(5): 848-857
- 8 Lim C J, Grace J R. Spouted bed hydrodynamics in a 0.91 m diameter vessel. *Can J Chem Eng*, 1992, 65(3): 366-372
- 9 Green M C, Bridgwater J. The behaviour of sector spouted beds. *Chem Eng Sci*, 1983, 38(3): 478-481
- 10 Zhang H Q. The Present status of study on hydrodynamics in larger-diameter spouted beds. *Journal of Shenyang institute of chemical technology*, 1991, 5(2): 105-114 (in Chinese)

- 11 Wei W S, Ji Y, Xu J, et al. Scaling-up of the gas-solid spouted bed. 2006 Annual Conference of Chinese Society of particuology cum symposium on particle technogy across Taiwan Straits, 2006, Beijing (in Chinese)
- 12 Béttega R, Freire J T. Scale-up study of spouted beds using computational fluid dynamics. *Can J Chem Eng*, 2010, 87(2): 193-203
- 13 Costa M D A, Taranto O P. Scale-up and spouting of two-dimensional beds. *Can J Chem Eng*, 2003, 81(2): 264-267
- 14 Lu H, He Y, Liu W, et al. Computer simulations of gas-solid flow in spouted beds using kinetic-frictional stress model of granular flow. *Chem Eng Sci*, 2004, 59(4): 865-878
- 15 Shirvanian P A, Calo J M. Hydrodynamic scaling of a rectangular spouted vessel with a draft duct. *Chem Eng J*, 2004, 103(1-3): 29-34
- 16 Wei D, Xu J, Ye J, et al. Scale-up relationships of spouted beds by solid stress analyses. *Powder Technol*, 2009, 192(3): 273-278
- 17 Németh J, Pallai E, Aradi E. Scale-up examination of spouted bed dryers. *Can J Chem Eng*, 1983, 61(3): 419-425
- 18 Chandnani P P, Epstein N. Spoutability and spout destabilization of fine particles with a gas. In *Fluidization V*, ed. Ostergaard K and Sorensen K. New York: Engineering Foundation, 1986, pp 233-240
- 19 Aradhya S, Taofeeq H, Al-Dahhan M. A new mechanistic scale-up methodology for gas-solid spouted beds. *Chem Eng Proces*, 2016, 110: 146-159
- 20 Ali N, Al-Juwaya T, Al-Dahhan M. An advanced evaluation of spouted beds scale-up for coating TRISO nuclear fuel particles using Radioactive Particle Tracking (RPT). *Exp Therm Fluid Sci*, 2017, 80: 90-104
- 21 Ali N, Al-Juwaya T, Al-Dahhan M. An advanced evaluation of the mechanistic scale-up methodology of gas-solid spouted beds using radioactive particle tracking. *Particuology*, 2017, 34: 48-60
- 22 Wang Q, Zhang K, Brandani S, et al. Scale-up strategy for the jetting fluidized bed using a CFD model based on two-fluid theory. *Can J Chem Eng*, 2009, 87(2): 204-210
- 23 Passos M L, Mujumdar A S, Raghavan V S G. Prediction of the maximum spoutable bed height in two-dimensional spouted beds. *Powder Technol*, 1993, 74(2): 97-105
- 24 Mujumdar A S. Spouted bed technology- a brief review. In *Drying '84*, ed. Mujumdar A S, New York: Hemisphere, 1984, pp.151-157
- 25 Foong S K, Barton P K, Ratcliffe J S. Characteristics of multiple spouted beds. *Mech and Chem Eng, Trans. Instn. Engrs. Aust.*, 1975, 11: 7-12
- 26 Hu G, Gong X, Wei B, et al. Flow patterns and transitions of a novel annular spouted bed with multiple air nozzles. *Ind Eng Chem Res*, 2008, 47(23): 9759-9766

- 27 Chen D, Liu X, Zhong W, et al. Interactions of spout jets in a multiple-spouted bed. *Can J Chem Eng*, 2014, 92(6): 1150-1159
- 28 Ren B, Zhong W, Zhang Y, et al. Investigation on flow patterns and transitions in a multiple-spouted bed. *Energ Fuel*, 2010, 24(3): 1941-1947
- 29 Murthy D V R, Singh P N. Minimum spouting velocity in multiple spouted beds. *Can J Chem Eng*, 2010, 72(2): 235-239
- 30 Freitas L A P, Dogan O M, Lim C J, et al. Hydrodynamics and stability of slot-rectangular spouted beds. II. Increasing bed thickness. *Chem Eng Commun*, 2000, 181: 243-258
- 31 Chen Z W Stability and scale-up of slot-rectangular spouted beds [D]: [Doctor Thesis] University of British Columbia, 2007
- 32 Dogan O M, Freitas L A P, Lim C J, et al. Hydrodynamics and stability of slot-rectangular spouted beds. Part I : thin bed. *Chem Eng Commun*, 2000, 181(1): 225-242
- 33 Du W, Bao X, Xu J, et al. Computational fluid dynamics (CFD) modeling of spouted bed: Assessment of drag coefficient correlations. *Chem Eng Sci*, 2006, 61(5): 1401-1420
- 34 Du W, Bao X J, Xu J, et al. Computational fluid dynamics (CFD) modeling of spouted bed: Influence of frictional stress, maximum packing limit and coefficient of restitution of particles. *Chem Eng Sci*, 2006, 61(14): 4558-4570
- 35 Lan X, Xu C, Gao J, et al. Influence of solid-phase wall boundary condition on CFD simulation of spouted beds. *Chem Eng Sci*, 2012, 69(1): 419-430
- 36 Duarte C R, Neto J L V, Lisboa M H, et al. Experimental study and simulation of mass distribution of the covering layer of soybean seeds coated in a spouted bed. *Braz J Chem Eng*, 2004, 21(1): 1229-1232
- 37 Duarte C R, Olazar M, Murata V V, et al. Numerical simulation and experimental study of fluid-particle flows in a spouted bed. *Powder Technol*, 2009, 188(3): 195-205
- 38 Santos K G, Murata V V, Barrozo M A S. Three-dimensional computational fluid dynamics modelling of spouted bed. *Can J Chem Eng*, 2009, 87(2): 211-219
- 39 Liu X, Shao Y, Zhong W, et al. Prediction of minimum spouting velocity by CFD-TFM: Approach development. *Can J Chem Eng*, 2013, 91(11): 1800-1808
- 40 Huang M H. Numerical simulations on spouted beds. Dissertation for master degree. College of Chemical Engineering, Northwest University, Xi'an, 2009
- 41 Schaeffer D G. Instability in the evolution equations describing incompressible granular flow. *J Differ Equations*, 1987, 66(1): 19-50
- 42 Syamlal M, O'Brien T J. Computer simulation of bubbles in a fluidized bed. *AIChE Symp. Ser.*, 1989, 85(270): 22-31

- 43 Vasquez S, Ivanov V. A phase coupled method for solving multiphase problems on unstructured meshes[C]. ASME FED Summer Meeting, 2000, Boston, MA
- 44 Liu X, Zhong W, Shao Y, et al. Evaluation on the effect of conical geometry on flow behaviours in spouted beds. *Can J Chem Eng*, 2014, 92(4): 768-774
- 45 He Y L, Qin S Z, Lim C J, et al. Particle velocity profiles and solid flow patterns in spouted beds. *Can J Chem Eng*, 1994, 72(4): 561-568
- 46 He Y L, Lim C J, Grace J R, et al. Measurements of voidage profiles in spouted beds. *Can J Chem Eng*, 1994, 72(2): 229-234
- 47 Zhong W Q. Study on the hydrodynamic characteristics and scaling of the spout-fluid bed. Doctor Dissertation, Southeast University, Nanjing, 2007
- 48 Olazar M, Jose M J S, Aguayo A T, et al. Stable operation conditions for gas-solid contact regimes in conical spouted beds. *Ind Eng Chem Res*, 1992, 31(7): 1784-1792
- 49 Shan J, Hu Q, Wang J, et al. Fluidization of coarse particles in gas-solid conical beds. *Chem Eng Proces*, 2000, 39(4): 379-387
- 50 Bi H T. A discussion on minimum spout velocity and jet penetration length. *Can J Chem Eng*, 2010, 82(1): 4-10
- 51 Zhang S F, Wang S H, Zhao J B. Experimental study on hydrodynamics characteristics of double-nozzle rectangular spouted bed. *Chem Eng*, 2006, 34(11): 33-36
- 52 Zhang S F, Wang S H, Zhao B, et al. Hydrodynamics and desulphurization effectiveness of double-nozzle rectangular spouted bed reactor. *Environmental Pollution & Control*, 2006, 28(6): 419-422
- 53 Ren B, Zhong W, Zhang Y, et al. Investigation on flow patterns and transitions in a multiple-spouted bed. *Energ Fuel*, 2010, 24(3): 1941-1947
- 54 Mathur K B, Gishler P E. A technique for contacting gases with coarse solid particles. *AIChE J*, 1955, 1(2): 157-164
- 55 Du W, Bi X, Epstein N. Exploring a non-dimensional varying exponent equation relating minimum spouting velocity to maximum spoutable bed depth. *Can J Chem Eng*, 2009, 87(2): 157-162
- 56 Anabtawi M Z, Uysal B Z, Jumah R Y. Flow characteristics in a rectangular spout-fluid bed. *Powder Technol*, 1992, 69(3): 205-211
- 57 Olazar M, José M J S, Aguayo A T, et al. Hydrodynamics of nearly flat base spouted beds. *Chem Eng J Biochem Eng J*, 1994, 55(1-2): 27-37
- 58 Choi M, Meisen A. Hydrodynamics of shallow, conical spouted beds. *Can J Chem Eng*, 1992, 70: 916-924
- 59 Uemaki O, Yamada R, Kugo M. Particle segregation in a spouted bed of binary

**CHAPTER 6 MIXING BEHAVIORS IN AN INDUSTRIAL
SPOUT-FLUID MIXER**

6.1 Introduction

Biomass utilization technology has attracted increasing attention from both academia and industry, due to its considerable contribution to the current energy requirements, superior performance with regard to the greenhouse-gas neutrality and great capacity to reuse forest and agricultural wastes [1-3]. The thermochemical technologies, typically including gasification and pyrolysis, show outstanding prospects in converting wood, energy crops, agricultural and forest wastes to liquid, solid and gaseous fuels [1, 2, 4-6]. Continuous efforts have been made to develop the efficient biomass thermochemical techniques and new reactors. In this connection, process scale up represents a significant challenge [7-13].

One of the most promising techniques is to introduce heated inert particles, for example bauxite particles, as the heat source to quickly provide part of their energy for biomass gasification or pyrolysis. The heat of the inert particles comes from the exhaust heat of other processes. The most crucial step of this technique is to create sufficient contact between the heat-carrier and biomass particles to ensure that the heat transfer will be quick and uniform. Therefore, a device to mix particles quickly and uniformly is essential in this process.

Among various gas-solid reactors, spouted beds or spout-fluid beds have proved their enormous potential to deal with biomass particles in bench-scale testing, benefiting from their strong ability to provide good particle circulation and handle particles of all types, whether they are large, irregular in shape or complex in texture [10, 14-18]. The mixing in a spouted or spout-fluid bed has been investigated by many investigators [15, 16, 19-24]. For example, Ren et al. [23], Zhang et al. [24] and Liu et al. [24] respectively demonstrated the excellent mixing performance of such a bed in dealing with non-spherical biomass particles, such as corn, wood and bamboo particles, and spherical particles by experimental or simulation tests. However, to be used in a biomass mixing system of industrial-scale, the spouted or spout-fluid processes have many problems to overcome. For example, in order to achieve a continuous operation and best mixing

performance, the first difficulty lies in the proper structural arrangements of the ports of the spouted bed (or spout-fluid bed) for materials feeding and discharge. In a spouted bed, to mix with each other, two kinds of particles need to together undergo at least one spouting circulation. When feed and discharge ports coexist, they need to be elaborately arranged to prevent particles directly getting out of the bed without experiencing any spouting circulation. Considering the treatment capacity at an industrial-scale, the number of the feed and discharge ports and their dimensions also need to be optimized. For biomass particles with relatively low density and small size, another problem is how to arrange their inlets to effectively feed them into a reactor filled with gas. Moreover, the current knowledge on a binary spouting system and its scale-up is significantly deficient. Consequently, to date, it is not clear how to determine the optimum operating conditions of a large-scale spouted bed (or spout-fluid bed), and how to assess the degree of mixing of biomass and inert particles when they come out from the mixer. Solutions to these problems are the key to the successful design and control of such a mixer.

Currently, computational fluid dynamic (CFD) has been increasingly employed as an efficient tool to design dense gas-solid reactors and understand the flow behaviors [25-29]. The Eulerian-Eulerian multiphase model (two-fluid model, TFM) has a distinct advantage to handle large-scale systems because of its effectiveness and relatively low cost [30-32]. In the Eulerian-Eulerian approach, both the fluid and particle phases are treated as inter-penetrating and interacting continua, and in principle this approach can simulate multiphase systems as long as the properties of each phase and interactions between phases are properly described. Therefore, in the present study, CFD (TFM) are chosen to simulate the mixing behaviors of biomass and inert particles in a spout-fluid bed mixer, and three phases, including one gas phase and two solid phases, are involved.

A continuously-operating industrial-scale spout-fluid bed with a capacity to deal with 18.75 t/h of biomass is designed to mix the biomass and heat-carrier particles in the current study. The corresponding three-dimensional (3D) Eulerian-Eulerian multiphase model with a gas-solid-solid multiphase flow is established to investigate and test the

performance characteristics of the mixer, mainly including the flow behaviors and mixing effectiveness of biomass and carrier particles, and the effects of operating conditions, including the spouting and fluidizing gas flowrates, on the mixing behaviors.

6.2 Particle properties and mixer structure

Figure 6-1(a) shows the photographs of biomass particles and heat-carrier particles used in the real industrial process. The biomass is the crushed cornstalk or Mulberry stalk, and the carrier is bauxite particle. Biomass particles are slender and thin with lengths ranging from 1 to 5 mm, while bauxite particles are spherical. According to the sieve analysis, the average nominal diameter of biomass particles is 2.0 mm and that of bauxite particles is 0.5 mm. Based on the practical requirement, the mixer is designed to handle 1.5 million tons of biomass per year (8,000 hours), i.e. 18.75 t/h, and the required heat-carrier is 22.5 million tons per year (281.25 t/h). The feeding mass flowrate ratio, R_{in} , between the heat-carrier and biomass is 15. The gas is superheated steam with temperature of 700 °C and pressure of 0.17 MPa. Other detailed properties of the operating materials are listed in Table 6-1.

To mix above materials, an industrial-scale spout-fluid mixer of the configuration shown in Figure 6-1(b) is designed, its main sizes being listed alongside the figure. The mixer is 3.4 m high and mainly contains four parts: the feed chamber (A), distribution region (B), transition region (C) and mixing region (D). The solid inlets are located at the top section of the system. The relatively heavy heat-carrier particles are poured into the feed chamber from its top, while the light biomass particles are conveyed into the chamber from the two side-entrances by screw feeders. A triangular beam is located at the middle of distribution region (B) to prevent the solid flows from falling onto the central area of the bed surface in the mixing region (D). The mixing region is a spout-fluid bed whose bottom consists of a cone-shaped distributor with porosity 2.6% and a central orifice with diameter 0.1 m. The superheated steam is introduced into the mixer respectively through the central orifice as spouting gas and through the cone-shaped distributor as fluidizing gas. Four outlets are equidistantly located on the flank of the

mixing region at the same height, with their locations kept away from the symmetric planes of the mixer, as seen in Figure 6-1(b). The mixture of biomass, carrier particles and a part of steam is designed to leave from these four mixture outlets, while most of the steam gets out through the two upper fluid outlets located on the lateral sides of the distribution region.

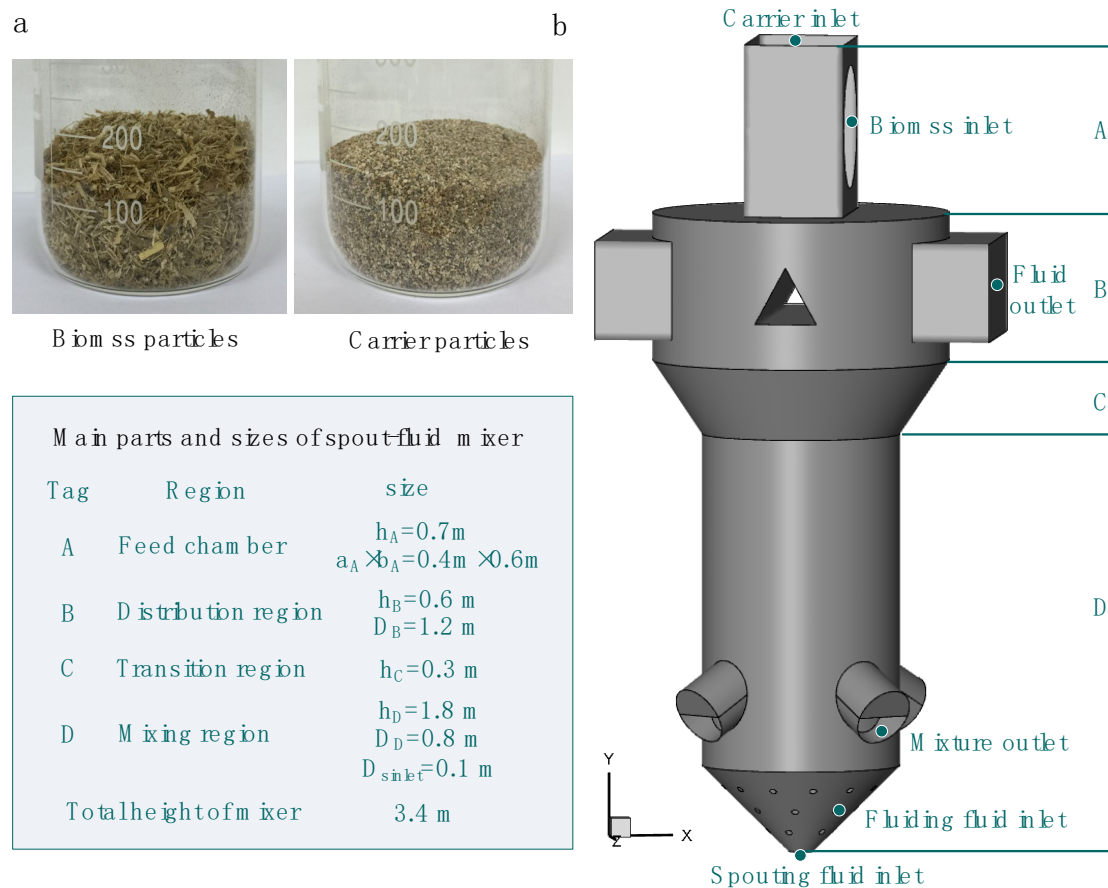


Figure 6-1 Industrial-scale spout-fluid bed mixing system: (a) materials in the given industrial process; (b) schematic of the proposed mixer and its main parts and sizes

6.3 Model description and numerical solutions

To study the performance of the spout-fluid mixer proposed in Section 6.2, the 3D CFD model developed in Chapter 5 based on the Eulerian-Eulerian approach is modified, with superheated steam, carrier particles and biomass particles being treated as three inter-penetrating continua. The motions of phases are respectively controlled by their continuity equations and momentum conservation equations. The viscosities and pressures of two solid phases are determined according to the Kinetic Theory of

Granular Flow (KTGF) [26, 29, 33, 34], which has been shown in Table 5-1. Interactions between gas phase and solid phases are described by the Syamlal-O'Brien drag model [33-35], while the interaction between two solid phases is described by the Morsi-Alexander model [36]. These interaction models are shown in Table 6-1 in detail. The dispersed k-ε multiphase model is adopted to predict the turbulence in the mixer [33, 34].

Table 6-1 Models for the interactions between phases

Interaction between gas and solid (Syamlal-O'Brien model)[35]:

$$\beta = \frac{3 \rho_g \alpha_g \alpha_s |\mathbf{v}_g - \mathbf{v}_s|}{4 v_{r,s}^2 \cdot d_s} C_D \left(\frac{Re_s}{v_{r,s}} \right)$$

$$C_D = \left(0.63 + \frac{4.8}{\sqrt{Re_s/v_{r,s}}} \right)^2, \quad Re_s = \frac{\rho_g \alpha_g |\mathbf{v}_g - \mathbf{v}_s| d_s}{\mu_g}$$

$$v_{r,s} = 0.5 \left(A - 0.06 Re_s + \sqrt{(0.06 Re_s)^2 + 0.12 Re_s (2B - A) + A^2} \right)$$

$$A = \alpha_g^{4.14}, \quad B = \begin{cases} 0.8 \alpha_g^{1.28}, & \alpha_g \leq 0.85 \\ \alpha_g^{2.65}, & \alpha_g > 0.85 \end{cases}$$

Interaction between solid and solid (Morsi-Alexander model) [36]:

$$K_{s_1 s_2} = \frac{3 \alpha_{s_1} \alpha_{s_2} (\alpha_{s_1} \rho_{s_1} + \alpha_{s_2} \rho_{s_2})}{4 (\alpha_{s_1} d_{s_1} + \alpha_{s_2} d_{s_2})} C_D |\vec{v}_{s_1} - \vec{v}_{s_2}|$$

$$C_D = a_1 + \frac{a_2}{Re_s} + \frac{a_3}{Re_s^2}$$

$$Re_s = \frac{(\alpha_{s_1} \rho_{s_1} + \alpha_{s_2} \rho_{s_2}) (\alpha_{s_1} d_{s_1} + \alpha_{s_2} d_{s_2})}{\alpha_{s_1} \mu_{s_1} + \alpha_{s_2} \mu_{s_2}} |\vec{v}_{s_1} - \vec{v}_{s_2}|$$

$$a_1, a_2, a_3 = \begin{cases} 0 & 18 & 0 & 0 < Re < 0.1 \\ 3.690 & 22.73 & 0.0903 & 0.1 < Re < 1 \\ 1.222 & 29.1667 & -3.8889 & 1 < Re < 10 \\ 0.6167 & 46.50 & -116.67 & 10 < Re < 100 \\ 0.3644 & 98.33 & -2778 & 100 < Re < 1000 \\ 0.357 & 148.62 & -47500 & 1000 < Re < 5000 \\ 0.46 & -490.546 & 578700 & 5000 < Re < 10000 \\ 0.5191 & -1662.5 & 5416700 & Re \geq 10000 \end{cases}$$

Table 6-2 Properties of materials for the mixer and numerical parameters

Properties	Unit	value
Temperature of superheated steam, T_{g0}	°C	700
Density of superheated steam, ρ_g	kg/m ³	0.377
Kinematic viscosity of superheated steam, μ_g	kg/(m·s)	3.665×10^{-5}
Nominal diameter of carrier, d_c	mm	0.5
Density of carrier, ρ_c	kg/m ³	2600
Nominal diameter of biomass, d_b	mm	2.0
Density of biomass, ρ_b	kg/m ³	400
Frictional angle of carrier, θ_c		33°
Frictional angle of biomass, θ_b		45°
Carrier-carrier restitution coefficient, e_{cc}		0.9
Biomass-carrier restitution coefficient, e_{bc}		0.25
Biomass-biomass Restitution coefficient, e_{bb}		0.2
Packing limit of carrier, $\alpha_{c,max}$		0.53
Packing limit of biomass, $\alpha_{b,max}$		0.3
Friction packing limit of carrier, $\alpha_{fc,min}$		0.48
Friction packing limit of biomass, $\alpha_{fb,min}$		0.24
Inlet velocity of carrier, $u_{c,inlet}$	m/s	0.28
Inlet concentration of carrier		0.45
Inlet velocity of biomass, $u_{b,inlet}$	m/s	0.167
Inlet concentration of biomass		0.2

A finite volume method is implemented to solve above equations and the unstructured grid is applied in the computational domain with the total number of cells being about 400,000. Finer grids were also tested, for example about 730,000 cells, which did not however have any obvious effect on the simulating results. The first-order upwind discretization is used to convert the partial differential equations to algebraic ones. The time step is 1×10^{-4} s as a compromise between the system stability and computation cost. The phase-coupled SIMPLE algorithm [37] is applied to solve the pressure-velocity coupling and correction. A convergence criterion of 10^{-4} for each scaled residual component is specified for the relative error between successive iterations [29, 33]. Other numerical parameters used in simulations can be found in Table 6-1.

At the inlets of biomass or carrier particles, the velocity and concentration of each solid

phase are specified according to the practical requirements and the detailed information can be found in Table 6-1. At fluid inlets, the velocities of steam at the Spouting fluid inlet and Fluidizing fluid inlets (see Figure 6-1(b)) are respectively specified, with their directions normal to the boundary surfaces. The turbulence kinetic energy of gas phase is $k = (3/2)(uI)^2$, where I is the turbulence intensity which is found from $I = 0.16(\text{Re}_{D_u})^{1/\gamma}$; the turbulence dissipation rate of the gas phase is $\varepsilon = C_\mu^{3/4}(k^{3/2}/l)$, with $C_\mu = 0.09$ and $l = 0.07D_h$.

The gauge pressure at two fluid outlets is 160 kPa. At the four mixture outlets, the pressures are about 163 kPa in the standard condition, and they need some adjustments (within ± 1.5 kPa in the current study) to control the discharge flowrates of mixture when the operating conditions change. For example, when the total steam flowrate entering the mixer increases, the discharge flowrates at the mixture outlets will consequently increase, and at this moment the boundary pressures at mixture outlets will need manual increases to decrease the discharge flowrates. Moreover, in some occasional situations when, for example, huge bubbles form near the mixture outlets blocking the discharge of solids and sharply increasing bed surface, the pressures of mixture outlets also need a slight and temporary decrease (within 0.5 kPa) to increase the mixture discharge flowrates and make sure the height of bed surface in the mixer kept about 0.8 m.

At the beginning of a simulation, mixture outlets are closed while only fluid outlets are open, and no solid materials are fed into the mixer. Some carrier particles are loosely packed in the mixing region ($\alpha_{c,initial} = 0.5$) with the height of 0.8 m. Superheated steam is then introduced from the spouting fluid inlet and fluidizing fluid inlets and interacts with the packed carrier particles. After the flow-time exceeds 5 s with the packed heat-carrier particles in the bed being completely fluidized, biomass and heat-carrier particles start to add from their respective inlets. At the same time the mixture outlets are opened. When the flow-time exceeds about 30 s, the gas-solid flows in the

mixer show some stable patterns. All the data used in the following sections are the results after 40 s.

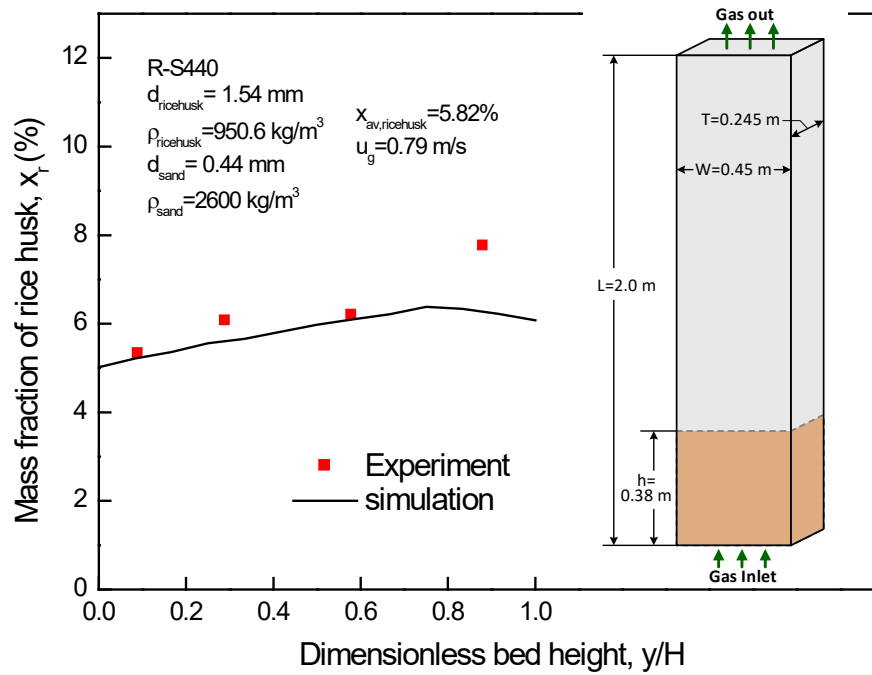


Figure 6-2 Comparison of simulation results with experimental data reported by Sun et al. [38]

6.4 Model validation

Experiment results from Sun et al. [38] for mixing rice husk (5.82 wt%) and sand (94.18 wt%) in a three-dimensional fluidized bed are employed to verify the current model. The experiment presents a typical gas-solid-solid three-phase system, and the rice husk with the size of 1.54 mm is a typically slender, thin and light biomass particles sharing high similarities with the cornstalk or mulberry stalk in our process. Simultaneously, the properties of sand ($d_{\text{sand}}=0.5 \text{ mm}$, $\rho_{\text{sand}}=2600 \text{ kg/m}^3$) are similar to that of carrier particles. Consequently, accurately simulating the flow behaviors of rice husk and sand in such a three-phase fluidizing system can effectively develop and test our current models and parameters about the interactions between phases, especially that between the two solid phases.

It should be mentioned that the main geometry of our industrial spout-fluid mixer (Figure 6-1(b)) is a cylinder, while the fluidized bed of Sun et al. [38] is a cuboid. In

my opinion, the variables that significantly affect the TFM simulations may include the key parameters and models that represent the properties of gas and solids and the interactions between phases, for example, the restitution coefficients, packing limits and friction packing limits of solid particles and the interactions of gas-solid and solid-solid and so on. The similarity in properties of solid particles is obviously much more important to model validations than the bed geometries if the similarities in these two aspects cannot be achieved simultaneously. As the experimental reports on spout-fluid bed similar to the current study are significantly scarce, using the experimental results from Sun et al. [38] in a typical 3D gas-solid-solid system with the solid materials being very similar to ours to validate our models is relatively reasonable although the bed geometries are somewhat different.

Figure 6-2 shows that the simulated time-averaged rice husk mass distribution over the dimensionless bed height is in good agreement with the experimental data, and the average deviation between them is about 5.8%. The noticeable deviation in the top section of the bed was mainly attributed to the experiment error [29], based on the fact that the weighted average mass fraction of rice husk calculated from experimental data ($X_{r,average}=6.3\%$) is larger than the actual initial value (5.82%). Therefore, the model and parameters in Section 6.3 are acceptable and the resulting outcomes are useful for engineering application.

6.5 Typical mixing process

With a number of numerical experiments, the typical operating conditions in the current spout-fluid mixer were obtained: the height of bed level is 0.8 m, and superheated steam (700°C, 0.17 MPa) is introduced with the spouting gas flowrate $Q_s=0.067$ kg/s and fluidizing gas flowrate $Q_f=0.035$ kg/s.

6.5.1 Flow behaviors of solids in the mixer

Typical flow behaviors of carrier particles and biomass particles are shown in Figure 6-3. The carrier particles are uniformly added into the feed chamber from the top inlet

(Figure 6-3(a) left) and they immediately encounter the biomass particles which are fed from the two side-inlets (Figure 6-3(b) left). Then the heavier carrier particles and the lighter biomass particles fall down together from the feed chamber. The triangular beam at the middle of distribution region splits this binary-solid flow into two branches falling downwards along the wall. These two branches then pass through the transition region and arrive at the bed surface in the mixing region.

In the mixing region, the spouting steam and fluidizing steam are respectively introduced from the central orifice and lateral distributor. Submerged cavities continuously form and grow near the central orifice and they eventually become bubbles or big voids getting lifted off and rising into the upper part of the bed level, as seen in Figure 6-3(a) (middle and right) and Figure 6-3(b) (middle and right).

During the formation and rising of bubbles, the particles in the spout-fluid bed are disturbed and entrained, with some being carried from the bed bottom to the top. When bubbles eventually break at the bed surface, some particles are thrown into the space above the bed surface, caused by bubble burst, and then rain back to the bed surface.

The processes of bubble formation, rising and bursting let particles in the bed circulate and mix. Figure 6-4 shows typical representations of the particle velocity field and particle motion paths in the mixer. When particles fall onto the bed surface in the mixing region, four situations possibly take place:

- a) A very small part of particles will directly leave the mixer without experiencing any circulation, as seen in Figure 6-4 middle;
- b) Most particles will move downwards in the annulus (the annular region between the spout and wall), and during this process, they are entrained by bubbles or jets (Figure 6-4, left) and carried back to the upper part of bed level (Figure 6-4, right), from where they leave the mixer. Most of these particles will go through one or more internal loops below the bed surface (Figure 6-4 middle).
- c) Some particles carried by the bubbles will be thrown into the space above the bed

surface when bubbles break up at the bed surface, and then fall back onto the surface of the annulus to finish their external circulations, as seen from Figure 6-4 middle.

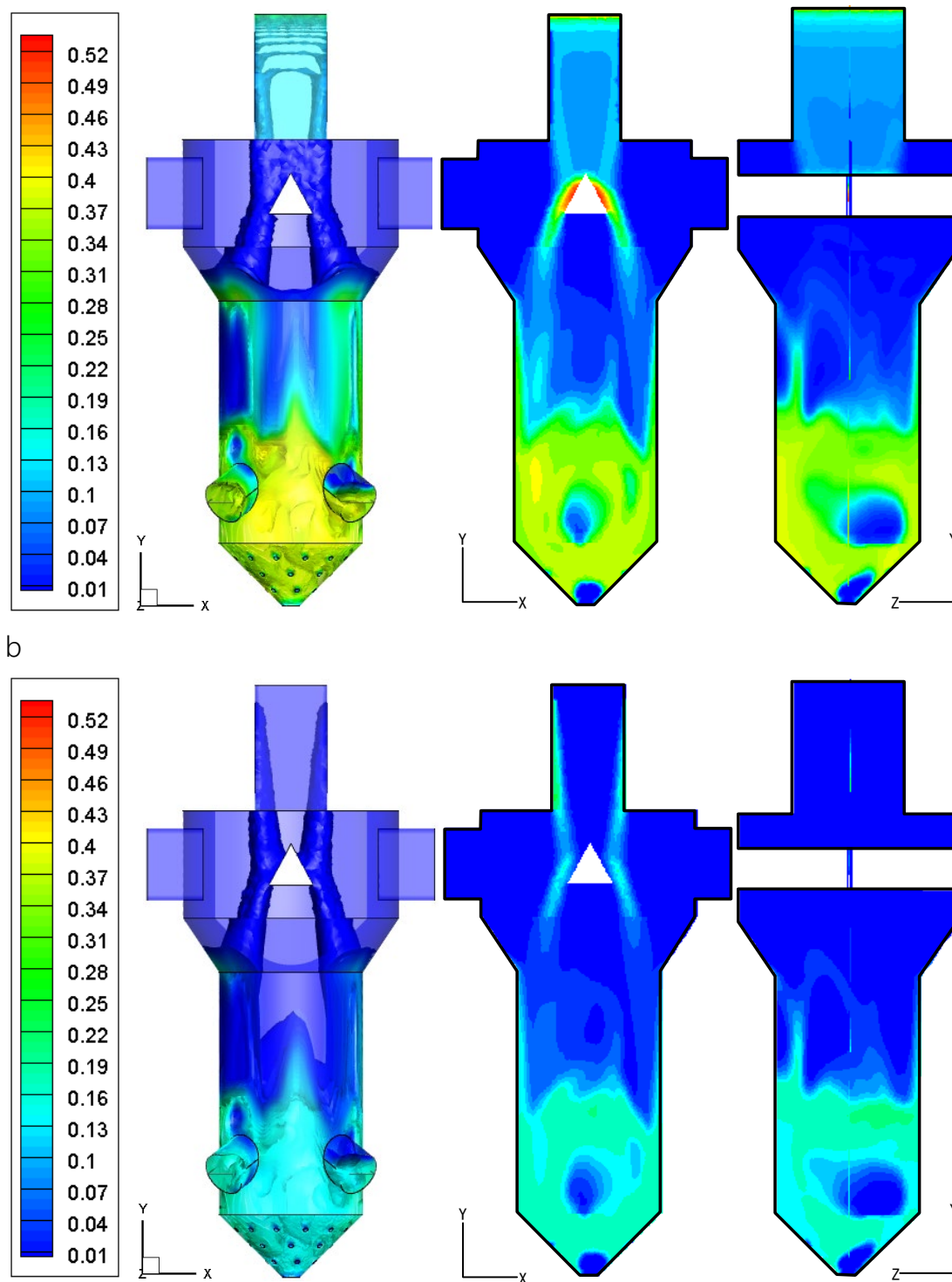


Figure 6-3 Typical flow behaviors of heat-carrier and biomass particles with $Q_s=0.067$ kg/s and $Q_f=0.035$ kg/s: (a) volume fraction of heat-carrier particles; (b) volume fraction of biomass particles. (left: 3D view; middle: $z=0$ section; right: $x=0$ section)

d) Another small group of particles on the loading region will be directly entrained by

the bursting bubbles and carried into the space above the bed surface.

A particle can experience one or more above paths in the mixer, thus causing complicated particle motion patterns. With this complex process, carrier and biomass particles spread from the two loading points to the whole bed and fully mix with each other. Meanwhile the mixed particles continuously leave the mixer from four outlets.

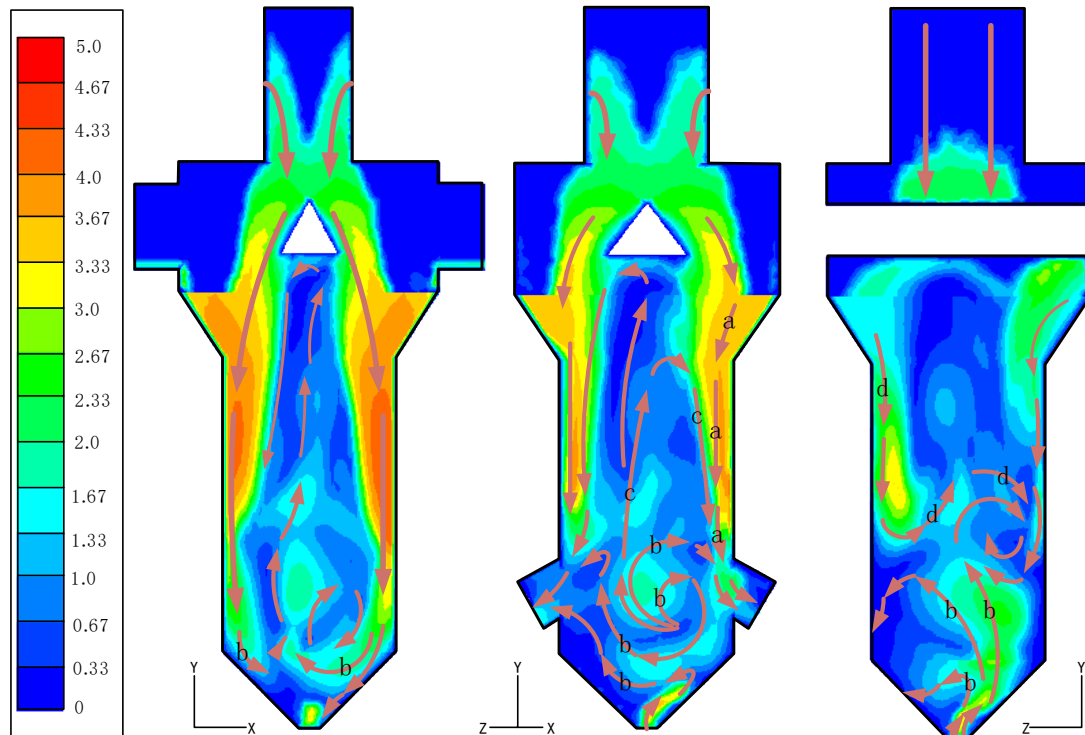


Figure 6-4 Typical velocity fields and motion paths of biomass particles with $Q_s=0.067$ kg/s and $Q_f=0.035$ kg/s. (left: $z=0$ section; middle: $z=x$ section; right: $x=0$ section)

6.5.2 Mixing effectiveness

Mixing effectiveness is one of the most important parameters for mixers. Various mixing indices based on statistical analysis have been employed to describe the solid mixing performance in different processes [6, 16, 39]. However most of them are difficult to implement in an industrial process with continuous operations. In the current work, the mixing effectiveness is evaluated by monitoring the mass ratios of carrier to biomass at the four mixture outlets, and comparing the mass ratio at each outlet with that at inlets. The carrier and biomass are fed into the mixer with a constant mass ratio ($R_{in}=15$) and within a long enough period of time, four sets of the mass ratios of carrier

to biomass at the mixture outlets, R_{out} , can be recorded with a sampling time interval. If the recorded values of R_{out} are always equal to 15 at every sampling time point, the mixing effectiveness, M_e , is considered as 100%. This situation is the fully mixed state. On the contrary, the more serious deviations between the recorded values and 15 will result in the worse mixing effectiveness.

Figure 6-5 gives a group of typical monitoring data for the mass flowrates of carrier and biomass at four outlets with the sampling time $T_s=10.2$ s and the sampling time interval $\Delta t_s=0.3$ s. Due to the unsteady process in the spout-fluid mixer, the mass flowrates of both carrier and biomass always fluctuate with time at the four mixture outlets, and it is impossible to maintain the discharge rate equivalent to the feed rate at every moment. However, by keeping the bed surface at a constant height (about 0.8 m), which can be done by adjusting the outlet flowrates, we can still approximately ensure the mass balance in the mixer. In Figure 6-5, at every outlet, the fluctuations of the mass flowrates of the two materials are very similar, and ratios of their mass flowrates are plotted in Figure 6-6(a). At the all four outlets, the mass flowrate ratios of carrier to biomass are all near to R_{in} ($R_{in}=15$), and the maximum deviation is less than 30%, which indicates a satisfactory degree of mixing.

To characterize the mixing effectiveness in more detail, the statistical treatment carried out on the 140 data samples is illustrated in Figure 6-6(b). During the sampling time ($T_s=10.2$ s), 69% of the data points have a deviation less than 10% from R_{in} . For each of these points, within its sampling time interval, the mixing degree in its local area is considered to reach 90%. This case is recorded as $P_1=0.69$ and $M_1=0.9$. Similarly, there are 24% of the sampling points with the local mixing degree reaching 80%, namely $P_2=24\%$ and $M_2=0.8$, while for the rest of sampling points (8%), the local mixing degree reaches 70% ($P_3=8\%$, $M_3=0.7$). The total mixing effectiveness in the whole sampling time is defined as the weighted average of the above sampling data:

$$M_e = \frac{\sum N_i M_i}{N_{total}} = \sum P_i M_i$$

Based on the above mathematical treatment, the mixing effectiveness for the current case is $M_e=86\%$.

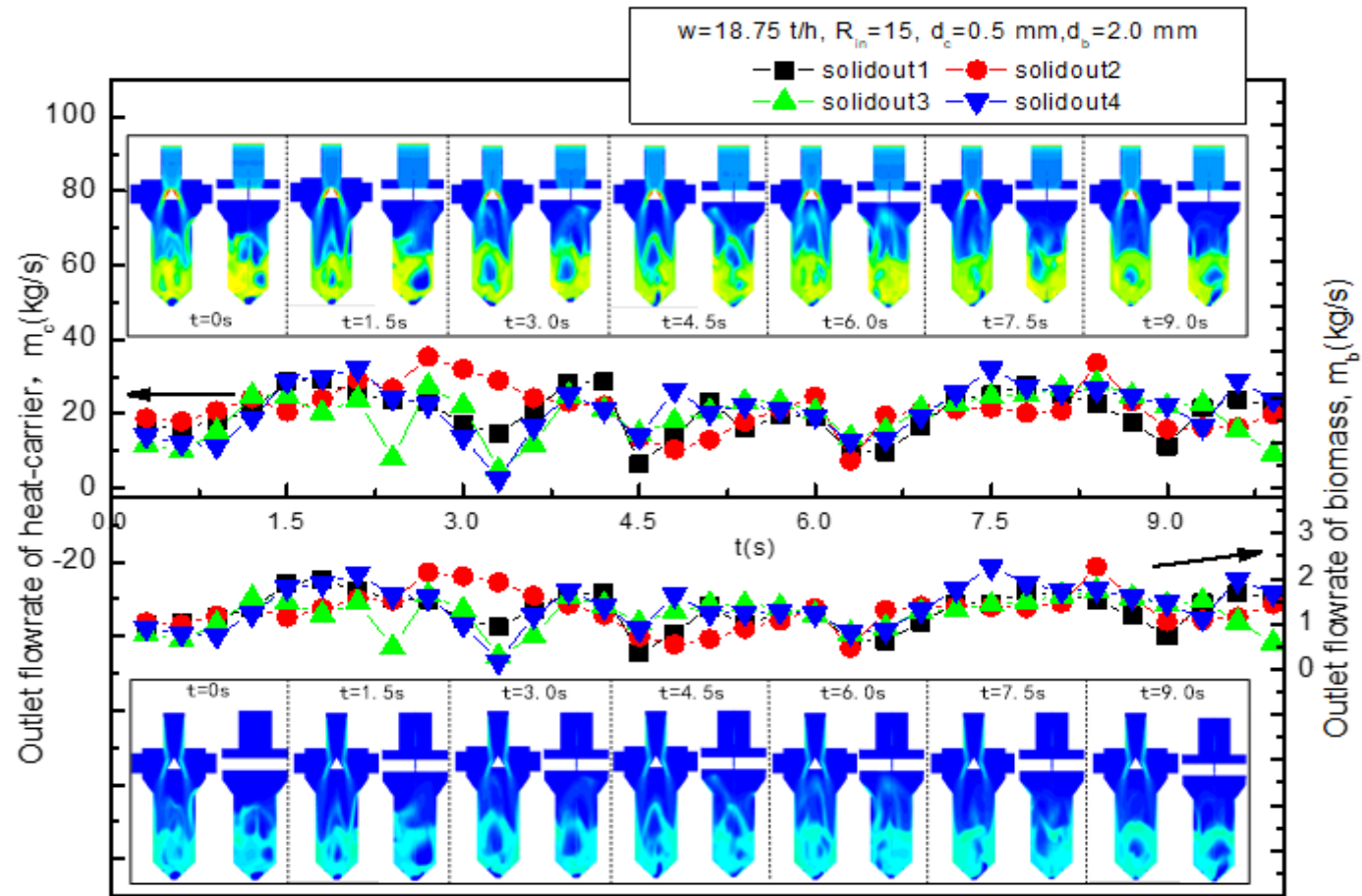
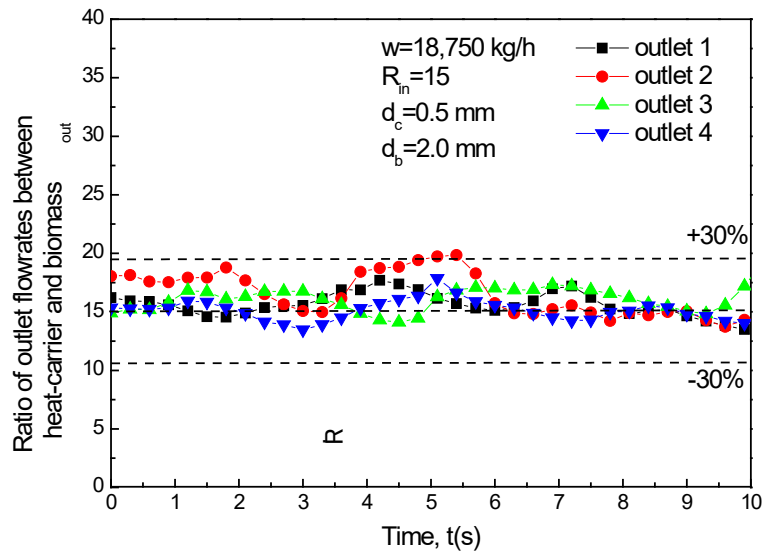
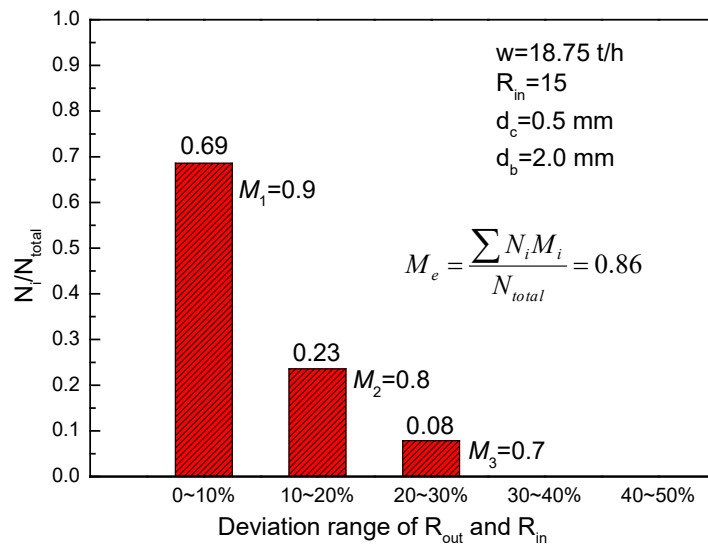


Figure 6-5 Monitoring results of the flowrates of heat-carrier and biomass at four outlets and the corresponding particle behaviors in the mixer with $T_s=10.2$ s, $\Delta t_s=0.3$ s, $Q_s=0.067$ kg/s and $Q_f=0.035$ kg/s

Figure 6-6(a) provides more information in detail. For example, the small deviations between four curves at the same moments show the good spatial uniformity of mass distributions of the two solids in the mixer, and the more moderate fluctuation of a curve presents a well temporal stability of mass distributions of the two solids in local areas, both of which significantly contribute to the good mixing in the mixer.



(a)



(b)

Figure 6-6 Evaluation of mixing effectiveness: (a) monitoring results of mass ratio of carrier and biomass at four outlets; (b) statistical analysis to sampling data. ($Q_s=0.067$ kg/s and $Q_f=0.035$ kg/s)

6.6 Effects of spouting gas flowrate

Spouting gas flowrate and fluidizing gas flowrate are two important operating parameters affecting the flow behaviors in the spout-fluid mixer. To investigate their influences on the mixer performance, the spouting gas flowrate, Q_s , is increased from $0.8Q_f$ to $2.0Q_f$ with the fluidizing gas flowrate, Q_f , being kept at 0.044 kg/s .

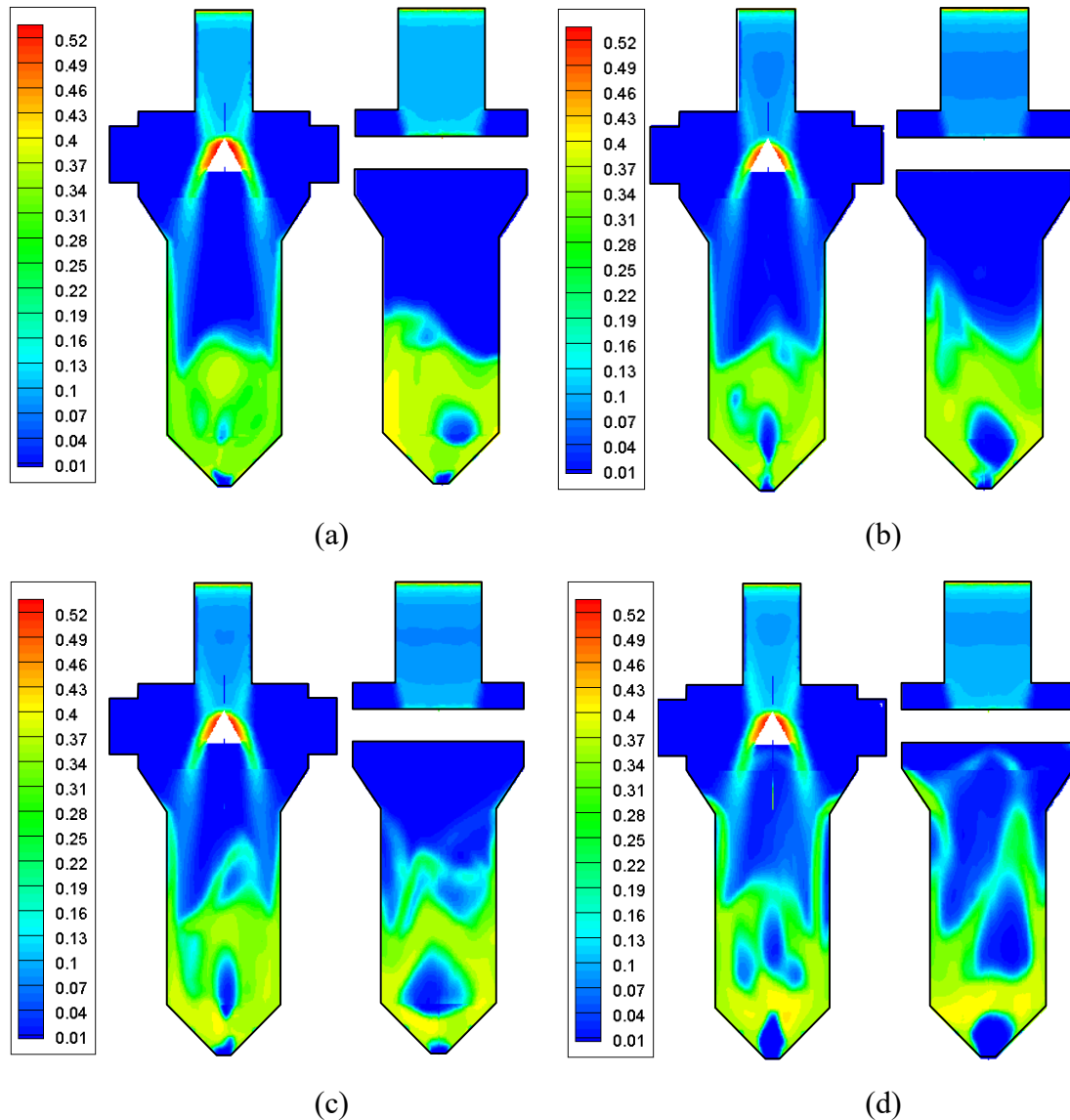


Figure 6-7 Effects of spouting gas flowrate on the flow behaviors in mixer with $Q_f=0.044 \text{ kg/s}$: (a) $Q_s/Q_f=0.8$; (b) $Q_s/Q_f=1.2$; (c) $Q_s/Q_f=1.6$; (d) $Q_s/Q_f=2.0$. (The contour is for the volume fraction of carrier particles. left: $x=0$ section, right: $z=0$ section)

Figure 6-7 shows the different flow phenomena in the spout-fluid mixer with varying Q_s . When Q_s increases from $0.8Q_f$ to $2.0Q_f$, the spout-fluid bed always keeps the state

of the jet with bubbling (JFB) [40]. Bubbles constantly lift off from the top of the short jet, causing bubbling in the upper part of the bed.

The spout-fluid bed has been reported to have at least 6 typical flow regimes in the literature [40]: fixed bed (FB), internal jet (IJ), spouting with aeration (SA), jet in fluidized bed with bubbling (JFB), jet in fluidized bed with slugging (JFS) and spout-fluidizing (SF). In the current case, the carrier particles from practical engineering system are very fine with a diameter of only 0.5 mm. Using too fine solid materials is partially responsible for the disappearance of other flow regimes in the mixer.

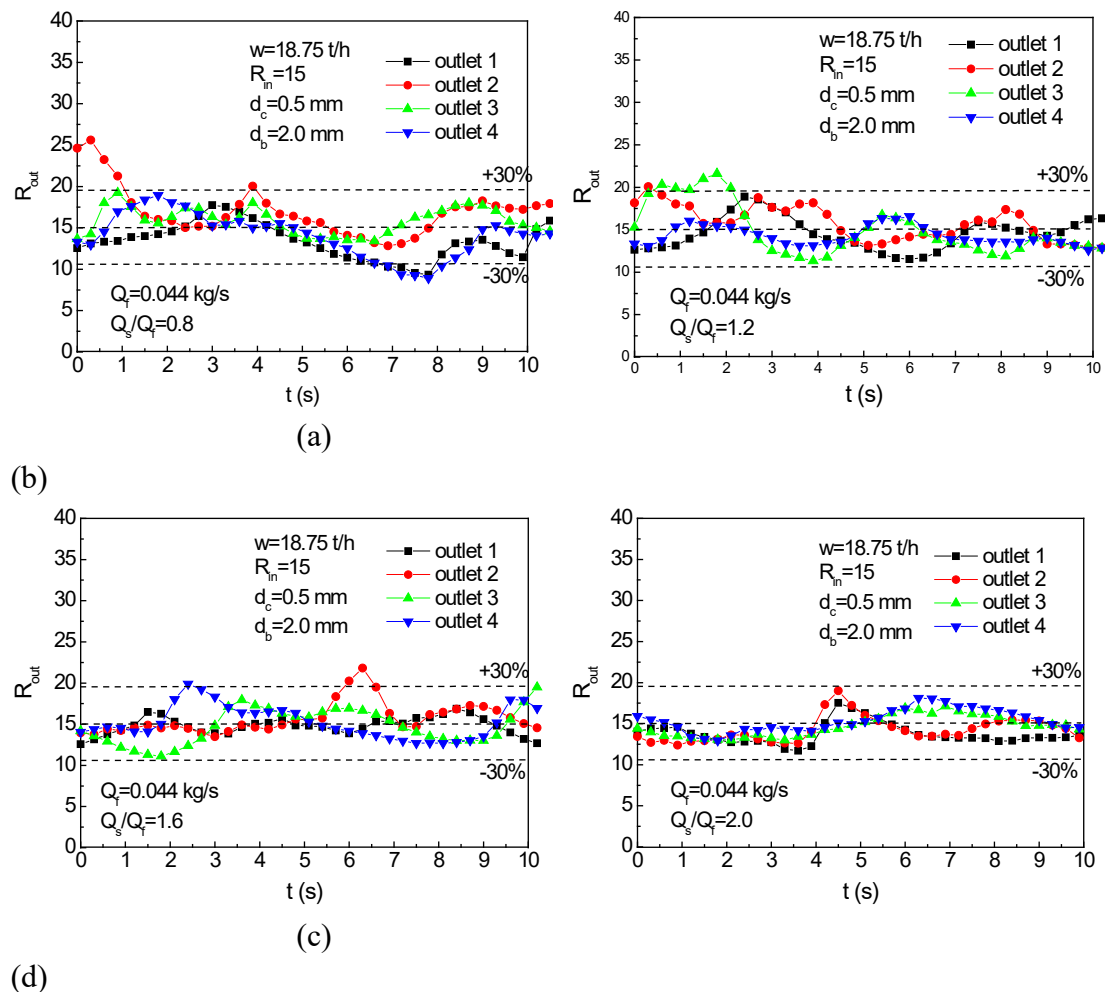
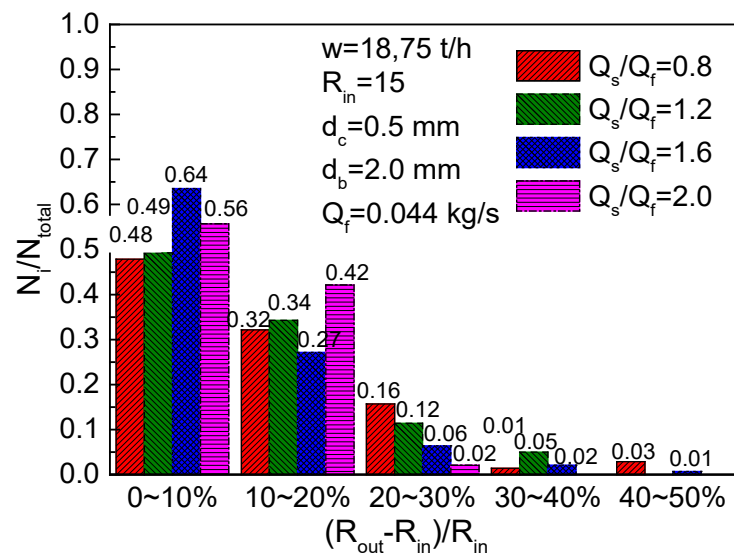


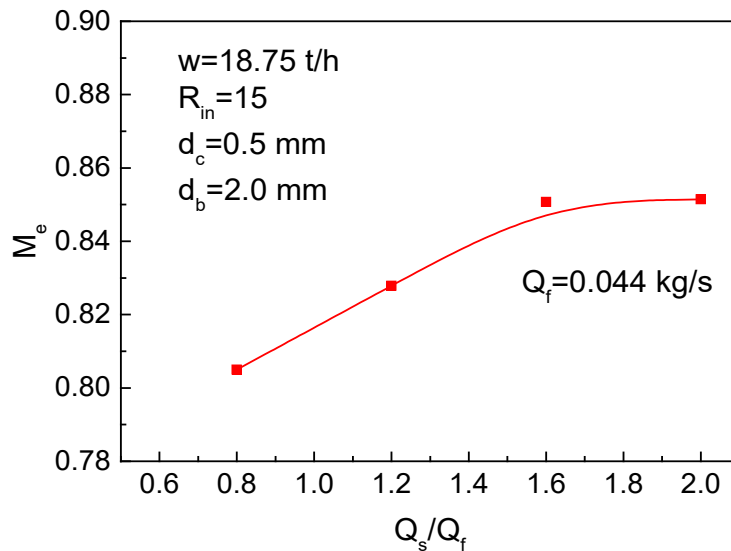
Figure 6-8 Monitoring results of mass ratio of carrier and biomass at four outlets under the conditions of $Q_f=0.044$ kg/s and: (a) $Q_s/Q_f=0.8$; (b) $Q_s/Q_f=1.2$; (c) $Q_s/Q_f=1.6$; (d) $Q_s/Q_f=2.0$

When $Q_s=0.8Q_f$, the bubbles are quite small. They slightly deflect to the wall of the mixer when they get lifted, as shown in Figure 6-7(a). This less severe disturbance

caused by small bubbles corresponds to the less satisfactory mixing effectiveness shown in Figure 6-8(a). The monitoring results reveal that the values of R_{out} at four outlets significantly deviate from each other at some sampling instants, which means the mass distributions of the carrier and biomass particles are spatially non-uniform at those moments. During the whole sampling time, considerable fluctuations in the four curves illustrate the changing mass distribution in their local areas. Additionally, at some sampling instants, the deviation between R_{out} and R_{in} ($R_{in}=15$) is more than 30%, which is unacceptable for the current engineering application.



(a)



(b)

Figure 6-9 Effects of spouting gas flowrate on mixing effectiveness with $Q_f=0.044$ kg/s: (1) statistical analysis to sampling data; (2) Change of M_e with varying Q_s/Q_f

When Q_s increases, bubble size obviously becomes bigger. Due to the impact of solid loading and jetsam, bubbles in the mixer are usually oblate, and their sizes in $x=0$ section are much larger than those in $z=0$ section, as shown in [Figures 6-7\(b\)](#) and [6-7\(c\)](#). At the same time, the increasing spouting gas velocity enhances the formation and rising of bubbles. When Q_s/Q_f is equal to 0.8 or 1.2, only one bubble can be observed in the bed. As a new bubble comes into being, the previous one has risen to the bed surface and burst. When Q_s/Q_f increases to 1.6 or 2.0, more than one bubble exists in the mixer at the same instant. The larger bubbles that form and rise more quickly will provide particles more energy for significant disturbance and fast circulations.

[Figures 6-8\(b\)-\(d\)](#) show the monitoring results of R_{out} when Q_s/Q_f increases from 1.2 to 2.0. With increasing Q_s , the differences of the four curves gradually decrease, and the fluctuation of R_{out} at each outlet becomes smoother. This means that increasing Q_s can efficiently improve the spatial and temporal uniformity of the mass ratio of the two solids in the mixer. [Figure 6-9](#) illustrates the statistical results of mixing effectiveness. When Q_s/Q_f increases from 0.8 to 2.0, M_e accordingly increases from about 0.81 to 0.85.

Although increasing Q_s is conducive to the mixing behavior, there is a limitation for Q_s in the current spout-fluid mixer. If Q_s is too large, the great energy from one or more big bubbles bursting on the bed surface will impact the falling solid flows in the distribution region and transition region. Considering the effective operation of the whole mixing system, it is suitable to keep Q_s in the range of 0.053~0.070 kg/s, when Q_f is fixed at 0.044 kg/s.

6.7 Effects of fluidizing gas flowrate

The fluidizing gas flowrate Q_f is increased from $0.5Q_s$ to $1.5Q_s$ to investigate its effect on the flow behaviors in the mixer under the condition that the spouting gas flowrate is fixed at 0.058 kg/s. Similar to the situations of spouting gas flowrate, when Q_f is increased from $0.5Q_s$ to $1.5Q_s$, the spout-fluid bed still maintains the state of JFB, but the number of bubbles and their rising speeds increase, which introduces increasingly severe disturbance and fast circulation in the spout-fluid mixer, as shown in [Figure 6-](#)

10. However, the significant difference is that the bubble shape becomes prolate rather than oblate when Q_f exceeds $0.5Q_s$. The fluidizing gas flowrate can loosen the packed particles in the bottom of the mixer, and promote radial mass exchange (including gas and solids) between annulus and central regions. When the fluidizing gas flowrate becomes large enough, the severe radial mass exchange prevents large bubbles forming in the central spout region.

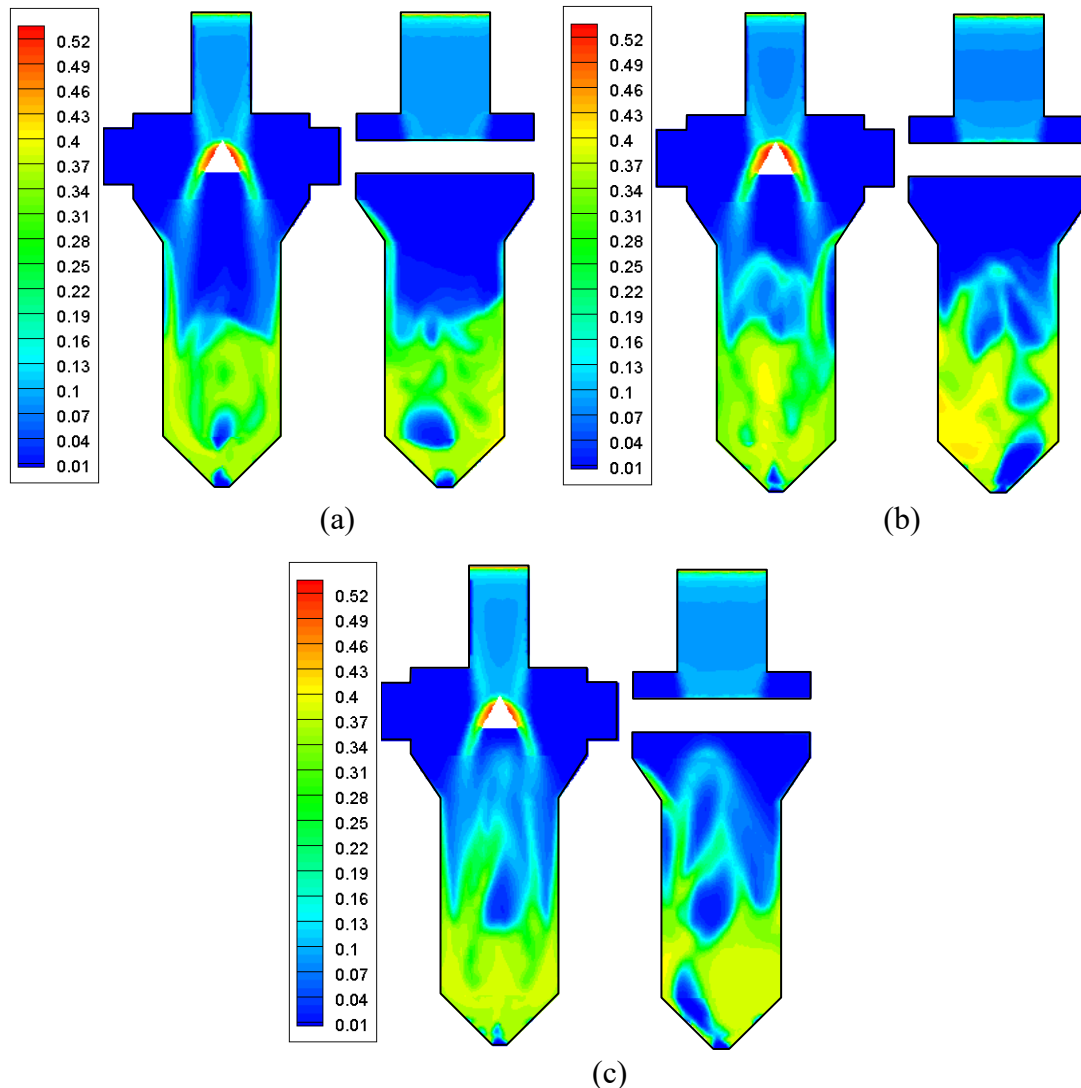


Figure 6-10 Effects of fluidizing gas flowrate on the flow behaviors in mixer with $Q_s=0.058$ kg/s: (a) $Q_f/Q_s=0.5$; (b) $Q_f/Q_s=1.0$; (c) $Q_f/Q_s=1.5$ (The contour is for the volume fraction of carrier particles. left: $x=0$ section, right: $z=0$ section)

When Q_f exceeds $0.5Q_s$, an unfavorable consequence is that the growing bubbles (or internal jets) always tend to deviate from the central region and lean towards the wall of mixer as shown in [Figures 6-10\(b\)](#) and [6-10\(c\)](#). The jets and bubbles in the mixer are

always swaying when they grow or rise. The increasing fluidizing gas loosens the particles near the distributor and even creates small cavities at the inlets of fluidizing gas. It becomes easier for the spouting gas to flow towards this loosely packed region near the distributor than to penetrate the relatively closely packed particles in the central region. To some degree, the swaying jets and bubbles will affect the uniformities of the mass distributions of carrier and biomass in the mixer. In addition, similar to the situation with the increasing Q_s , a too large Q_f will also affect the falling solid flows in the distribution region and transition region.

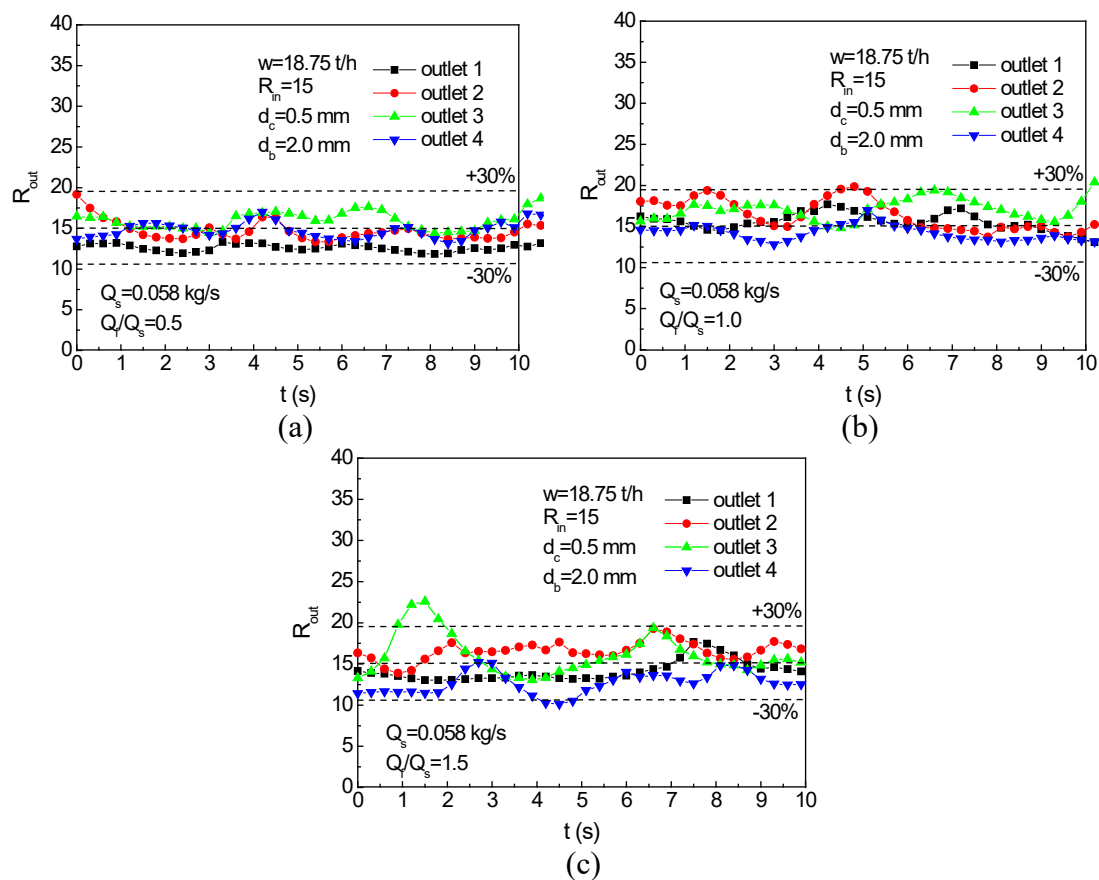
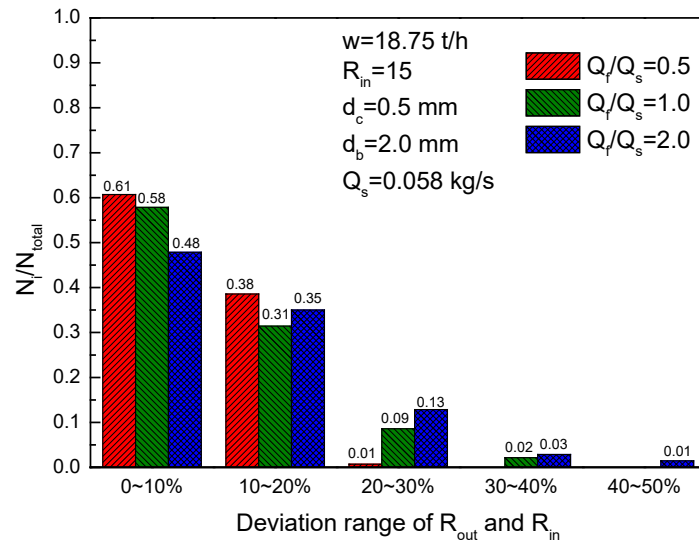


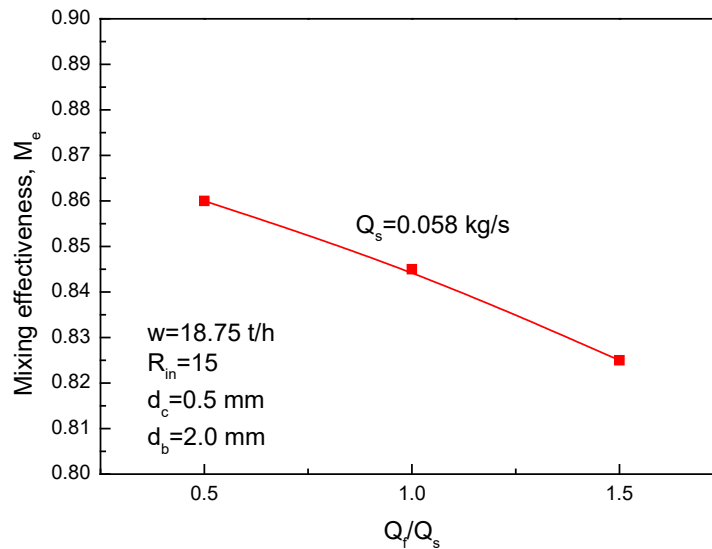
Figure 6-11 Monitoring results of mass ratio of carrier and biomass at four outlets under the conditions of $Q_s=0.058$ kg/s and: (a) $Q_f/Q_s=0.5$; (b) $Q_f/Q_s=1.0$; (c) $Q_f/Q_s=1.5$

The monitoring data of R_{out} and statistical analysis for the above three cases are shown in Figures 6-11 and 6-12. Generally, when $Q_s=0.058$ kg/s, the vast majority of sampling data in Figure 6-11 are within the deviation range of $\pm 30\%$ and the mixing in the mixer reaches a satisfactory level. In the case of $Q_f=0.5Q_s$, four curves have relatively less deviations, and their fluctuations are also less remarkable. With the increase of Q_f , large

fluctuations occur to the certain curves of R_{out} as shown in Figures 6-11(b) and 6-11(c), and several sampling data in Figure 6-11(c) even go beyond the deviation range of $\pm 30\%$. These fluctuations are partially attributed to the swaying jets and bubbles. The statistical results in Figure 6-12 also reveal a slight decrease in mixing effectiveness when Q_f is increased.



(a)



(b)

Figure 6-12 Effects of fluidizing gas flowrate on mixing effectiveness with $Q_s=0.058$ kg/s: (1) statistical analysis to sampling data; (2) Change of M_e with varying Q_f/Q_s

6.8 Summaries

A new industrial-scale spout-fluid mixer with the capacity dealing with 18.75 tons of

biomass per hour was developed to mix biomass and heat-carrier particles, and the corresponding three-dimensional (3D) Eulerian-Eulerian multiphase model with gas-solid-solid multiphase flow was established to investigate the mixer performance, mainly including the flow behaviors of biomass and carrier particles, and the mixing effectiveness. The effects of spouting gas flowrate and fluidizing gas flowrate on the mixing behaviors were numerically studied. The following conclusions can be drawn based on current simulation results:

(1) The proposed spout-fluid mixer with three solid inlets on the top and four mixture outlets near the bottom can successfully realize the industrial-scale continuous operations to mix heat-carrier and biomass particles. The structure of the jet in fluidized bed with bubbling (JFB) is mainly observed in the mixer, and it offers satisfactory mixing under the given industrial conditions ($Q_s=0.067$ kg/s and $Q_f=0.035$ kg/s) with the mixing effectiveness reaching above 80%.

(2) With the increase of spout gas flowrate, bubbles become oblate, and their sizes obviously increase. At the same time the forming frequency and rising speed of bubbles become faster. The mass distributions of the carrier and biomass become more uniform in space and time, and the mixing effectiveness correspondingly increases. There is however an upper limit for Q_s , meaning that a too large Q_s will impact or affect the falling solid flows in the distribution and transition regions, leading to bad mixing.

(3) Satisfactory uniformities of the mass distributions of carrier and biomass can be obtained when $Q_f=0.5Q_s$. When the fluidizing gas flowrate further increases, the bubbles change from oblate to prolate shape, and the growing bubbles (or internal jets) observed from simulations always sway and lean towards the wall of mixer. The distributions of the mass ratios of carrier to biomass show increasing deviations and fluctuations in space and time, leading to a slightly decreased mixing effectiveness.

Reference

1 Bridgwater A V., Renewable fuels and chemicals by thermal processing of biomass. Chem Eng J, 2003, 91: 87-102

- 2 Mohan D, Pittman C U, Steele P H, Pyrolysis of Wood/Biomass for Bio-oil: A Critical Review. *Energ Fuel*, 2006, 20: 848-889
- 3 Cui H, Grace J R, Fluidization of biomass particles: A review of experimental multiphase flow aspects. *Chem Eng Sci*, 2007, 62: 45-55
- 4 Bridgwater A V, Review of fast pyrolysis of biomass and product upgrading, *Biomass Bioenerg.* 2012, 38: 68-94
- 5 Bridgwater A V, Peacocke G, Fast pyrolysis processes for biomass, *Renew Sust. Energ Rev*, 2000,4: 1-73
- 6 Zhang Y, Jin B S, Zhong W Q, Experimental investigation on mixing and segregation behavior of biomass particle in fluidized bed. *Chem Eng Process*, 2009,48: 745-754
- 7 Badger P C, Fransham P, Use of mobile fast pyrolysis plants to densify biomass and reduce biomass handling costs-A preliminary assessment. *Biomass Bioenerg*, 2006, 30: 321-325
- 8 San Miguel G, Makibar J, Fernandez-Akarregi A R, New Advances in the Fast Pyrolysis of Biomass. *J Biobased Mater Bio*, 2012, 6: 193-203
- 9 Venderbosch R, Prins W, Fast pyrolysis technology development. *Biofuel Bioprod Bior*, 2010, 4: 178-208
- 10 Fernandez-Akarregi A R, Makibar J, Lopez G, et al. Design and operation of a conical spouted bed reactor pilot plant (25kg/h) for biomass fast pyrolysis. *Fuel Process Technol*, 2013, 112: 48-56
- 11 Butler E, Devlin G, Meier D, et al. A review of recent laboratory research and commercial developments in fast pyrolysis and upgrading, *Renew. Sust Energ Rev*, 2011, 15: 4171-4186
- 12 Freel B, Graham R, Bio-oil preservatives. [U6485841B1], 2002.
- 13 Faix A, Schweinle J, Scholl S, et al. (GTI-tcbiomass) Life-cycle assessment of the BTO-Process (biomass-to-oil) with combined heat and power generation. *Environ Prog Sustain*, 2010, 29: 193-202
- 14 Erkiaga A, Lopez G, Amutio M, et al. Steam gasification of biomass in a conical spouted bed reactor with olivine and γ -alumina as primary catalysts. *Fuel Process Technol*, 2013,116: 292-299
- 15 Liu X J, Zhong W Q, Jiang X F, et al. Spouting behaviors of binary mixtures of cylindroid and spherical particles. *AIChE J*, 2015,61: 58-67
- 16 Zhang Y, Zhong W Q, Jin B S, Xiao R, Mixing and Segregation Behavior in a Spout-Fluid Bed: Effect of Particle Size. *Ind Eng Chem Res*, 2012, 51: 14247-14257
- 17 Amutio M, Lopez G, Artetxe M, et al. Influence of temperature on biomass pyrolysis in a conical spouted bed reactor. *Resour Conserv Recy*, 2012, 59: 23-31

- 18 Zhu R R, Zhu W B, Xing L C, et al. DEM simulation on particle mixing in dry and wet particles spouted bed. *Powder Technol*, 2011, 210: 73-81
- 19 Zhong W Q, Zhang M Y, Jin B S, et al. Experimental investigation of particle mixing behavior in a large spout-fluid bed. *Chem Eng Process*, 2007, 46: 990-995
- 20 Jin B S, Zhang Y, Zhong W Q, et al. Experimental study of the effect of particle density on mixing behavior in a spout-fluid bed. *Ind Eng Chem Res*, 2009, 48: 10055-10064
- 21 Zhang Y, Jin B S, Zhong W Q, Experiment on particle mixing in flat-bottom spout-fluid bed. *Chem Eng Process*, 2009, 48: 126-134
- 22 Zhang Y, Jin B S, Zhong W Q, et al. DEM simulation of particle mixing in flat-bottom spout-fluid bed. *Chem Eng Res Des*, 2010, 88: 757-771
- 23 Ren B, Zhong W Q, Jin B S, et al. Numerical simulation on the mixing behavior of corn-shaped particles in a spouted bed. *Powder Technol*, 2013, 234: 58-66
- 24 Zhang Y, Zhong W Q, Jin B S, Experimental Investigation on the Translational and Rotational Motion of Biomass Particle in a Spout-Fluid Bed. *Int J Chem React Eng*, 2013, 11: 453-468
- 25 Lu H L, Gidaspow D. Hydrodynamics of binary fluidization in a riser: CFD simulation using two granular temperatures. *Chem Eng Sci*, 2003,58: 3777-3792
- 26 Lu H L, He Y R, Gidaspow D, Hydrodynamic modelling of binary mixture in a gas bubbling fluidized bed using the kinetic theory of granular flow. *Chem Eng Sci*, 2003, 58: 1197-1205
- 27 Nguyen D, Rasmuson A, Niklasson Björn I, Thalberg K, CFD simulation of transient particle mixing in a high shear mixer. *Powder Technol*, 2014, 258: 324-330.
- 28 Zhong H B, Gao J S, Xu C M, et al. CFD modeling the hydrodynamics of binary particle mixtures in bubbling fluidized beds: Effect of wall boundary condition. *Powder Technol*, 2012, 230: 232-240
- 29 Sharma A, Wang S, Pareek V, et al. CFD modeling of mixing/segregation behavior of biomass and biochar particles in a bubbling fluidized bed. *Chem Eng Sci*, 2014, 106: 264-274
- 30 Béttega R, Corrêa R G, Freire J T, Scale-up study of spouted beds using computational fluid dynamics. *Can J Chem Eng*, 2009, 87: 193-203
- 31 Zhong W Q, Liu X J, Grace J R, N, et al. Prediction of minimum spouting velocity of spouted bed by CFD-TFM: Scale-up. *Can J Chem Eng*, 2013, 91: 1809-1814
- 32 Du W, Xu J, Wei W S, et al. Computational fluid dynamics validation and comparison analysis of scale-up relationships of spouted beds. *Can J Chem Eng*, 2013, 91: 1747-1754
- 33 Liu X J, Shao Y J, Zhong W Q, et al. Prediction of minimum spouting velocity by

CFD-TFM: Approach development. *Can J Chem Eng*, 2013, 91: 1800-1808

34 Almohammed N, Alobaid F, Breuer M, et al. A comparative study on the influence of the gas flow rate on the hydrodynamics of a gas-solid spouted fluidized bed using Euler-Euler and Euler-Lagrange/DEM models. *Powder Technol*, 2014, 264: 343-364

35 Syamlal M, O'Brien T J, Computer simulation of bubbles in a fluidized bed. *AIChE Symposium Series*, 1989, 85:22-31

36 Morsim S A, Alexander A J, An investigation of particle trajectories in two-phase flow systems. *J Fluid Mech*, 1972, 55: 193-208

37 Vasquez S, Ivanov V A, A phase coupled method for solving multiphase problems on unstructures meshes. *ASMEFED Summer Meeting*, Boston, 2000.

38 Sun Q Q, Lu H L, Liu W T, et al. Simulation and experiment of segregating/mixing of rice husk-sand mixture in a bubbling fluidized bed. *Fuel*, 2005, 84: 1739-1748.

39 Ren B, Shao Y J, Zhong W Q, et al. Investigation of mixing behaviors in a spouted bed with different density particles using discrete element method. *Powder Technol*, 2012, 222: 85-94.

40 Epstein N, Grace J R. *Spouted and spout-fluid beds: fundamentals and applications*, Cambridge University Press, 2011.

CHAPTER 7 CONCLUSIONS AND FURTHER STUDIES

7.1 Conclusions

Spouted bed, as one of the typical fluidization reactors, has been widely used in many industrial areas, including agriculture, food, pharmacy, energy, environment, and chemical industry, demonstrates commercial successes in a variety of physical operations such as drying, blending, granulation, cooling, coating, as well as the attractive prospects in the thermochemical processes including coal gasification, resource utilization of biomass, oil shale pyrolysis, petroleum catalytic cracking, etc. Nevertheless, our knowledge on spouted beds is still very limited, especially in the aspects of spouting dynamics for non-spherical particles and the methodology regarding the scale-up of reactors, causing difficulties in the design, operation or optimization of spouted beds. The current work is devoted to revealing the complex spouting characteristics of non-spherical particles by physical experiments and numerical simulations and developing a numerical scale-up methodology for spouted beds. These knowledge and method are lastly used to solve a practical engineering issue regarding to biomass utilization.

(1) Macroscopic spouting and mixing behaviors of non-spherical particles

A spouted bed experimental system was established and the spouting and mixing behaviors of cylindroid particles and spherical bed materials were investigated. Results demonstrated that in the case of spouted bed with two kinds of particles, the spouting process and mixing process usually develop synchronously. Once the spouting is well established, the particles in the bed will easily achieve the completing mixing. Such coupled spouting and mixing in the spouted bed can significantly simplify the unknown problems about mixing behaviors in spouted beds by assessing the spouting behaviors which have been understood relatively more comprehensively.

The effects of particle properties (cylindroid particles and spherical bed materials) and operating conditions on the minimum spouting velocity of the mixing system were found closely related to the volume fraction of non-spherical particles. In general, when the volume fraction of cylindroid particles is small, the minimum spouting velocity

increases with the increasing particle size of bed material and static bed height, while the effect of non-spherical particle shape on the minimum spouting velocity of the system is not obvious; When the volume fraction of the non-spherical particles is large, the minimum spouting velocity of the system increases obviously with the increasing aspect ratio of cylindroid particles, as well as the static bed height, and the tendency of the minimum spouting velocity to increase with the increasing sizes of bed material obviously slow down.

Two different system types that dominated by non-spherical particles and spherical bed material were proposed. Generally speaking, when the volume fraction of non-spherical particles is greater than 40%~50%, the spouting system with binary particles is dominated by non-spherical particles with the non-spherical particle properties showing significant influences on the dynamic characteristics and key parameters of spouting, and the particle shape effects cannot be neglected; On the contrary, if the mixing systems is dominated by the spherical bed material, the spouting characteristics and key parameters of the system mainly depend on the properties of bed material .

(2) Dynamics of cylindroid particles in the spouted bed

For the typical spouting systems dominated by the non-spherical particles, the Computational Fluid Dynamics-Discrete Element method (CFD-DEM) approach for cylindroid particles was developed to study the effects of particle shape on spouting behaviors in a flat-bottomed spouted bed. The gas motion was modelled with $k-\varepsilon$ turbulent model, and the particles were represented with realistic cylindroid shapes. The drag force model and various contact forces for cylinders were comprehensively investigated and modified to describe the particle motions more accurately. With the aspect ratio of particle varying from $\gamma=0.25$ to 3.0, spouting behaviors including flow pattern, particle velocity, orientation and contact details were investigated. Results found that cylindroid particles tend to put their longer dimension vertically in spout, while in annulus the orientation tendency is contrary to the prior scenario. The particle with $\gamma=1.0$ obtains the maximum projected area in spout and thus achieved the largest

drag force and particle velocity. When particle shape becomes more flat or long, the particle projected area in spout decreases accordingly, resulting in the decreasing particle velocity and particle circulation rate. On the other hand, when aspect ratio deviates from 1.0, the obviously increasing particle contact number in annulus demonstrates their increasing interlocking effects and worse flowability.

(3) The scale-up and design of spouted beds

The numerical scale-up and design method were developed. By directly predicting the gas-solid flow behaviors in small- and large-scale spouted bed with the CFD approach, the effects of particle properties, bed structures and operating conditions on the dynamic behaviors in spouted beds with different scales were systematically studied.

The angle of the conical bottom of spouted bed significantly influences the gas-solid flows in the bed. When the angle is less than 30° , the stable external spout cannot form in the spouted bed. The gas-solid flow behavior in the spouting zone is bounded by the conical angle of 105° . When the conical angle is less than 105° , the particle velocity, voidage and fountain height in the spout decrease with the increasing conical bottom; when the conical angle is larger than 105° , the above parameters show the opposite trends.

The gas-solid flow characteristics in the multi-spouted bed in different operating modes and the effects of the baffle structure were revealed. The significant interactions between the jets and between the jet and the wall make it difficult to form the stable and balanced three-spouting mode in a conventional three-spout bed. With the equal gas velocity in each spouting cell, the lateral spoutings may be subject to the wall resistance and pressed by the central spouting fountain to form the unstable single-spouting mode, or the three jets would strongly interact and merge with each other to form the unstable bubbling state in the bed. Setting baffles with the same height in the bed can effectively balance the wall resistances on each jets and block the interactions between them, which is beneficial to the stable spoutings in the bed, but would at the same time increase the circulation resistance inside the bed and consume more system kinetic energy.

The hydrodynamics characteristics in the spouted beds with varying scales were directly predicted and analyzed by the simulations. The key parameters for example the minimum spouting velocity in the process of scale-up are obtained with the effects of material properties, bed structure and operating parameters being figured out and a new correlation was proposed to predict the minimum spouting velocity in both small and large spouted beds. Additionally, this developed numerical scale-up method and related conclusions were successfully used to design an industrial scale biomass-carrier mixer.

7.2 Future work

(1) The gas-solid flow characteristics and the effects of particle shapes need to be studied more comprehensively. More kinds of particles with typical non-spherical shapes (for example cuboid, cone and so on) and varying densities and textures should be included and more parameters apart from the minimum spouting velocity that influence or can quantitate the spouting and mixing characteristics of multi-component particle systems need to be identified and investigated. In addition to the simple findings in the regularities and tendencies, more deep understanding and accurate mathematical descriptions should be worked out on the key phenomena and parameters of the spouting or even fluidizing systems with non-spherical particles.

(2) Experiments and simulations on the spouted beds with non-spherical particles were carried out under the normal pressure and temperature in this project. The flows and reactions in the spouted beds with the elevated pressure and high temperature need to be further studied. The clear understanding about the effects of pressure and temperature on the flow and reaction characteristics in the spouted bed is of significant importance to the applications of spouted bed in the practical engineering.

(3) On the basis of the CFD-DEM for cylindroid particles established in this project, simulation methods for the particles with other shapes, as well as for complicated systems that include more than one kind of particles should be further developed. The codes for the turbulent gas phase require urgent improvement to adapt to more complex bed geometries, for example, the three-dimensional spouted beds, the spouted beds with

conical bases and so on. The numerical methods and calculation models with wider applicability and higher accuracy for the representations and contact detections of non-spherical particles, contact forces between particles and interaction forces between particles and fluids in the multi-phase flows with non-spherical particles need to be further investigated. The large-scale and high-accurate simulations for the complex engineering processes involving the multi-phase flows and reactions also require the significant progress in the parallel computing technology.

(4) The industrial-scale spout-fluid reactors proposed in this project need further optimizations. More detailed investigations and discussion have to be conducted on the structure, for example, the effects of internal devices (draft tube, fountain confiner) and so on. On the other hand, as the design was finished on the basis of simulation, some tests and verifications from the engineering practice are required after the real mixer is established in practice. More adjustments and optimization based on the engineering practice are also necessary and inevitable. In addition, to pass as a real reactor to be used in practical industry, detailed control strategy, devices and operating regulations are also required.

List of publications

- [1] **Liu XJ**, Zhong WQ*, Yu AB, Xu B, Lu JD, Mixing behaviors in an industrial-scale spout-fluid bed mixer by 3D CFD-DEM. Powder Technology. 2017, 314:455-465
- [2] Zhong WQ*, Yu AB, **Liu XJ**, Tong ZB, Zhang H, DEM/CFD-DEM modelling of non-spherical particulate systems: theoretical developments and applications. Powder Technology. 2016, 302:108-152. (review article)
- [3] **Liu XJ**, Zhong WQ *, Jiang XF, Jin BS. Spouting behaviors of binary mixtures of cylindroid and spherical particles. AIChE Journal. 2015, 61(1):58-67
- [4] **Liu XJ**, Zhong WQ *, Shao YJ, Ren B, Jin BS, Evaluation on the effect of conical geometry on flow behaviors in spouted beds. Can J Chem Eng. 2014, 92(4):768-774
- [5] Chen DL, **Liu XJ**, Zhong WQ*, Shao YJ, Jin BS, Interactions of spout jets in a multi-spouted bed, Can J Chem Eng. 2014, 92(6) :1150-1159.
- [6] **Liu XJ**, Shao YJ, Zhong WQ *, Grace J R, Epstein N, Jin BS, Prediction of minimum spouting velocity by CFD-TFM: Approach development. Can J Chem Eng, 2013, 91 (11):1800-1808.
- [7] Zhong WQ*, **Liu XJ**, Grace J R, Epstein N, Ren B, Jin BS, Prediction of minimum spouting velocity of spouted beds by CFD-TFM: Scale-up. Can J Chem Eng, 2013,91 (11):1809-1914.